Università degli Studi della Basilicata

Dottorato di Ricerca in

"Ingegneria per l'innovazione e lo Sviluppo Sostenibile"

TITOLO DELLA TESI

"Innovative Techniques for the Retrieval of Earth's Surface and Atmosphere Geophysical Parameters: Spaceborne Infrared/Microwave Combined Analyses"

Settore Scientifico Disciplinare

FIS/06, ING-INF/03

Coordinatore del Dottorato

Prof. Aurelia Sole

Dottorando

Pietro Mastro

Relatori

Prof. Carmine Serio

Prof. Guido Masiello

Dott. Antonio Pepe

Ciclo XXXV

Declaration

I hereby declare that, the contents and organization of this dissertation constitute my own original work and does not compromise in any way the rights of third parties, including those relating to the security of personal data.

Pietro Mastro

2022

* This dissertation is presented in partial fulfillment of the requirements for the **Ph.D. degree** in the Graduate School of the University of Basilicata (UNIBAS).

Success is not final, failure is not fatal, it is the courage to continue that counts.

(Sir Winston Churchill)

Introduction

With the advent of the first satellites for Earth Observation: Landsat-1 in July 1972 and ERS-1 in May 1991, the discipline of environmental remote sensing [1] has become, over time, increasingly fundamental for the study of phenomena characterizing the planet Earth. The goal of environmental remote sensing is to perform detailed analyses and to monitor the temporal evolution of different physical phenomena, exploiting the mechanisms of interaction between the objects that are present in an observed scene and the electromagnetic radiation detected by sensors, placed at a distance from the scene, operating at different frequencies. The analyzed physical phenomena are those related to climate change, weather forecasts, global ocean circulation, greenhouse gas profiling [2], [3], earthquakes, volcanic eruptions, soil subsidence, and the effects of rapid urbanization processes [4], [5], [6]. Generally, remote sensing sensors are of two primary types: active and passive [7]. Active sensors use their source of electromagnetic radiation to illuminate and analyze an area of interest. An active sensor emits radiation in the direction of the area to be investigated and then detects and measures the radiation that is backscattered from the objects contained in that area. Passive sensors, on the other hand, detect natural electromagnetic radiation (e.g., from the Sun in the visible band and the Earth in the infrared and microwave bands) emitted or reflected by the object contained in the observed scene. The scientific community has dedicated many resources to the development of techniques to estimate, study and analyze Earth's geophysical parameters. These techniques differ for active and passive sensors because they depend strictly on the type of the measured physical quantity. In my Ph.D. work, inversion techniques for the estimation of Earth's surface and atmosphere geophysical parameters will be addressed, with emphasis on methods based on machine learning (ML). In particular, the study of cloud microphysics and the characterization of Earth's surface changes phenomenon are the key points of this work, which is organized as follows:

- Chapter I: After a brief characterization of ice and liquid water clouds in terms of their microphysics, the state-of-the-art algorithms for the retrieval of key cloud parameters from observations of the Earth's atmosphere in IR and MW bands will be presented and discussed.

- Chapter II: The topics of this chapter are: i) the description of the radiative transfer equation (RTE) solved within radiative transfer model (RTM) codes for calculating radiances in the IR and MW part of the spectrum and ii) the presentation of the rationale of machine learning (ML)-based inversion algorithms, with emphasis on neural networks (NN) and random forest (RF).

- Chapter III will present an inversion framework for the regression of cloud microphysics parameters from IR and MW observations, developed during the Ph.D. period of activity [1]–[3]. I will refer in particular to IR and MW synergy using simulated satellite observations of the first- and second-generation MetOp platforms (e.g., IASI, IASI-NG, MWS, MHS, and AMSU). Accordingly, to demonstrate the value of MW and IR synergy, a comparison is shown considering architectures based only on MW and IR observations, respectively. Equally important is the description of data processing, with a special emphasis on data dimensionality reduction for the optimization of the regression architectures. Finally, the results obtained using a set of real observations are discussed thus also evaluating the performance against standard numerical weather prediction requirements.

- Chapter IV: Within the context of greenhouse gas analysis this chapter aims to present two studies:

    i) The former that investigates the capability of a machine learning based cloud detection scheme, implemented through the use of a feed-forward NN and principal component analysis (PCA). A

discussion concerning the achieved results and the future improvement of the presented techniques will also finally be considered.

ii) The latter concerns the extension of the ML inversion methodologies to the analysis and study of the dynamics of atmospheric CH_4 at a global scale, using predictive features provided by IASI L1C simulated observations. A regression structure based on deep learning is discussed [4]. The regression performance is evaluated by exploiting a whole set of real IASI sea surface clear sky soundings collocated with representative CH_4 profiles collected from the NDACC (Network for the Detection of Atmospheric Composition Change) FTIR (Fourier-Transform Infrared Spectrometers) network. As such, this approach requires the use of complex pre-processing chains based on dimensionality reduction of input and output features. Therefore, a comprehensive overview of data pre-processing is proposed, emphasizing the role played by PCA.

- Chapter V: A short introduction concerning the basic principles of the synthetic aperture radar (SAR) interferometry for the estimation of the scene topography and surface displacement is first presented. Then, the multiple aperture synthetic aperture radar interferometric (MAI) technique, which is primarily used to measure the along-track components of the Earth's surface deformation is discussed by investigating its capabilities and potential applications. Such a method is widely used to monitor the time evolution of ground surface changes in areas with large deformations (e.g., due to glaciers movements or seismic episodes), permitting one to discriminate the three-dimensional (up–down, east-west, north-south) components of the Earth's surface displacements. Ph.D. activities have also concerned the study of MAI and its specific application for the retrieval of 3-D ground displacement maps from sets of multi-orbit/multi-

track satellite observations [5]. The MAI technique relies on the spectral diversity (SD) method, which consists of splitting the azimuth (range) SAR signal spectrum into separate sub-bands to get an estimate of the surface displacement along the azimuth (sensor line-of-sight (LOS)) direction. The underlying rationale and effectiveness of the MAI and SD techniques, as well as their application, will finally be presented.

- Chapter VI aims to clarify the potential of incoherent and coherent change detection (CD) approaches for detecting and monitoring ground surface changes using sequences of synthetic aperture radar (SAR) images. The Chapter also presents the results of an investigation [6] regarding mainly the mutual interaction of different SAR based coherent/incoherent change detection indices (CDIs) for the rapid mapping of "changed" areas. Specifically, an analysis of the CDIs that synthetically describe ground surface changes associated with a disaster event (i.e., the pre-, cross-, and post-disaster phases), based on the generation of sigma nought and InSAR coherence maps is presented. In this context, artificial intelligence (AI) algorithms have been demonstrated to be beneficial for handling the different information coming from coherent/incoherent CDIs in a unique corpus. For this reason, a publication based on the use of a random forest (RF) classifier is introduced to readers. The classifier is trained to produce CD maps and study the impact on the final binary decision (changed/unchanged) of the different layers representing the available synthetic CDIs. Conclusions concerning the achieved results and future perspectives are eventually considered.

- Chapter VII shortly presents and discusses additional research works related to SAR remote sensing applications performed during the three-year Ph.D. period. Specifically, an innovative space-time adaptive multi-looking technique that operates on a sequence of multitemporal, differential synthetic aperture radar interferograms is presented [7]. Innovative methodologies for studying multi-scale earth surface

deformation phenomena and the correction of TOPS SAR data co-registration errors for non-stationary scenes are also presented [8], [9]. Finally, the analysis of groundwater depletion/inflation and freeze-thaw cycles of ground in the Urumqi region, China [10], and a discussion regarding recent advancements of multi-temporal methods applied to new generation SAR systems and applications are presented [11].

The main achievements of my works have been addressed in the following publications, see [1], [5]–[7], [10]–[14], [14].

CONTENTS

List of Figures

List of tables

Chapter 1

CLOUD MICROPHYSICAL PARAMETERS

Seen from space, Earth looks dominated by clouds. Generally, clouds regularly occupy more than 50% of the planet. The existence of clouds on Earth is mainly driven by the physical phenomenon of condensation of atmospheric water vapor particles. Condensation occurs in the troposphere and stratosphere in response to dynamic processes, such as i) widespread vertical air motion, ii) convection, and iii) mixing. These dynamics are not the only reason for cloud existence; radiation transfer through the atmosphere and the interaction with condensed water vapor layers also play a central role. Such interaction depends mainly on particle concentration, size distribution, shape, thickness, and geometry. In this way, clouds directly force radiation balance and energetics of the earth-atmosphere system. Therefore, an understanding of their composition and structure is of vital importance. In this Chapter, the characterization of ice and liquid water clouds in terms of their microphysics will briefly be presented. This is of fundamental importance to understand the developments made in this Ph.D. thesis. A discussion regarding the state of the art of cloud microphysics parameters retrieval algorithms will also be presented and discussed.

1.1 LIQUID CLOUDS

Liquid water particles are spherical and scatter an amount of radiation proportional to their cross-sectional area [15]. Starting from these two assumptions, it is possible to determine the effective radius of liquid water particles such as:

$$r_e = \frac{\int_{r_{\min}}^{r_{\max}} r \cdot \pi r^2 n(r) dr}{\int_{r_{\min}}^{r_{\max}} r^2 \cdot \pi n(r) dr} = \frac{1}{G} \int_{r_{\min}}^{r_{\max}} r^3 \cdot \pi n(r) dr \quad (1.1)$$

where G and r are the geometric cross-sectional area per unit volume and the radius of a water particle; $n(r)$ is the distribution of water particles size of limits $\left[r_{\min}, r_{\max}\right]$. Considering Equation (1.1), the expression of cloud liquid water content can be defined as:

$$CLWC = \frac{4\pi}{3} \rho_{water} \int_{r_{\min}}^{r_{\max}} r^3 n(r) dr \quad (1.2)$$

where ρ_{water} indicates the density of water. Finally, being Δz the size of a liquid water cloud, it is possible to determine the cloud liquid water path (CLWP) as follows:

$$LWP = LWC \cdot \Delta z \quad (1.3)$$

1.2 ICE CLOUDS

The definition of ice clouds' microphysical state is much more complicated because of the non-spherical nature of ice particles. The ice particle shapes depend mainly on the variation of atmospheric temperature and humidity [16], [17]. From aircraft observations at midlatitudes, hollow columns and hexagonal plates are the most abundant types of shapes near the cloud top for most ice clouds. Bullet rosettes are predominant shapes above about -40°C, while hollow or solid columns prevail below temperatures of about -50°C. Across these temperatures, collision, and coalescence phenomena aggregate ice particles into spatial crystalline forms (e.g., hollow columns) that become the predominant shape within the cloud. Ice particle size varies greatly in time and space and the correct definition of its size distribution is an open problem in

the literature. In this way, a general definition of ice cloud effective radii could be written in terms of volume V[1] of an ice particle and the geometric area projected on a surface perpendicular to incident radiation A:

$$d_e = \frac{\int_{L_{\min}}^{L_{\max}} V \cdot n(L)\, dL}{\int_{L_{\min}}^{L_{\max}} A \cdot n(L)\, dL} \tag{1.4}$$

where L is the size of ice particles and $n(L)$ is the distribution of ice particles size limited in $[L_{\min}, L_{\max}]$. Thus, the definition of the cloud ice water content (CIWC) is:

$$CIWC = \int_{L_{\min}}^{L_{\max}} V \rho_{ice} n(L) dL \tag{1.5}$$

where ρ_{ice} is the ice density. Finally, considering an ice cloud of layer size Δz the cloud ice water path (CIWP) is determined as follows:

$$CIWP = CIWC \cdot \Delta z \tag{1.6}$$

1.3 RETRIEVAL ALGORITHMS FOR CLOUD PRODUCTS

Observations from space offer a powerful tool for the study of the cloud-radiation interaction and the retrieval of cloud properties. The parameters introduced in Sections 1.1 and 1.2 are essential to investigate the way clouds affect the hydrological cycle and radiative components of the climate system.

In the last four decades, the continuous improvements in spatial and spectral resolutions of satellite-borne sensors have promoted more sophisticated retrieval procedures to estimate new cloud products with enhanced accuracy. In this framework, several methodologies have been developed to retrieve cloud properties

[1] For a hexagonal ice crystal $V = \frac{3\sqrt{3}LD^2}{8}$ with D the ice crystal width.

from satellite observations. Hereinafter, there is a literature review of the methods using microwave (MW) and/or infrared (IR) atmosphere measurements acquired by passive satellite sensors.

1.3.1 MICROWAVE OBSERVATION

Passive MW observations are sensitive to atmospheric temperature, humidity, and liquid water/ice within the observed volume. Liquid water and ice particles affect the observed brightness temperature (BT) in diverse ways due to the different spectral properties of the refractive index of water/ice. For example, the BT at 23.8 and 89 GHz is more strongly influenced by liquid clouds than cirrus for equivalent water paths. In contrast, channels near 157 and 183 GHz are more strongly influenced by ice clouds. Since the 1980s, MW radiometric applications for estimating cloud microphysical parameters are based on both physical and empirical approaches, becoming well consolidated. Atmospheric water vapor and cloud liquid water information can generally be obtained from channels at 23.8, 31.4, 90, and 183 GHz. Information on ice clouds and precipitation can be obtained from millimeter-wave measurements at 90 and 150 GHz and possibly from higher frequency window channels. Most of the early developments to retrieve geophysical variables from MW radiances exploited the Special Sensor Microwave/Imager (SSM/I) including, total precipitable water (TPW) [18], CLWP, CIWP, and precipitation [19], CLWP and cloud frequency [20].

With the launch of the Advanced Microwave Sounding Unit (AMSU) Grody et al. 2001, present a regression algorithm for retrieving TPW and CLWP over oceans using AMSU channels at 23.8 and 31.4 GHz. The theoretical background of the TPW and CLWP algorithm is the same as for the SSM/I, but it accounts for the geometrical and spectral differences between SSM/I and AMSU. Extensive comparisons have been made between the TPW and CLWP retrievals from AMSU and other satellite instruments (e.g., SSM/I), ground-based radiometers [21], and radiosonde data. It was shown that the CLWP time series of the AMSU and ground-based sensors follow each other within the 0-0.5 kg/m^2 dynamic range. Radiosonde comparison showed differences less than 3 kg/m^2 in terms of Root Mean Squared (RMS) difference and biases less than 1 kg/m^2 over the range between 5 and 60 kg/m^2.

The authors of [22] report an algorithm to derive *CIWP* and ice particle effective radii d_e from AMSU measurements. The algorithm relates both *CIWP* and

d_e to the ice particle scattering parameters, which are determined from AMSU measurements at 89 and 150 GHz. The algorithm was found to miss the detection of thin cirrus surrounding the precipitating areas, suggesting that synergic use of higher frequencies in Infrared (IR) or Visible (VIS) measurements would be helpful to detect these thin clouds. The major error sources affecting the retrievals are identified in terms of cloud-base BT estimation, retrieved particle d_e , and volume density. It is shown that d_e possibly contains an error of 5%–20%. A 30% error in bulk volume would alone result in a 25% error in retrieved *CIWP*.

In [23], the authors describe the operational hydrological products from AMSU, named Microwave Surface and Precipitation Products System (MSPPS), and present some inter-comparisons with other satellite products and ground-based observations. TPW and CLWP are estimated using 31 and 23 GHz channels, mainly based on the algorithms reported by [24], while CIWP and ice particle effective diameters d_e are simultaneously derived from 89 and 150 GHz using the algorithm in [22]. TPW and CLWP are retrieved only over the ocean, while CIWP is computed over both land and ocean, but only if there is no ice/snow on the background surface, as inferred from AMSU lower frequency channels. Validation is reported for radiosonde TPW at nine stations, and ground-based radiometric CLWP estimates at the ARM sites in Manus Island and Nauru, which are representative of open ocean conditions, for 6 months. Note that since CLWP is not nearly as spatially homogeneous as TPW, special treatment of the ground-based reference data is applied to better utilize them for the AMSU validation, as described by Grody et al., 2001. This resulted in approximately 190 CLWP match-up points for NOAA-15 and 160 for NOAA-16, showing ~0.6 correlation, ~0.05 kg/m^2 RMS difference, and a small bias (<0.01 kg/m^2). A binned analysis is also reported, to reduce the nonuniform data distribution across the available range. This is obtained by binning CLWP retrievals into 0.01 kg/m^2 bins based on the ground-based reference measurements in the 0-0.10 kg/m^2 range. The main conclusions drawn from the binned analysis are: (i) there is little bias in the AMSU-derived CLWP for values < 0.3 kg/m^2, which indicates that the algorithm is adequate under non-raining conditions; (ii) there is some angular dependency on the retrievals, most likely attributed to the larger FOV of the AMSU-A sensor as the view angle increases.

The work [25] presents the retrieval of CLWC profiles. This CLWC profiling algorithm is based on a model for moisture condensation in which the relative humidity for the onset of clouds is a retrieved parameter, which makes the retrieval

more robust to errors in the retrieved temperature profile and horizontal inhomogeneities of the moisture field within an instrument footprint. This work represents the first phase of developing algorithms for retrieving geophysical parameters from observations from AMSU and other sensors (e.g., the Atmospheric Infrared Sounder (AIRS)). The vertical distribution (cloud mean pressure) is compared to relative humidity profiles from dedicated radiosondes launched during the Aqua satellite overpass, while the CLWP obtained from the retrieved CLWC is compared with ground-based radiometric measurements. Results for CLWP over ocean show 0.35 correlation and 0.05 kg/m^2 RMS difference, while over land 0.51 correlation and 0.12 kg/m^2 RMS. The main conclusions are that the developed algorithms have some abilities in estimating the vertical distribution of cloud liquid water, as well as the integrated amount over a water surface. Retrievals over a land surface are also demonstrated, although only in a fraction of cases. Also here, the author suggests that the incorporation of infrared measurements will improve cloud detection and the overall performance of the algorithm.

In [26] the authors present a one-dimensional variation method (1D-Var) to retrieve the profiles of atmospheric temperature, water vapor, and cloud water from simultaneous satellite MW imaging and sounding channels. At first, the profiles of temperature, water vapor, and cloud liquid water are derived using only the AMSU-A measurements at frequencies less than 60 GHz. The second step is to retrieve rain and ice water using the AMSU-B measurements at 89 and 150 GHz. Finally, all AMSU-A/B sounding channels at 50–60 and 183 GHz are utilized to further refine the profiles of temperature and water vapor while the profiles of cloud, rain, and ice water contents are constrained to those previously derived. The 1D-var retrieval algorithm is validated in terms of TPW against radiosonde data and collocated satellite measurements. TPW biases are relatively small (<0.3 kg/m^2) and RMS difference is 2.7, 2.3, and 2.5 kg/m^2, depending on platform (NOAA-15, -16, -17, respectively). The performance of the 1D-var algorithm is also tested using the global AMSU data over land and oceans (but excluding the data over high latitudes beyond 60° north and south) against GDAS global reanalysis. The TPW bias and RMS difference of the zonal means are 0.15 and 0.75 kg/m^2, respectively.

The works [27], [28], and [29] present the design of a constellation of mini-satellite, deploying millimeter-wave (MMW) scanning radiometers. The proposed mission aims at the retrieval of thermal and hydrological properties of the troposphere, specifically temperature and water-vapor profiles, *CLWC* and *CIWC* profiles, and rainfall and snowfall rates. The channels are selected following the

ranking based on a reduced-entropy method between 90 and 230 GHz. Only simulated data are available since the mission was limited to the feasibility study. In particular, in [27] the authors evaluate quantitatively the benefit of a 1D-Var scheme to derive hydrometeor profiles from the proposed set of MMW observations. Results are shown for the channel combination that provided the best performances in the reduced-entropy ranking (10 channels from 89 to 229 GHz). The retrieval performance is quantified in terms of statistics of the residual error between the true profiles and the profiles retrieved from the simulated observations using 1D-Var. The accuracy of the retrieved hydrometeor profiles over land and sea for a winter and summer season at several latitudes shows the beneficial performance. The error std statistics demonstrate that the contribution to the forecast is rather small but consistently positive for both *CLWC* and *CIWC*, and it is more significant over the ocean than over land. In [28] the exploitation of two statistical inversion schemes (the multiple regression and the maximum likelihood) to quantify the overall accuracy of four selected MMW radiometer configurations is investigated. The performances of two inversion schemes are shown to be comparable, indicating a retrieval uncertainty only slightly algorithm-dependent. Specifically, considering multiple regression with their best channel configuration (10 channels from 89 to 229 GHz), the authors report the following expected correlation (R) and RMS uncertainty (σ):

- CLWP (0-1.4 kg/m^2): R=0.70; σ=0.08 kg/m^2 over land; R=0.87; σ=0.04 kg/m^2 over ocean.

- CIWP (0-0.25 kg/m^2): R=0.58; σ=0.01 kg/m^2 over land; R=0.64; σ=0.03 kg/m^2 over ocean.

Note that the correlation increased significantly for precipitation-sized ice particles (i.e., graupel), R=0.86 over land and 0.97 over the ocean.

Finally, the expected RMS uncertainty for CLWC profiles is also provided, within 0.1 g/m^3 over land and 0.04 g/m^3 over the ocean, though the authors warn that these results should be considered valid for the available dataset only.

[30] presents a Neural Network (NN) algorithm, applicable for high latitude open water areas, to retrieve TPW and CLWP from SSM/I and Advance Microwave Sounding Radiometer for EOS (AMSR-E) observations. Products are validated against radiosonde data from a polar station. They show that NN performs better than the conventional regression techniques. The resulting SSM/I and AMSR-E

retrieval errors are 1.09 kg/m^2 and 0.90 kg/m^2 respectively. For SSM/I, the TPW algorithm is compared with the global operational algorithm in Wentz and Spencer 1998. The retrieval errors are 1.34 kg/m^2 and 1.90 kg/m^2 (~40% worse) for the two algorithms, respectively, demonstrating the advantages of NN.

In [31], the Microwave Integrated Retrieval System (MIRS) algorithm, a 1D-Var scheme developed at NOAA in 2007, is applied to data from the ATMS onboard SNPP. The products are inverted simultaneously in a land-ocean-atmosphere-cryosphere coupled inversion approach, ensuring that all radiances are fitted simultaneously and ensuring that the geophysical consistency is also satisfied. The assessment of the MIRS performances used a mixture of in situ measurements (radiosondes, radar, gauges, and ground-based surface sensors) as well as ECMWF-generated analyses and heritage algorithms (e.g., MSPPS). Indeed, MIRS is supposed to replace the MSPPS as the NOAA operational product, through a multi-phase smooth transition[2]. The authors provide an example of TPW validation against the European Centre for Medium-Range Weather Forecasts (ECMWF) predictions for one day, showing a 0.99 correlation and 3.1 kg/m^2 RMS difference. Such a daily validation is now produced operationally at: https://www.star.nesdis.noaa.gov/mirs/geonwp.php. However, the authors note that hydrometeor parameters cannot be validated directly because of the absence of reliable ground truth, and thus, given the mechanism employed by MIRS by which the hydrometeor profiles are used to generate a surface rainfall rate, assume the validation of the surface rainfall rate as a proxy for the validation of all MIRS-based hydrometeors. Using this approach, the MIRS ATDB (v1.0[3]) reports the expected bias and RMS uncertainty for TPW over land (1.5 and 2.5 kg/m^2, respectively) and ocean (1.7 and 2.2 kg/m^2), and for CLWP over ocean (0.03 and 0.10 kg/m^2).

Two algorithms were proposed in [32] to estimate TPW and CLWP from FY-3D sensor observations over the ocean, by combining two oxygen band channels (52.80 and 118.75 $\pm$ 2.5 GHz), instead of relying on the classical low-frequency window channels (23.8 and 31.4 GHz), which are missing in FY-3 sensor. Four groups of experiments and verifications were conducted to evaluate the performance of the algorithms. The estimations from FY-3C double oxygen-absorption band observations were compared with retrievals from the traditional [33] scheme applied to MetOp-B AMSU measurements at 23.8 and 31.4 GHz. It is

[2] https://www.star.nesdis.noaa.gov/mirs/documents/documentation/doc_v11r3/NOAA_Products_MSPPS2MIRS_Transition.pdf

[3] https://www.star.nesdis.noaa.gov/jpss/documents/ATBD/ATBD_MIRS_v1.0.pdf

shown that the CLWP retrievals from the double oxygen absorption band have close correlation coefficients, biases, and RMS values with the results of the AMSU traditional scheme. Conversely, the performances of TPW retrievals from double oxygen-absorption band observations are significantly worse than those obtained with AMSU traditional scheme. More recently, [34] reports a machine learning technique used to generate BT at the two missing low-frequency channels from observations at a higher frequency, with a mean absolute error between 3 and 4 K. A statistical inversion method is adopted to retrieve TPW and CLW over oceans, which compares well in magnitude and distribution with estimates from Suomi NPP ATMS.

[35] presents an assessment of CLWP retrievals from MIRS. The CLWP product is assessed by using both ground-based radiometric observations (ARM site in Azores, Portugal) and a satellite-based reference dataset (NASA GPROF). For the ground-based comparison, the collocation method considers FOV that falls within a 3-km radius centered at the site and observations that fall within 30 minutes from the satellite overpass. A 3-year dataset is collected (1535 match-ups), with overall all-season correlation coefficient, bias, and standard deviation of 0.59, -0.065 kg/m^2, 0.2 kg/m^2, respectively. The seasonal analysis shows correlation coefficients for all four seasons higher than 0.5 with fall having the highest value of 0.66. Fall also has the smallest bias (-0.052 kg/m^2) and standard deviation (0.16). In contrast, summer has the lowest correlation coefficient (0.51) and highest bias (-0.076 kg/m^2). The comparison with GPROF shows correlation coefficient, bias, and standard deviation of 0.71, 0.005 kg/m^2, and 0.07 kg/m^2, respectively.

Finally, in recent days, the advancement of MMW radiometry and miniaturized components has enabled the exploitation of cm-sized mini-satellites (CubeSat) for Earth observation. At least two NASA-funded missions are currently exploiting MW radiometers aboard CubeSat modules, TROPICS, and TEMPEST-D. TROPICS [36] aims at providing the temperature and water vapor profiles, and liquid and ice precipitation, exploiting seven channels near the 118.75 GHz oxygen absorption line, three channels near the 183 GHz water vapor absorption line, and single channels near 90 and 205 GHz. TEMPEST-D [37] exploits frequencies between 89-183 GHz to provide measurements of water vapor profiles, and CLWP and CIWP with an accuracy of 0.1 kg/m^2. Note that some of these channels have never been tested in space (e.g., the 118-GHz band and the 205 GHz channel), and could serve as a proxy for channels foreseen for MWI (118.75 GHz) and MWS (229 GHz).

1.3.2 INFRARED OBSERVATION

Also, passive IR observations are sensitive to atmospheric temperature, humidity, and liquid/ice clouds as well as some trace gases within the observed volume. Since the early years of satellite meteorology, methods for deriving cloud properties from IR observations have been developed [38]–[40], followed by the development of methods for inferring cloud microphysics, such as cloud particle size and optical thickness [41]–[43].

The authors of [44] developed a statistical technique for inferring optimum values of the optical thickness and effective radius of clouds. The procedure incorporates a new discrete ordinates radiative transfer method as well as some asymptotic expressions for the reflection function of thick layers. In this investigation, the authors use for the optical thickness and effective radius of stratiform cloud retrievals a single non-absorbing visible wavelength (0.75 μm) and two absorbing near-infrared wavelengths (2.16 and 3.7 μm). The two absorbing near-infrared wavelengths are used to reduce the ambiguity in deriving the effective radius for optically thin clouds. For optically thin clouds the retrievals become ambiguous. Following [45], they examine the optical thickness and the effective radius uncertainty (5%) as a function of errors in the measured reflection function as well as in the surface albedo, phase function, and similarity parameter. [46] studied the performance of their method using data measured by the Advanced Very High-Resolution Radiometer (AVHRR) over the ocean (channels 1-3-4 at 0.64, 3.75 11.0 μm). They found a good agreement between satellite-derived and in situ microphysical quantities.

The work made by Han et al. [47] reports a method based on a radiative transfer model to retrieve r_e in liquid water clouds from AVHRR data. Results of sensitivity tests and validation studies have provided error estimates. The work [48] reports a method based on AVHRR reflectivity measurements at 0.63 and 1.6 μm to estimate *CLWP*. The cloud analysis involves cloud particle phase classification and estimation of the spatial distribution of the optical thickness and droplet effective radius. The retrieved *CLWP* is validated against ground-based measurements retrieved from microwave radiometers during the intensive measurement campaigns of the Cloud Liquid Water Network project (CLIWA-NET). The relationship between the satellite and ground-based measurements depends on many aspects of the atmospheric conditions, such as the structure of the cloud field and the wind speed at cloud height, causing a temporal and spatial mismatch

between the two observing strategies. On average, *CLWP* derived from ground and satellite measurements correlates with a 0.88 correlation coefficient. In general, the slope of the linear regression is close to 1, and the intercept is smaller than 10 g/m^2. No systematic bias was found, but *CLWP* from the satellite is usually higher than that from ground-based. The authors relate this to the effective radius retrieved from the satellite, used to link optical thickness to *CLWP*, which is representative of larger particles at the cloud top. This may lead to an overestimation of the particle size and thus of the *CLWP* (Dong et al., 2002). This problem may be partly solved using more realistic parameterization of the vertical droplet size distribution in radiative transfer calculations [49], [50].

Using airborne multispectral MAS [51] data over the arctic, King et al., 2004 showed that the 1.62 μm and 2.13 μm algorithm is more robust at determining the cloud optical thickness and effective radius r_e for water clouds over snow and sea ice surfaces, due primarily to the fact that both snow and sea ice have very low surface reflectance at these wavelengths. Therefore, liquid water clouds provide a relatively strong reflectance contrast to the dark underlying surface. However, this algorithm is less reliable for ice clouds due to the strong absorption by ice particles in both bands.

The work [52] presents a comparison of Meteosat Second Generation Spanning Enhanced Visible Infrared Imager (MSG-SEVIRI) and AVHRR retrievals of cloud optical thickness (COT) and CLWP from the Cloud Physical Properties (CPP) scheme, developed in the framework of the EUMETSAT Climate Monitoring (CM) Satellite Applications Facility (SAF). The principle of methods to retrieve cloud physical properties is that the reflectance of clouds at a non-absorbing wavelength in the visible region (0.6 or 0.8 μm) is strongly related to the optical thickness and has very little dependence on particle size, whereas the reflectance of clouds at an absorbing wavelength in the near-infrared region (1.6 or 3.8 μm) is primarily related to particle size. In this framework, the retrieval of particle size from near-infrared reflectances is weighted toward the upper part of the cloud [53].

The authors of [54] presented a NN method to retrieve cloud properties like effective radius, optical thickness, and cloud temperature from the Moderate Resolution Imaging Spectroradiometer (MODIS) infrared observations. The different sources of uncertainties have been analyzed to evaluate the robustness of the method. These uncertainties are mainly related to measured radiances, cloud temperature specification, and lower boundary conditions (i.e., surface

temperature). The total error when simultaneous uncertainties are considered is between 0.25-0.45 μm for the effective radius and between 0.05-0.88 for the COT. The authors conclude that these uncertainties dominate the uncertainty budget over the errors introduced by the NN inversion, estimated within 1%.

Besides, in [55] an optimal estimation-based cloud retrieval algorithm (ICAS) developed for MODIS observations using ten thermal infrared (TIR) bands, was presented. They utilize four TIR bands sensitive to cloud properties, centered at 8.6, 10.4, 11.2, and 12.4 μm. These four bands are sensitive to cloud properties such as cloud top height (CTH), COT, and effective radius (r_e). Performance tests by retrieval simulations show that ice cloud properties are retrieved with high accuracy when COT is between 0.1 and 10. Cloud-top pressure is inferred with an uncertainty lower than 10% when COT is larger than 0.3. ICAS has been used also for the Himawari-8 instrument (Iwabuchi et al. 2018). A sensitivity study demonstrates that the addition of the single CO2 band of Himawari-8 is effective for the estimation of CTH. For validation, retrieved cloud properties are compared systematically with collocated active remote sensing counterparts with small time lags. While retrievals agree reasonably for single-layer clouds, multilayer cloud systems with optically thin upper clouds overlying lower clouds are the major source of error. The measurement noise is estimated from the variance of measurement model differences within a $(10\ km)^2$ area. For validation, ICAS retrieval is compared with the RADAR/LiDAR (DARDAR) cloud product. DARDAR provides vertical profiles of cloud mask and ice cloud properties including the ice water content, $r_{e,}$ and extinction coefficient, inferred from combined observations from MODIS, CloudSat radar, and CALIPSO lidar and TIR measurements. DARDAR has a horizontal spatial resolution of 1.1 km and a vertical resolution of 60 m.

High-spectral-resolution IR sounder data can provide consistent cloud microphysical properties during both daytime and night-time. The use of advanced sounder data has been demonstrated since the 1970s [56], and later for cloud properties, from aircraft [57], [58] as well as satellites [59], [60].

The work made by Smith et al. [58] presents a technique for inferring water and cirrus cloud radiative and microphysical properties. The technique was tested using theoretical calculations and applied to observations made from ground-based observations and the NASA aircraft-based High-resolution Interferometer Sounder (HIS) instrument, made in conjunction with lidar cloud backscatter and situ

atmospheric temperature and moisture measurements. The study depicts the spectral variability of cloud optical properties within the window region.

The work [60] proposes an approach to infer the optical thickness of semitransparent ice clouds (COT<5) from AIRS. The authors investigate the sensitivity of the Atmospheric Infrared Sounder (AIRS) spectral BTs and brightness temperature difference (BTD) values between pairs of wavenumbers to COT. The spectral BTs for the atmospheric window channels within the region 1070–1135 cm^{-1} are sensitive to the ice COT, as is the BTD between 900.562 cm^{-1} (atmospheric window) and 1558.692 cm^{-1} (in a strong water vapor absorption band). Similarly, the BTD between a moderate absorption channel (1587.495 cm^{-1}) and the strong water absorption channel (1558.692 cm^{-1}) is sensitive to ice COT. The ice COT derived from the AIRS measurements is compared with those retrieved from MODIS 1.38- and 0.645-μm bands. The COT inferred from MODIS measurements is collocated and degraded to the AIRS spatial resolution. The AIRS-retrieved COT agrees with that from MODIS for thin to moderately thick cirrus clouds (COT<5). AIRS-retrieved COT tends to be smaller compared to MODIS as COT increases. This is attributed to the BTD signal saturation for large COT values.

In [59], a review of the theoretical basis for inferring the microphysical properties of ice clouds from high spectral resolution IR observations was proposed. The simulations shown in that paper evidence that the slope of the IR BT spectrum between 790–960 cm^{-1} is sensitive to the effective particle size. Strong sensitivity of the IR BT to cloud optical thickness is noted within the 1050–1250 cm^{-1} region. Based on these spectral features, the authors present a technique for the simultaneous retrieval of the visible optical thickness and effective particle size of ice clouds from high spectral resolution IR data. The uncertainty analysis shows that the uncertainties of the retrieved COT and effective particle size have a small range of variation. The uncertainty for particle size corresponding to an uncertainty of 5 K in cloud temperature, or a surface temperature uncertainty of 2.5 K, is less than 15%. The corresponding uncertainty for optical thickness is 5% to 20%, depending on the COT value.

In [61], the authors describe two approaches for synergistic use of the MODIS mask products (cloud mask, cloud-phase mask, and cloud classification mask), the operational MODIS cloud microphysical cloud products, and the AIRS radiance measurements for retrieving the COT and cloud particle size. The MODIS cloud mask with the 1-km spatial resolution is used to characterize the AIRS subpixel

cloud condition (clear/cloudy, ice/water, single/multilayer) during both daytime and nighttime. The MODIS + AIRS 1D-VAR [62], [63] algorithm is used for cloud microphysical property retrieval during the daytime, with the operational MODIS COT and cloud particle size as the background information, while minimum-residual (MR) is used during both daytime and nighttime. In both 1DVAR and MR procedures, the CTP is derived from the AIRS radiances at CO2 channels while the cloud-phase is derived from the collocated MODIS 1-km phase mask. Results from 1D-VAR are compared with the operational MODIS products and MR cloud microphysical property retrieval during one case study, showing that 1D-VAR retrievals have a high correlation with either the operational MODIS cloud products or MR cloud property retrievals.

In [64], a physical inversion scheme dealing with cloudy and cloud-free radiances observed with ultra-spectral infrared sounders to simultaneously retrieve surface, atmospheric thermodynamic, and cloud microphysical parameters is proposed. Also, in this work, a 1D-VAR approach is used to improve an iterative background state defined by an eigenvector-regression retrieval. For both optically thin and thick clouds, the cloud-top height can be retrieved with relatively high accuracy (i.e., error <1 km). The authors point out that the idealized assumption on cloud habits introduces errors and indicates more realistic cloud habit assumptions as a way to improve retrieval performances.

The work [65] describes a method for simultaneously retrieving atmospheric temperature, moisture, and cloud properties using all available IASI channels without sacrificing computational speed. The essence of the method is to convert the IASI channel radiance spectra into super-channels by an Empirical Orthogonal Function (EOF) transformation. Studies show that about 100 super-channels are adequate to capture the information content of the radiance spectra. A Principal Component-based Radiative Transfer Model (PCRTM) is used to calculate both the super-channel magnitudes and derivatives for atmospheric profiles and other properties. They have applied the super channel retrieval algorithm to IASI spectra taken during the JAIVEx field campaign[4].

The work [66] presents the structure of the operational IASI L2 processing chain (version 5), including the individual retrieval modules, their algorithms and configuration, and a summary of the performance assessment through various internal and external validation studies. The validation of the retrieved geophysical

[4] http://cimss.ssec.wisc.edu/jaivex/about/

parameters has been conducted with a wide range of satellite products (including CALIOP, AATSR, MODIS, AVHRR, SEVIRI), with numerical weather predictions and chemistry models and with in-situ measurements (including radiosondes and buoys). L2 products include cloud detection, fractional coverage, height, and phase. Cloud detection is assessed through multiple tests (based on NWP, AVHRR, and NN). Significant improvements are obtained in cloud products with respect to previous processing chains. The authors demonstrated also that the introduction of an artificial NN (ANN) for cloud detection has increased the global ability to detect clouds by approximately 25% with respect to the NWP test only, with an overall success rate exceeding 90%. This outcome improved the cloud phase retrieval, whose methodology is based on the different spectral emissivity of water and ice clouds in the spectral region between 8 and 12 μm. An additional test is applied in version 5, identifying ice clouds based on the fact that super-cooled water cannot exist at temperatures below -40 °C. For the validation of cloud-phase determination, a set of globally distributed co-located IASI and AVHRR data has been compiled. The final version of the tuned algorithm detects 84.5% of the cloud phases correctly. Among the ice samples, 97.3% are correctly determined, while of the liquid samples 84.6% are determined correctly. However, the algorithm does not show any skill in detecting mixed-phase clouds, only 5.5% are correctly identified, and the majority of mixed-phase clouds are reproduced as ice clouds

The feasibility of adding CLWC and CIWC profiles of a 1D-Var assimilation system was investigated by [67]. The proposed approach avoids the conventional use of cloud parameters (CTP and effective cloud fraction) deduced from a CO2 slicing algorithm and the modeling of clouds by single-layer clouds [39]. They use RTTOV [68] radiative transfer code (version 10.1), which features an interface to include CLWC and CIWC and cloud-fraction profiles, called RTTOVCLD. RTTOVCLD enables multilayer mixed-phase clouds (two cloud types per layer). The validation is performed through observing-system simulation experiments (OSSE), showing that the 1D-Var is working reasonably, adding ice or liquid-water cloud in the correct region of the atmosphere. For high opaque clouds, an encouraging result is obtained for the extraction of information about CIWC, while little information is extracted for CLWC. However, this study is limited to homogeneous cloudy scenes with small background departures. A consecutive work [69] using the same 1D-Var framework, investigated a reduced set of IASI channels that could be exploited for data assimilation in cloudy conditions. The channel selection aims to minimize the total loss of information, following the approach discussed in [70]. The study demonstrated that the channel selections are

quite independent of the air-mass type and are capable of improving the retrieval of cloud variables by ~8% RMS to the operational set exploited at NWP centers. Following this research, consequently, in [71] the authors demonstrated the persistence of cloud information produced by 1D-Var assimilation of cloud-affected IASI radiances in a convective scale NWP. In this framework, a significant reduction of the forecast error of CLWC and particularly CIWC is observed. The average error reduction reaches 15–20% for the CIWC of semi-transparent clouds and 9% for opaque clouds, while 10% for the CLWC of semi-transparent clouds, and 3% for opaque clouds, confirming that CLWC is not well analyzed by the 1D-Var, which can be explained by a relatively small sensitivity of the IR data to the liquid cloud. Finally, to better constrain the analysis of CLWC as well as improve the sensitivity of 1D-Var to the liquid cloud, the authors suggest the use of MW radiances.

A physical inversion methodology based on PCRTM has been used in [72] to simultaneously retrieve cloud radiative and microphysical properties. In their work, the authors applied the methodology using single FOV spectral radiances measured by IASI under all-sky conditions. The retrieval uncertainty has shown great sensitivity to ultra-thin clouds demonstrating in the simulation study the success of using the PCRTM retrieval method to detect thin clouds with a COT as low as 0.04. As COT increases from 0.5 to 4, the retrieval uncertainty increases only moderately. For COT>4, the retrieval performance degrades significantly.

1.3.3 COMBINED INFRARED AND MICROWAVE OBSERVATIONS

Since the hydrometeors forming clouds strongly absorb IR wavelengths, the IR radiation reaching a spaceborne radiometer is mostly generated close to the cloud top. On the other hand, MW radiation emitted from the Earth's surface is only slightly affected when passing through nonprecipitating clouds. MW is also complementary to IR because MW radiation is sensitive to larger ice crystals and thicker cirrus layers whereas IR radiation is more sensitive to smaller particles and cirrus clouds having lower CIWP. Therefore, it appears that a proper combination of IR and MW multispectral measurements could help in determining the cloud's vertical structure and composition, particularly in the case of overlapping cloud layers.

The synergy between MW and IR observations of Earth's atmosphere has been explored since the late 1990s. In fact, [73] proposed a method for deriving CLWP and cloud water temperature (Tw) from MW observations, and validated results with radio soundings and retrieval from a combined VIS and IR retrieval method. The two retrieval methods are combined into a single technique, called MVI (microwave, visible, and infrared), to estimate the frequency of multilayered clouds and the effective droplet radius in water clouds. MVI was applied to Meteosat and SSM/I data taken during the Atlantic Stratocumulus Transition Experiment (ASTEX, June 1992) [74]. Matched satellite and ground-based radar data show that the MVI technique can separate cloud layers when high ice clouds overlap lower liquid water clouds. A comparison of CLWP from the method and ground-based observation has been reported. The mean difference between the ground-based and the SSM/I CLWP estimates is 0.034 kg/m^2 or about 30% of the mean value, while the correlation coefficient is 0.54. The largest differences occur when the ground instrument locally observes relatively high (> 0.2 kg/m^2) CLWP values.

The work [75] examines the cloud base signal in a combination of MW observations from a theoretical point of view. The authors showed that the signal is strong enough for a useful retrieval only over the ocean. Using MW and IR data acquired from the same platform (AMSU and AVHRR on NOAA-K) they showed that the cloud top temperature constraint provided by IR observations improves the retrieval skills over a relevant range of CLWP values.

The work [76] presents a 1D-Var approach to analyze cloud-affected observations including both IR and MW sensors (HIRS/3 and AMSU-A aboard NOAA-15). The linearized versions (tangent-linear and adjoint) of the fast radiation model RTTOV were used for the computation of cloud-affected BT. In the IR, cloudiness is treated as a single semi-transparent layer, defined by only two parameters: the cloud-top pressure and its effective amount (i.e., the cloud-layer emissivity times the cloud fraction). In the MW, cloud absorption is computed from the profiles of cloud cover, liquid water, and ice water given on any vertical pressure grid. The 1D-Var scheme is tested on individual profiles with synthetic observations and it is applied for cloud retrieval with real observations (on 15 March 2001). Rain-affected MW observations are detected following [77] and removed consistently. The application shows that 1D-Var can extract some information about liquid and ice water contained in the radiances. Although they do not report retrieval uncertainty, a closure comparison with CERES OLR observations shows the improvement of the model ice-cloud representation by the 1D-Var retrieval. A small positive impact is found for low clouds that are controlled

in the 1D-Var mostly by the broad MW information. The validation of the 1D-Var puts into evidence the limits of the sensitivity of passive IR and MW radiation to cloud vertical distribution. The authors also acknowledge that the specification of the background-error covariance matrix is made particularly difficult by the nonlinearity of the cloud variables, due to their on/off nature.

In [78] Shao et al. developed a method to detect drizzle in marine warm clouds by combining VIS, near-IR, and MW measurements from the TRMM satellite. A VIS/near-IR algorithm is used to simultaneously retrieve COT and effective radius, while an MW algorithm is developed to retrieve CLWP. The relationship among CLWP, optical depth, and effective radius is investigated by using radiative transfer model simulations and by analyzing satellite observations. Coincident airborne cloud radar measurements were used to verify the capability for drizzle detection.

The work made by Huang et al. [79] presents a method to estimate CLWP and CIWP of double-layer clouds using combined MODIS and AMSR-E measurements. In this method, the CLWP of the lower layer water cloud is estimated from AMSR-E measurements. With the lower layer LWP known, the properties of the upper-level ice clouds are then derived from MODIS measurements by matching simulated radiances from a two-cloud layer radiative transfer model. Comparisons with single-layer cirrus systems and surface-based radar retrievals show that the approach can significantly improve the accuracy and reduce the overestimation of COT and CIWP retrievals for ice-over-water cloud systems.

In the work of Romano et al. [80], a technique based on multispectral satellite observations (AIRS and AMSU) to improve the retrieval of cloud parameters also in presence of scenes with overlapping cloud layers is presented. The authors assert that IR-only observations have little chance to retrieve cloud properties below the upper-most cloud top unless the clouds are thin and/or not completely overlapping. This approach exploits both MW and IR observations to penetrate the cloud top, showing better agreement with ground-based observations. Satellite retrievals are validated against ground-based observations collected at the Chilbolton Observatory Facilities (UK) during spacecraft overpasses and compared with retrievals using the CO_2 slicing technique (CTH only), often used for cloud top retrieval, which gives accurate results for a single cloud layer. For the data set considered in this study (40 cases), RMS agreement with ground-based observations is within 295, 905, 1094, and 1862 m for the first two CTH and CBH, respectively, and 0.62, 0.08, and 0.02 kg/m^2 for TPW, CLWP, and CIWP,

respectively. Finally, the authors conclude that HIRS has better capability in discriminating ice/no-ice clouds than AMSU-A or MHS.

Holl et al. 2010, in their paper [81] present a method for collocating satellite radar and radiometric measurements. In this framework, the authors use collocations to validate an operational CIWP product from MHS measurements, the NOAA MSPPS, against CIWP values from CloudSat. The authors report that the MSPPS CIWP is systematically smaller than the CPR CIWP, by approximately 70–90%. For many nonzero CloudSat measurements, the MSPPS CIWP is zero, likely because thin clouds are relatively transparent at MHS frequencies. To overcome this low sensitivity, the authors also tested the added value of adding two HIRS channels (8 and 11) to the MHS CIWP retrieval. From a subsequent analysis, the authors found only a small retrieval improvement for small values of CIWP and attributed the modest improvements to the footprint difference between HIRS and MHS and beam-filling problems.

Islam et al. present an algorithm [82] for detecting ice clouds by using a support vector machine (AID-SVM). The AID-SVM algorithm is applied and tested for the AMSU-A, MHS, and HIRS instruments aboard the NOAA-19 satellite. The algorithm is based on satellite BT measurements and developed as well as validated by using collocated ice/no-ice cloud information acquired from the CloudSat cloud-profiling radar. Over the ocean, they report a 0.37 probability of detection for AMSU/A, 0.51 for MHS, 0.83 for HIRS, and 0.83 for the combined AMSU/A, MHS, and HIRS. Over land, 0.42 for AMSU/A, 0.50 for MHS, 0.76 for HIRS and 0.80 for AMSU/A+MHS+HIRS.

In [83] Holl et al. present a CIWP product based entirely on passive operational sensors (SPARE-ICE). By collocating NOAA-18 with the CloudSat 2C-ICE CIWP product, the authors obtained an observation-based training dataset of AVHRR and MHS measurements on the one hand and joint radar-lidar CIWP on the other. With this dataset, they trained a set of NN for the detection of atmospheric ice and the retrieval of CIWP, using 2C-ICE CIWP as a reference. The algorithm exploits three AVHRR channels, three MHS channels, and auxiliary information (satellite angles, surface temperature, and surface elevation). The correlation between 2C-ICE and SPARE-ICE is very good for IWP > 10 g/m^2. For smaller values of CIWP, SPARE-ICE tends to be larger than 2C-ICE, and levels off at a median of around 1–2 g/m^2 for 2C-ICE CIWP < 1 g/m^2. They found that SPARE-ICE is not sensitive to such small values of CIWP. For uncertainty quantification, they use the validation data

set, i.e., not used in the training, to define a fractional error[5] and get an estimate of the retrieval fractional error as a function of CIWP. They report a median fractional error of about 2 % between SPARE-ICE and CloudSat 2C-ICE, similar to the random error between 2C-ICE and in situ CIWP measurements.

Cloud properties retrieval is also addressed by Susskind et al in [84]. Specifically, in this paper the author reports the AIRS Science Team version-6 level-2 retrieval algorithm and the products generated near real-time at the NASA Goddard Data and Information Services Center. The algorithm takes advantage of the AIRS/AMSU colocation on the same satellite platform, Aqua, to perform an AIRS/AMSU combined retrieval. AMSU observations are used together with AIRS ones in the start-up procedure to generate the initial state, including cloud properties (radiatively effective cloud fraction and cloud top pressure), as well as in the subsequent physical retrieval procedure. The AIRS science team version-6 retrieval algorithm contains many significant improvements compared to the previously operational version, including the methodology used to determine cloud parameters. Cloud properties are given for each of up to two layers of clouds in a given scene. A basic simplifying assumption of the cloud retrieval methodology used in version 6 is that the clouds are gray, that is, the radiatively effective cloud fraction is independent of frequency. Version-6 also has an additional AIRS-only (AO) processing capability, which utilizes only AIRS observations. No AMSU observations are used in any way in the generation of the version-6 AO initial state, which uses coefficients that are trained separately from those of version-6 and are generated without the benefit of any AMSU observations. The version-6 AO processing mode is an important backup to version-6 in case AMSU noise performance degrades below a practical level. Globally, version-6 AO retrievals are slightly less accurate than those of full (utilizing both AIRS and AMSU) version-6 near the surface. This difference between the results of version-6 and version-6 AO occurs primarily over the ocean and is a result of the benefit over the ocean of the 22- and 31-GHz channels of AMSU-A, which are not included in the AIRS-only retrieval procedure.

In 2016 Marke et al. present a method [85] to infer liquid water cloud microphysical properties from a combination of MW and high-resolution IR ground-based observations. They focus on single-layer thin liquid water clouds

[5] $FE = \exp\left|\ln\left(\frac{CIWP_{retr}}{CIWP_{ref}}\right)\right| - 1$

($CLWP < 0.1$ kg/m^2), for which MW and IR observations show relative lower and higher sensitivity, respectively. A synergistic retrieval based on NN is built to estimate both CLWP and cloud effective radius r_e. For their analysis, they used a synthetic data set of MW observations and additional spectrally highly resolved and broadband IR observations. The NN retrievals are shown to be able to infer *CLWP* and r_e for thin clouds with a mean relative error of 9% and 17%, respectively. In contrast, an MW-only retrieval provides high relative error for thin clouds, but reasonable low errors beyond the point of saturation for the infrared retrievals (*CLWP*~40–60 g/m^2). The addition of broadband IR observations is shown to improve *CLWP* retrievals with respect to the MWR-only retrieval. Adding the high-resolution IR spectrometer instead of the broad-band IR radiometer decreases the relative error by 5%, for *CLWP* and 7% for r_e. The NOAA Unique Combined Atmospheric Processing System (NUCAPS) is a heritage algorithm based upon the AIRS Science Team algorithm [84]. The NUCAPS algorithm holds a modular architecture that was specifically designed at NOAA/STAR to be compatible with "AIRS-like" sounding systems. The same retrieval algorithm and the same underlying spectroscopy are currently used to process the AIRS/AMSU suite, the IASI/AMSU/MHS suite (operational since 2008), and more recently the CrIS/ATMS suite operational since April 8, 2014. The NUCAPS algorithm consists of six modules: (1) a preliminary input quality control, look-up tables, and ancillary product acquisition; (2) an MW retrieval module that derives cloud liquid water flags and MW surface emissivity uncertainty; (3) a fast eigenvector regression retrieval for temperature and moisture; (4) a cloud clearing module that combines a set of MW and IR channels; (5) a second fast eigenvector regression retrieval for temperature and moisture for cloud cleared radiances; (6) a final IR physical retrieval, which employs the previous regression retrieval as a first guess. NUCAPS has been extensively validated [86] and transitioned to operations in April 2018.

Chapter 2

FORWARD AND INVERSE MODELS

In this Chapter, radiative transfer models (RTM) used to compute radiances in the infrared (IR) and microwave (MW) bands and the machine learning (ML) inversion solutions will be described in terms of their rationale.

2.1 RADIATIVE TRANSFER IN EARTH'S ATMOSPHERE

Radiative transfer models have become an indispensable tool for a variety of applications, including data assimilation in NWP, producing simulated satellite imagery in several bands of the light spectrum (e.g., MW, IR, and VIS), and assessing the performance of future instruments. In addition, the development of an accurate set of observational data to study the global change of Earth's atmosphere was one of the major challenges of the last four decades and it remains an ongoing open problem. Most of the radiative transfer codes were developed for a particular sensor or remote sensing technique, so there are dedicated codes for active or passive sensors, operating in MW, IR, and VIS frequencies with up-looking, down-looking, and limb-looking geometry. Here, I want to clarify to the reader that the subsequent discussion of the radiative transfer equation is contextualized within the applications of the broad field of remote sensing from space with satellite infrared sensors operating in the so-called *nadir looking mode*.

Generally, assuming the Earth's atmosphere is non-scattering, plane-parallel, and in local thermodynamic equilibrium, these codes rely on the solution of a radiative transfer equation (RTE) which expresses the monochromatic upward vertical radiance $R(\sigma)$ $[W \cdot m^{-2} \cdot sr^{-1} \cdot cm^{-1}]$ of wavenumber σ $[\mathrm{cm}^{-1}]$ that is altitude z dependent and satisfies the following Equation (2.1):

$$\frac{dR(\sigma,z)}{dz} = -K(\sigma,z)\left[R(\sigma,z) - B(\sigma,T(z))\right] \tag{2.1}$$

where $K(\sigma,z)$ is the absorption coefficient and $B(\sigma,T(z))$ the Planck function at temperature $T(z)$ whose general expression is:

$$B(\sigma,T)=\frac{c_1\sigma^3}{\exp\left(c_2\sigma/T\right)-1} \tag{2.2}$$

where $c_1=1.1911\times10^{-8}\left[W\cdot m^{-2}\cdot sr^{-1}\cdot\left(cm^{-1}\right)^{-4}\right]$ and $c_2=1.4388\left[\mathrm{K}\left(cm^{-1}\right)^{-1}\right]$ in Equation (2.2) are the radiation constants.

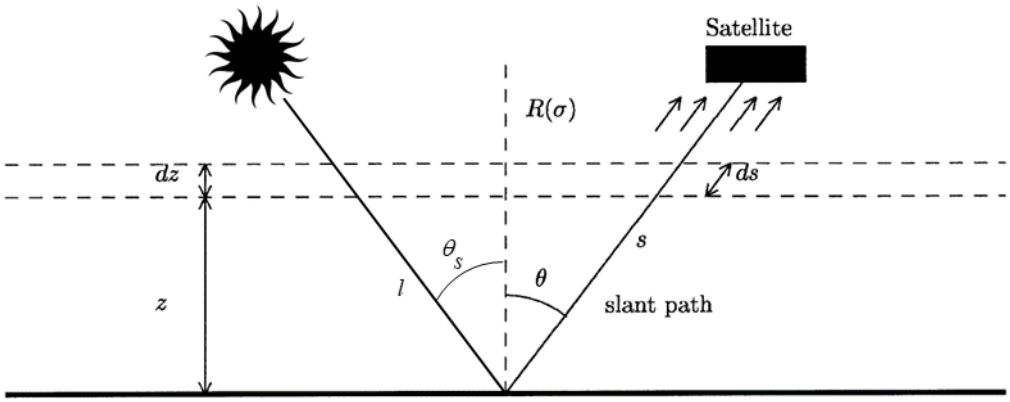

Figure 1 Sun and sensor radiation traveling slant path *s* and *l* forming angles θ and θ_s with the vertical height *z*. In a practical case θ is the satellite viewing angle.

By integrating the Equation (2.1) in the height coordinates from surface to TOA the upwelling radiance in $\theta-direction$ along a path s (see Figure 1) can be written as:

$$R_{\uparrow}(\sigma)=\varepsilon_g B(T_g)\tau_0+\int_0^{+\infty}B(T)\frac{\partial\tau}{\partial z}dz \tag{2.3}$$

where T_g is the surface temperature, ε_g is the ground emissivity, τ_0 and τ indicate the total and the *upwelling* transmittances from 0 to ∞ and from the level *z* to ∞, respectively.

In the same way as Equation (2.3) we can compute the atmospheric downwelling radiance, that is the radiance emitted from the atmosphere and reaching the surface along the path *s* defined by the $\theta - direction$ as follows:

$$R_{\downarrow}(\sigma) = \int_{+\infty}^{0} B(T)\frac{\partial \tau^{*}}{\partial z}dz \tag{2.4}$$

In Equation, (2.4) the term τ^{*} expresses the *downwelling* transmittance from level *z* to the surface. Holding the relation $\tau \cdot \tau^{*} = \tau_0$, $R_{\downarrow}(\sigma)$ can be expressed in terms of τ as follows:

$$R_{\uparrow^{*}}(\sigma) = -\tau_0 \int_{0}^{+\infty} B(T)\frac{\partial}{\partial z}\left(\frac{1}{\tau}\right)dz \tag{2.5}$$

The downwelling radiance is emitted to all directions, it is back-reflected to space and may reach a satellite (see Figure 1) and may be rewritten as follows:

$$R_{\uparrow^{*}}(\sigma) = -r\tau_0^{\,2}\int_{0}^{+\infty} B(T)\frac{\partial}{\partial z}\left(\frac{1}{\tau}\right)dz = (\varepsilon_g - 1)\tau_0^{\,2}\int_{0}^{+\infty} B(T)\frac{\partial}{\partial z}\left(\frac{1}{\tau}\right)dz \tag{2.6}$$

Finally, by combining Equations (2.3) and (2.6), and considering additional terms from the contribution from the solar irradiance[6] Equation (2.1) can be expressed as follows:

$$\begin{aligned} R(\sigma) &= \varepsilon_g B(T_g)\tau_0 + \int_{0}^{+\infty} B(T)\frac{\partial \tau}{\partial z}dz + \\ &\left(\varepsilon_g - 1\right)\tau_0^{2}\int_{0}^{+\infty} B(T)\frac{\partial}{\partial z}\left(\frac{1}{\tau}\right)dz + \frac{1-\varepsilon_g}{\pi}\tau'\mu_s I_s(\sigma) \end{aligned} \tag{2.7}$$

where $R_s(\sigma) = \frac{1-\varepsilon_g}{\pi}\tau'\mu_s I_s(\sigma)$ is the solar radiance with $I_s(\sigma)$ $[W \cdot m^{-2} \cdot cm^{-1}]$ incident extra-terrestrial solar spectral irradiance on a normal

[6] Solar radiation is transmitted through the atmosphere to the surface, from where it can be partially reflected to outer space.

surface, $\mu_s = \cos(\theta_s)$ sun cosine director, and $\tau' = \tau_0(\mu)\tau_0(\mu_s)$ the two path transmittance which accounts for the interaction of sun radiance in the Earth's atmosphere toward the *downwelling* $\theta_s - direction$ and the *upwelling* $\theta -$ direction along the slant paths *l* and *s*; $\mu = \cos(\theta)$ is the satellite cosine director. In Equation (2.7), we are considering specular reflection for Earth's radiation and Lambertian diffusion for solar one[7]. Note that the expression of solar contribution in Equation (2.7)[8] holds only in the infrared region; it is no longer correct in the visible spectrum since it neglects scattering.

The model in the Equation (2.7) refers to clear-sky conditions but as discussed in Chapter 1, clouds are an important regulator of the Earth's radiative budget. Therefore, they need to be incorporated as part of the radiative transfer calculation. In the assumption of a single cloud layer, the radiative transfer of a cloudy atmosphere can be modelled [87]–[89] as follows:

$$R(\sigma) = (1-\alpha)\cdot R_0(\sigma) + \alpha \cdot R_{cld}(\sigma) \tag{2.8}$$

where α is the fractional amount of cloud to be considered throughout the slant path *s*, $R_0(\sigma)$ is the clear-sky radiance as expressed in the Equation (2.7), and $R_{cld}(\sigma)$ is the cloudy-sky radiance and can be expressed as follows:

$$\begin{aligned} R_{cld}(\sigma) = & \varepsilon_g(1-\varepsilon_c)B(T_g)\tau_0 + (1-\varepsilon_c)\int_0^{L_c} B(T)\frac{\partial \tau}{\partial z}dz \\ & + \varepsilon_c B(T_c)\tau_c + \int_{L_c}^{+\infty} B(T)\frac{\partial \tau}{\partial z}dz \end{aligned} \tag{2.9}$$

where L_c and T_c are the cloud top height and temperature, τ_c is the cloud transmittance from L_c to the space; ε_c is the cloud top emissivity.

[7] The Lambertian assumption transform the highly directional solar radiation field in a uniformly diffuse one which is more consistent with the Earth's emission radiation. In this form the radiative transfer calculus is suitable for infrared band.

[8] This solar term has units of spectral irradiance $[W \cdot m^{-2} \cdot cm^{-1}]$ and becomes a spectral radiance after dividing it by the solid angle π.

Finally, as mentioned at the beginning of this section, the Equation (2.8) is solved using RTM codes. Over the past three decades, several RTM codes have been developed that are quite broad in scope and used for a wide range of applications. Notable examples are the σ-IASI [87], the family of models developed by the Atmospheric and Environmental Research (AER) [90], libRadtran (Emde et al., 2016), the Atmospheric Radiative Transfer Simulator (ARTS) [91], the Community Radiative Transfer Model (CRTM) [92], and the Radiative Transfer for Television Infrared Observation Satellites Operational Vertical Sounder (RTTOV) [68]. σ-IASI and RTTOV are the RTM codes selected in this work for the simulation of IR and MW observations from optical satellites of the MetOP platform. To this end, further details will be presented in the next subsections.

2.1.1 IR FORWARD MODEL

All the radiative transfer codes introduced above could fit the purpose of simulating upwelling TOA radiances measured by satellite-based IR spectrometers. In this work, the state-of-the-art radiative transfer code framework σ-IASI is selected. σ-IASI is a forward model (FM) The forward model (FM) σ-IASI consists of a monochromatic radiative transfer module, which has been designed for the fast computation of spectral radiance and its derivatives (Jacobian) to a given set of geophysical parameters. The forward model σ-IASI has been initially developed in the framework of a long collaboration between SI (formerly DIFA (Department of Environmental Engineering and Physics of the University of Basilicata) and EUMETSAT to assist the various developing phases of the Infrared Atmosphere Sounding Interferometer (IASI) instrument.

The code can generate radiances in both up-welling and down-welling modes and can perform the computation of the derivatives to spectroscopic parameters, such as the water vapor continuum (self and broadened components) and CO_2 continuum absorption coefficients. Although initially developed for IASI, σ-IASI is presently a generic radiative transfer model, which is well suited for nadir viewing satellite and airplane infrared sensors with a sampling rate in the range of 0.1–2 cm^{-1}. The software has been developed in Fortran and has been tested to run on Linux platforms and MS Windows. In its latest version [93], which we call σ-IASI_as, the model can deal with clouds and aerosol.

The code computes transmittances on an equally spaced wavenumber grid. For each layer, species, and wavenumbers, optical depths are pre-computed and stored in a look-up table. The temperature dependence is parameterized by a second-order

polynomial. Infinite-resolution optical depths are generated with the generic line-By-Line Radiative Transfer Model (LBLRTM). The newest σ-IASI_as uses Atmospheric Environmental Research (AER) line parameter database (v_3.2) and water vapor continuum model MT-CKD (v_2.5.2).

Clouds and aerosols are specified with their profile and transmittance calculations are performed at the level of the single layers, the same as for gas species. Embedded Mie routines calculate extinction due to the clouds and aerosols [93] as a function of their a) concentration; b) radii; and c) size distribution. Multiple scattering is dealt with by the scaling scheme of [94]. With this scaling scheme, the radiative transfer equation for a cloudy atmosphere is identical to that for a clear atmosphere, and the difficulties in applying a multiple-scattering algorithm to a partly cloudy atmosphere (assuming homogeneous clouds) are avoided. The computational efficiency is practically the same as that for a clear atmosphere. Chou's scaling approximation is now the basis of operational radiative transfer for the retrieval of cloud parameters from satellite data [95]. Based on this scaling, it is possible to compute an equivalent cloud optical depth at each layer, which can be added to that of molecular absorption to compute the layer and total transmittances. In this way, the water/ice/aerosol particles are dealt with as they were absorbing/emitting atmospheric gases. This scaling approximation has been also embedded in σ-IASI_as. Using Chou's scaling approximation, the optical depth, $\chi(\sigma)$ at wave number σ, throughout the slant path *s* of the cloud or aerosol layer is given by:

$$\chi(\sigma) = k_{cld}(\sigma) \cdot s \tag{2.10}$$

where $k_{cld}(\sigma)$ is the equivalent absorption coefficient of the cloud particles and it is expressed as follows:

$$k_{cld}(\sigma) = \beta_{ext}(\sigma)\left[(1-\omega(\sigma)) + b(\sigma)\omega(\sigma)\right] \tag{2.11}$$

In Equation (2.11) $\beta_{ext}(\sigma)$ [m^{-1}] indicate the Mie extinction coefficient, $\omega(\sigma)$ is the single scattering albedo and $b(\sigma)$ refers to the mean fraction of the radiation scattered in the upward direction for isotropic radiation incident from above according to Chou et al. 1999[94] can be computed using a polynomial fitting as follows:

$$b = 1 - \sum_{i=1}^{4} a_i g^{i-1} \tag{2.12}$$

where g is the asymmetry factor. Finally, $a_1 = 0.5$, $a_2 = 0.3738$, $a_3 = 0.0076$, and $a_4 = 0.1186$ are the coefficients.

2.1.2 MW FORWARD MODEL

Concerning the radiative transfer calculus in the MW band, in this work, the RTTOV code has been selected. RTTOV is a fast radiative transfer model for simulating top-of-atmosphere radiances from passive visible, infrared, and microwave downward-viewing satellite radiometers. RTTOV was developed in the 1990s to enable the direct assimilation of radiances at ECMWF. The development of RTTOV was subsequently taken on within the EUMETSAT-funded Numerical Weather Prediction Satellite Application Facility (NWP SAF) in 1998. Nowadays, there are over 1000 users worldwide, and it is widely used in satellite retrieval and data assimilation communities. The current RTTOV version (v13) is described in [68] and referenced therein. The full documentation is also available from the NWP SAF website[9]. RTTOV can now simulate around 90 different satellite sensors measuring radiances at MW, IR, and VIS channels. Many of these instruments are now retired, but their data is still required in support of the ongoing global atmospheric reanalysis efforts. Temperature and water vapor profiles are the default input to RTTOV. For the surface variables, skin temperature, 2m temperature and water vapor concentration, wind speed (over ocean only), surface type, and elevation all have to be defined. The satellite zenith, and optionally azimuth angle at the surface, are also required.

The radiative transfer calculation in RTTOV is performed on the user-defined pressure levels input to RTTOV. This allows more accurate calculations for cloud-affected radiances as the cloud top can be defined by the user at the required level. The profiles can be input on any user-defined pressure level, and these input profiles are then interpolated to the levels on which the RTTOV coefficients are supplied to compute the gaseous transmittance. The vertical layering for the coefficients has been optimized to 53 layers from 1050 to 0.005 hPa. Once the gas optical depth

[9] https://nwp-saf.eumetsat.int/site/software/rttov/documentation/

profiles have been computed, they are interpolated back to the user levels for the radiative transfer computation.

Currently, 83 atmospheric profiles on 101 levels are used to compute the layer-to-space transmittances, which are computed through AMSUTRAN [96] an MW line-by-line model specifically developed to produce channel-averaged profiles of layer-to-space transmittances for calculating RTTOV satellite coefficients. The MW line-by-line calculation includes only N_2, O_2, and O_3 as fixed gases from a standard atmosphere. RTTOV coefficients are updated regularly to account for improved transmittances computed from the latest line-by-line models for the IR and MW wavelength regions. The so-called linear in τ assumption is used to compute the radiance across each layer. This assumes the source function throughout the layer is a linear function of the optical depth and allows for more accurate radiative transfer calculation, especially in presence of relatively more opaque layers.

RTTOV offers the option to accept user-input surface emissivity/reflectance for each channel, or it can calculate it, using physical models such as FASTEM or TESSEM2 at MW frequencies. MW radiometers measure polarized radiances in a polarization plane that can be either (or both) vertical and horizontal polarization or a mixture of the two. For simulation over sea background, the emissivity is modified according to windspeed to account for ocean roughness on all scales, from small ripples to large-scale swell, and also foam arising from breaking waves. MW reflectance/emissivity atlases, e.g. TELSEM [97] and the CNRM atlas [98], are provided over the land as part of the RTTOV package. RTTOV is regularly validated against line-by-line computations as well as real observations. RTTOV computations at AMSU channels using a 52-profile independent set agree with AMSUTRAN line-by-line computations within 0.1 K, an order of magnitude below the instrument noise.

Concerning real observations, measurements from a variety of satellite sensors and for 1 month have been compared with RTTOV calculations from the global ECMWF NWP model, to provide the atmospheric state coincident with the observation locations. AMSU temperature sounding channels show mean biases and standard deviations of differences all within 0.5 K. Water vapor channels show larger standard deviations (1–3 K), mainly due to the water vapor fields from the NWP model not being so accurate. Overall, the bias for all AMSU channels is within +/- 0.5 K, while std range from 0.3 up to 3 K. These statistics are considerably larger than the comparisons of RTTOV with the line-by-line model

but include instrumental calibration biases and also biases in the NWP model temperature and humidity fields.

Cloud liquid/ice water profiles and aerosol profiles can also optionally be provided to enable absorption/scattering calculations. The cloud fraction profile can also be provided to enable simulations for atmospheres partially covered by clouds. In such a case the radiative transfer is solved by using the maximum random overlap method. In the MW region, clouds can be treated as simple absorbers; such approaches are fast, but their validity is limited mainly to water clouds. To accurately simulate the effect of liquid and frozen precipitation in the MW region, it is necessary to represent the effects of multiple scattering. Hence, several more sophisticated models are also available.

However, scattering by hydrometeors (e.g., rain and snow) at MW frequencies are not included in the core RTTOV package but a wrapper program [99], named RTTOV-SCATT provides this capability outside RTTOV. RTTOV-SCATT is a multiple-scattering radiative transfer model which enables all-sky MW radiance. The scattering calculation in the cloudy column is based on the Delta-Eddington approximation so only the observation angle is needed. The hydrometeor types assumed in RTTOV-SCATT are rain, snow, cloud liquid water, and cloud ice. Tables of hydrometeor optical properties are pre-calculated for the required frequencies, temperatures, and hydrometeor classes. As a function of hydrometeor water content, these give the bulk (i.e., integrated over an assumed particle size spectra) extinction coefficient, single-scattering albedo, and asymmetry parameter as required to perform the radiative transfer calculations. The optical properties are stored in sensor-specific coefficient files.

Cloud ice, cloud water, and rain hydrometeors are represented by spheres, with their optical properties computed from Mie theory. Snow hydrometeors are treated as non-spherical particles through discrete dipole simulations. This more realistic representation of the complex 3-D shapes of frozen particles has led to improved simulations of deep convective clouds. Compared to reference doubling-adding simulations, this produces mean errors of less than 0.5 K at the targeted MW frequencies between 10 and 200 GHz, based on a dataset of 8290 model profiles located in tropical areas to ensure the presence of deep clouds and intense precipitation so that multiple scattering is maximized. The all-sky brightness temperature is calculated, as the combination of independent clear and cloudy columns weighted by an effective cloud fraction. The effective cloud fraction is computed through a hydrometeor-weighted average across the vertical profile of

the input cloud fraction [100]. Although the treatment of microwave scattering is highly simplified, this model gives errors much smaller than the many other uncertainties involved, and, critically, it is fast enough for operational use [101], [102].

2.2 ML-BASED INVERSION TECHNIQUES

ML methods, like artificial neural networks (NN) and random forests (RF), are increasingly applied to data inversion because of their ability to find non-linear statistical relationships between target variables and input variables, such as those arising in satellite remote sensing of geophysical parameters through spectral radiances [103]–[105]. This Section reports the NN and RF architectures intended for use in this work. The former consists of feedforward NN normally referred to as multilayer perceptron (MLP) systems. This kind of NN has been demonstrated to be a "universal approximator" [106]. The latter consists of an RF regressor, normally referred to as an ensemble learning method [107], because they operate by constructing a structure composed of several decision trees. Within this work, NN algorithms were developed for the retrieval of *CLWC, CIWC, CLWP, and CIWP*, while an RF algorithm was developed for the retrieval of effective radii of liquid and ice water clouds (e.g., r_e, d_e).

2.2.1 NN-BASED INVERSION RATIONALE

In recent years, NN learning has risen to the top in numerous areas, namely computer vision, speech recognition, natural language processing, and remote sensing. This Section briefly reports and introduces the basis of NN algorithms applied to regression problems. For a broad review of NN applied to remote sensing we refer to [108]. This document is not intended to cover the very broad field of NN applications. Here we limit to retrieval or non-linear regression problems and will focus on multilayer backpropagation feedforward NNs, which are normally referred to as MLP systems.

A NN is a highly connected system (e.g., Chicocki and Unbehauen, 1993 [109]), whose elementary unit is the artificial neuron that reproduces in some way the nonlinear function of a biological neuron of the brain. Neuron has many input lines (dendrites) and only one output line (axon), which, through a connection (synapses), goes to another neuron or is taken as one output of the system.

MLP [108], [110] is nowadays the leading architecture used for implementing NN-supervised regressors. From a set of samples $S(X, y)$, where X represents the set of inputs and y the corresponding outputs, MLP emulates a neural structure, linking many parallel processors called "perceptrons" to map $X \rightarrow y$. These processors are organized in distinct layers: 1) the first layer represents the set of network inputs X, 2) the last layer represents the output of the mapping $X \rightarrow y$, and 3) some intermediate layers, also called "hidden layers". The entire neuronal structure is connected via perceptons links associated with network weights θ. The ensemble of perceptons, links, and weights, enables the NN architecture to learn from examples and make predictions.

To streamline the discussion, let us refer to the artificial neuron represented in Figure 2, which exemplifies the processing at a single given node of the net.

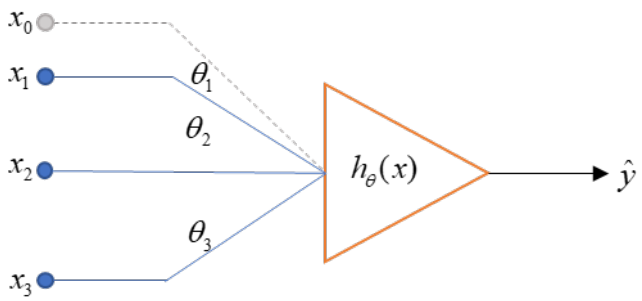

Figure 2. Schematic representation of an artificial neuron.

Each artificial neuron thus consists of inputs *x*, a set of parameters or weights θ, and a single output $h_\theta(x)$ corresponding to a function called activation function such as the sigmoidal one:

$$h_\theta(x) = \frac{1}{1+e^{-\theta^T x}} \tag{2.13}$$

where T indicates the transpose operation; x_0 is called the bias unit, generally, it always has value 1, it is not connected with previous layers and helps fit the prediction better to the data [110], [111].

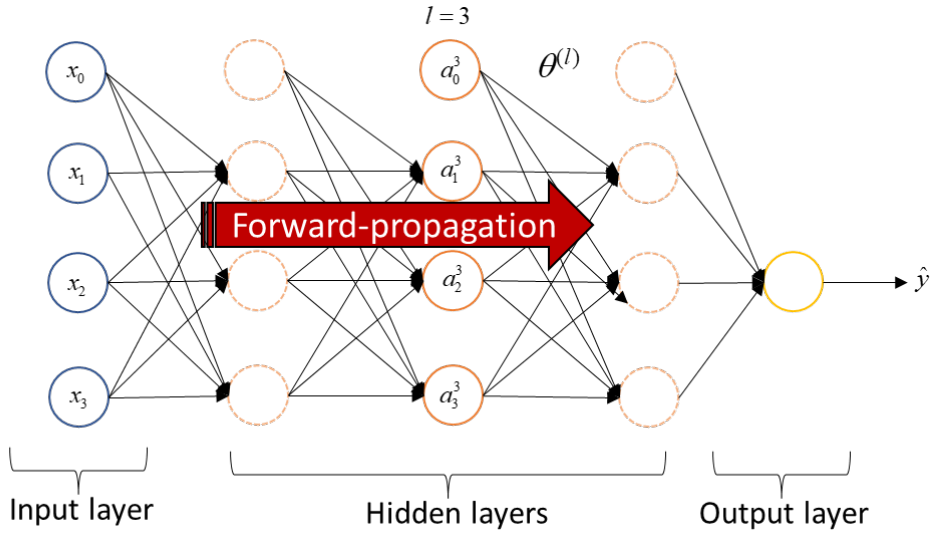

Figure 3. Schematic representation of a feed-forward neural network structure. The red arrow indicates the forward propagation process.

Considering a neural network structure composed of n different layers (see Figure 3) $a_i^{(l)}$ denotes the $i-th$ neuron of the $l-th$ layer and $\theta^{(l)}$ the matrix of weights controlling function mapping from layer l to layer $l + 1$. Thus, if a network has s_l units in layer l, s_{l+1} units in layer $l+1$, then $\theta^{(l)}$ has $s_{l+1} \times (s_l + 1)$ where +1 recalls the bias term. Specifically, each layer of the network performs a computational step equivalent to linear regression, allowing complex nonlinear functions to be computed on the input/activation values that go to every node in the following layers. This transition process is indicated in the literature as *forward* propagation. Each layer transition uses the matrix of parameters $\theta_{ji}^{(l)}$ where j ranges from 1 to the number of units in layer $l+1$, i ranges from 0 to the number of units in layer l, that is the layer where the transition starts.

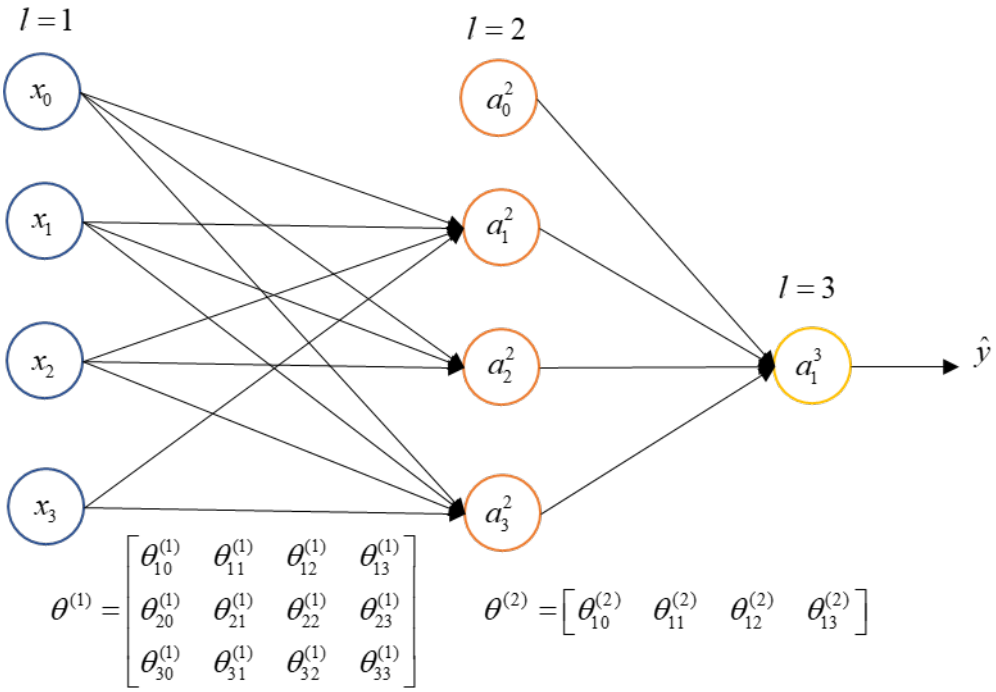

Figure 4. Example of a NN structure composed of one single hidden layer. $\theta^{(1)}$ and θ^{2} indicate the NN weights in between layers 1-→ 2 and 2→3.

At this point, assuming the structure of a NN with one single hidden layer composed of three units (see Figure 4), the activations (see Equations (2.13)) will have the following expressions:

$$\begin{aligned} a_1^{(2)} &= g\left(\theta_{10}^{(1)}x_0 + \theta_{11}^{(1)}x_1 + \theta_{12}^{(1)}x_2 + \theta_{13}^{(1)}x_3\right) \\ a_2^{(2)} &= g\left(\theta_{20}^{(1)}x_0 + \theta_{21}^{(1)}x_1 + \theta_{22}^{(1)}x_2 + \theta_{23}^{(1)}x_3\right) \\ a_3^{(2)} &= g\left(\theta_{30}^{(1)}x_0 + \theta_{31}^{(1)}x_1 + \theta_{32}^{(1)}x_2 + \theta_{33}^{(1)}x_3\right) \end{aligned} \tag{2.14}$$

where g indicates the activation function. Accordingly, the NN output is determined as follows:

$$h_\theta(x) = a_1^{(3)} = g\left(\theta_{10}^{(2)}a_0 + \theta_{11}^{(2)}a_1 + \theta_{12}^{(2)}a_2 + \theta_{13}^{(3)}a_3\right) \tag{2.15}$$

Finally, I want to remark that neural networks can have different architectures, i.e., different numbers of layers, different numbers of neurons for each layer, and different types of activation functions the only constraints being the number of nodes in the input layer and the one node in the output layer.

In NN inversion MLP structure is trained by minimizing a cost function L; which in classical regression task is chosen to be the squared distance between the desired y and predicted $\hat{y}$ output at multiple training steps. Suppose to have several n training examples to use for training, the NN cost function can be computed as follows:

$$L = \frac{1}{n}\sum_{i=1}^{n}(\hat{y}_i - y_i)^2 \tag{2.16}$$

Minimizing the Equation (2.16) would mean designing an MLP structure whose prediction $\hat{y} = y$ or more straightforwardly minimizing the Euclidean distance between the predicted and the reference values:

$$L = \frac{1}{n}\|\hat{y} - y\|_2^2 \tag{2.17}$$

In this way, taking into account the *forward-propagation* scheme where $\hat{y} = h_\theta(x)$ we will tune the NN weights θ accordingly to minimize the distance expressed in the Equation (2.17). By using simple algebra, we will solve the Equation (2.17) where it gradient is 0. In NN theory, the algorithm designed to compute this gradient is known as backpropagation. The backpropagation algorithm was originally introduced in the 1970s, but its importance was not fully appreciated until the famous paper by [112]. That paper describes several NN where backpropagation works far faster than earlier approaches to learning, making it possible to use NN to solve problems that had previously been insoluble.

Given one training example (x, y), and an MLP structure composed of $l = 1, 2, ..., L$ layers the backpropagation algorithm starts differentiating Equation (2.17) from the output layer L in this way:

$$\delta^{(L)} = \hat{y} - y \tag{2.18}$$

That represents the error the NN made in predicting the true value y. The Equation (2.18) means that we know how a change in the total input determined by the *forward propagation*, will affect the error for the state of the lower levels units and the weights θ of the connections from the lower layer to the output one.

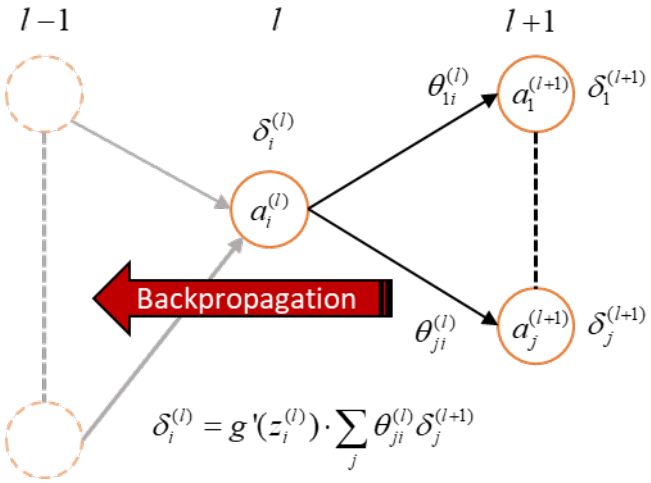

Figure 5. Simple representation of the NN backpropagation algorithm.

After that let $l \neq L$ a layer of the MLP structure, the error is backpropagated as follows:

$$\delta^{(l)} = \left(\theta^{l}\right)^{T} \delta^{l+1} \cdot g'\left(z^{(l)}\right) \tag{2.19}$$

where $g'\left(z^{(l)}\right) = a^{(l)} \cdot (1 - a^{(l)})$ that is the derivative of the activation of layer l (see Figure 5). Note that, $\delta^{(1)}$ is not determined since it would not make sense to calculate the error of the inputs. Finally, it is demonstrated that the derivative of the cost function expressed in the Equation (2.17):

$$\frac{\partial}{\partial \theta_{ij}^{(l)}} L(\theta) = a_j^{(l)} \delta_i^{(l+1)} \tag{2.20}$$

which assesses that by doing backpropagation and computing the terms of the partial derivatives δ, it is possible to minimize the cost function L.

These operations are repeated in training for each training sample and different epochs [110]. For each training sample in the first stage, the derivatives of the cost function *w.r.t.* the weights θ are evaluated (see Equations(2.20)). then in the second stage, these derivatives are used to compute the adjustments to be made to the weights θ, using gradient descent, or more sophisticated and efficient techniques [113] to improve the NN regression performance.

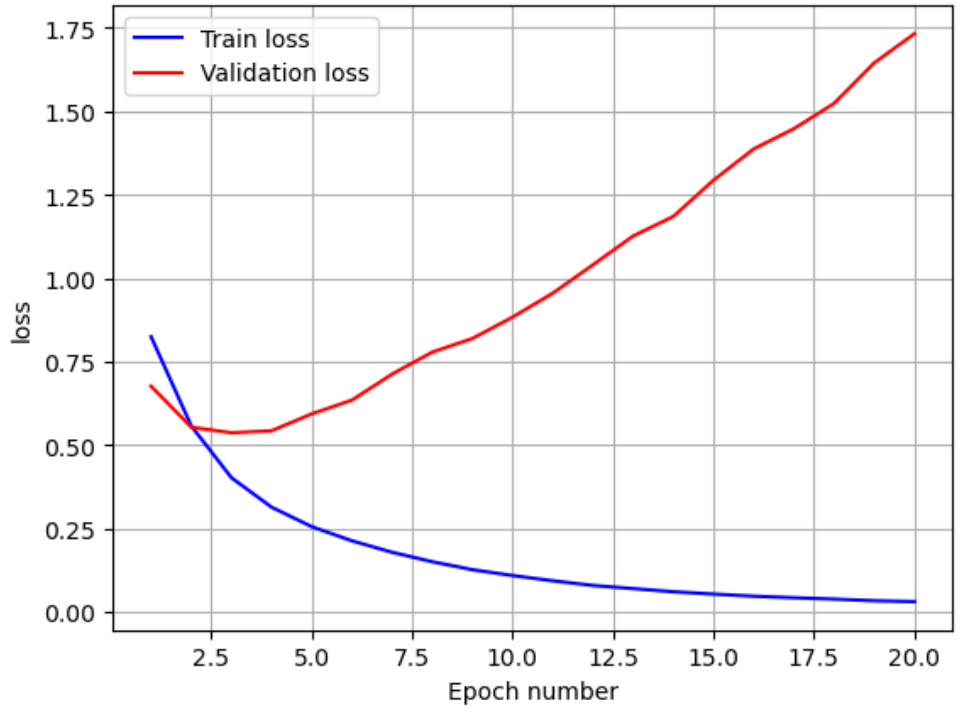

Figure 6. Example plot of the error on training and validation set.

However, one possible disadvantage of the backpropagation algorithm is that it can take a large number of iteration steps to converge to the desired solution. It is not possible to know a priori when to stop iterations. Normally, the procedure is stopped when a given threshold on the error, i.e., the cost function, L has been reached. However, also in this case there is the possibility that the NN has been overfitted [110]. One approach to avoid overfitting is to use different and independent training and validation data sets and cross-validating among those the cost functions (see Figure 6) in learning and training [111], [114].

Finally, the learning phase of a neural network requires the use of several auxiliary methodologies such as i) regularization, ii) weight initialization, iii) cross-validation, and iv) hyperparameter tuning [115] to achieve optimal training. A more complete explanation is beyond the scope of this work. An interested reader can find more information in [110]–[112].

2.2.2 RF-BASED INVERSION RATIONALE

RF is an ML technique based on an ensemble of multiple decision trees (see Figure 7). These types of structures can solve both classification and regression problems

and are found to be particularly convenient when dealing with high-dimensional feature spaces, due to their intrinsic ability to select and rank the predictor variables that perform best in discriminating between target values.

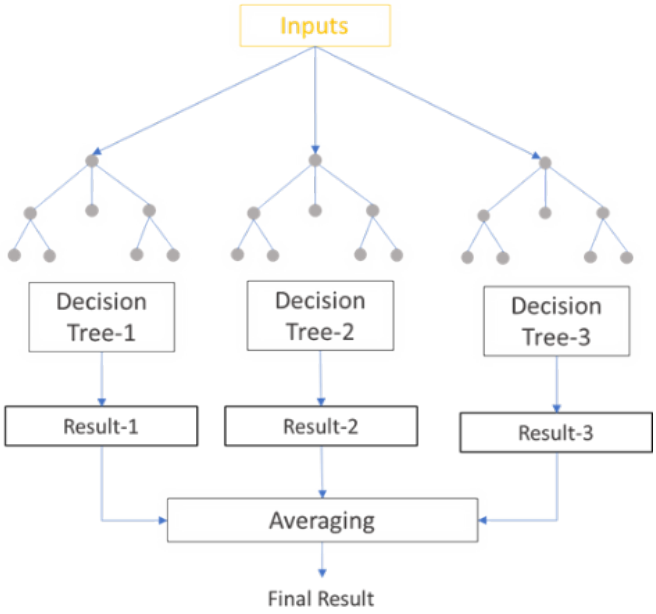

Figure 7. Random forest regressor architecture.

These ensemble algorithms often address non-linear inversion and dimensional problems and were introduced for classification tasks. Here I introduce the rationale for random forests in terms of classification tasks. However, I want to point out that regardless of the task for which they are used (e.g., regression or classification), random forests' rationale remains the same.

Specifically, differently to Maximum Likelihood Classification (MLC) classifiers that assume a normal data distribution, the RF method is based on the Classification and Regression Tree (CART) algorithm [104], [107] that, does not make any assumptions regarding the frequency distribution of data. To this aim, the RF method is very suitable for inferring information of input data from remotely sensed acquisitions, which have multi-modal distribution and very rarely the normal one. In Breiman's RF, the tandem use of randomness in CART and bagging techniques is the key that allows this model to perform better than many other classifiers [116].

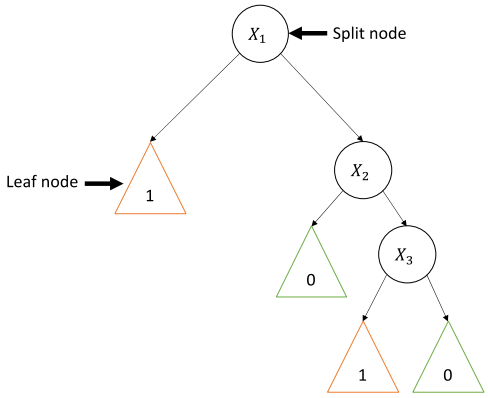

Figure 8. Simple sketch of a decision tree for binary classification. Split nodes are depicted as circles with $d = 3$ features. Leaf nodes are represented as triangles, colored orange and green for $y = 1$ and $y = 0$ classes, respectively.

Given a training dataset $S(X, y)$ representing the set of inputs and $y \in R^m$ the corresponding outputs where m is the size of training data and d the number of features, the RF learning is pursued by applying the CART algorithm on several L training subsets $S_k(X_k, y_k)$, $k = 1, ..., L$, produced by random sampling $S(X, y)$, either with or without replacement.

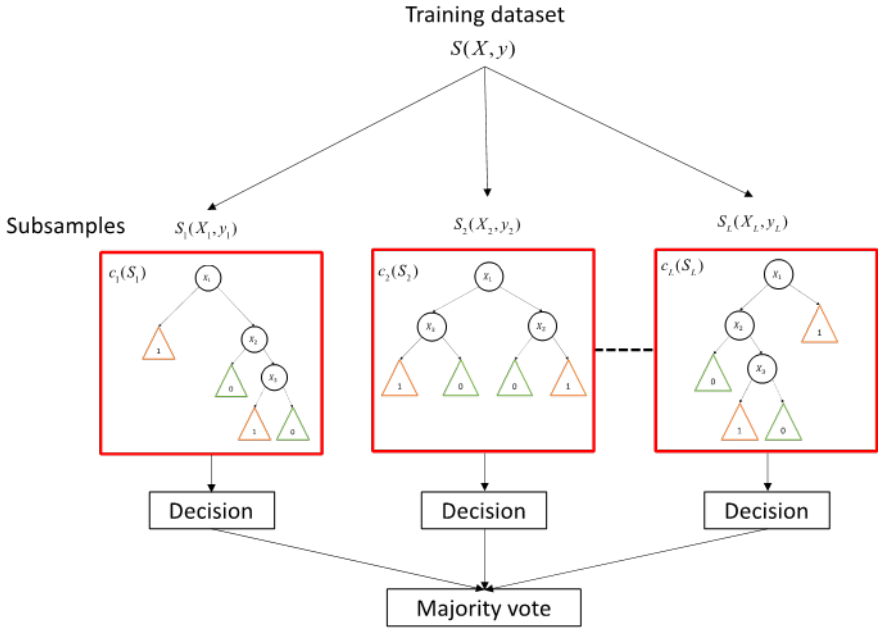

Figure 9. Example of Breiman's random forest classifier. For a regression task, the "*Decision*" blocks are replaced with the values predicted by each tree and the "*Majority vote*" block with the "*Averaging*" block (see Fig. 7).

In this framework, each decision tree is grown by the CART algorithm that works by recursively splitting the subsets of $S_k(X_k, y_k)$, randomly sampling input features d and choosing from among those as split nodes the ones that better optimize a specific error function (e.g., Gini or Entropy for classification, and MSE for regression tasks). The recursive subdivision process stops once the maximum depth is reached, or no further subdivisions can be performed. Within the decision tree structure, subsets that are not split are called leaf nodes. In classification tasks, a class label designates each leaf node while in regression the prediction of a target variable. Figure 8 shows a decision tree structure for a binary classification problem.

This process allows the construction of L decision tree classifiers $c_k(S_k)$ by maximizing their strength and jointly minimizing their correlation [107], [117], forming a bagged predictor able to map $X \rightarrow y$. Finally, RF prediction is computed as the majority votes overall trees predictions (see Figure 9).

RF models further produce additional information about the analyzed data: i) the feature importance [118] used to perform the classification or regression task and ii) the internal structure of the data in terms of the similarity of different data samples to one another. The RF model determines the former during its training (tree by tree as the RF structure is formed), estimating each feature's error rate variability when permuted while all others remain unchanged. The latter is determined in terms of proximity matrix $P(i, j) \in R^{m \times m}$ where the element (i, j) represent the fraction of trees in which the samples i, j fall in the same leaf node. The higher the proximity measure, the more similar the pair of samples.

As with many other ML methods also, RF uses different hyperparameters. Nowadays, hyperparameter optimization is one of the most important tasks to perform. In recent literature [115], [119]–[122] hyperparameter optimizations have been extensively addressed, demonstrating that the correct tuning of an ML model hyperparameter is mandatory to obtain high generalization performance. Specifically, RF models depend mainly on three hyperparameters: i) the number of decision trees (n_{tree}) that compose the model, ii) the number of features (m_{try}) that will be considered in the CART splitting procedure, and iii) the tree depth k_n. Only the first hyperparameter has a robust analytical demonstration [121] of its impact on forest generalization performance. For the other two, there is no theory to guide

the best choice; they are strictly dependent on the problem to solve, and the related dataset of measurements [121], and this aim has to be tuned appropriately.

Chapter 3

CLOUD MICROPHYSICS PARAMETERS REGRESSION FROM IR AND MW SPECTRA

In December 2019 the study Combined MWS and IASI-NG Sounding for Cloud Properties (ComboCloud) was selected by the EUMETSAT to prototype and validate algorithms for the retrieval of cloud microphysical properties from the synergy of passive MW and hyperspectral IR observation. Specifically, the main objectives of this project were:

1. Exploit IASI-NG/MWS synergy for the retrieval of cloud products currently not available from EPS sensors:
    - Cloud Liquid Water Content (CLWC)
    - Cloud Ice Water Content (CIWC)
    - Cloud Liquid Water Path (CLWP)
    - Cloud Ice Water Path (CIWP)
2. Investigate the benefits of future IASI-NG for current IASI for the retrieval of:
    - Cloud effective radius (Re)
    - Thin cirrus detection
3. Adapt the algorithms to work with current EPS sensors, i.e., AMSU/MHS and IASI.
4. Validate the retrievals against existing products from other space-borne sensors.

In this context, my Ph.D. studies and analysis have been involved in all four points mentioned above. The main focus was the development of an AI-based framework for the regression of cloud microphysical parameters, which details will be provided in the following chapter. The dataset of measurements used includes real and simulated observations in the IR and MW bands from first- and second-generation METOP platforms. To this end, details regarding their processing will be provided. After that, we will concentrate on the presentation of the inversion framework, realized within the framework of the doctoral studies, for the regression of cloud microphysics parameters.

3.1 IR SATELLITE INSTRUMENTS

In this work, the dataset of measurements in the IR band is referred to as the sensor of the first and second generation of MetOp platforms. The former is the Infrared Atmospheric Sounding Interferometer (IASI) [123] which is currently a key payload element of the EUMETSAT (MetOp-FG) series, and its main purpose is to provide temperature and humidity profiles, to deeply understand and make numerical forecast weather studies and predictions. IASI measures in the thermal infrared (TIR) part of the emitted/reflected Earth's electromagnetic spectrum with coverage extending from 645 to 2760 cm^{-1}, with a resolution of $\Delta\sigma$=0.25 cm^{-1}, providing radiances of 8461 spectral samples (channels), along 14 orbits in a sun-synchronous observation mode. Data samples are taken at intervals of 25 km along and across the track, each sample having a maximum diameter of about 12 km. Table 1 presents a summary of the IASI principal characteristics.

Table 1. IASI-NG technical characteristics.

Characteristic	IASI
Spectral Coverage	continuous in 645 $cm^{-1} - 2760\ cm^{-1}$range
Spectral Sensing	0.25 cm^{-1}, 8461 channels
Acquisition angles	$\pm 48.3°$
Sounding Point Density	$50 \times 50\ km^2$ (2×2 IFOV matrix)
Nadir Instantaneous Field of View (IFOV)	12 km diameter

Nadir IFOV shape	Circular
Altitude	819 km

Designed and built on the heritage of the IASI the latter sensor is the Infrared Atmospheric Sounding Interferometer New Generation (IASI-NG) that will be a key payload sensor of the second generation of European meteorological polar-orbit satellites (MetOp-SG) dedicated to operational meteorology, oceanography, atmospheric chemistry, and climate monitoring; the launch is scheduled for 2022 (read Table 2 for more information).

Table 2. IASI-NG technical characteristics.

Characteristic	**IASI-NG**
Spectral Coverage	continuous in 645 cm^{-1} – 2760 cm^{-1}range
Spectral Sensing	0.125 cm^{-1}, 16921 channels
Acquisition angles	$\pm$46.5°
Sounding Point Density	25 km × 25 km
Nadir Instantaneous Field of View (IFOV)	12 km diameter
Nadir IFOV shape	Circular

Also, IASI-NG is a Fourier transform spectrometer, but with 16921 spectral samples in the same range (645 and 2760 cm^{-1}). The spectral resolution and the spectral sampling of IASI-NG are improved by doubling their respect to the IASI, respectively, at 0.25 cm^{-1} and 0.125 cm^{-1}.

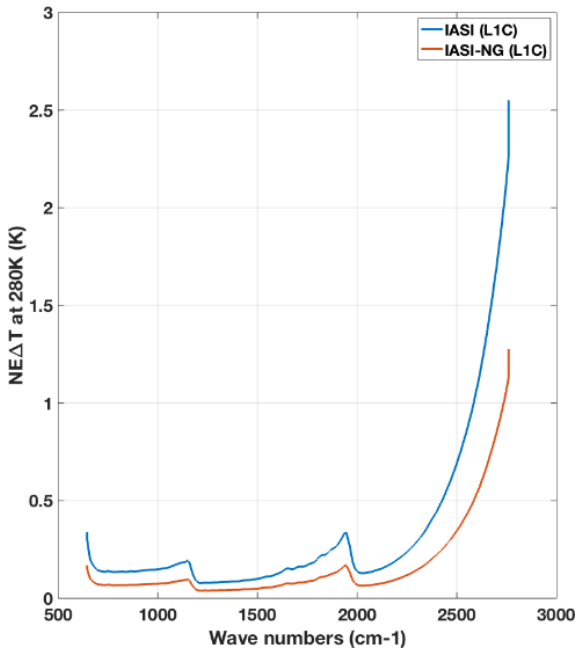

Figure 10. Equivalent brightness temperature $\boldsymbol{NE\Delta T}$ at 280K for IASI (blue curve) and IASI-NG (orange curve).

The increase in spectral resolution of IASI-NG will result in a better vertical resolution and a reduction in noise expected to be at least a factor of 2, compared to IASI [124] (see Figure 10), resulting in an improvement in the accuracy of the IASI-NG products.

3.2 MW SATELLITE INSTRUMENTS

MW passive-sounding systems have a long heritage in operational meteorology. Also, for the MW, the dataset of measurements is referred to MW passive sensor mounted onboard the MetOp platforms of first- and second-generations. Concerning the MetOp-FG instruments, the Advanced Microwave Sounding Unit-A (AMSU-A) and the complementary Microwave Humidity Sounder (MHS) have been considered. These sensors are currently the leading sensors in providing operational sounding observations. The primary role of the sounder is to provide temperature and humidity sounding under completely overcast conditions and to aid in cloud detection. AMSU-A is a multi-channel microwave radiometer that measure scene radiances in 15 different frequency

channels (23-90GHz). At each channel frequency, the antenna beamwidth is a constant 3.3 degrees (at the half power point). The AMSU-A instrument collects 30 consecutive Earth view scenes in 15 individual channels in a stop and stare mode. The scanned swath is ± 48.33 degrees, which translates into ± 1037 km at a satellite altitude of 820 km (see Table 3).

Table 3. AMSU-A technical characteristic

Characteristic	**AMSU-A**
Spectral Coverage	not-continuous in 23.0 –90.0 GHz range
Spectral Sensing	15 Channels
Acquisition angles	±48.33°
Polarisation	QH and QV
Nadir Instantaneous Field of View (IFOV)	49 km diameter
Swath width	ca. 2074 km
Nadir IFOV shape	Circular

The 12 oxygen-band channels (channels 3–14) will provide microwave temperature sounding for regions from the Earth's near-surface up to about 42 kilometers (from 1000 hPa to 2hPa). The extreme spectral windows (channels 1, 2, and 15) allow correction of the other measurements for surface emissivity, atmospheric liquid water, and total precipitable water. These channels also provide information concerning precipitation, sea ice, and snow coverage.

MHS is a five-channel across-track scanning radiometer of the millimetre-wave band (89-190 GHz) with 90 fields of view (FOV). It has a scan range of ±49.44° to the nadir direction leading to a swath of 2310 km, while the FOV size is about 16 km at the nadir. Each scan consists of four views of the onboard calibration target (OBCT), followed by the 90 Earth views and the four views of deep space (see Table 4).

Table 4. MWS technical charaeristic

Characteristic	MHS
Spectral Coverage	not continuous in the 89.0 – 190.3 GHz range
Spectral Sensing	5 Channels
Acquisition angles	±49.44°
Polarisation	QH and QV
Nadir Instantaneous Field of View (IFOV)	16 km diameter (at nadir)
Swath width	ca. 2310 km
Nadir IFOV shape	Circular

There are three water vapor-sensitive channels around the 183 GHz absorption line with frequencies 183.31±1.0 GHz, 183.31±3.0 GHz, and 190.31 GHz (Table 6). The first two channels are double-sideband symmetric about the water vapor line, while the 190.31 GHz has a single bandpass.

MWS inherits many features from these sensors by enhancing them by adding two temperature and two humidity-sounding channels, plus one high-frequency

window channel sensitive to ice clouds. MWS is a 24-channel microwave radiometer covering the frequency range from 23.8 to 230 GHz. Using a single rotating antenna MWS scan the Earth's surface and atmosphere in footprints ranging from 40 to 17 km at the lowest and high frequencies, respectively. Calibrated using an internal hot target and a cold sky, MWS provides a scan angle range of $\pm 49°$ to nadir (see Table 5).

Table 5. MWS technical characteristic

Characteristic	MWS
Spectral Coverage	not continuous in the 23.8 – 230.0 GHz range
Spectral Sensing	24 Channels
Acquisition angles	$\pm 49°$
Polarisation	QH and QV
Nadir Instantaneous Field of View (IFOV)	17-40 km diameter
Swath width	ca. 2200 km
Nadir IFOV shape	Circular

The smallest footprints provide contiguous sampling, which defines the scan cycle of the instrument. Larger footprints will then provide an overlapping spatial sampling. MWS is calibrated using an internal hot target and a cold sky. Table 6 reports the channel comparison between MWS and AMSU/MHS.

Table 6. Channel comparison between MWS and AMSU/MHS. Channels 5, 7, 20, 22, and 24 are new to AMSU/MHS. Channels 18, 19, 21, and 23 have either central frequency, polarization, or passband differences to the closest AMSU/MHS channels.

AMSU/MHS			MWS		
Ch.	**GHz**	**Pol.**	**Ch.**	**GHz**	**Pol.**

1	23.8	QV	**1**	23.8	QV
2	31.4	QV	**2**	31.4	QV
3	50.3	QV	**3**	50.3	QV
4	52.8	QV	**4**	52.8	QV
			5	53.246±0.08	QH
5	53.595±0.115	QH	**6**	53.596±0.115	QH
			7	53.948±0.081	QH
6	54.4	QH	**8**	54.4	QH
7	54.94	QV	**9**	54.94	QV
8	55.50	QH	**10**	55.50	QH
9	57.290344	QH	**11**	57.290344	QH
10	57.290344±0.217	QH	**12**	57.290344±0.217	QH
11	57.290344±0.3222±0.048	QH	**13**	57.290344±0.3222±0.048	QH
12	57.290344±0.3222±0.022	QH	**14**	57.290344±0.3222±0.022	QH
13	57.290344±0.3222±0.010	QH	**15**	57.290344±0.3222±0.010	QH
14	57.290344±0.3222±0.0045	QH	**16**	57.290344±0.3222±0.0045	QH
15	89.0	QV			
16	89.0	QV	**17**	89.0	QV
17	157.0	QV	**18**	165.5±0.725	QV
18	183.311±1.0	QH	**23**	183.311±1.0	QV
			22	183.311±1.8	QV
19	183.311±3.0	QH	**21**	183.311±3.0	QV
			20	183.311±4.5	QV
20	191.31	QV	**19**	183.311±7.0	QV
			24	229.0	QV

The primary purposes of MWS are atmospheric temperature and water vapor sounding, as well as CIWP estimates.

3.3 REGRESSION FRAMEWORK DESCRIPTION

This Section reports the NN and RF architectures that compose the inversion framework developed in this work. The framework is an ensemble of NN

algorithms that were developed for the retrieval of CLWC, CIWC, CLWP, and CIWP, while an RF algorithm was developed for the retrieval of Re.

Specifically, the developed framework is composed of three processors that for sake of simplicity we will refer to as:

- SW1: That is composed of two NN algorithms to retrieve CLWC and CIWC profiles;
- SW2: That is composed of a NN algorithm to retrieve both the vertically integrated paths of liquid water and ice clouds, namely CLWP and CIWP;
- SW3: That is composed of two RF algorithms to retrieve the cloud effective radius of liquid water and ice clouds, r_e and d_e.

For all three SWs, a dataset containing the cloud properties and simulated measurements is generated and divided into three subsets for training, validation, and testing. Then, the feed-forward NN and RF regressor are developed, based on the training and test datasets, and finally evaluated with the validation dataset.

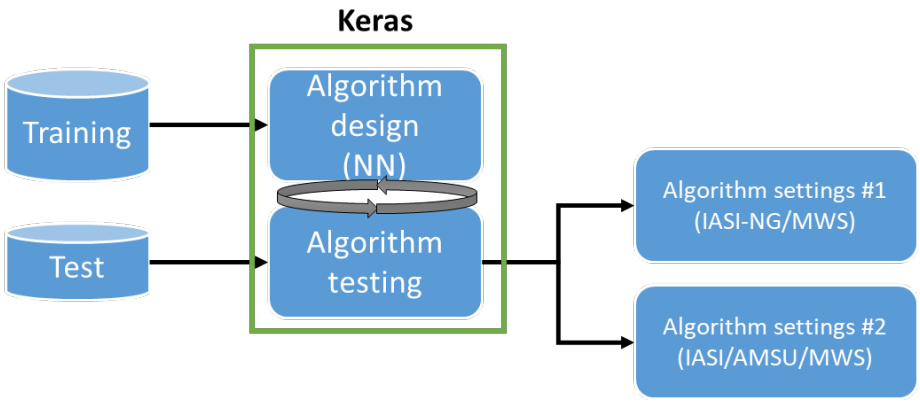

Figure 11. Schematic representation of the NN training and test.

The processing scheme for SW1 and SW2 is pictured in Figure 11, which shows the main steps involved in the designing and development of the statistical retrieval algorithms. For SW1 and SW2, the core framework for the NN designing and testing is Keras [125], which is a powerful Python-based library that contains numerous implementations of commonly used NN building blocks such as layers, objectives/activation functions, and optimizers. Keras [126] also presents an additional framework, useful to tune NN hyperparameters to optimize the training

of a specific dataset. Two different NN architectures are designed and tested: one with IASI-NG/MWS inputs and the other with IASI/AMSU/MHS inputs.

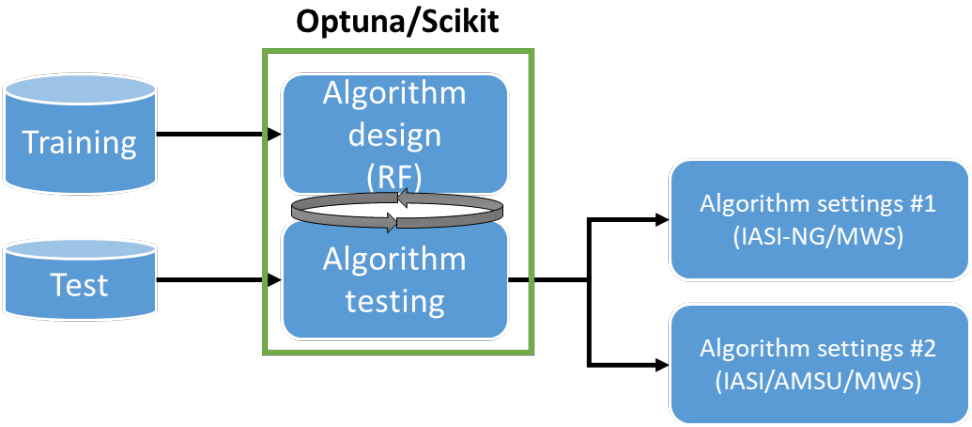

Figure 12. Schematic representation of the RF training and test

The processing scheme for SW3 is shown in Figure 12, consisting of a multitude of decision trees with different depths. The core software framework for the RF design is scikit-learn [127], a very powerful Python-based library that includes ensemble methods for classification and regression. The Python-based automatic hyperparameter optimization framework Optuna [120] is used to tune the RF architecture and optimize the training on a specific dataset. Finally, in terms of algorithm settings, four different architectures are designed and tested: The former two with IASI-NG/MWS inputs and IASI/AMSU/MHS inputs for the effective radius of liquid water clouds. The latter two with IASI-NG and IASI inputs the effective radius of ice water clouds.

3.3.1 Dataset simulation

All the developed SWs[10] have been trained, tested, and validated using a dataset of simulated geophysical data collected selecting from the fifth generation ECMWF global reanalysis ERA5 [128] archive the 2-D and the 3-D surface and atmospheric fields, consisting of temperature, water vapor, ozone (namely: T, Q, and O) and profiles of cloud liquid and ice water contents (CLWC/CIWC) for the computation of simulated MW and IR observation of AMSU/MHS/MWS and IASI/IASI-NG sensors. ERA5 is developed through the Copernicus Climate Change Service (C3S) and produced using 4D-Var data assimilation in CY41R2 of ECMWF's Integrated

[10] Both algorithm settings #1/#2 indicated in section 3.3 are included.

Forecast System (IFS). ERA5 hourly data on pressure levels and single levels have been used to build the dataset of atmospheric profiles on 37 pressure levels and surface parameters, respectively. Global data for four representative days (1st of Jan, Apr, Jul, Oct 2019), each at four synoptic hours (00, 06, 12, 18), have been selected to capture both seasonal and diurnal cycles. Data are available on regular latitude-longitude grids at 0.125° x 0.125° resolution. The file dimension for each variable is $2880 \times 1441 \times 16$ ($logitude\_dim \times latitude\_dim \times time$).

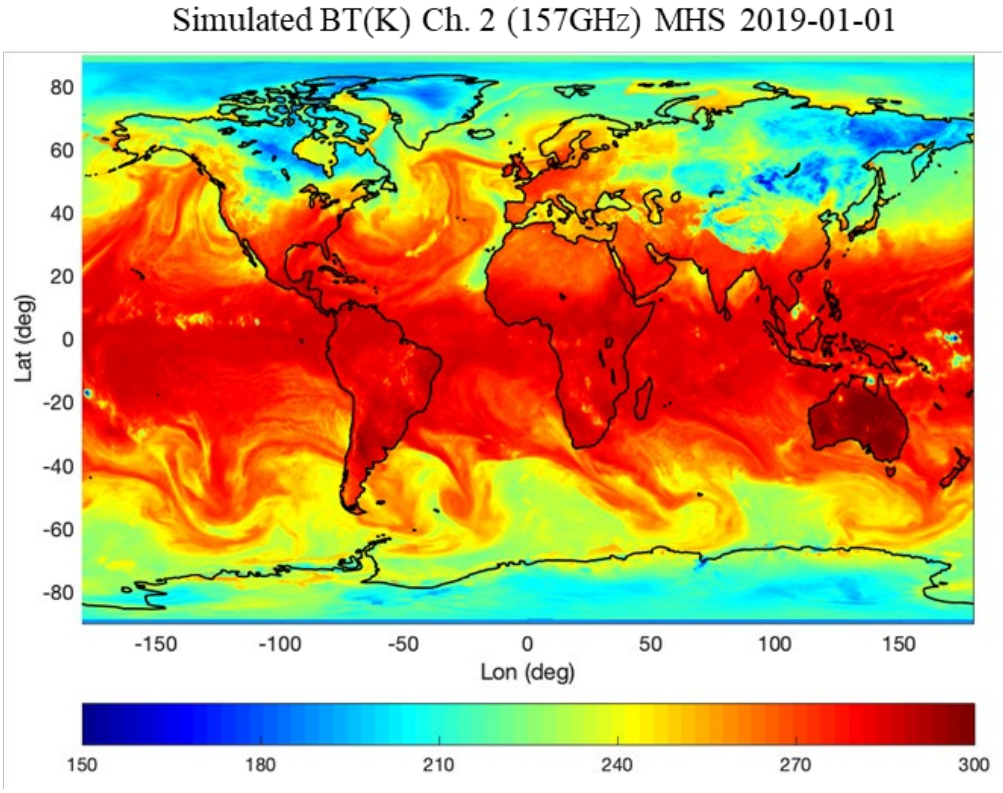

Figure 13. Simulated brightness temperature at MHS channel 2 (157 GHz) 2019/01/01 00:00 UTC.

The reason behind the use of simulated observations is driven mainly to provide machine learning algorithms, in the training phase measurements of earth radiation and investigated cloud microphysical parameters that are perfectly collocated (temporally and spatially) with each other. The validity of the simulated measurements is certified by the use of state-of-the-art radiative transfer codes used for the simulation of measurements in the infrared (σ-IASI_as [93]) and microwave bands (RTTOV-SCATT [68]).

Figure 13 shows the simulated brightness temperature at MHS channel 2 (157 GHz) for 1st Jan 2019 at 00 UTC. Real MHS observations for the same day (though covering 24h) are shown in Figure 14.

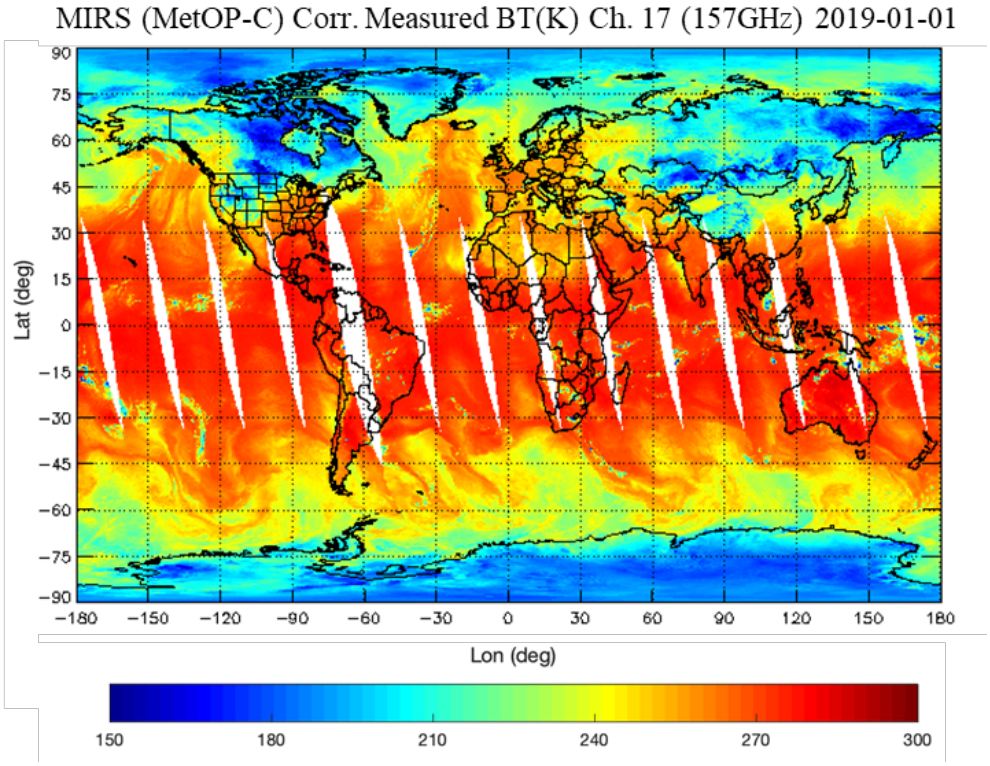

Figure 14. Observed brightness temperature at MHS channel 2 (157 GHz) 2019/01/01 (from NOAA MIRS).

The qualitative comparison of two BT maps suggests the simulations show realistic features and capture the variability of the observations. Figure 15 reports the quantitative comparison for selected AMSU/MHS channels through scatter plots of spatially and temporally nearly collocated simulations and observations. This confirms that simulations capture the variability of the corresponding observed brightness temperature field.

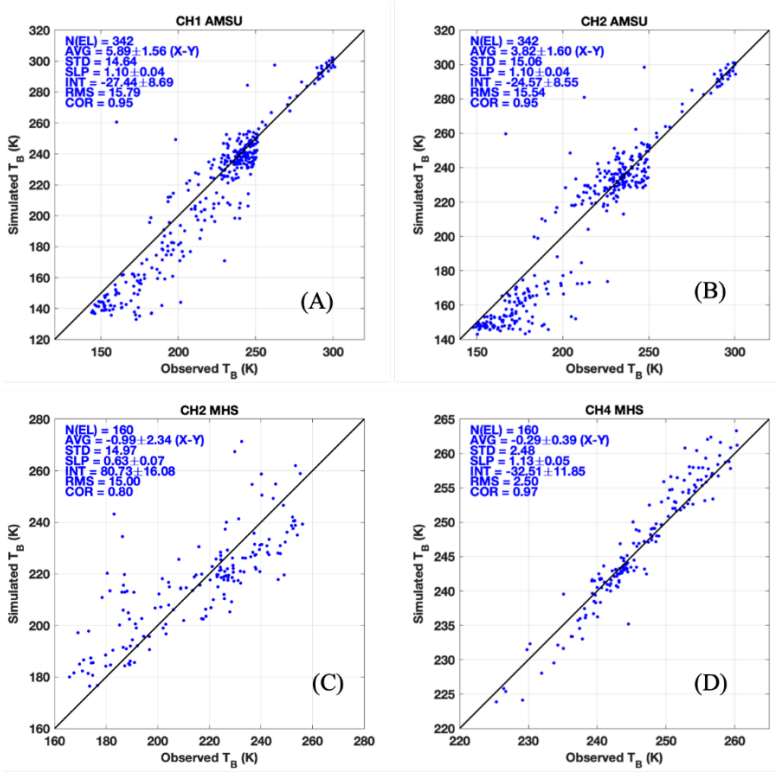

Figure 15. Simulated vs observed brightness temperatures at selected AMSU and MHS channels, after temporal and spatial colocation (2019/01/01 00:00 UTC).

In the same way, simulated infrared measurements were validated.

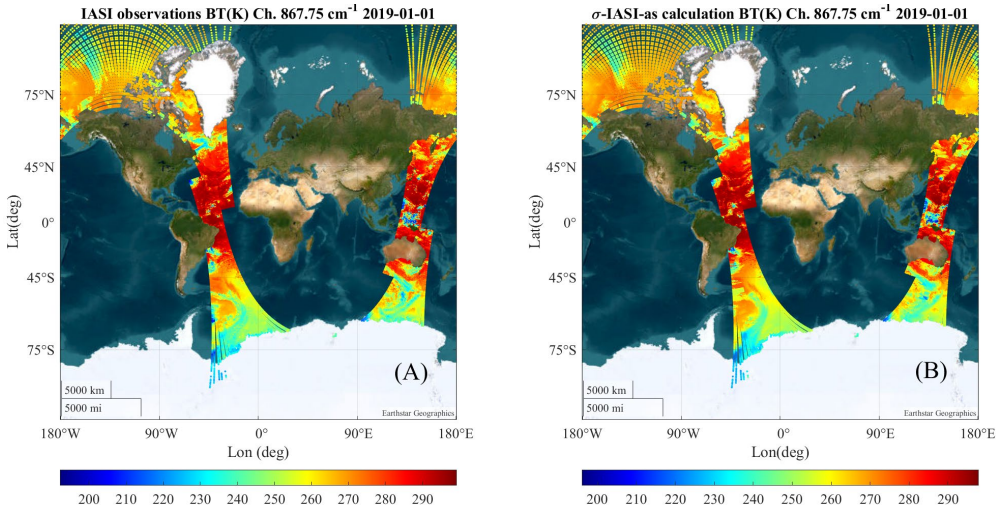

Figure 16. (A) Observed and (B) simulated brightness temperature at IASI channel 867.75 cm^{-1} 2019/01/01.

Also, in this case, the qualitative comparison of two BT maps in Figure 16 suggests the σ-IASI-as simulations show realistic features and capture the variability of the observations.

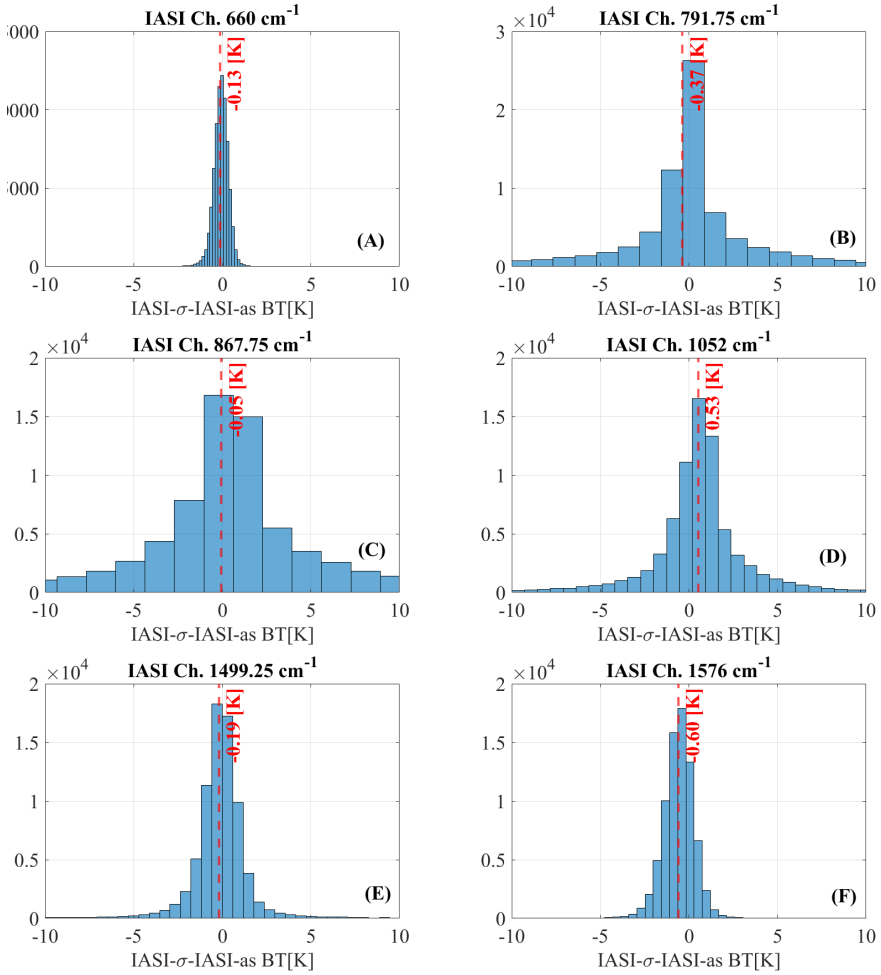

Figure 17. Histogram of residuals between real and simulated IASI BTs at different sensing channels (A) 660 cm^{-1}, (B) 791.75 cm^{-1}, (C) 867.75 cm^{-1}, (D) 1052 cm^{-1}, (E) 1499.25 cm^{-1} and (F) 1576 cm^{-1}

Figure 17 reports the quantitative comparison for selected IASI channels through the histograms of the residuals. For each selected sensing channel, the mean value is a fraction of Kelvin.

However, I would like to stress to the reader that the validity of the measurements simulated by the radiative transfer codes used in this work has been extensively demonstrated in the literature [87], [93], [129]–[133]. See Figures 1 and 2 in [93] for σ-IASI-as validation.

To reduce the computational burden in simulation, data were decimated by resampling with a latitude/longitude sampling step of 2.5°, resulting in 53 latitudes and 26 longitudes (see Figure 18) from -86.875° to 85° and from 0° to 357.5°, respectively. All atmospheric profiles were recomputed on a pressure grid of 60 levels with the σ-IASI-as algorithm and spanning the range 10 -1000 hPa. Simulated MW and IR satellite observations at IASI, IASI-NG, AMSU, MHS, and MWS channels at 3 scan angles (0°, 20° e 44°) have been computed for each of the 16 (4 synoptic hours for 4 days) ERA5 global datasets. Recommended RTTOV-SCATT optical properties have been used [134], including Mie spheres for rain and non-precipitating hydrometeors and sector snowflakes for solid precipitation.

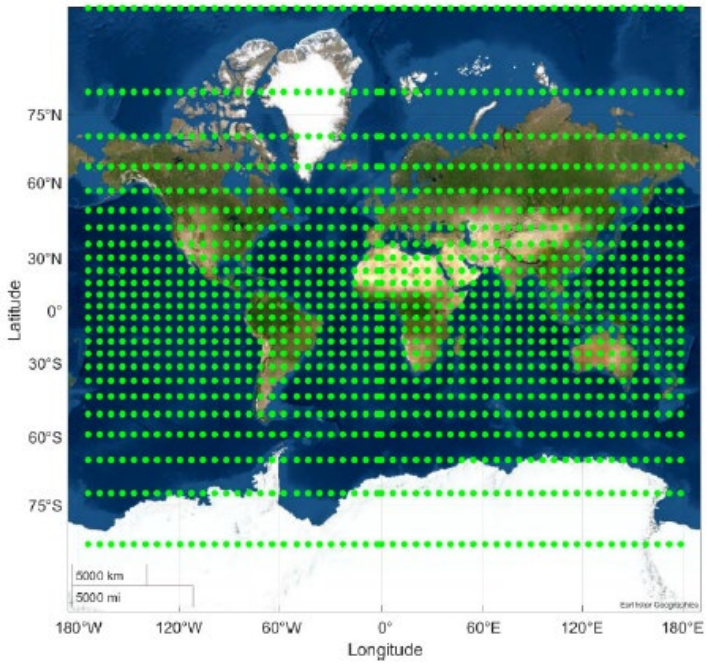

Figure 18. Map of geographical coordinates of simulated measurements.

Realistic assumptions on cloud effective radius and size distributions are made to produce IR radiative transfer calculations with σ-IASI_as, ice cloud d_e from [135] in which the shape distribution $n(L)$ (see Equation (1.4)) is determined by the use of a *mixed distribution,* Γ distribution [136] for small particles ($L \leq 20\ \mu m$) and power-law distribution [17] for the larger one ($L > 20\ \mu m$). Both these distributions are parametrized with respect to the B parameter:

$$B = -2 + 10^{-3}(273 - T)^{1.5} \log_{10}\left(\frac{CIWC}{CIWC_0}\right) \tag{3.1}$$

Where T is the atmospheric layer temperature expressed in Kelvin, $CIWC$ the corresponding ice water content in $g \cdot m^{-3}$, and $CIWC_0 = 50\ g \cdot m^{-3}$. Thus, d_e is obtained with *B* using a third-order polynomial approximation:

$$d_e = 377.4 + 203.3B + 37.91B^2 + 2.3696B^3 \tag{3.2}$$

Accordingly to [135], the range of values is limited in $[10 - 100\mu m]$.

The liquid water cloud droplet effective radius is calculated by the use of [137] parametrization:

$$r_e = \left(\frac{3CLWC}{4\pi\rho_\omega N_d k}\right)^{\frac{1}{3}} \tag{3.3}$$

$\rho_\omega = 997\ [kg \cdot m^{-3}]$ is the density of water, N_d is the number of cloud condensation nuclei, assumed $300\ cm^{-3}$ over land and $100\ cm^{-3}$ over sea accordingly to [138] analysis; $CLWC$ is given in $[kg \cdot m^{-3}]$. k is a constant formulated in terms of the relative dispersion D ($D = 0.33$ over the land and $D = 0.43$ sea) of the particle size distribution:

$$k = \frac{\left(1 + D^2\right)^3}{\left(1 + 3D^2\right)^2} \tag{3.4}$$

r_e is limited in $[4 - 16\mu m]$ range [138].

For the optical properties of ice and liquid water particles, the LBLDIS [139] library and the Chou scaling [94] approximation were used.

Auxiliary input data are collected to account for surface emissivity at MW and IR frequencies while computing simulated MW and IR radiances. The TELSEM2 MW atlas is available through EUMETSAT NWP SAF as part of the RTTOV

auxiliary data. TELSEM2 is provided as ASCII files and includes a Fortran module to handle them. IR surface emissivity is computed based on the Masuda model [140]for sea surface (available for the 15 IASI Field of Regard angles). These are provided as ASCII files (actually providing the percentage reflectance). The IR emissivity for the land surface is derived from the University of Wisconsin Global Infrared land Surface Emissivity (UWIREMIS, also known as UW/BFEMIS, Baseline Fit Emissivity Database) and it was implemented in σ-IASI cod in [141]. The database is freely available from the website (http://cimss.ssec.wisc.edu/iremis/) [142]. The database provides emissivity at ten hinge points (3.6, 4.3, 5.0, 5.8, 7.6, 8.3, 9.3, 10.8, 12.1, and 14.3 microns), with 0.05° angular resolution.

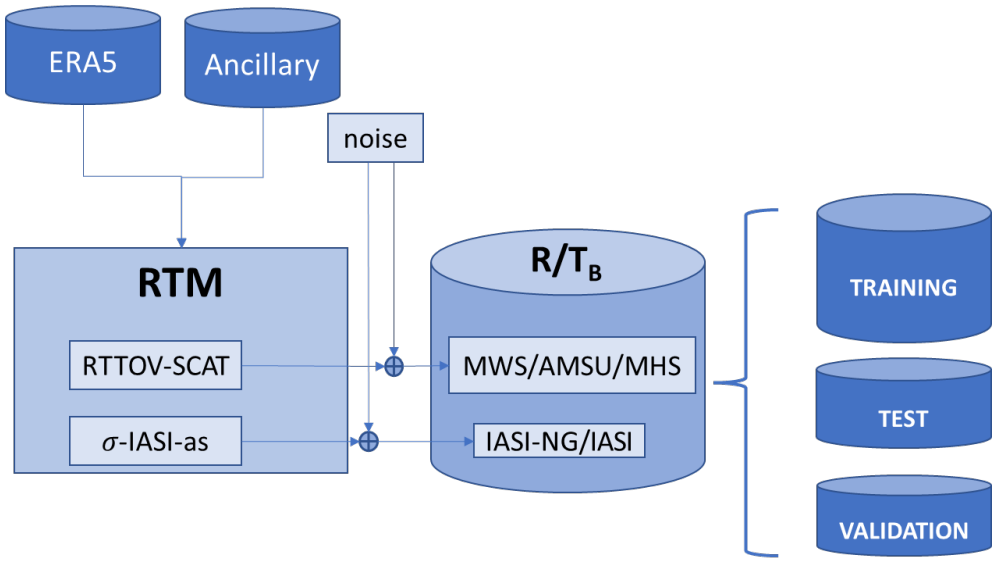

Figure 19. Processing scheme of the dataset of simulated IR (IASI-NG/IASI) and MW (MWS/AMSU/MHS) measurements.

Simulated observations do include the radiometric noise accordingly to the noise figure of each sensor. For IASI and IASI-NG measurements, the radiometric noise was characterized following the [14] theory. Both sensors have spectral radiance correlated along the wavenumber because of Gaussian apodization. After this operation, the noise for level 1C (L1C) measurements is obtained accordingly. In this framework, being S_ε the L1C covariance matrix of IASI/IASI-NG, then the observations are simulated based on the signal-noise additive model as follows:

$$R = r + S_\varepsilon^{\frac{1}{2}} \cdot \eta \tag{3.5}$$

where, R is the vector (size N = 16921 for IASI-NG and N = 8961 for IASI) of simulated spectral radiances; r (same size as R) is the signal computed according to the forward model and η is vector-valued (same size as R) of Gaussian noise sample with zero mean and unit variance; finally, we note the size of S_ε is $N \times N$. Basically the same approach has been followed for AMSU, MHS, and MWS sensors using the radiometric noise available through the WMO Observing Systems Capability Analysis and Review (Oscar) tool (https://space.oscar.wmo.int/instruments), although for these sensors channels the covariance matrix S_ε is assumed to be diagonal.

The total number of simulated soundings is 22048 samples per scanning angle. Only sea surface samples were selected. Finally, the dataset was split into three subsets for training, testing, and validation of the three SWs (see Figure 19).

3.3.2 DATA DIMENSIONALITY REDUCTION

The quality of data used in predictive methodologies directly affects their ability to learn and obtain valuable generalization performances. In the context of high spectral resolution observations, such as those measured by IASI, IASI-NG, MWS, and AMSU sensors, it is extremely important to pre-process the data to filter redundant information and infer only those that best expose the unknown underlying structure of the prediction problem to the inversion algorithms. With these statements, the curse of dimensionality problem [143], [144] is addressed. To overcome this problem, we adopted the principal component analysis (PCA) method for the simulated observation.

For sake of presentation, here we show the dimensionality reduction of IASI measurements. The basis we use to pursue the projection is that of the PCA from the definition of the covariance matrix S of IASI observations. Specifically, considering $R^{m \times s}$, the matrix of simulated m spectral radiances (see Section 3.3.1 for more details), the covariance matrix is determined starting from the following standardization:

$$\hat{R} = S_\varepsilon^{-\frac{1}{2}} \left(R - \overline{R}_{clr} \right) \tag{3.6}$$

Where $\overline{R}_{clr}$ is the *computed* mean value of IASI-NG clear-sky spectra that is used as a proxy of cloud emissivity parameter ε_c [145] and $S_{\varepsilon}^{-\frac{1}{2}}$ the level 1C IASI noise covariance matrix. In this way, using Singular Valued Decomposition (SVD):

$$S = \frac{1}{m}\hat{R}\hat{R}^T \tag{3.7}$$

$$S = V\Sigma V^T \tag{3.8}$$

The *computed* projection base V of eigenvectors retains a memory of differentiation against the clear sky, Σ is the eigenvalue matrix. Both are orthogonal and have $s \times s$ dimensions, respectively; T is the transpose operator. In this way, the projection of IASI radiances in a low dimensional subspace considering only the first $d < s$ columns of V :

$$C = V_d^T \hat{R} \tag{3.9}$$

yields a *d*-dimensional vector C of principal components that contain information about cloud emissivity and best expose information about cloud microphysics parameters.

With this in mind, we would like to anticipate to the reader that the dimensionality preprocessing step is heterogeneous among the various software that makes up the inversion framework developed. In some of them (see Sections 3.4-3.6), dimensionality reduction is applied only to the input quantities, as in the case of the regression of CLWP, CIWP, and effective radii (SW1 and SW3). Whereas, in the case of the CLWC and CIWC profiles regression (SW2), as we will illustrate (see Section 3.5), dimensionality reduction will also be applied to the output quantities.

3.4 CLWP AND CIWP REGRESSION (SW1)

In the context of the SW1 task, two NN algorithms were developed for the retrieval of CLWP and CIWP from different combinations of IR and MW satellite observations. Specifically, the simulated radiances (IASI or IASI-NG) and the brightness temperatures (AMSU/MHS or MWS), and the satellite vertical zenith angle (VZA) are the inputs for the development of two NN algorithms.

Table 7. Summary of NN parameters for the IR-MW (IASI-NG & MWS and IASI & AMSU/MHS) configurations

	MWS & IASI-NG	IASI & AMSU/MHS
N. layers	5	5
N. hidden layers	3	3
N. input units	55 (30 IASI-NG PCs + 24 MWS Channels + VZA)	51 (30 IASI-NG PCs + 15 AMSU + 5 MHS Channels + VZA)
N. hidden units of the hidden layer 1	1024	32
N. hidden units of the hidden layer 2	1024	256
N. hidden units of the hidden layer 3	64	32
N. output units	2 (CLWP and CIWP)	2 (CLWP and CIWP)
Units activation function	ReLU	ReLU
Optimization algorithm	Adam [113]	Adam
Implicit regularization	Early stopping [110]	Early stopping
Explicit regularization	Weight decay [146]	Weight decay
NN architecture finder	Bayesian tuner [147], [148]	Bayesian tuner
Loss function	MSE	MSE

The former takes into input the synergy of IASI-NG and MWS, while the latter takes IASI and AMSU/MHS. As introduced in Section 3.3.2 data preprocessing is mandatory to determine a regression framework less complex and more feasible for the regression of the CLWP/CIWP parameters. A criterium for selecting IASI PCs is suggested in [149], where they demonstrate that the number of PCs that would separate the signal from noise ranges between 10–100. In this way, to be conservative we select 30 IASI and IASI-NG PCs for the retrieval process, which span 99.96% of the total variance. The dataset was preliminarily filtered to avoid extremely large CLWP/CIWP values (i.e., CLWP and CIWP larger than 0.6 kg/m^2 and 0.5 kg/m^2, respectively) that may harm the NN training, screening out less than 0.3% of the initial dataset. In addition, to avoid uncertainty due to surface emissivity in the MW spectral region, only simulations over the ocean are considered in this analysis. These two screenings leave 31593 samples in total, which are then divided into three sets used to train ($70\% = 22746$ samples), validate ($20\% = 5687$ samples) and test ($10\% = 3160$ samples) the NN model. The partitioning of the samples into training, validation, and test datasets was such to keep the same variability to the VZA parameter. Because the dynamic range of IASI/IASI-NG PCs and AMSU/MHS/MWS brightness temperatures (BT) may greatly differ, it is good practice to normalize the two data spaces. This is achieved using standard normalization (i.e., inputs are normalized to the training set by removing the mean

and scaling to unit variance), applying both IR and MW inputs. Thus, in SW1 the first 30 PCs (see Section 3.3.2 for further information) of the IASI and IASI-NG radiances are determined and used together with the MW brightness temperatures and the VZA to constitute the NN input layer that is of 55 nodes for IASI-NG and MWS and 51 nodes for IASI and AMSU/MHS configurations, respectively. The target outputs are the CLWP and CIWP vertical integrated contents.

The learning is pursued by the adoption of forward- and backward-propagation algorithms whose objective is to minimize the error between NN predictions and training outputs. Keras-python framework [150] has been used to build and implement the NN structures. To this end, Keras offers a built-in tuner [151] to optimize the search for the best NN structure to the input/output units and a set of "hyperparameters" (e.g., the number of hidden layers, hidden units, activation function, optimizer, and so on). In this work, the Bayesian tuner [147], [152] has been used. Based on random selection, the Bayesian tuner addresses the problem of finding the best NN architecture for a given learning task and dataset. The search for the best hyperparameters is based on network morphism in NN architecture search (NAS) [152] and a tree-structure search space [148]. Two NN structures composed each of three hidden layers, respectively of 1024, 1024, and 64 hidden units for the IASI-NG & MWS configuration, and 32, 256, and 32 hidden units for the IASI & AMSU/MHS configuration were chosen by the tuner. The ReLU [153] function is used to activate the network units, and the MSE is used as the loss function. Adam algorithm [113], regularized according to the weight decay algorithm [146] has been used as a backpropagation algorithm to optimize the learning of the two selected NN structures. Adam is a mini-batch optimization algorithm, representing nowadays the de facto standard to train deep learning NN models [110], due to its high versatility in adapting to complex architectures with high capacity cost functions [154]. Read Table 7 for more information. With limited training data, however, this complex architecture could lead to overfitting; for this reason, we adopted regularization, aiming at making the model generalize better, i.e., produce better results on the test set [155]. The use of regularization to avoid overfitting has been proved empirically [110]. There are many worked examples in the open literature showing how high-capacity architectures, i.e., NN with more parameters than training data couples, can improve the generalization performance. In other words, contrarily to overfitted architectures, the validation error remains close to the training one. This empirical evidence has been rigorously proved in mathematical form by [154]. In effect, [154] demonstrates that the deep learning architecture is the condition needed to move beyond the classical under-

parameterized regime to the modern interpolation where the predictors have negligible training risk. Since we move to the interpolating regime, in this retrieval we dedicate particular care to the training, validation, and test steps of the NN. For sake of simplicity, we will call the two configurations C1 (IASI-NG & MWS) and C2 (IASI & AMSU/MHS). C1 and C2 have been trained and tested for 100 epochs on training and validation sets.

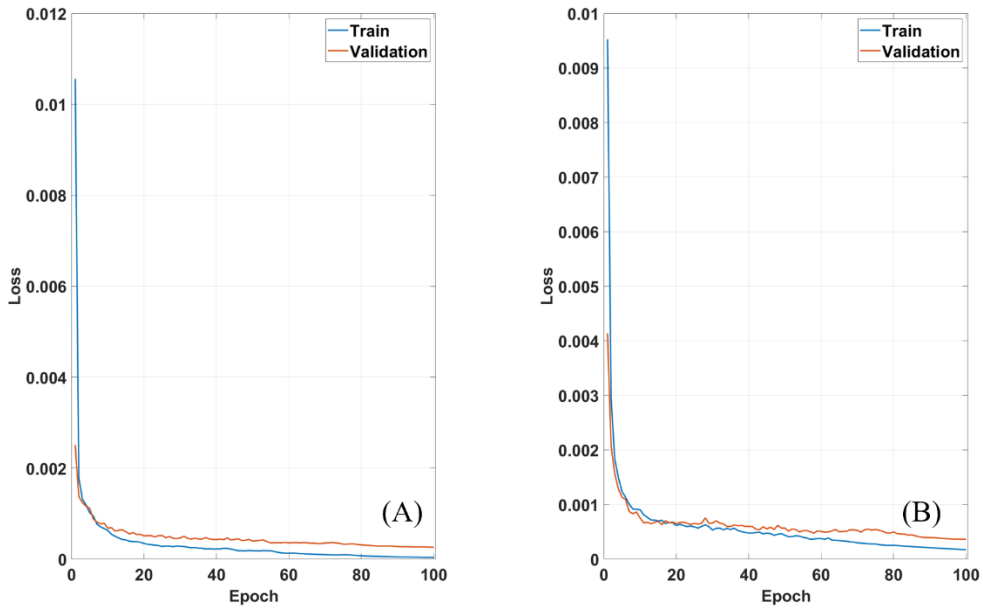

Figure 20. Neural network training and validation loss function history for configuration C1 (A) IASI-NG & MWS and C2 (B) IASI & AMSU/MHS configurations.

Figure 20 reports the NN's learning performances in the training and validation steps, showing that the validation error is stable and follows the training error for both architectures.

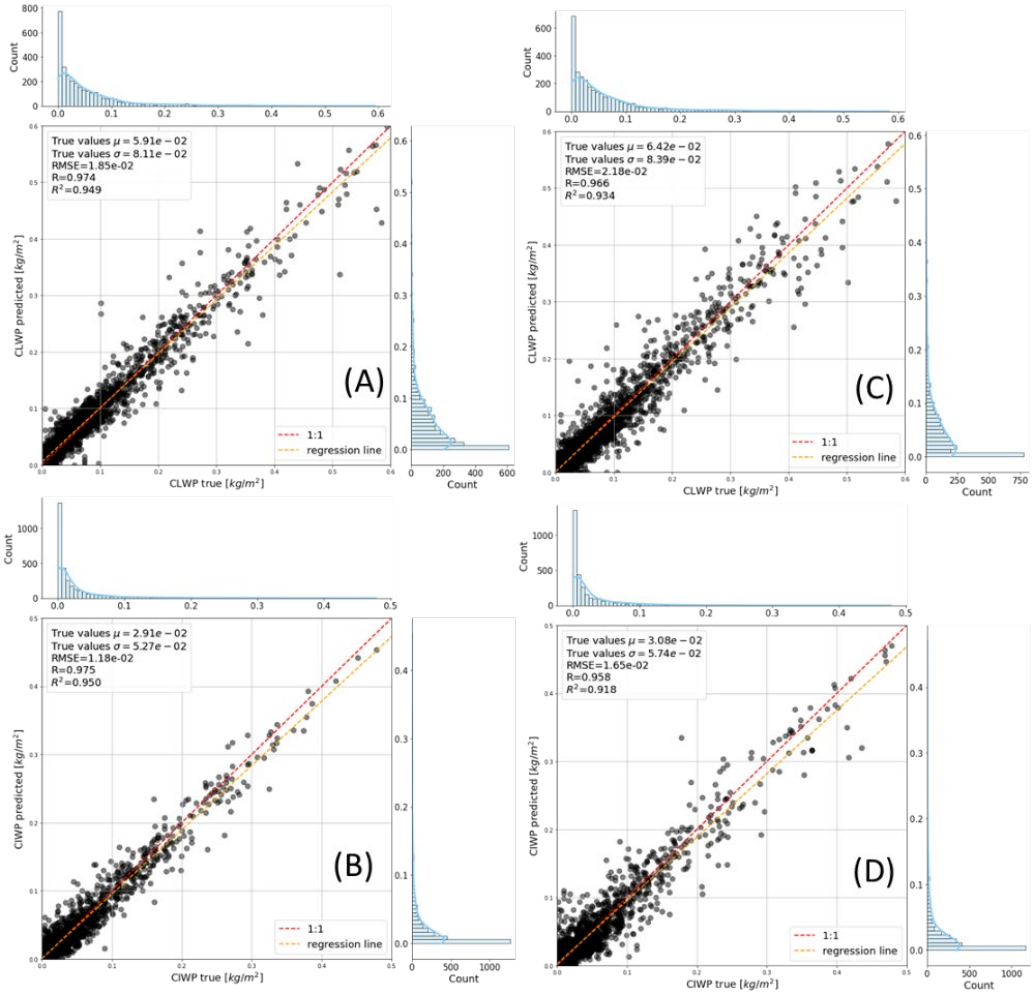

Figure 21. Scatterplot of the NNs prediction for CLWP and CIWP. (A)-(B) These results correspond to the C1 configuration, taking into input the combination of IASI-NG & MWS observations. (C)-(D) is referred to the C2 configuration that takes into input the combination of IASI & AMSU/MHS observation. μ and σ indicate the mean and std of the reference true values. Except for correlation and determination coefficients (R and R^2), units are in kg/m^2.

As anticipated in Section 3.3.1, after the NNs learning process the regression performances are tested on a set of unseen simulated measurements. The results are shown in Figure 21, indicating a good capability to infer both CLWP and CIWP from the combination of the MW and IR observations. For configuration C1 the overall rmse for CLWP is 1.85×10^{-2} kg/m^2, while 1.18×10^{-2} kg/m^2 for CIWP. The rmse for CLWP results in about 30% of the mean value and 22% of the variability (1-sigma). Similarly, the rmse for CIWP results in about 41% of the mean value and 22% of the variability (see Figure 21 (A) and (B)). Also, configuration C2 show high performance the overall rmse for CLWP is 2.18×10^{-2} kg/m^2, while 1.65×10^{-2}

kg/m^2 for CIWP (see Figure 21 (C) and (D)). These results are comparable with, though better than, previously reported, e.g., [27] using 3rd order multiple regression and maximum likelihood algorithms to retrieve CLWP and CIWP from a simulated dataset of MW observations at a subset of MWS channels. To further assess the performance of the C1 and C2 configurations, we performed a binning analysis of the scatter plots. For this aim, the *x*-axis is divided into ten bins; for each bin, the average and standard deviation of true and the corresponding predicted values are computed. These are displayed in Figure 22, for both C1 and C2 configurations, providing information on the systematic and random error as a function of the absolute values.

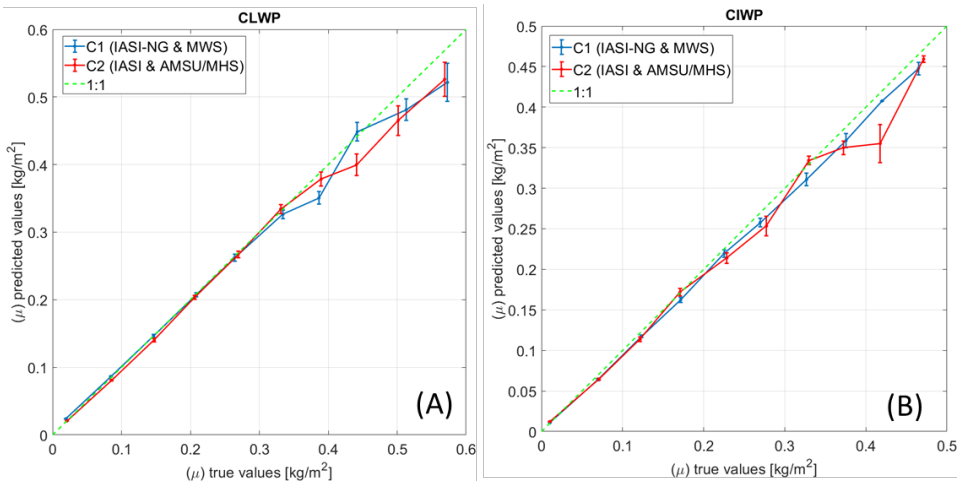

Figure 22. Error analysis comparison of the NN C1 and C2 configurations to estimate CLWP (A) and CIWP (B). The figure shows the mean of predicted values as a function of true ones. The errorbars indicate the uncertainty corresponding to each binned estimate.

By analysing Figure 22 A and B it is straightforward to note the goodness of the implemented C1 and C2 configurations in reproducing mean predicted CLWP/CIWP. For almost the entire range of measurements ($CLWP < 0.4 kg/m^2$ and $CIWP < 0.4 kg/m^2$) the predictions have an almost negligible bias.

Figure 22 also helps highlight the sensing potential of the new incoming generation of high-spectral sensors (IASI-NG and MWS) with respect to the current one (IASI, AMSU, and MHS). As expected, configuration C1 is less affected by bias due to the enhanced sensing capabilities of the new IASI-NG and MWS sensors. This result is strongly shown in the binned analysis for CIWP (see Figure 22 B). In the case of the C1 configuration, the binned analysis is almost a straight

line, consistent with the bisector one. Conversely, the C2 configuration shows some variations.

To demonstrate the value of MW and IR synergy, we also developed two reference NN architectures, based respectively on IASI-NG only and MWS only. By comparing the performances of the three different configurations, the advantage of combining IR and MW with respect to either one can be quantified. For MW-only, the NN configuration takes in input the VZA and the 24 MWS channels. For IR-only, the configuration takes in input the VZA and the first 30 IASI-NG PCs. Similarly, to the IR-MW combined architecture, the MW-only and IR-only NN configurations are optimized by the Bayesian tuner, as reported in Tables Table 8 and Table 9. The three architectures are hereafter indicated as M1 (combined IASI-NG & MWS), M2 (MWS), and M3 (IASI-NG).

Table 8. Summary of NN parameters for the MW-only configuration.

N. layers	5
N. hidden layers	3
N. input units	25 (24 MWS Channels + VZA)
N. hidden units of the hidden layer 1	64
N. hidden units of the hidden layer 2	32
N. hidden units of the hidden layer 3	64
N. output units	2 (CLWP and CIWP)
Units activation function	ReLU
Optimization algorithm	Adam
Implicit regularization	Early stopping
Explicit regularization	Weight decay
NN architecture finder	Bayesian tuner
Loss function	MSE

Table 9. Summary of NN parameters for the IR-only configuration.

N. layers	5
N. hidden layers	3
N. input units	31 (30 IASI-NG PCs + VZA)
N. hidden units of the hidden layer 1	1024
N. hidden units of the hidden layer 2	256
N. hidden units of the hidden layer 3	32
N. output units	2 (CLWP and CIWP)
Units activation function	ReLU

Optimization algorithm	Adam
Implicit regularization	Early stopping
Explicit regularization	Weight decay
NN architecture finder	Bayesian tuner
Loss function	MSE

In this case, also a binned analysis comparison has been performed. These are displayed in Figure 23, for both CLWP and CIWP and all three configurations, picturing the contribution of the IR and MW observations to the combined approach.

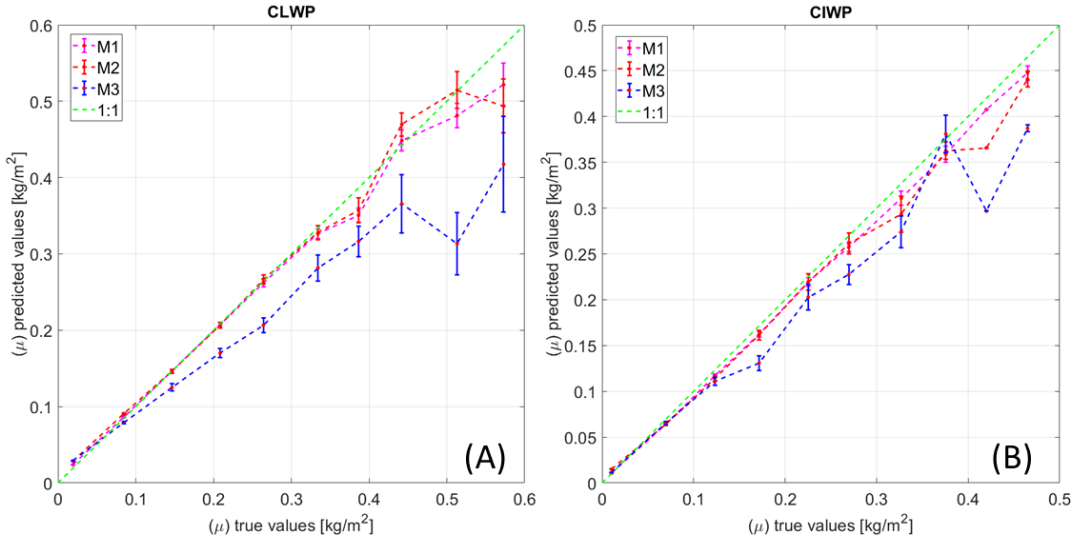

Figure 23. Error analysis of the NN to estimate CLWP (A) and CIWP (B). The figure shows the mean of predicted values as a function of true ones. Same as the one shown in Figure 22 but for the comparison of M1, M2, and M3.

For CLWP it is seen that M3 (IASI-NG) yields unbiased values only for small values (<0.1 kg/m^2). The reason is that IASI-NG radiances soon saturate in presence of thicker water clouds. In contrast, MWS predictions are fairly unbiased up to the value of ≅ 0.30 kg/m^2. As expected, the MW-IR combination provides more information and thus predictions are closer to the 1:1 line. Similar comments apply to CIWP. The same binned analysis is used to estimate the root mean square error (rmse) as a function of the predicted values, as shown in Figure 24. The binned analysis shows that the rmse tends to increase with the estimated value, staying between 5-25% for both CLWP and CIWP, except for values lower than 0.1 kg/m^2.

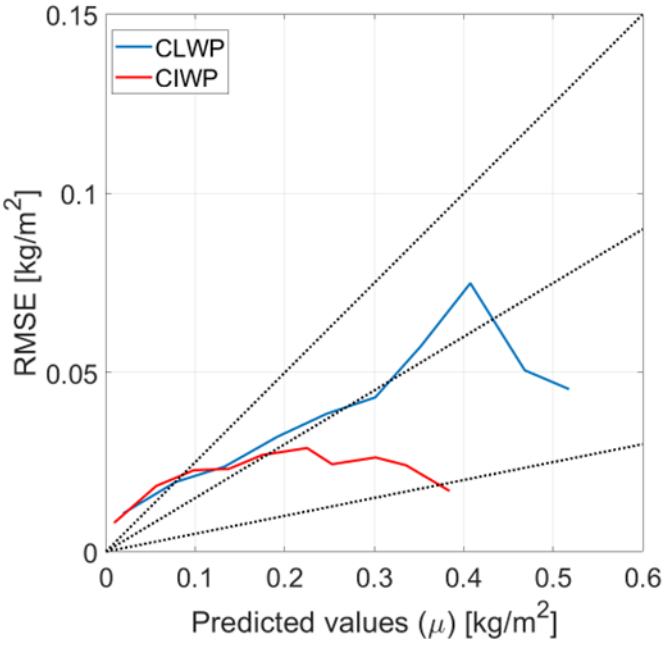

Figure 24. Root mean square error of the estimate of CLWP and CIWP obtained from the NN approach. The three dotted lines correspond to 5% (lower), 15% (middle), and 25% (higher) error. Results for the M1 configuration (MWS+IASI-NG combination) are shown.

To illustrate the value of IR+MW combination with respect to the individual systems (IR- and MW-only), in Figure 25 a comparison using the Taylor diagram [156] is shown. The Taylor diagram provides a graphical and intuitive method to compare the performances of the three NN configurations to retrieve CLWP and CIWP. The performances are quantified in terms of three statistics: i) the Pearson correlation coefficient, ii) the root mean squared error (RMSE), and iii) the standard deviation. From Figure 25, the relative merit of the different NN configurations is evident. Concerning CLWP predictions (Figure 25 A), it is straightforward that M1 shows the best retrieval performances. M2 also shows good performances, confirming the ability of the MW sensor to infer CLWP, while M3 performances are worst. A similar consideration applies to the CIWP retrieval (Figure 25 B), where the configuration performances are considerably better for M1 than for M2 and M3. Quantitatively, the IR and MW combination (M1) provides CLWP with a 2% higher correlation and a 1.4 factor lower rmse to MW only (M2), and a 14% higher correlation and a 2.4 factor lower rmse to IR only (M3). Concerning CIWP, the IR and MW combination provides a 4% higher correlation and a 1.7 factor lower rmse to MW only, and an 8% higher correlation and a 2.1 factor lower rmse to IR only.

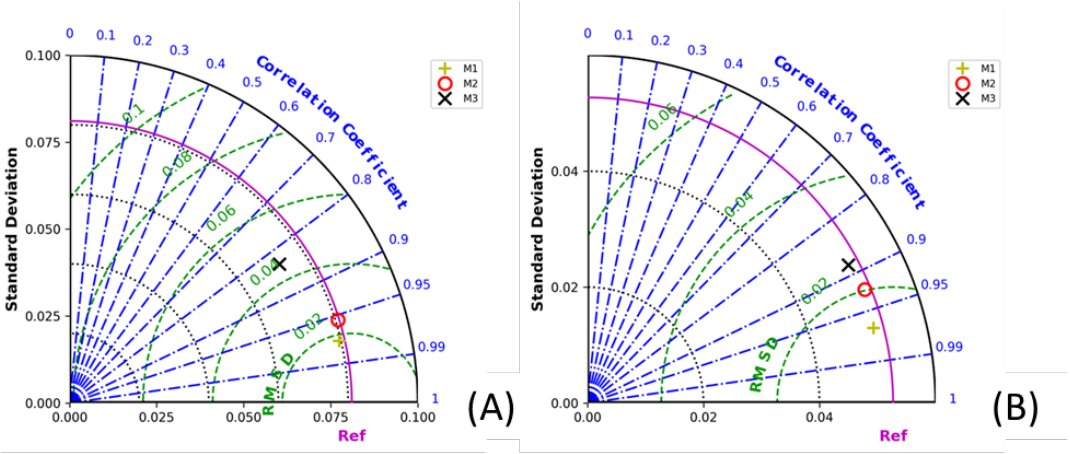

Figure 25. Taylor diagram analysis for CLWP (A) and CIWP (B). The analysis refers to the three NN architectures, M1, M2, and M3 developed in this study.

Finally, to further demonstrate that the implemented approach, which operates in the interpolating regime, does not lose in terms of generalization, Table 10 shows the RMSE computed for the training, validation, and test datasets for both CLWP and CIWP and the three configurations. Note that the performances for the validation and test datasets are nearly the same, indicating that a fair generalization has been achieved.

Table 10. M1, M2, and M3 performances in terms of RMSE of the CLWP and CIWP regression for the training, validation, and test datasets. Units are in 10^{-2} kg/m^2.

	CLWP			CIWP		
	Train	**Valid**	**Test**	**Train**	**Valid**	**Test**
M1	0.65	1.85	1.85	0.52	1.34	1.18
M2	2.09	2.59	2.52	1.94	2.09	2.04
M3	1.94	4.65	4.50	1.50	2.42	2.51

To conclude, the synergy of IR and MW has been proved, paving the road to more complete exploitation of next generation satellite platforms for weather and climate. IR and MW combination provides CLWP with higher correlation (2-14%) and lower rmse (factor of 1.4-2.4) than single MW and IR only, respectively. Similarly, for CIWP, with 4-8% higher correlation and 1.7-2.1 factor lower rmse, respectively.

3.5 CLWC AND CIWC REGRESSION (SW2)

SW2 focuses on the regression of CLWC and CIWC profiles. The simulated radiances (IASI or IASI-NG) and brightness temperatures (AMSU/MHS or MWS) and the satellite VZA are the input for the development of four NN algorithms. The

first two take in input IASI-NG and MWS, while the other two take IASI and AMSU/MHS.

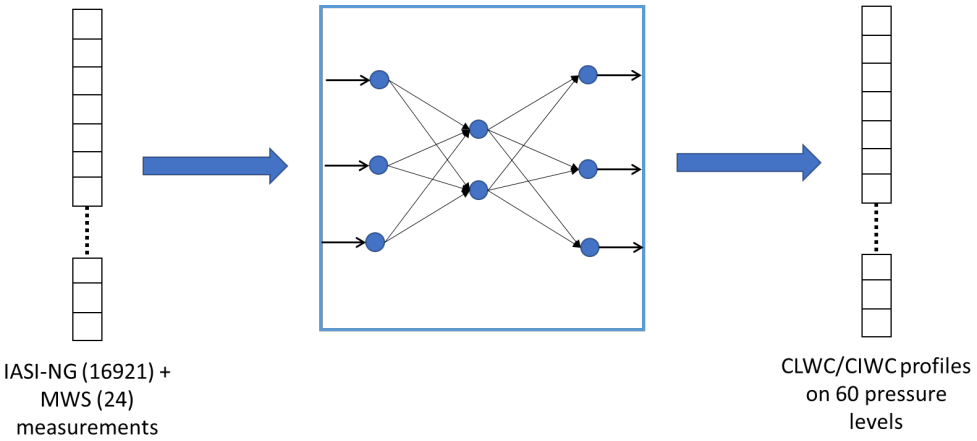

Figure 26. SW2 baseline regression architecture.

As discussed in Section 3.3.1, the physical data and parameters we are dealing with are the spectral radiation and brightness temperature at the top of the atmosphere and the liquid and ice water content profiles of the atmosphere. These quantities are observed through a high number of spectral infrared and microwave channels and over different homogeneous atmospheric layers. In practice, considering the k = 16921 IASI-NG, d = 24 MWS sensing channels, and the definition of the CLWC and CIWC profiles over m = 60 homogeneous atmospheric layers several $(k+d)\times m$ regression problems have to be considered (see Figure 26). It is quite obvious that the solution of a regression problem defined by the above quantities is made difficult, if not unpractical, also by NN inversion approaches. In such context, to overcome this high dimensionality problem, we considered the use of different functional basis, one for each physical data and parameter, that allows us to project them from a high dimensional to low dimensional space, making the regression problem more suitable and easier to solve by a NN model. For NNs inputs, the functional basis and the PCA analysis are the same as SW1. For what concern the NN outputs, the projection was made by using a functional base of eigenvectors, corresponding to the first ten and five eigenvalues of the corresponding CLWC and CIWC covariance matrices. Both profiles are normal standardized before the application of the PCA to improve the fit of the data by avoiding giving too much weight to variance caused by noise. Figure 27 shows a sketch of the implemented regression architecture.

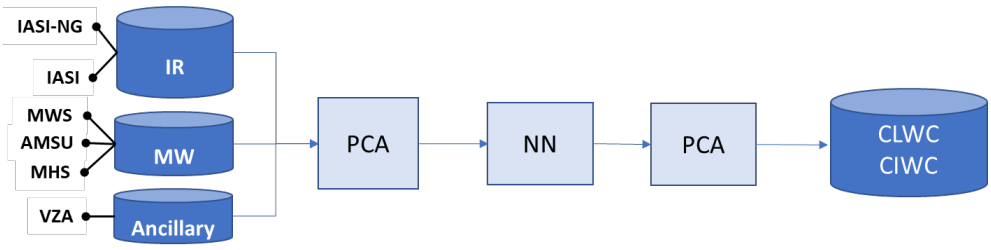

Figure 27. Sketch of NN regression architecture of CLWC and CIWC profiles.

Similarly, to SW1 Bayesian tuner was used to select the best NN configurations. In SW2 the hyperparameters search space comprises the number of hidden layers (value in [1, 2, 3]), the number of hidden units for each hidden layer (value in [16, 32, 64, 128, 256, 512, 1024]), the dropout rate for each hidden layer (value in [0.0, 0.25, 0.5]), the optimizer (Adam, SGD [157] and Adam weight decay [146]), and the optimizer learning rate (value in [1e-1, 1e-2, 1e-3, 1e-4, 1e-5]). ReLU and linear activation functions have been used for the hidden and the output units, respectively. The maximum number of different models to try in the search space is set by default to 100, though the tuner may interrupt the search before reaching the maximum number of trials if the search space has been covered. Finally, the tuner selects the best performing NN architecture, which minimizes the test MSE loss. Adam optimizer is used to train the NN models. The final configuration details are reported in Table 11.

Table 11. Parameters of the implemented NN structure in SW2.

	Configuration	Input	Hidden layers (units)	Activation function	Loss function	Optimizer	Output
CLWC	**MWS & IASI-NG**	- 30 IASI-NG PCs - 10 MWS PCs - VZA	2 (128-256)	ReLU	MSE	Adam	5 CLWC PCs
CLWC	**AMSU/MHS & IASI**	- 30 IASI PCs - 4 AMSU / 1MHS PCs - VZA	3 (64-1024-512)	ReLU	MSE	Adam	5 CLWC PCs
CIWC	**MWS & IASI-NG**	- 30 IASI-NG PCs - 10 MWS PCs - VZA	3 (512-256-32)	ReLU	MSE	Adam	10 CIWC PCs
CIWC	**AMSU/MHS & IASI**	- 30 IASI PCs - 4 AMSU / 1MHS PCs - VZA	2 (128-256)	ReLU	MSE	Adam	10 CIWC PCs

The NNs in Table 11 are trained on a global dataset (66144 match-ups), representative of both the diurnal and seasonal cycles. After filtering, the dataset is divided into 70% of the samples for training (32002), 20% (8001) for testing, and 10% (4445) for validation. Also, in this case, the dataset was preliminarily filtered

considering only sea surface acquisitions. After the NN learning process, which uses the training and test datasets, the NN performances are tested on the previously unseen validation dataset. Naturally, the PCA operated on either the input or the output vector can lead to an optimized definition of the inversion problem for the NN implemented architectures. However, each of those NN models does not perform by themself the inversion from the measured output data to the desired parameters. Consequently, the predictions of the CLWC and CIWC PCs are used to reconstruct the cloud liquid/ice water profiles defined on the 60-level pressure grid used by σ-IASI.

The results for the four NN configurations, of Table 11 are shown in Figure 28 for CLWC and CIWC profiles, in terms of rms (Figure 28 A and B) and fractional error decrease (Figure 28 C and D). We will refer to C1(IASI-NG & MWS) and C2(IASI & AMSU/MHS) as the configurations for the CLWC retrieval. C3(IASI-NG & MWS) and C4 (IASI & AMSU/MHS) are the configurations for the CIWC retrieval. The fractional error decrease is defined as follows (Equation (3.10)), and thus indicates the percentage retrieval error decrease to a simple mean value estimate:

$$f_{rmse} = 100 \cdot \frac{rmse_{true,x} - rmse_{predicted,x}}{rmse_{true,x}} \tag{3.10}$$

Where $x = CLWC$ or $x = CIWC$.

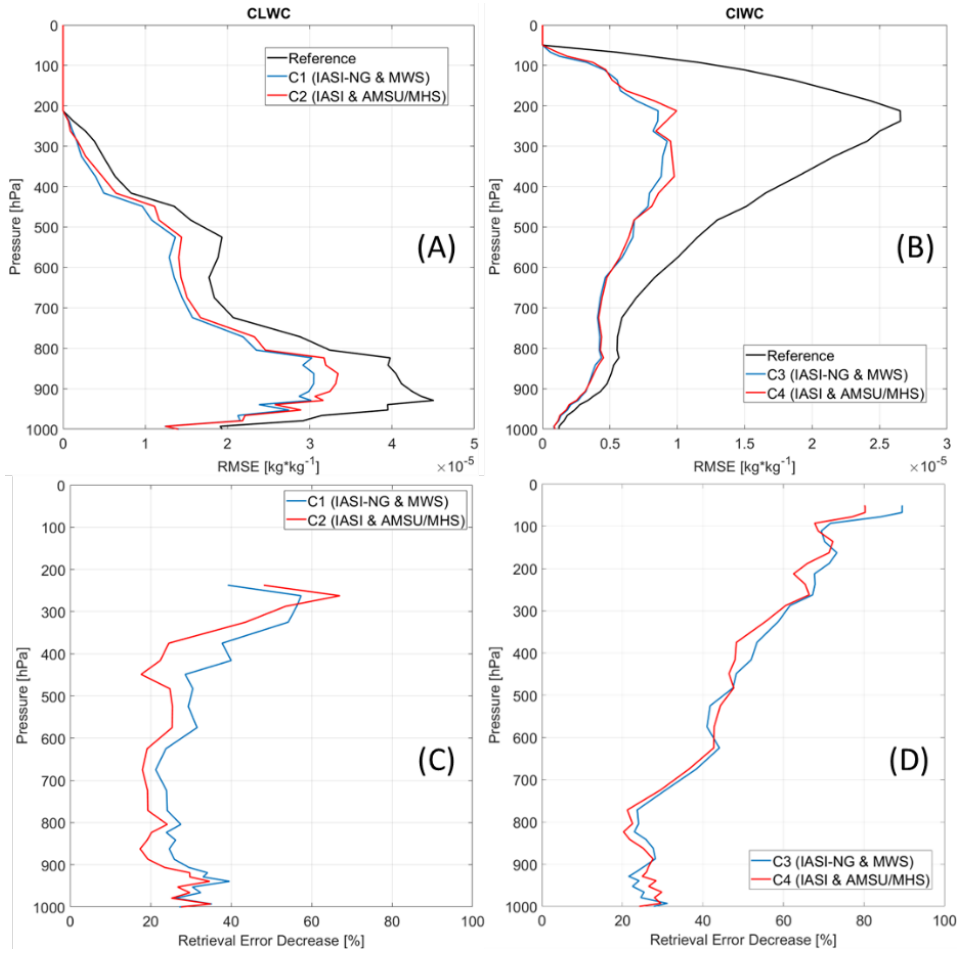

Figure 28. (A) and (B) profiles of CLWC and CIWC retrieval error (in terms of rms difference to reference truth) of the four NN configurations using IASI-NG and MWS (C1 and C3 configurations) and IASI, AMSU, and MHS (C2 and C4 configuration) combinations, respectively. (C) and (D) corresponding profiles of retrieval error decrease to a simple mean estimate for the same NN configurations.

From Figure 28 we can quantify that the IR & MW synergy allows an error reduction for CLWC within 20-40% for pressures lower than 500 hPa. Similar results are obtained also for CIWC retrieval. As expected, for CIWC retrieval the error reduction is larger in the upper troposphere (where most ice clouds occur) reaching 45-65% in the 500-100 hPa. Comparing C1 and C2 in Figure 28 A and C and C3 and C4 in Figure 28 B and D, it is straightforward to deduce that the error reduction for CLWC and CIWC profiles using new generation sensors (IASI-NG & MWS) is better (of about 5-10%) than using the current generation one (IAI & AMSU/MHS). A humble result which, however, echoes what we observed in the performance analysis of SW1 that is, the improved atmospheric sensing capability of the new generation sensors.

To demonstrate the consistency of the NNs configuration, we integrated the CLWC and CIWC predictions and compared them with the reference ERA5 ones.

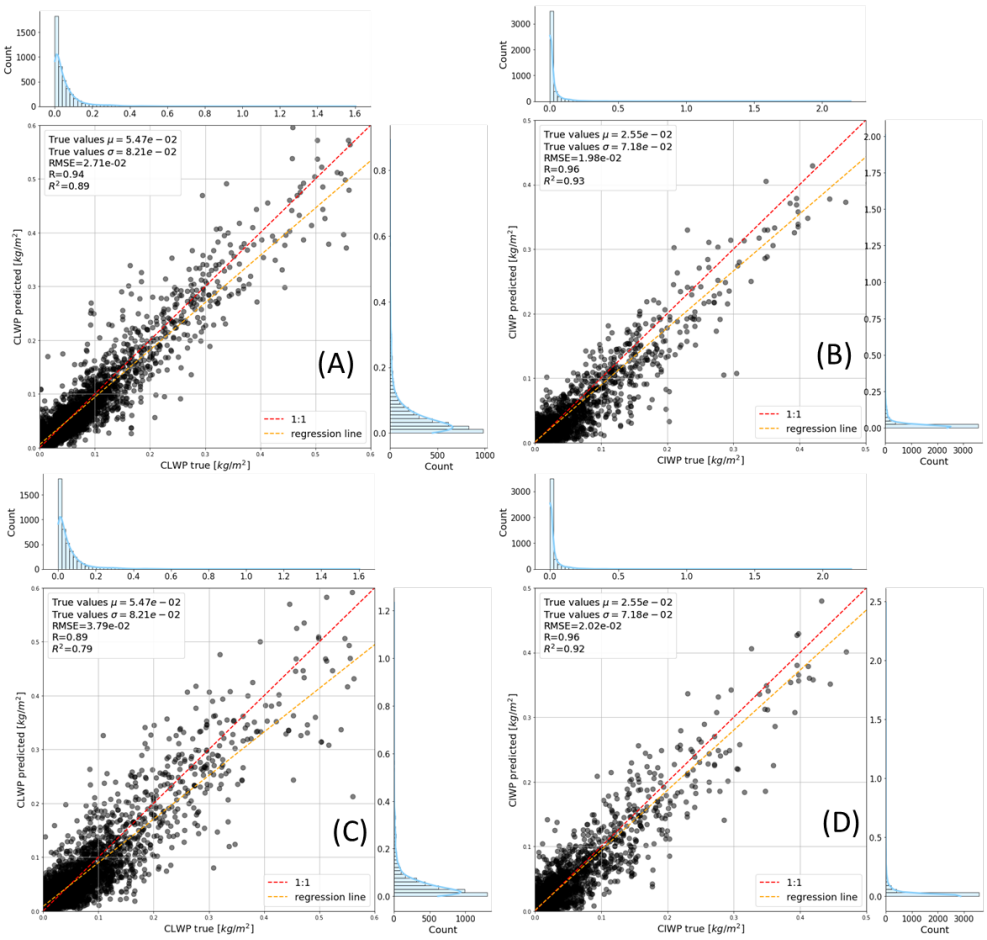

Figure 29. Scatter plots of CIWP (B and D) and CLWP (A and C) integrated reference vs predicted values. (A) and (C) regard configurations C1 and C3, (B) and (D) regard C2 and C4.

Figure 29 presents the scatter plots between CIWP and CLWP integrated from the retrieved CLWC and CIWC profiles vs those obtained integrating over the reference (ERA5) profiles. Configurations C1 and C2 that uses inputs from new generation sensors (IASI-NG & MWS) show very high R^2 values of about 0.90 for CLWP and 0.93 for CIWP. Configurations C3 and C4 (IASI & AMSU/MHS inputs) also show good retrieval performance with high $R^2 = 0.92$ for CIWP and moderate $R^2 = 0.79$ for CLWP; all the rms differences are well below 10%. The results obtained allow us to attest that the obtained predictions of integrated content paths are consistent with those of profiles. In addition, another important result is possible to observe by comparing the CLWP regression performance of C1 and C3

configurations. The spectral contributions from the new generation sensors allow us to obtain predictions with smaller variance and bias. In terms of R^2 we have an improvement of about 13%. The same conclusions appear from the binned analysis shown in Figure 30 A and B.

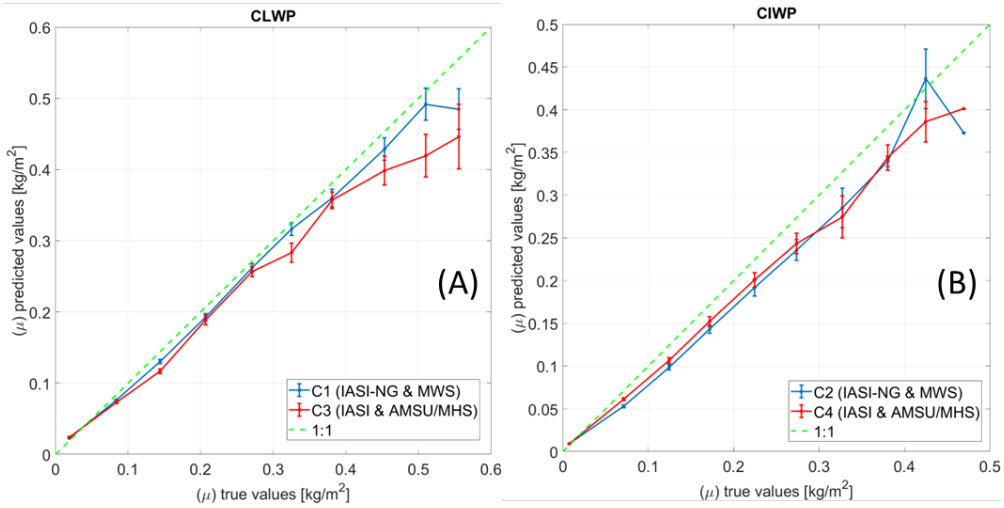

Figure 30. Error analysis comparison of (A) CLWP between C1 and C3 configurations and (B) CIWP between C2 and C4.

3.6 CLOUD EFFECTIVE RADII REGRESSION (SW3)

The simulated radiances (IASI or IASI-NG) and brightness temperatures (MWS or AMSU/MHS) are the inputs for the development of four RF regressors of cloud drop liquid water r_e and ice d_e -effective radii. The first 100 PCs of the IASI and the IASI-NG observations are computed and retained, following the analysis made in [149]. The computed IASI-NG PCs, tighter with the 24 MWS, and the VZA constitute the input for the C1 configuration. IASI PCs with the 15 AMSU-A and 5 MHS constitute the input for the C2 configuration. In both cases the target output is r_e. While, IASI-NG and IASI PCs and VZA constitute the input features of the C3 and C4 configurations, whose target output is d_e. In this last case this case MW measurements did not provide any help or useful information in predicting d_e. See Figure 31 for a schematic representation of the implemented configurations.

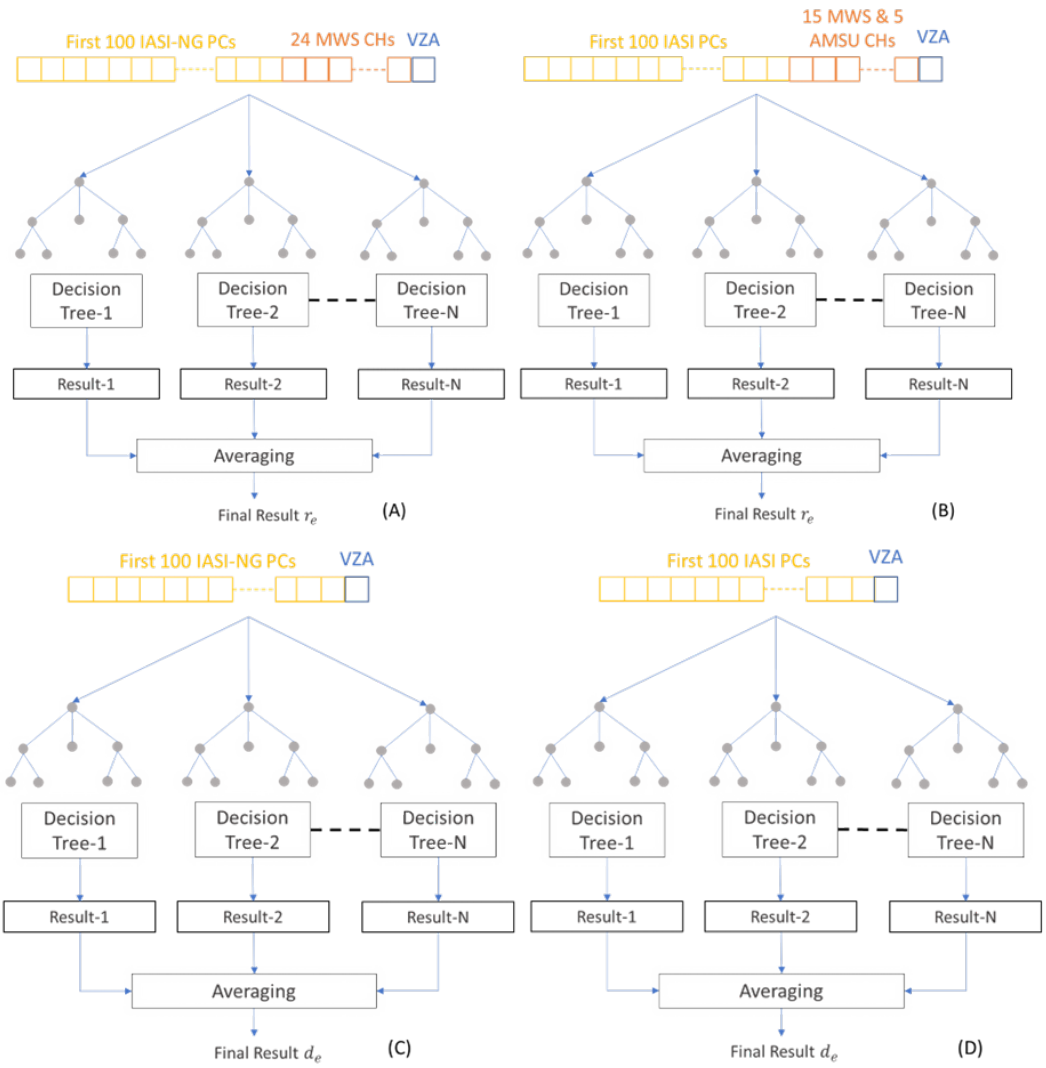

Figure 31. Schematic representation of the RF architectures used in this work in terms of inputs, namely (A) the first 100 IASI-NG PCs, the 24 MWS channels, and the VZA. (B) the first 100 IASI, the 15 AMSU-A, and 5 MHS channels, and the VZA, (C) the first 100 IASI-NG PCs and VZA and (D) the first 100 IASI PCs and VZA. The outputs, namely "Final Result," are the predicted values of liquid and ice cloud drop effective radii.

The training step involved the use of the K-fold strategy[158] with ten splits to cross-validate the RF models. Specifically, this validation technique divides all the samples in the training dataset into k groups of samples, called folds. The random forest models are trained using $k - 1$ folds, and the fold left out is used for the test (see Figure 32).

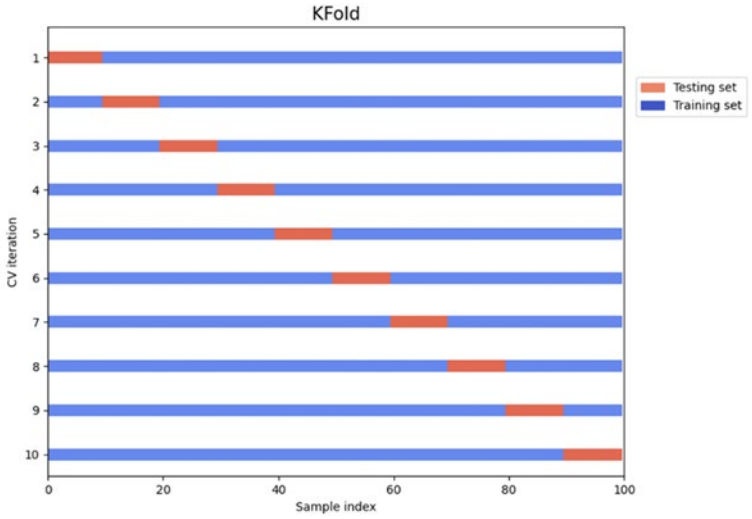

Figure 32. Representation of ten split K-fold cross-validation strategies used in this work.

The MSE is used as a splitting rule by each tree within the RF. To search for the best RFs architectures, the *Optuna* [120] optimization framework was used. Specifically, starting from the set of RF hyperparameters. Optuna formulates the hyperparameter optimization as a process of minimizing the MSE loss objective function that dynamically constructs the search space of the RF architecture taking a set of hyperparameters as input and returning its validation score. Optuna makes this dynamic search of hyperparameters by the combined use of relational and independent sampling hyperparameters methods and an efficient pruning algorithm that monitors the intermediate objective values and terminates the training if no improvement, in terms of R^2 in this case, is observed.

The training and fine-tuning of RF models are more expensive and time consuming compared to NN models. In Optuna, the maximum number of different models to try in the search space is set by default to 100. Finally, the RF models with the best set of hyperparameters (see Section 2.2.2 for more details), the ones that maximize the R^2 are returned. However, to explore and test more hyperparameter combinations, we augmented the maximum number of trials within the Optuna hyperparameters search space to 150. To reduce the training time, several RF models were trained together using all processors of our workstation that comprises a CPU (AMD Ryzen Threadripper 2990WX) of 32 cores (64 virtual) with 64Gb of DDR4 (3000 MHz) memory. The total tuning time is of about 6 hours each, for ice and liquid configurations. Figure 33 shows the Optuna parallel tuning process of hyperparameters for the ice cloud drop radii RF model.

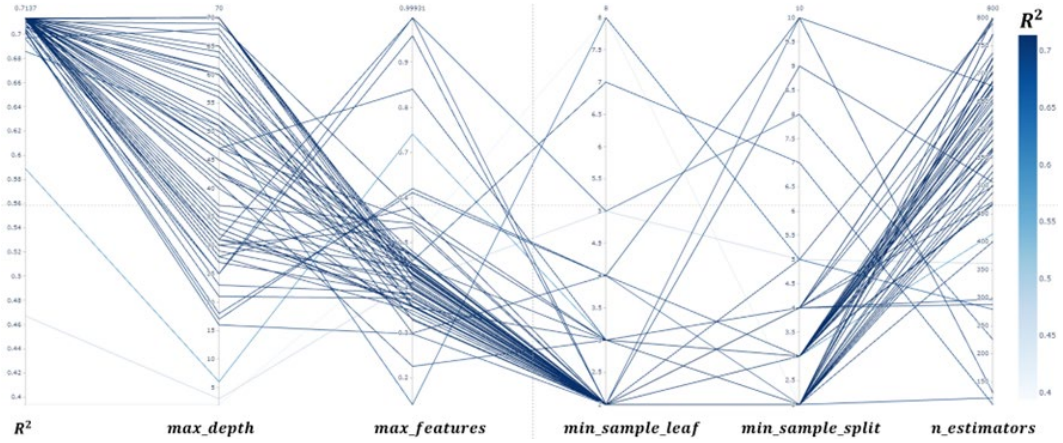

Figure 33. A plot of hyperparameters tuning for RF algorithm exploiting MWS and IASI-NG for ice cloud drop effective radii (150 trials). The darker blue line, corresponding to the highest R^2, indicates the selected best combination of hyperparameters.

Finally, four RF architectures with the best set of hyperparameters, the one that maximizes the R^2 returned. Table 12 reports hyperparameters of the selected RF architectures.

Table 12. Hyperparameters of the optimized RF architectures for liquid and ice cloud drop radii retrievals.

	Configuration	Input	N. estimators	Max. depth	Min. sample split	Min. sample leaf	Max. features
r_e	**MWS & IASI-NG (C1)**	- 100 IASI-NG PCs - 24 MWS channels - VZA	627	64	3	2	0.97
	AMSU/MHS & IASI (C2)	- 100 IASI PCs - 15 AMSU and 5 MHS channels - VZA	729	29	2	2	0.39
d_e	**IASI-NG (C3)**	- 100 IASI-NG PCs - VZA	799	44	2	2	0.88
	IASI (C4)	- 100 IASI PCs - - VZA	757	51	4	2	0.42

As for SW1 and SW2, the complete dataset was divided in liquid and ice clouds (only over sea and non-zero values) and then further divided into two subsets: 90% (Liquid = 19110, Ice = 28760) for the training/test and 10% (Liquid = 2124, Ice = 3196) for the validation. The validation dataset consists of unseen data produced with the same method as the training and test data.

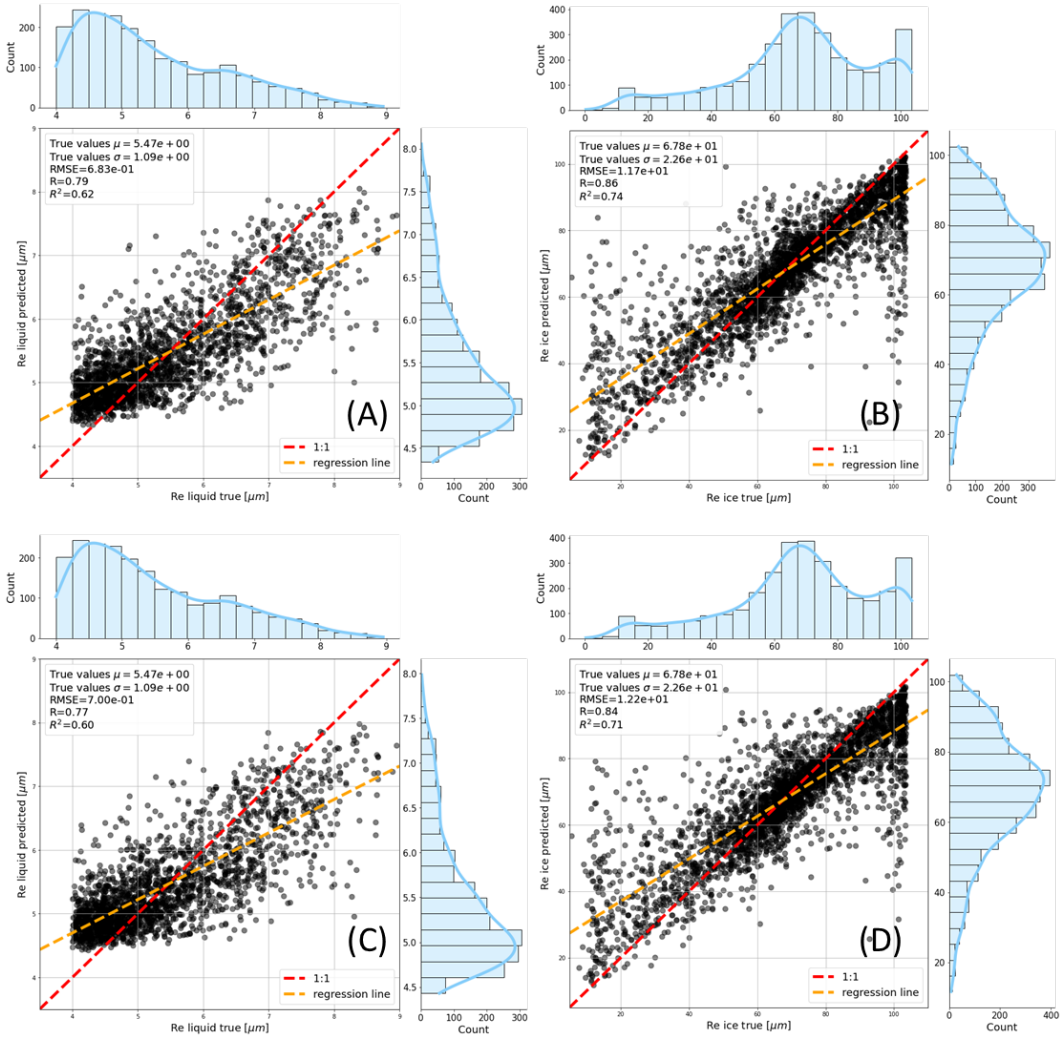

Figure 34. Scatter plots of effective radii retrieval for (A)/(C) liquid and (B)/(D) ice clouds. Marginal histograms on the side of the scatter plots show the distribution of reference true and predicted ice and liquid cloud drop radii. C1 and C2 configurations' performance are those shown in (A) and (C), C3 and C4 configurations refer to (B) and (D).

Scatter plots showing retrieval performance for both liquid (C1 and C2 configurations) and ice (C3 and C4 configurations) clouds are shown in Figure 34.

In terms of correlation, all configurations show strong values. C1 and C2 show 0.79 and 0.77 for liquid clouds, whereas C3 and C4 reach 0.86 and 0.84 for ice clouds, respectively. Such results demonstrate the goodness of the generalization performances of the four implemented RF configurations. This is also highlighted by comparing the marginal histograms of reference and predicted values which have very similar skewness and median values. Comparing Figure 34 (A) and (C) and (B) and (D), it is possible to deduce that future IASI-NG and MWS sensors

would increase the effective radius retrieval performance with respect to current sensors (IASI, AMSU, and MHS) by a fraction of microns in rmse (0.17 for liquid and 0.05 for ice) and 2-3% in correlation.

3.7 REGRESSION UNCERTAINTY ESTIMATION

A single-pixel uncertainty estimate for each cloud product has been implemented within the three SWs. The single-pixel uncertainty is estimated through the validation process, computing a binning analysis of the residuals between the output product and the corresponding target. A polynomial curve is fitted through the error model resulting from the binned analysis (ε_M), and the single-pixel uncertainty estimate is generated evaluating the fit of the error model as a function of the retrieved product:

$$u(P_i) = \text{fit}(\varepsilon_M, P_i) \tag{3.11}$$

Where P_i indicates the i-th prediction. Specifically, a linear spline interpolation has been implemented.

3.7.1 CLWP AND CIWP (SW1 UNCERTAINTY)

The uncertainty for CLWP and CIWP retrievals (SW1) is estimated as a curve fit through the binned analysis resulting from the validation dataset. Figure 35 shows the results from the binned analysis, i.e., mean and std of the residuals (true minus predicted) values evaluated on the validation dataset.

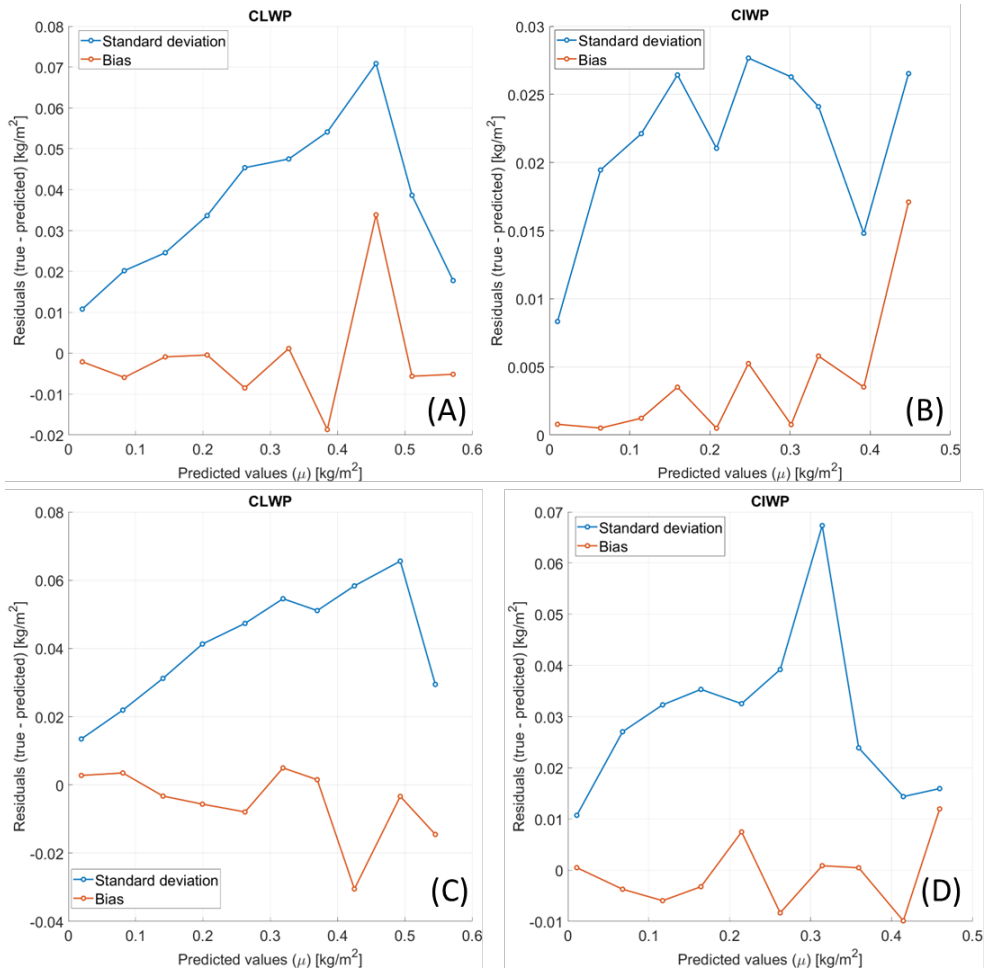

Figure 35. Mean and std of binned (true-predicted) residuals for CLWP (left) and CIWP (right) retrievals from combined (A-B) IASI-NG and MWS and (C-D) IASI and AMSU/MHS.

3.8.2 CLWC AND CIWC (SW2 UNCERTAINTY)

The uncertainty for CLWC and CIWC profile retrievals (SW2) is pursued following the same uncertainty estimation process of SW1. Figure 36 shows the results from the binned analysis, i.e. mean and std of the residuals (true minus predicted) values evaluated on the validation dataset. The mean, std, and rms of the residuals are assumed as representative of systematic, random, and total uncertainty. For any values of CLWC and CIWC, SW2 provides an estimate of the total uncertainty corresponding to the spline fit of the residuals rms evaluated at the CLWC and CIWC values, respectively.

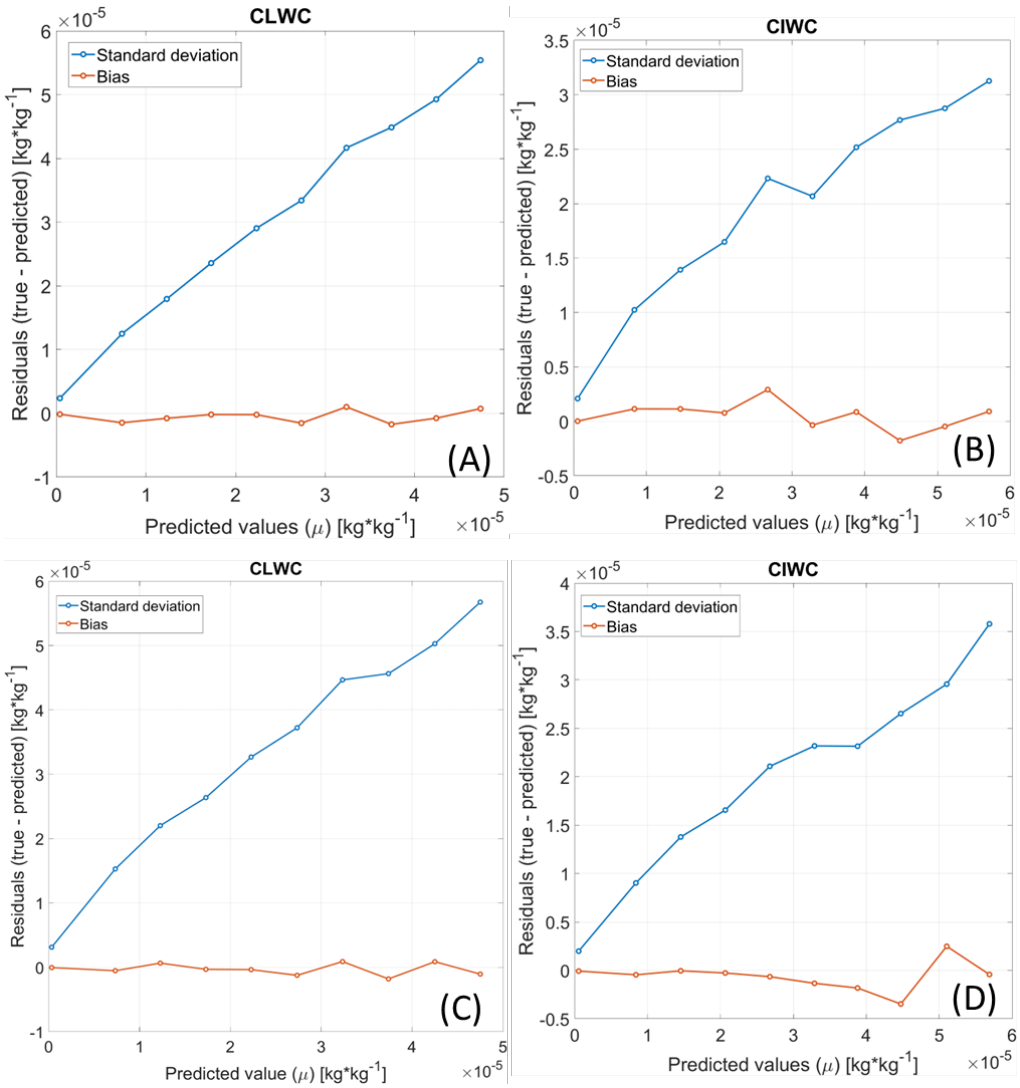

Figure 36. Mean and std of binned (true-predicted) residuals for CLWC (left) and CIWC (right) retrievals from combined (A-B) IASI-NG and MWS and (C-D) IASI and AMSU/MHS.

3.8.3 CLOUD EFFECTIVE RADII (SW3 UNCERTAINTY)

Figure 37 shows the uncertainty results for SW3 retrievals, estimated as a curve fit through the binned analysis resulting from the validation dataset. Also in this last case, for any values of cloud effective radius, SW3 provides an estimate of the total uncertainty corresponding to the spline fit of the rms of the residuals evaluated at the predicted value.

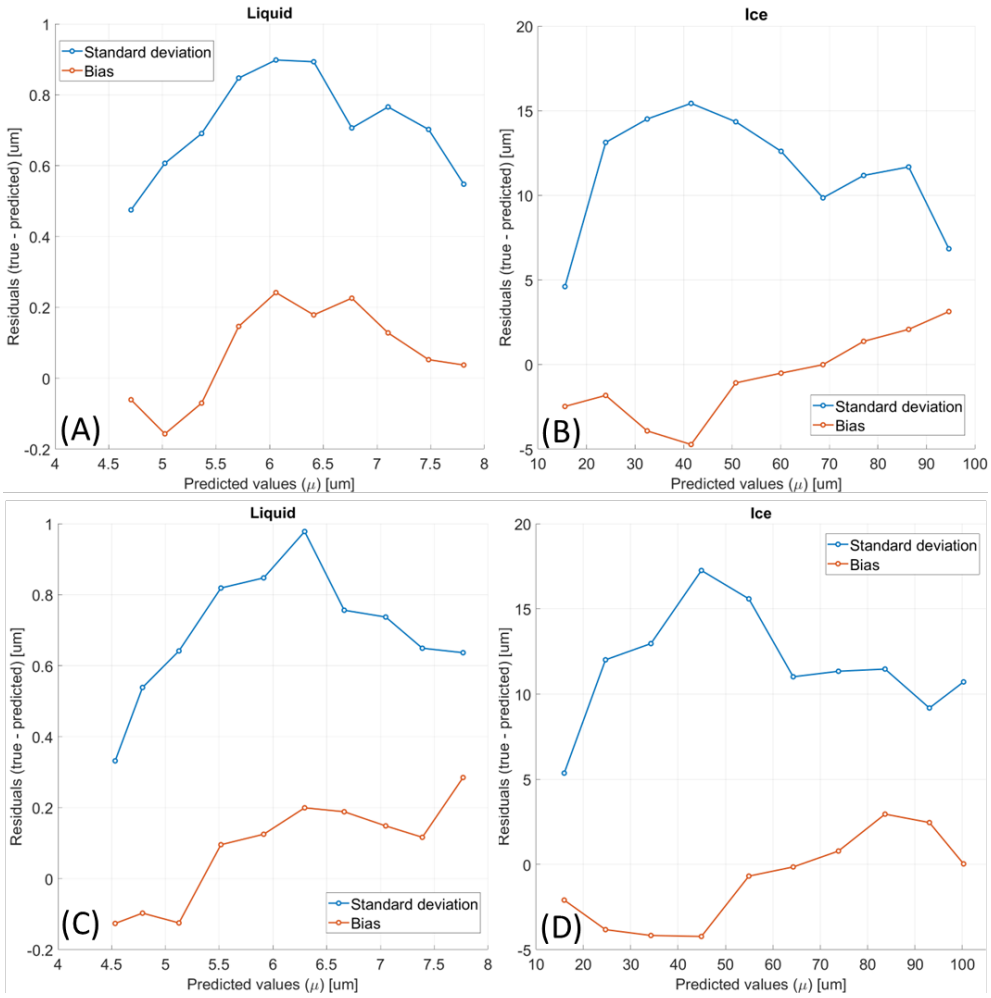

Figure 37. Mean and std of binned (true-predicted) residuals for liquid water (left) and ice (right) cloud effective radii retrievals from combined (A) IASI-NG /MWS and (C) IASI/AMSU/MHS and (B) IASI-NG and (D) IASI measurements.

3.8.4 TRACEABILITY TO REQUIREMENTS

A diagnostic analysis has been performed to validate the SWs product against an independent reference database for Numerical Weather Prediction (NWP) requirements. Specifically, the Observing Systems Capability Analysis and Review Tool (OSCAR) database of the World Meteorological Organization (WMO) was used for the evaluation. This database specifies four levels of performance:

T: Threshold level below which the product becomes ineffectual and is of no use for the targeted application;

B: Breakthrough level beyond which a significant improvement in the target application is achieved;

O: Objective level beyond which the observation gives no significant improvement for the targeted application;

G: Goal level considered achievable with the proposed approach/algorithm/instrument.

Table 13. Traceability of settings #1 and settings #2 configurations to WMO OSCAR NWP requirements.

	Product	**T**	**B**	**O**	**G**	**Settings #1**	**Settings #2**
SW1	CLWP	50 g/m^2	20 g/m^2	10 g/m^2	50 g/m^2	18.5 g/m^2	22 g/m^2
	CIWP	20 g/m^2	10 g/m^2	5g/m^2	20 g/m^2	11.8 g/m^2	17 g/m^2
SW2	CLWP from (CLWC)	50 g/m^2	20 g/m^2	10 g/m^2	50 g/m^2	27.1 g/m^2	38 g/m^2
	CIWP from (CIWC)	20 g/m^2	10 g/m^2	5 g/m^2	20 g/m^2	19.8 g/m^2	20 g/m^2
SW3	Re	5 μm	2 μm	1 μm	4 μm	0.68 μm (liq) 11.7 μm (ice)	0.7 μm (liq) 12.2 μm (ice)

From the comparison shown in Table 13 the performances for CLWP and CIWP both for SW1 and SW2 are between threshold and breakthrough levels, more in agreement for SW1 but SW2 demonstrates the consistency of CLWC and CIWC profiles predictions. For the retrieval of effective radii, the achieved performances meet the objective level when limited to liquid clouds. For ice clouds, currently, no information is available within the WMO database to track the requirements of the effective radius of ice clouds. In this sense, therefore, these measurements could be considered a new result.

3.8 VALIDATION WITH EXTERNAL OBSERVATIONS

To assess the generalization performance of the implemented regression framework all SWs were validated by the use of an external validation dataset of real observation. Only setting #2 configurations (see Section 3.3) using observations from current generation sensors (e.g., IASI, AMSU, and MHS) as inputs are going to be used in this validation. Specifically, we collected recent

measurements from MetOp-B and MetOp-C with colocated ECMWF analysis covering a larger range of latitudes. In more detail, we selected MetOp measurements from 23:30 UTC on 8 September 2021 to 00:30 UTC on 10 September 2021, corresponding to MetOp-B orbits 46574-46589 and MetOp-C orbits 14732-14746). Among these, we selected the measurements within +/- 30 minutes from the ECMWF analysis base time. Figure 38 shows the 16 MetOp orbits selected with this criterion: 8 for MetOp-B (46574, 46575, 46578, 46581,46582, 46585, 46588, 46589) and 8 for MetOp-C (14732, 14733, 14735, 14736, 14739, 14742, 14743, 14746). The final dataset consists of 538880 IASI spectra collocated with MHS and AMSU collocated spectra. Among these, 387472 spectra are recorded over the sea. Note that in Figure 38 the colors indicate the measurement time.

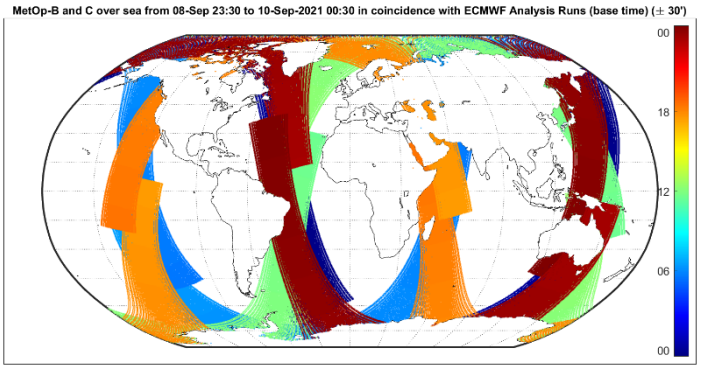

Figure 38. MetOp footprints in the selected. The color indicates the spectrum measurement time.

Dark blue, light blue, green, orange, and dark red indicate respectively the spectra collocated with 00, 06, 12, 18, and 24 ECMWF base time hours. The distribution with the latitude of the collocated spectra is shown in Figure 39.

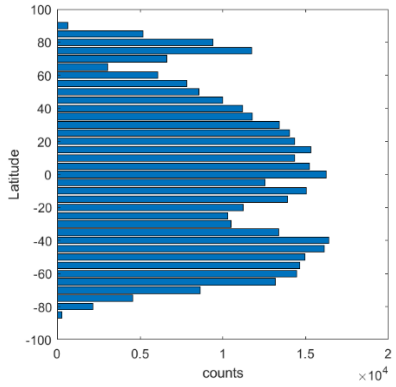

Figure 39. Latitude distribution of the dataset.

Each bin spans 5° latitude. Each IASI/AMSU/MHS combined spectrum is associated with the geophysical state vector from ERA5 reanalysis, providing CLWC and CIWC profiles over 137 pressure levels from surface to 0.01 hPa.

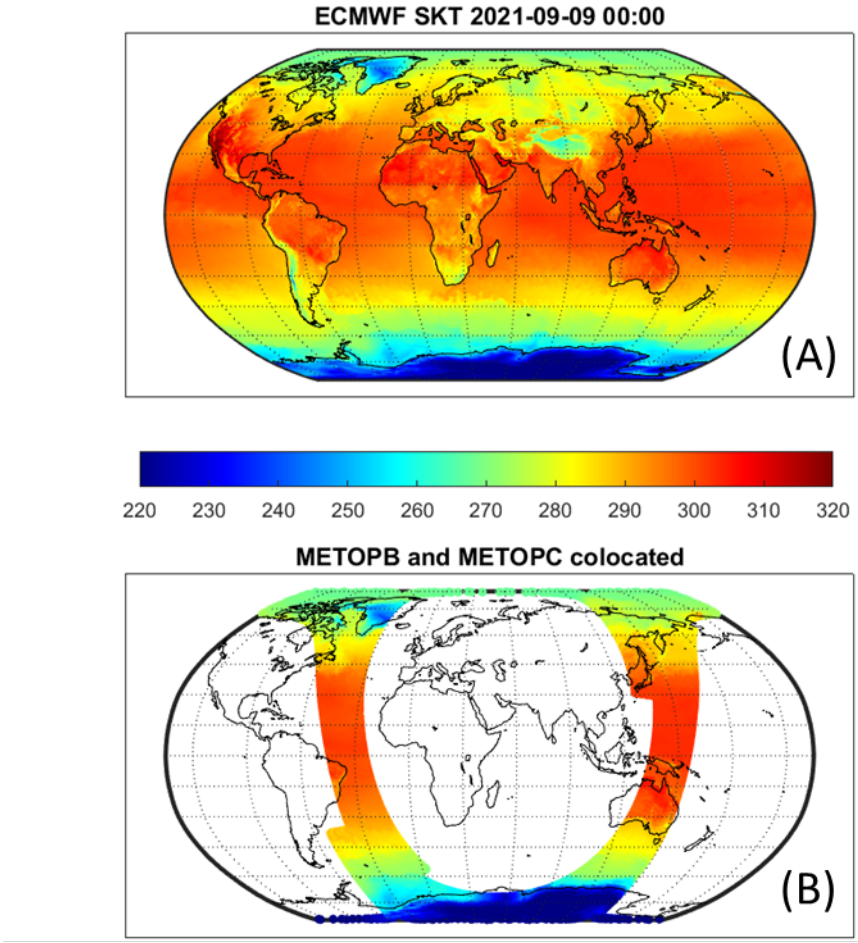

Figure 40. The figure illustrates the colocation of the MetOp spectrum with ECMWF analysis. (A) shows the temperature from ECMWF analysis at 00 on 9 September. (B) shows the surface temperature associated with MetOp footprints between 23:30 of 8 September and 00:30 of 9 September.

One example of colocated ECMWF and MetOp-B/C observations is shown in Figure 40, showing ECMWF skin temperature at 00:00 UTC of 9 September 2021 and the field retrieved by MetOp footprints between 23:30 of 8 September and 00:30 of 9 September 2021.

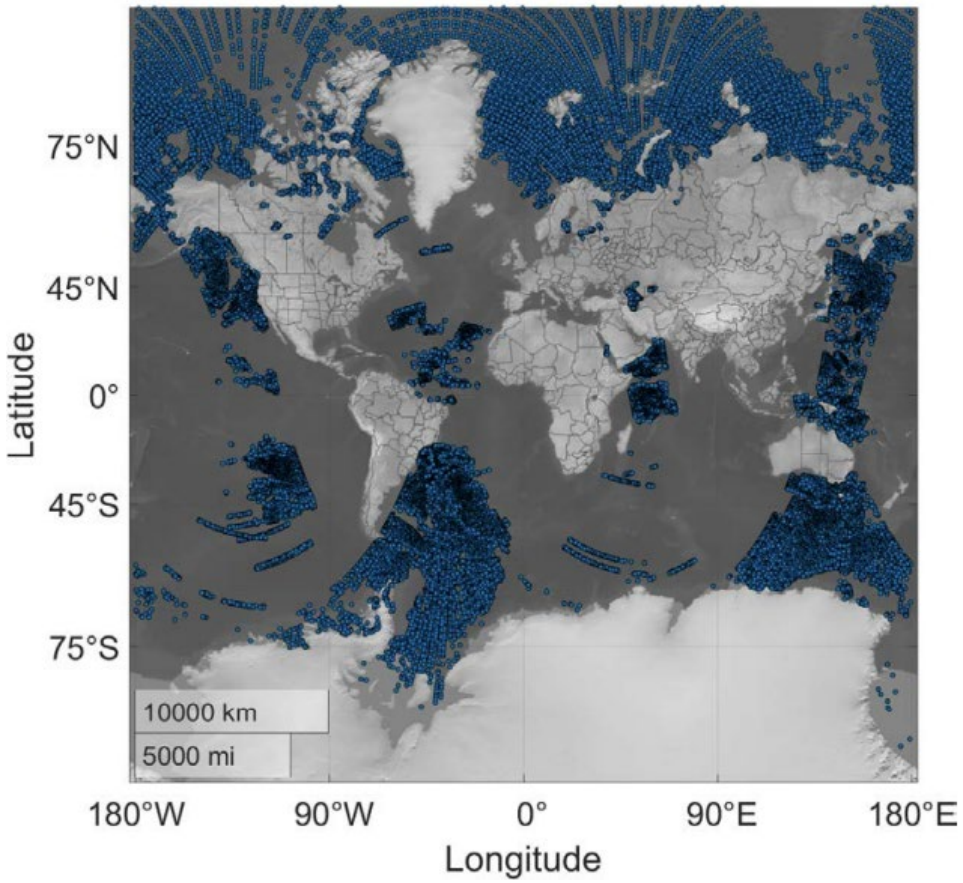

Figure 41. Spatial distribution of selected colocations between MetOp-B/C IASI/AMSU/MHS observations and ECMWF analysis.

Finally, Figure 41 shows the spatial distribution of the match-ups between ECMWF analysis and MetOp-B/C observations for the period from 23:30 UTC on 8 September 2021 to 00:30 UTC on 10 September 2021. Specifically, 57097 match-ups have been selected according to the filtering criteria indicated in the SW1 NNs training step (i.e., only acquisitions over sea and overcast cloudy with CLWP and CLWP less than 0.5 and 0.6 kg/m^2 , respectively).

3.8.1 SW1 VALIDATION

The C2 implemented NN configuration of the SW1 package has been validated on the selected 57097 matchups between MetOp-/B/C and ECMWF analysis. Figure 42 shows the histograms of the CLWP and CIWP ECMWF analysis predicted by the C2 NN configuration developed for SW1.

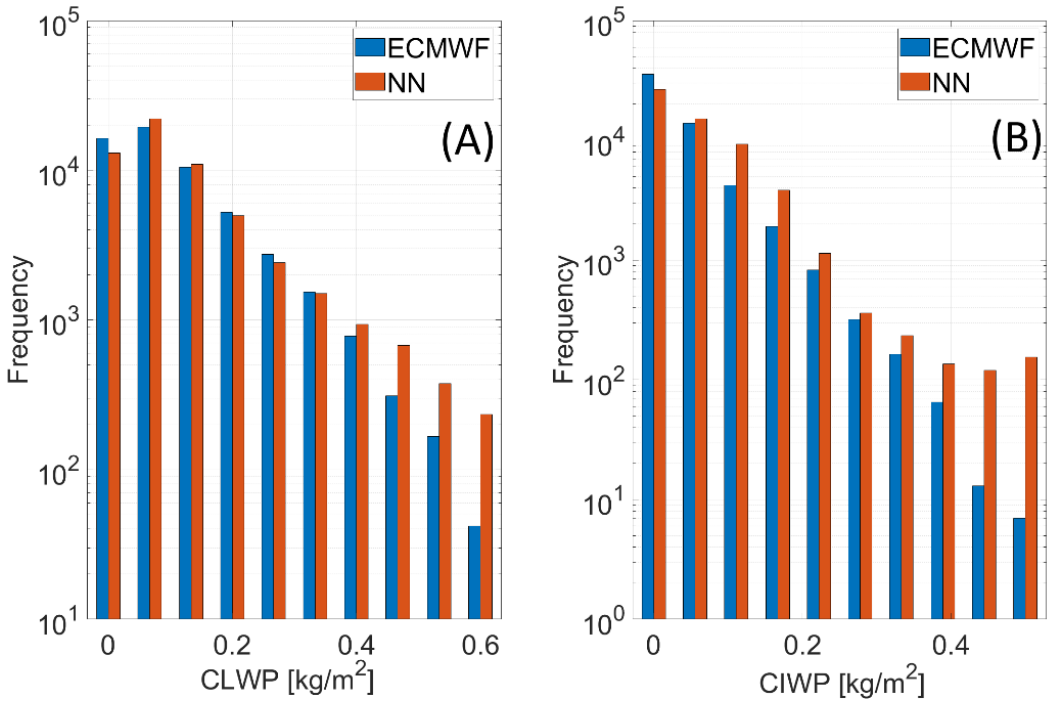

Figure 42. Comparison of histograms of CLWP (A) and CIWP (B) values from ECMWF analysis (blue) and implemented SW1 NN C2 configuration (orange).

It is clear from Figure 42 that C2 follows the ECMWF CLWP and CIWP distribution very well. At the same time, however, it is also evident that C2's predictions seem to slightly overestimate larger values.

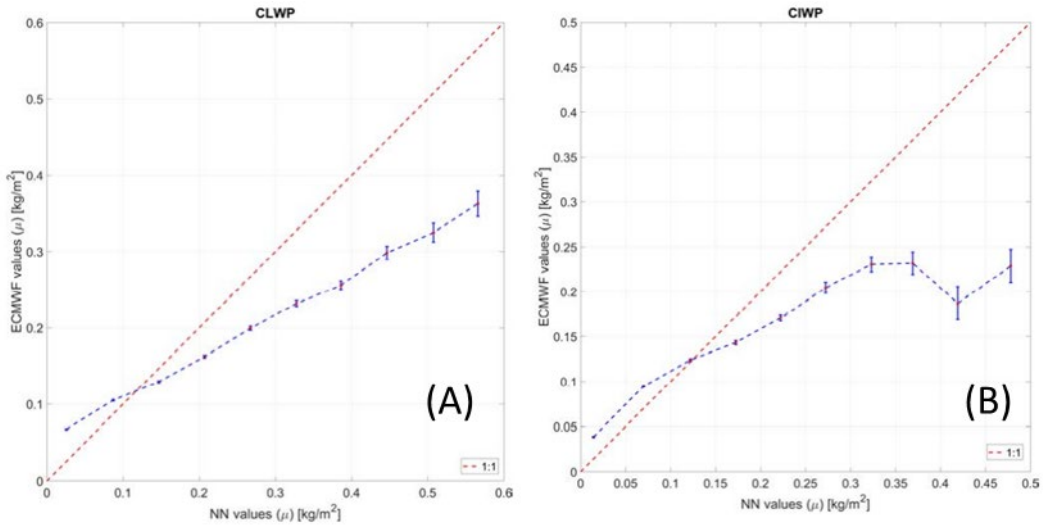

Figure 43. Binned analysis of collocated CLWP (A) and CIWP (B) from ECMWF analysis and the C2 implemented configuration in SW1. The red dots indicate the mean value, while the error bars are one standard deviation.

In addition, the binned analysis in Figure 43 shows also a saturation tendency of C2 toward higher CLWP and CIWP values. Finally, Figure 44 and a selected zoomed area in Figure 45 shows a qualitative comparison from ECMWF analysis and C2 SW1 CLWP and CIWP retrieval. From his analysis, it is clear how the predictions obtained from SW1 are very close to the reference ECMWF spatial patterns. In particular, it remarkable from Figure 45 how well the areas of major concentration of CLWP and CIWP are identified.

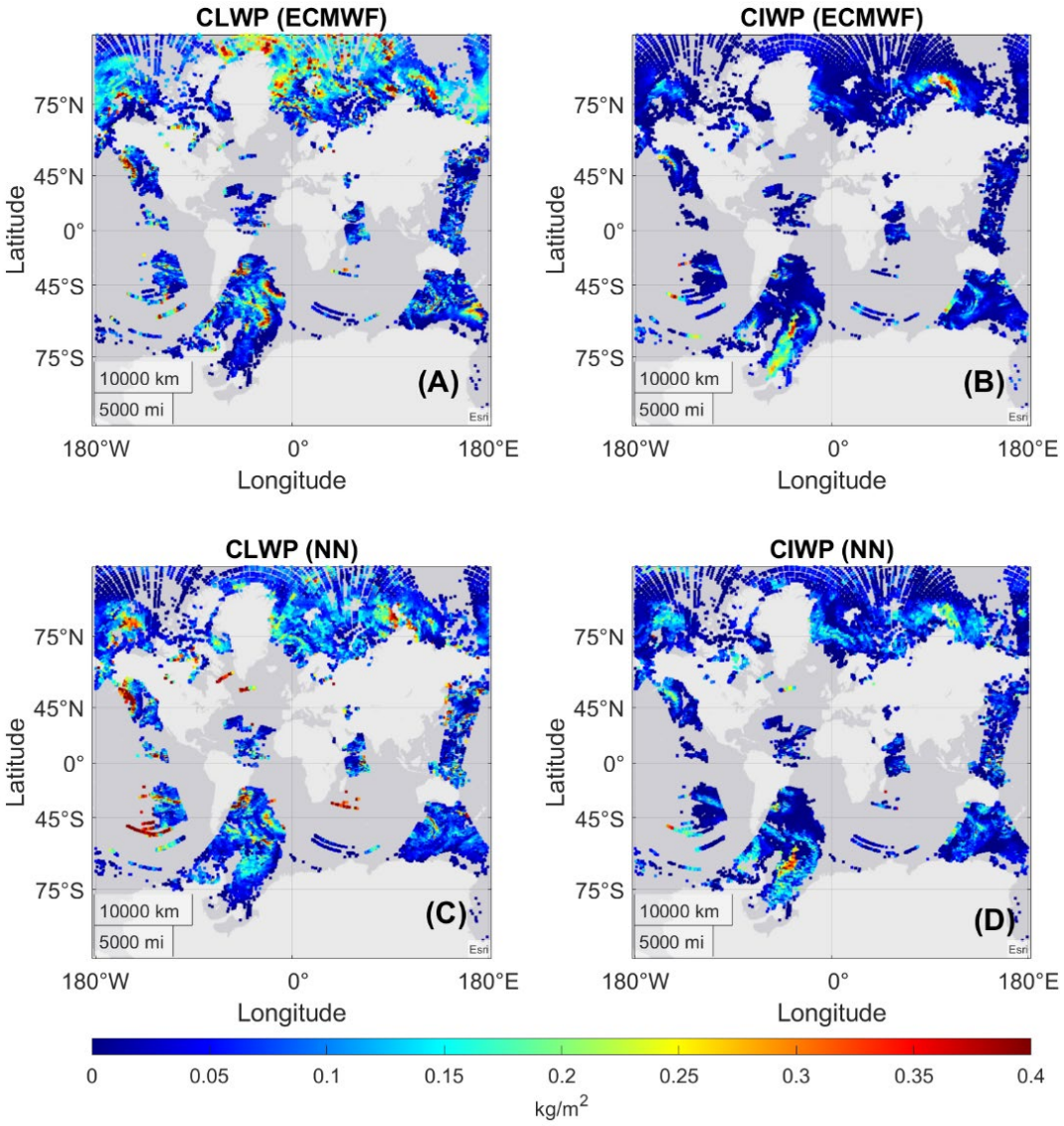

Figure 44. Maps of collocated CLWP (right) and CIWP (left) from ECMWF analysis (A) and (B) and C2 SW1 (C) and (D).

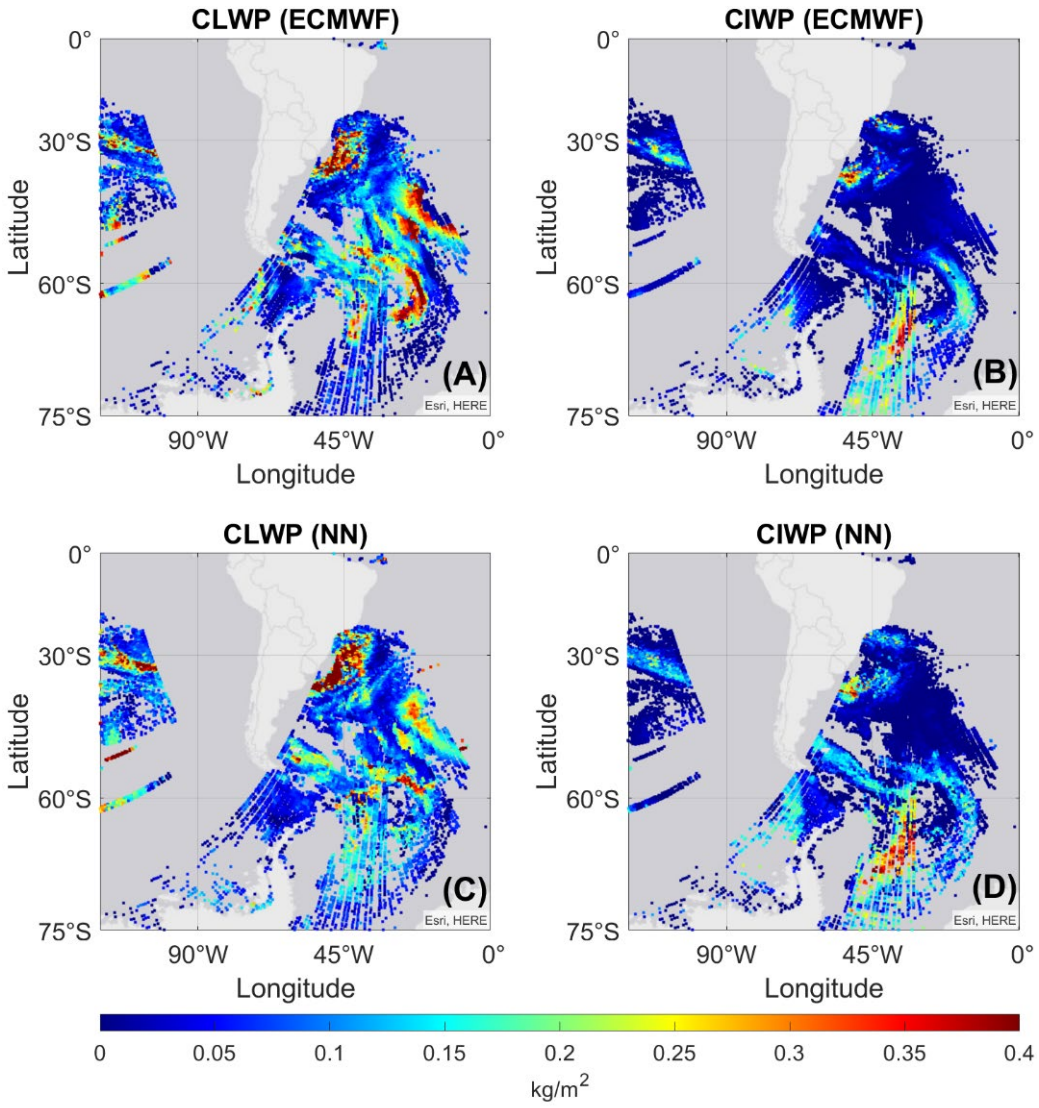

Figure 45. Same as Figure 44 but with a selected zoom area.

3.9.2 SW2 VALIDATION

Retrieval of CLWC and CIWC profiles from real observations have been validated against the ECMWF analysis profile. The dataset is the same as in Section 3.9, 57097 matchups between MetOp-B/C IASI/MASU/MHS and ECMWF analysis grid points. The histograms in Figure 46 show that the distribution of C3 and C4 (see Section 3.5 for more details of the implemented configurations) NN predictions agree fairly well with the distribution of CLWC and CIWC values given by ECMWF.

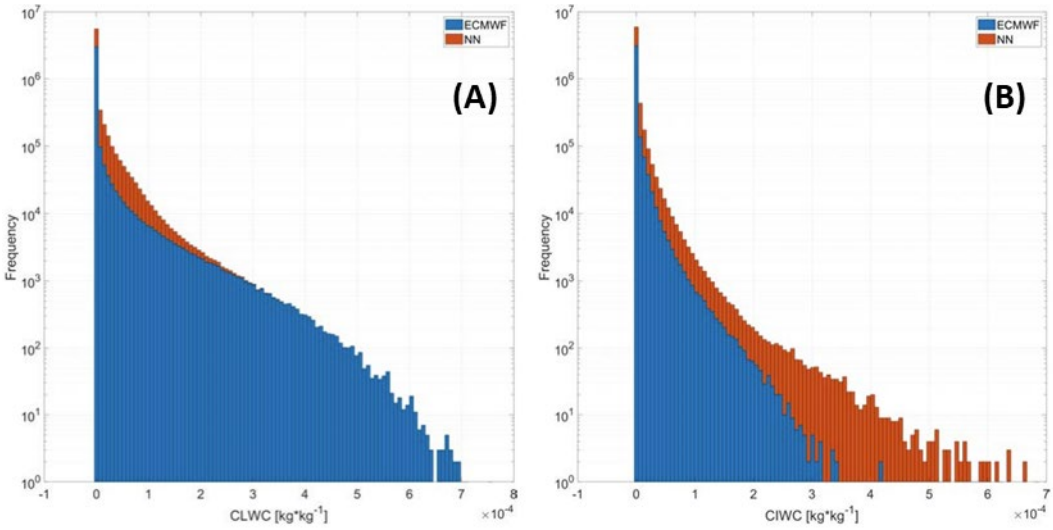

Figure 46. Histograms of CLWC (A) and CIWC (A) values from ECMWF analysis (blue) and the C3, C4 NN SW2 implementations (orange).

Although the NN tends to underestimate larger values of CLWC and overestimate larger values of CIWC.

Profile statistics are presented in Figure 47 for CLWC and in Figure 48 for CIWC. For CLWC, ECMWF and C3 SW2 report similar values for the main profile and the variability, with a bias up to -5 10-5 kg/kg. The rmse of residual is up to 6 10-5 kg/kg, about 2-time larger than in the validation with simulated data (see Figure 28).

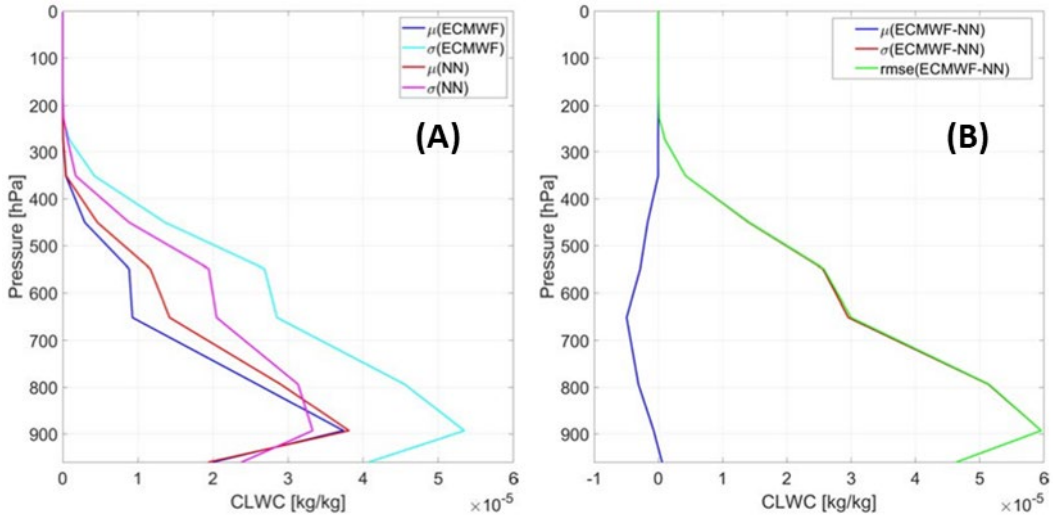

Figure 47. (A) Mean and std profiles of CLWC from C3 SW2 and ECMWF. (B) Statistics of CLWC residuals (ECMWF minus C3 SW2): mean difference, std, and rms.

For CIWC, the C4 SW2 configuration confirms an overestimate at higher levels, with bias up to -1.0 10-5 kg/kg. Also, in this case, the rmse of residual is up to 3

10-5 kg/kg, about 3-time larger than in the validation with simulated data (see Figure 28).

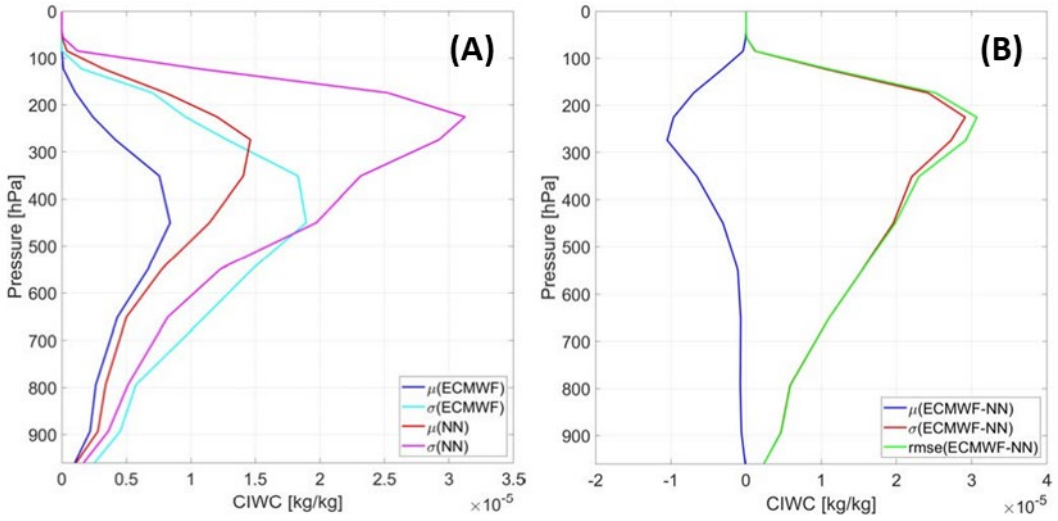

Figure 48. (A) Mean and std profiles of CIWC from C4 SW2 and ECMWF. (B) Statistics of CIWC residuals (ECMWF minus C4 SW2): mean difference, std, and rms.

Finally, to further demonstrate the consistency of the SW2 retrievals a spatial comparison (see Figure 50 and Figure 51) of the vertical integrated CLWC and CIWC contents between ECMWF and the C3 and C4 configurations has been determined.

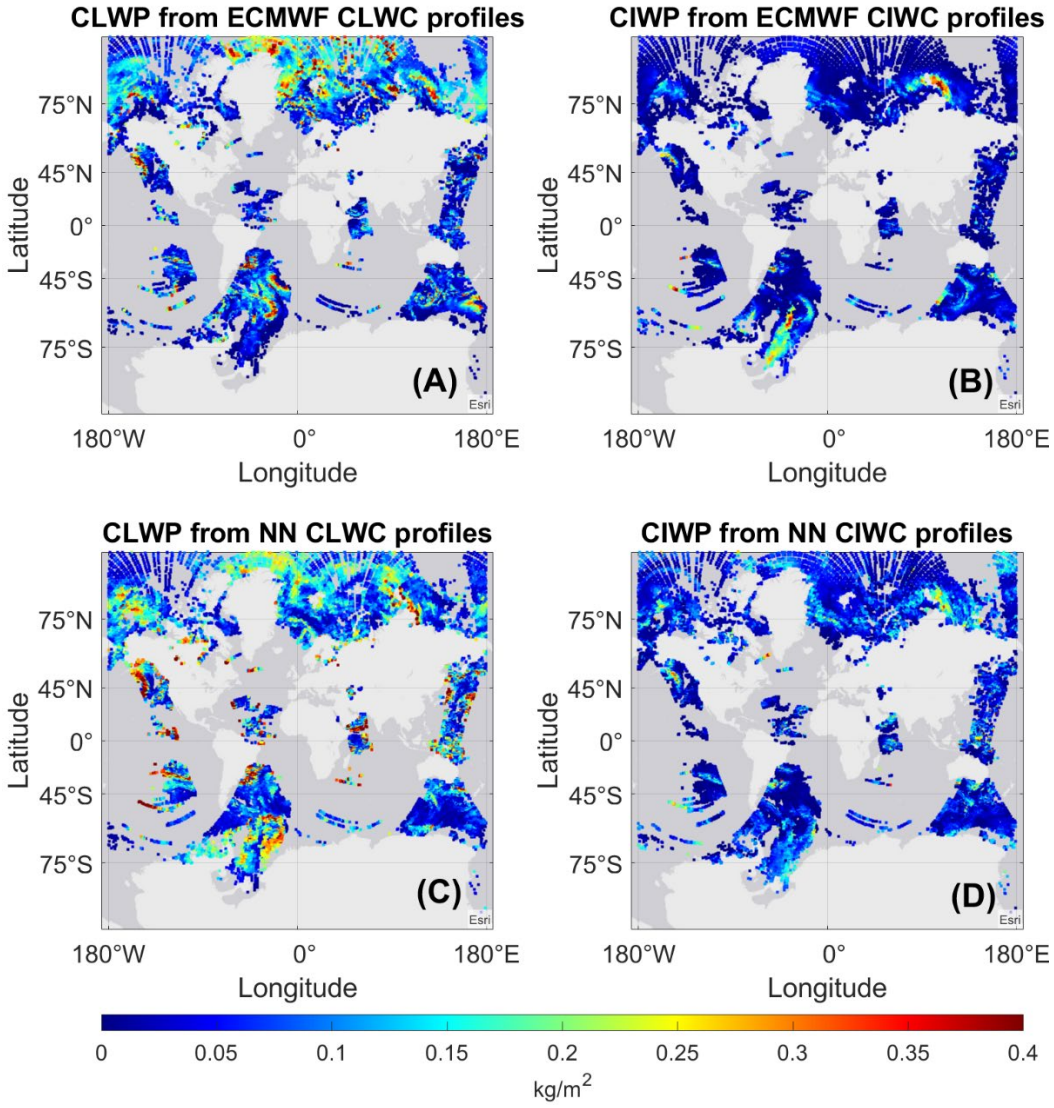

Figure 49. Maps of CLWP (right) and CIWP (left) from ECMWF analysis CLWC (A) and CIWC (B) contents. (C) and (D) same as (A) and (B) but from C3 and C4 predictions.

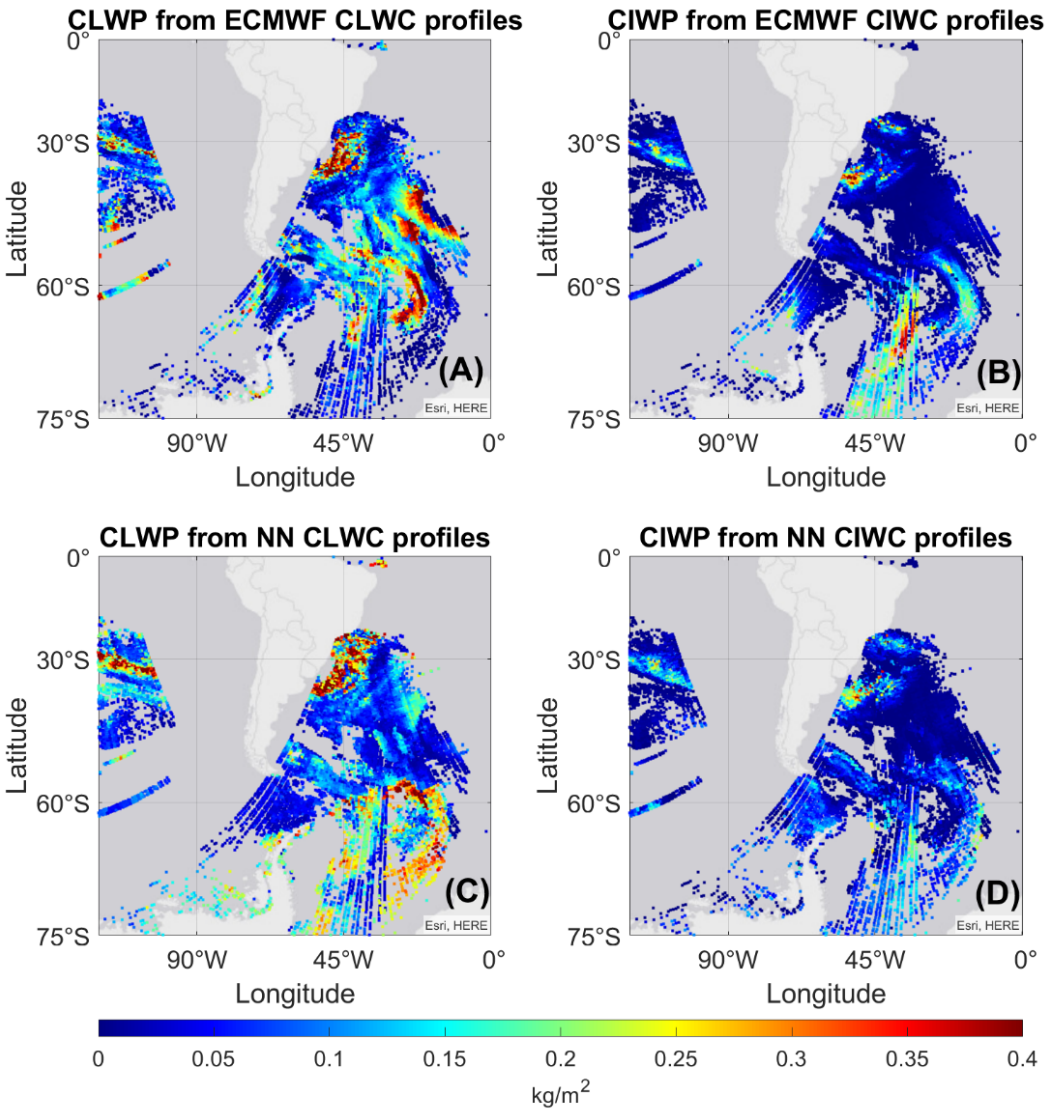

Figure 50. Same as Figure 49 but with a selected zoom area.

3.9.3 SW3 VALIDATION

Also, SW3 has been validated against the ECMWF analysis dataset. Drop effective radius for liquid and ice clouds from ECMWF data have been determined with the parameterized methods as in the SW3 training step of C2 and C4 [135], [137]. The histograms in Figure 51 show a comparable distribution for the effective radius of liquid and ice clouds, although the RF tends to underestimate both low and high values at the extremes.

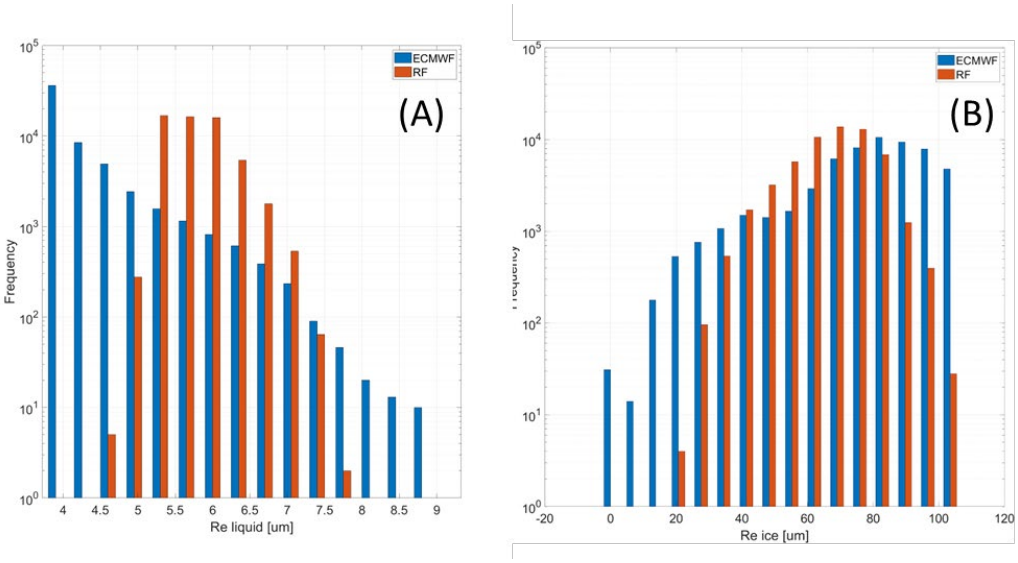

Figure 51. Histograms of liquid water (A) and ice (A) cloud drop effective radii values from ECMWF analysis (blue) and the C2, C4 NN SW3 implementations (orange).

Finally, the spatial comparison of the drop effective radius maps of liquid water and ice clouds are shown in Figure 52 and Figure 53 between the C2/C4 configurations and the ECMWF analysis indicates a fair agreement of spatial patterns and dynamics.

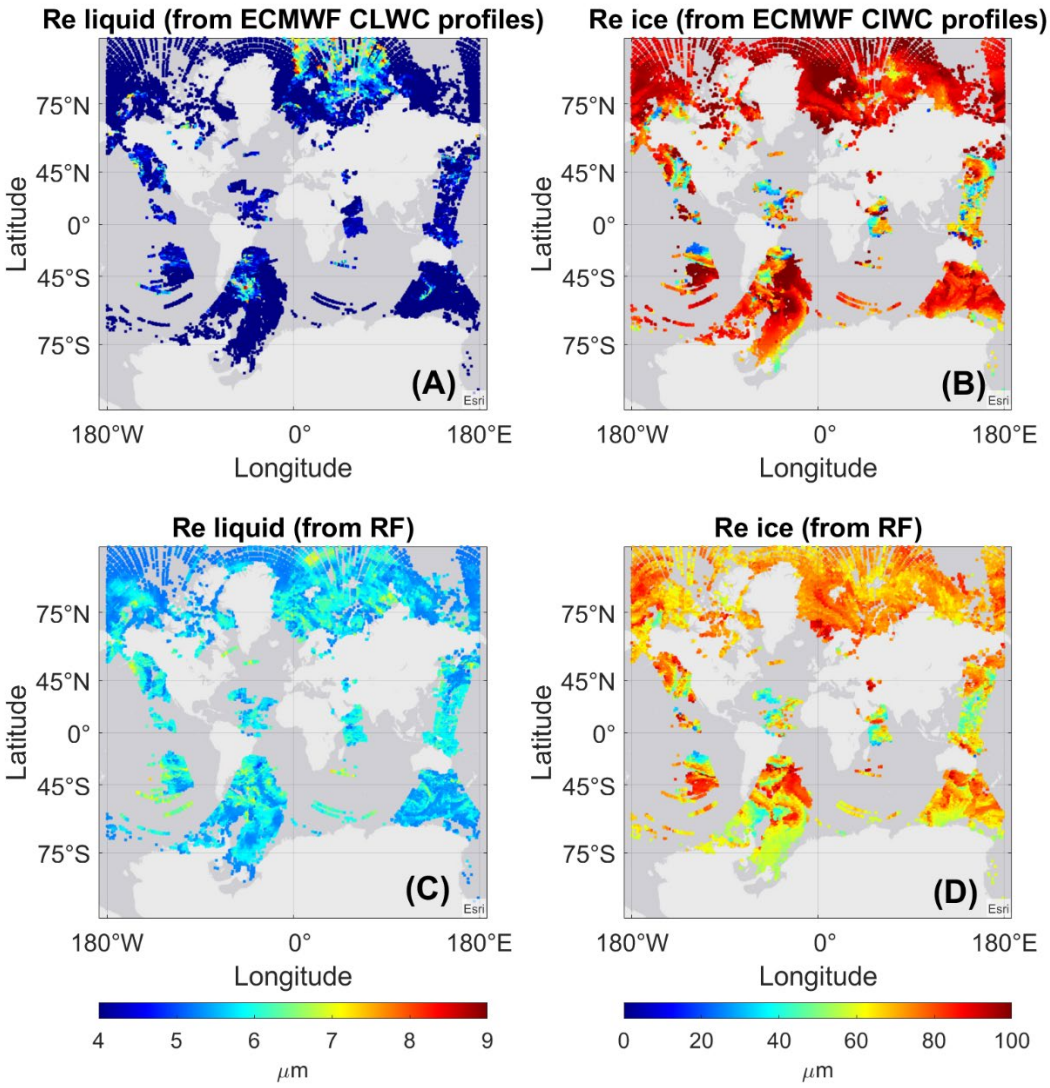

Figure 52. Maps of collocated liquid water (right) and ice (left) cloud drop effective radii values from ECMWF analysis (A) and (B) and C2/C4 SW3 implemented configurations (C) and (D).

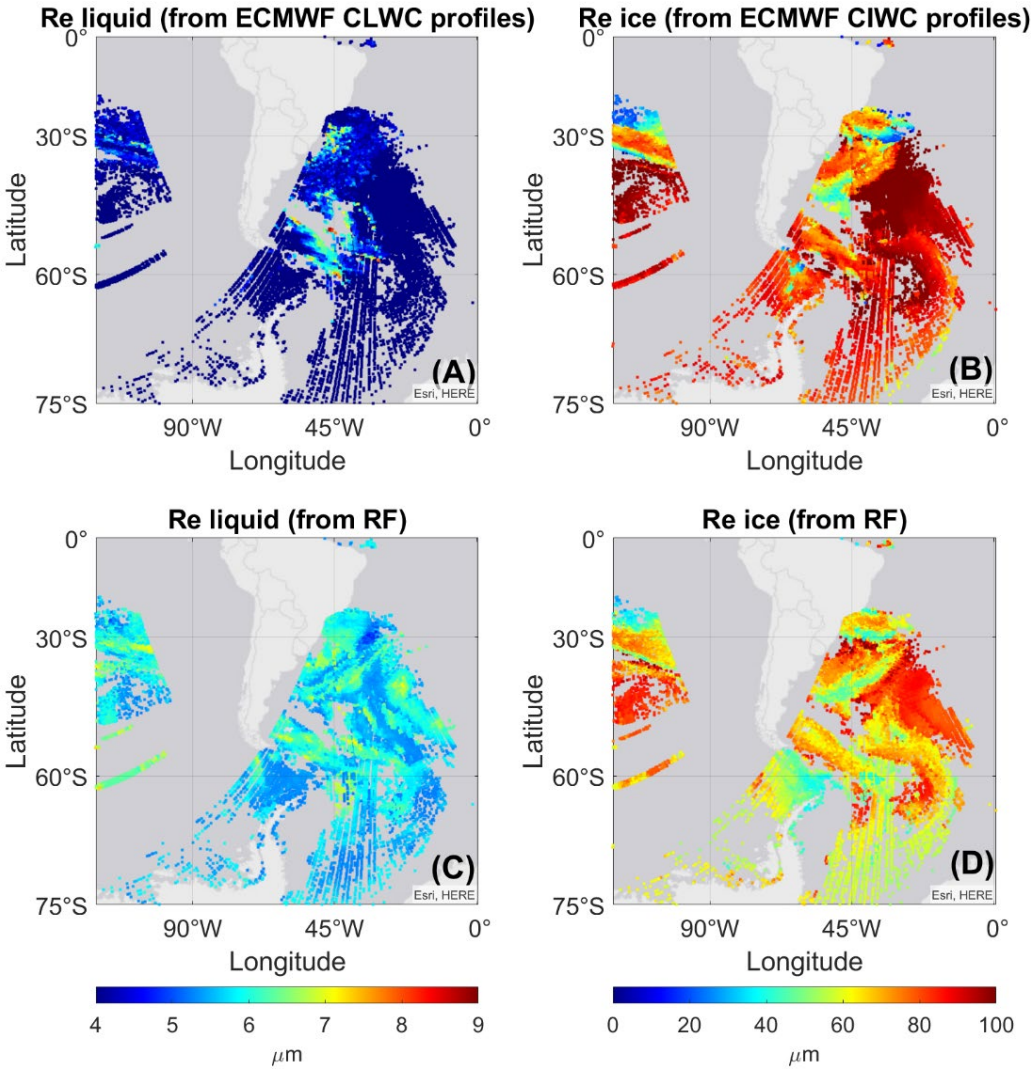

Figure 53. Same as Figure 52 but with a selected zoom area.

Chapter 4

CLOUD DETECTION IN GREENHOUSE GAS ANALYSIS

As illustrated in previous chapters, the identification of clouds and the study and analysis of their microphysics are fundamental to understanding Earth's energy balance, climate, and weather. In addition to cloud characterization, of paramount importance is profiling the Earth's greenhouse gases. Their quantitative presence in the Earth's atmosphere and their dynamics in terms of absorption of solar radiation are equally important for understanding the effects of global warming. Greenhouse gases are critical to maintaining our planet at a temperature suitable for life. Without the natural greenhouse effect, the heat emitted by the Earth would simply pass from the Earth's surface outward into space, and the Earth would have an average temperature of about -20°C.

Remote sensed IR and MW observations, as expected, are frequently affected by clouds. Therefore, observations must be processed for operational data assimilation and inversion for geophysical parameters, which may be related to cloud microphysics (as shown in the previous chapters) or not. In this last case, the presence of cloud signals causes the data to be unreliable for a wide range of remote sensing analyses (e.g., greenhouse gas profiling). As a result, cloud detection from remotely sensed observation is a very open and important task in literature.

These kinds of analyses were a fundamental part of the research activities carried out in my doctoral program. This chapter aims to present two studies made by me in this framework during my Ph.D. period. The former, investigates the capability of a machine learning based cloud detection (MLCD) scheme, implemented through the use of a feed-forward NN and PCA. The latter addresses the potential of a nonlinear statistical regressor method based on deep learning feed-forward neural network (NN) for the retrieval of atmospheric CH_4. The regression framework is based on the PCA of the IASI L1 radiances and of the CH_4 profiles. The choice of the number of principal components has been addressed by the study

of their eigenvalues, to filter redundant information from IASI channels and extract the most significant information from the CH_4 profiles.

The analyses performed in this studies and the results obtained were published in the following papers [4], [5].

4.1 MLCD USING HYPERSPECTRAL DATA

As shown in previous Chapters 3, clouds strongly interact with the radiative properties of Earth's system [159], influencing the retrieval of geophysical parameters such as greenhouse gasses, aerosol, and surface temperature. Estimating their microphysical parameters is critically important for assessing the Earth's radiation budget and addressing climate warming. In the wide range of remote sensing applications, such as those for the recovery of thermodynamic parameters of the atmosphere, such as temperature and water vapor, or the profiling of greenhouse gases such as CO2 and CH4, cloud detection is a mandatory requirement for obtaining optimal analyses.

Many cloud detection algorithms have been developed in literature and most of them use multispectral approaches [160]–[165], to infer clouds' behavior and its detection through some decision rules. Moreover, in the last decades, the introduction of new advanced hyperspectral sensors, such as the IASI [166], [167] and the Advanced Infrared Radiometer Sounder (AIRS) [168], has allowed sensing information (up to 8K bands) [166] from surface and atmosphere with unprecedented accuracy and resolution. Anyway, despite the consolidated literature, conventional cloud detection algorithms applied to these sensors are not yet very effective, because the physical and theoretical implications of hyperspectrality are required [167], besides an ad-hoc manual selection of more informative spectral bands. Therefore, innovative methods for cloud detection from hyperspectral data are required, which can handle the full set of spectral radiances, rather than a few channels. From the heritage of existing cloud detection algorithms, MLCD algorithms are developed.

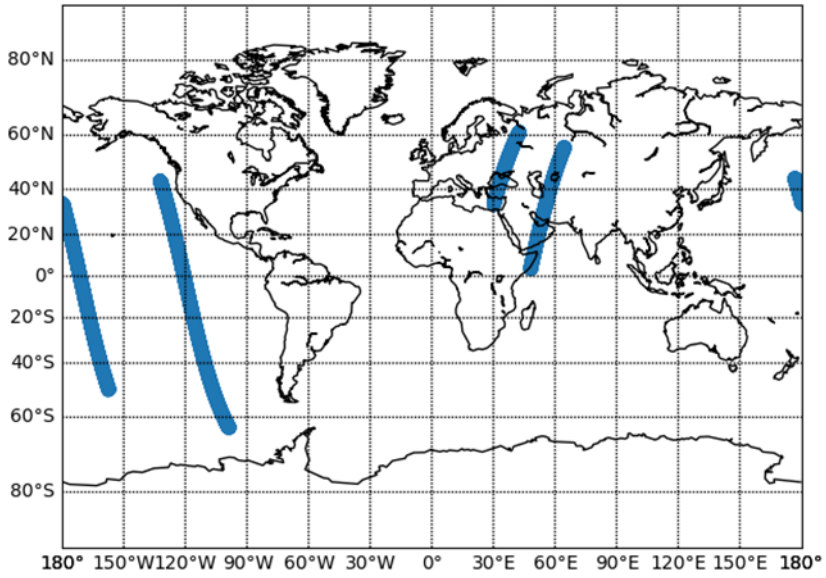

Figure 54. IASI-A L1C blue footprints related to the dataset used in this study.

The data we use in this analysis have been obtained with IASI operated in the so-called external calibration mode or ExtCal. In this mode, each scanning line, which in normal operation mode spans an angle range of ± 48.33° on either side of the nadir, is squeezed into the nadir view. In other words, at the same time as that taken for a complete ± 48.33° scan, IASI is operated to look exactly at the nadir (for more details about this mode we refer the interested reader to [149]). Specifically, IASI L1C spectral radiances acquired from Jan. 2016 to Nov. 2016 and related to Eastern Europe and tropical areas have been used. In ExtCal mode, data are available one day per month alone. Therefore, we have one daily orbit for each month (see Figure 54).

Table 14. Datasets of IASI-A L1C spectra were used in this analysis.

Dataset Number	Month	Number of spectra
0	January	65340
1	February	65124
2	March	65340

3	April	65340
4	May	65232
5	June	65340
6	July	65340
7	August	65232
8	September	65340
9	October	65232
10	November	65340

In this way, we are sure to have the right time-space variability to represent cloud diversity and surface conditions. The total number of observations is 652968 (see Table 14 for the detail of the number of IASI spectra for each month). We also stress that in the ExtCal mode the horizontal spatial resolution along the satellite track is increased at the expense of that along the cross-track direction. It is expected that the set of data acquired in the ExtCal mode will show a better coverage of cloud fields, with an increased probability to observe clear-sky conditions. In effect, one of the main issues in designing effective cloud detection schemes is the lack of data sets with enough clear-sky radiances. Any given classification analysis could be misleading in the case of the training data set not being balanced between the two classes, cloudy- and clear-sky (e.g., see [161]). Then, since the cost function minimizes the overall error, the threshold naturally outweighs the most populated class that will be better classified at the possible detriment of the smaller class. If the actual scene to be classified is poorly balanced in favor of the other one (less populated in the training data set), then the overall misclassifications will increase. The data set of IASI spectra acquired in ExtCal tends to limit this issue because of the better horizontal spatial sampling which can increase the number of clear-sky IFOVs (see e.g., [169]).

4.2 MLCD ALGORITHM DESCRIPTION

The MLCD is an algorithm based on PCA. The PCA involved in this study follows what was introduced in Chapter 3 (see Section 3.3.2) to extract more significative information about clear- and cloudy-sky acquisition from the set of IASI-A radiances.

Specifically, starting from a set of an observed k-dimensional vector of IASI radiances R_i, with $i = 1, 2, ..., N$ and $N > k$, a subset of clear-sky condition spectra was selected, using the AVHRR cloud and land masks, as follows:

$$\begin{aligned} R_{clear} &= \bigcap_{i=1}^{N} \{R_i \in Q_i\} \\ Q_i &= \{AVHRR(i)_{cloud\_frac.} \leq 5 \wedge AVHRR(i)_{land\_frac.} = 0\} \end{aligned} \tag{4.1}$$

where Q_i is the ith element of the intersection of the elements related to the AVHRR elements of cloud and land masks, respectively. Next, following what we have shown in Section 3.2 a clear-sky V orthogonal projection basis is determined, and each IASI-A L1C spectra is projected in a low dimensional subspace considering only the first columns of V, resulting in a set of 100 regressors capable of discriminating between clear/cloudy radiances (see Figure 55).

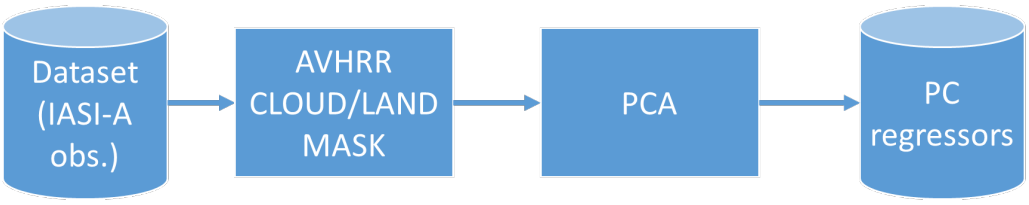

Figure 55. Scheme of PC regressors determination for the cloud detection algorithm.

Starting from the definition of the set of PC regressors, a statistical cloud detector was implemented in this study by the use of a multilayer feed-forward NN. Also in this case the Keras-python framework [150] has been used to build and deploy the NN structure. For the learning step, in this study, we partitioned the IASI-A L1C total dataset using an 80/20% ratio, 80% of the entire dataset for training, 20% of the entire dataset for validation, and testing (10% validation and 10% test), respectively. Finally, truth data to predict (cloud- or clear-sky condition) have been classified from a cloud mask product of the AVHRR sensor.

Using the Hyperband tuner [170], in this work a neural network structure composed of 5 layers was designed: i) one input layer composed of 100 input units, related to the first 100 principal components of the IASI-A L1C measurements, ii) 3 hidden layers each one composed of 256, 236, and 114 hidden units, iii) one output layer composed by 2 outputs units because the softmax [171] activation function is used to turn the neural network outputs into probability-like values and allow one class of the 2 (cloudy or clear) to be selected as the model's output prediction, see Table 15 for a summary of the neural network structure.

The Exponential Linear Unit (ELU) [172] activation function is used on the hidden layers, whereas the Logarithmic Categorical Cross entropy function[171] is used as a loss function:

$$L = \sum_{i=1}^{N} y_i \cdot \log\left(p\left(y_i\right)\right) \tag{4.2}$$

where, N indicates the number of classes to predict, two in our case (cloudy or clear), y_i and $p\left(y_i\right)$ are the true value of the ith class and the probability to predict it, respectively. Finally, the efficient Nesterov ADAM gradient-based optimization algorithm [173], [174] is used to minimize the neural network cost function in training and validation steps.

Table 15. MLCD model summary.

N. of neural network layers	5
N. of hidden layers	3
N. of input units	100
N. of hidden units of the hidden layer 1	256
N. of hidden units of the hidden layer 2	236
N. of hidden units of the hidden layer 3	114
N. of output units	2

Loss Function	Categorical Cross-Entropy
Hidden units activation function	Elu
Output units activation function	Softmax
Optimization algorithm	Nesterov-ADAM

Finally, the network has been trained and validated on 30 epochs on the total IASI-A L1C dataset as explained in Section 4.1. Also, to prevent overfitting, regularization techniques such as early stopping [175] and class balancing [176] approaches have been used.

4.2.1 CLASSIFICATION RESULTS

After the tuning and the learning, the neural network classification performances have been tested on a set of unseen IASI-A L1C data. The confusion matrix [171] and Receiver Operating Characteristic (ROC) curve [177] have been used to assess the neural network performances (see Figure 56 A and B).

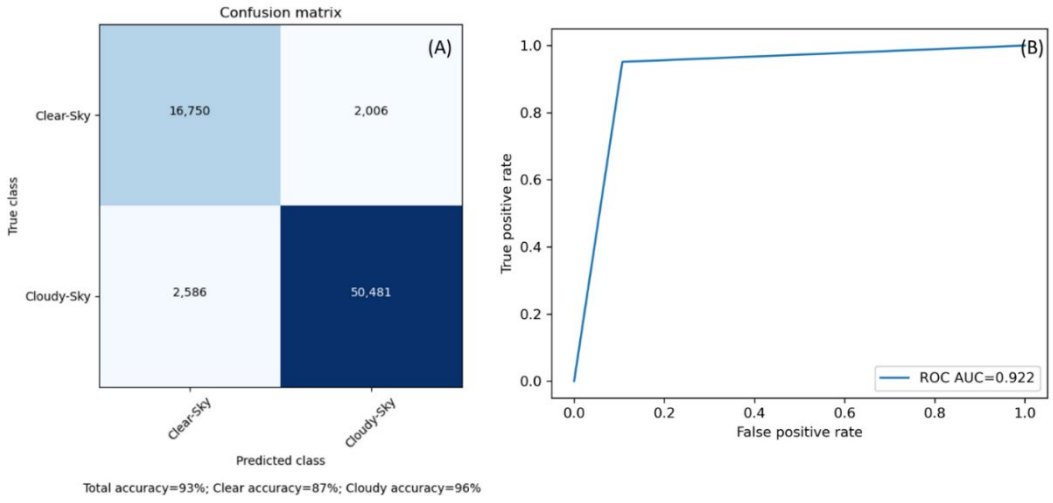

Figure 56. (A) Confusion matrix and, (B) ROC curve related to the classification performances.

From the confusion matrix depicted in Figure 56 A and the ROC curve in Figure 56 B, is easy to see the goodness of the neural network performances in the classification of clear, cloudy sky IASI spectra radiances. Particularly informative, are the results shown by the ROC curve, whose True-/False- positive rate

comparison, shows a desirable curve shape, with an Area Under the Curve (AUC) of about 92%. In addition, using the information given by the confusion matrix, i) accuracy, ii) precision, iii) recall, and iv) F1 scores [177] have been calculated. The results are shown in Table 16.

Table 16. NN classification scores report.

	Precision	**Recall**	**F1**	**N. test dataset samples**
Clear-Sky	87%	89%	88%	18756
Cloudy-Sky	96%	95%	96%	53067
Clear-Sky accuracy	86%			18706
Cloudy-Sky accuracy	96%			53117
Total accuracy	93%			71823

Analyzing the results shown in Table 16, from the precision and recall scores, related to the classification of clear-/cloudy- spectral radiances, is evident to see that our neural network model expresses a good generalization capacity. F1 scores that are both high for clear- and cloudy-sky classification, are also confirming this trend, stating that the developed neural network can classify with high precision and accuracy new unseen IASI-A L1C spectral radiances.

The MLCD achieves the accuracy to classify clear- and cloud-sky spectra of about 86% and 96% (totally 93%). It has to be stressed that this performance is, to my knowledge, unprecedented. In effect, especially for tropical settings, the performance for IASI standalone algorithm is of the order of 80% (see e.g., Ref. [161]), because of the difficulty to deal with the dense distribution of cirrus clouds, which cover permanently the tropical belt.

Finally, from this study, some advantages arise. The former is that the MLCD is based only on the spectral radiance signal and does not rely on any ancillary

information or model output. Therefore, it can potentially be applied to any spectral sensor in the infrared on ground-based, airborne, or satellite platforms, and it can work, with the same performances, in the daytime or nighttime. The latter is that the NN is extremely fast and computationally efficient in classifying the spectra. It runs on a Graphical Processing Unit (GPU) and takes only three seconds in classifying hundred thousand spectra, making it particularly suitable for real-time classification scenarios.

4.3 ATMOSPHERIC METHANE PROFILING

Among the greenhouse gases in the Earth's atmosphere, methane (CH_4) is the third most important after water vapor (H_2O) and carbon dioxide (CO_2) [178]. In the context of global warming, while CO_2 is more abundant and longer-lived, CH_4 is far more effective at trapping heat [179]. Over the first two decades after its release, CH_4 is more than 80 times more powerful than CO_2 in terms of boosting the warming of the climate system. Unlike CO_2, the bulk of methane emissions (ca. 60 %) are anthropogenic[180]; these include (i) agricultural sources (such as livestock, manure, and rice paddies) [181], (ii) waste disposal, (iii) fossil fuel extraction, and (iv) deforestation.

This anthropogenic pollution worsens the already complicated situation of thawing Antarctic permafrost [182] it is estimated that amount of methane deposited beneath is about 540 Gt and its release would lead to unpredictable global warming consequences. In the last decades, the global atmospheric growth rate of CH_4 is in the range of about 10 ppb/year, setting in 2021 an increase of 17 ppb, the largest annual increase ever.

Thus, the global monitoring of CH_4 emissions is mandatory to study and analyze the global warming phenomenon. In the last decades, atmospheric CH_4 has been extensively measured from space [178] using measurements acquired by sensors working in the shortwave infrared (SWIR) and thermal infrared (TIR) bands and in this way, many inversion methodologies have been developed to retrieve CH_4 [183]–[186] signature. In the TIR band, the Infrared Atmospheric Sound Interferometer (IASI) mounted onboard the MetOp platform is the leading sensor for the retrieval of Atmospheric CH_4 because of its ability to sense the atmosphere with unprecedented resolution and accuracy [166]. CH_4 is also indicated in the literature as a “long-lived tracer” because of its long lifetimes in the troposphere and lower stratosphere. The CH_4 concentration varies significantly in height (from

the upper troposphere to the lower stratosphere) and with latitudes and seasons [187]–[189]

The combination of these sources of variability constitutes the main weakness of traditional inversion algorithms in correctly estimating the vertical distribution of CH_4. Therefore, the development of new advanced retrieval methodologies, such as those based on Machine Learning (ML), which can extrapolate with high accuracy the dynamic of greenhouse gasses and information about their vertical profiles [2] and total contents[1], is mandatory. Toward this objective, the primary aim of this exercise is the application of a nonlinear statistical regressor method based on deep learning feed-forward NN for the retrieval of atmospheric CH_4 at a global scale using predictive features provided by IASI L1C simulated observations.

4.4 DATA AND METHOD

In this Section, some details about the dataset of IASI simulated observation used in our analysis will be presented. Finally, the architecture of the methodology developed to perform the CH4 inversion exercise will be also discussed.

4.4.1 DATASET OF SIMULATED MEASUREMENTS

The IASI measurements we use in this work have been simulated with the latest version of σ-IASI-as [87], [89], [93], [133], [161], [186], [190], [191] (RTM). The atmospheric state vector used for the simulation of IASI spectra is the Monitoring Atmospheric Composition and Climate (MACC) Reanalysis dataset [192], [193] of the European Centre for Medium-Range Weather Forecasts (ECMWF). This dataset is a global model of atmosphere chemical species that provides measurements with a spatial resolution of 80 km on a latitude/longitude grid of $1.125° \times 1.125°$ and 60 vertical levels from the surface up to the mesosphere ($\sim$1000 to 0.1 hPa); it covers the period 2003 to 2012.

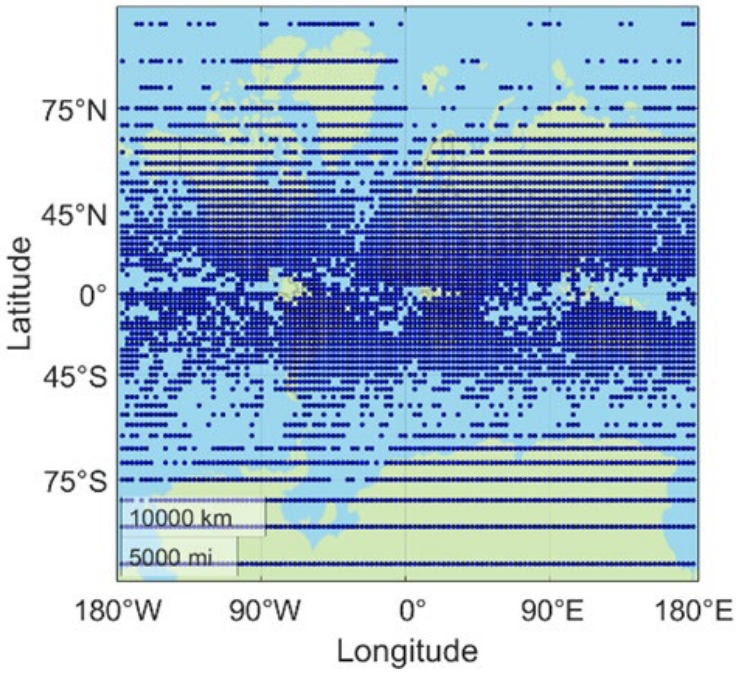

Figure 57. Map of selected geographical coordinates from MACC Reanalysis dataset.

A subsampling of the grid of points by a factor of four and a random selection of about 10.000 samples per month (see Figure 57) to reduce the simulation load has been performed. The data were selected for one day of the 12 months of 2012 at four synoptic hours (00-06-12-18 UTC) to capture typical seasonal and diurnal cycles. Furthermore, starting from the original state vector we generated three additional ones with increments of 5%, 10%, and 15% of the CH_4 total column to have a representation of its annual growth behavior within the data. For the sea surface, the emissivity was derived according to Masuda's emissivity model [194], while for the land surface, the Combined ASTER MODIS Emissivity over Land (CAMEL) was used [195], [196]. Finally, each sample was simulated in a cloud-free situation and with a uniformly randomly selected scan angle in the range $\pm 48.3^{\circ}$. Finally, a total number of 168.000 IASI-L1 spectral radiances are simulated.

4.4.2 NN REGRESSION ARCHITECTURE

The regression architecture, which performs the inversion of CH_4 profiles from IASI observations, is implemented by a combination of a neural network algorithm and principal component analysis (PCA). We use the PCA to decompose both the data and parameters space, a methodology that has been already explored and tested

by the authors within the framework of physical inversion of IASI radiances, see [87], [89], [93], [133], [161], [186], [190], [191]

Similarly to what is presented in Chapter 3, the motivation behind the adoption of PCA to define the NN regression framework is to reduce the impact of the curse of dimensionality in NN learning, since it has been shown in the literature [197] that NNs suffer in performing inversion when using large layers of input and output measurements. Specifically, the data we use for NN learning is observed using a large number of spectral measurements (the IASI 8461 spectral samples) and defined over tens of atmospheric layers (the 60 pressure levels over which the CH_4 contents are profiled). In this way, it is pretty clear that the PCA of NN inputs and outputs allows the definition of a regression framework that is less complex to solve (see Figure 58).

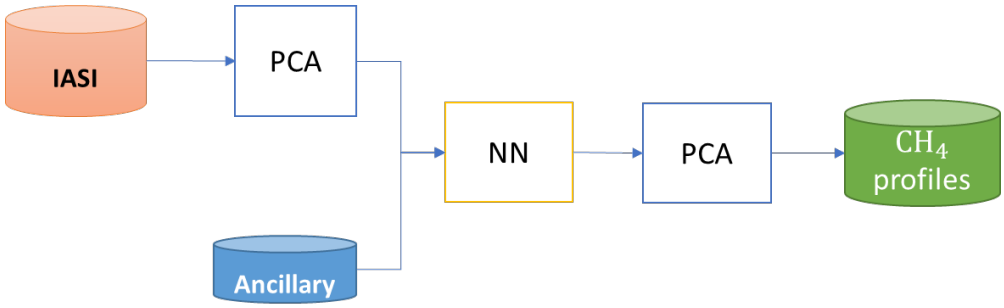

Figure 58. Simple sketch of the regression framework used in this work.

PCA of the IASI spectrum was performed using different functional bases, one for each of the IASI spectral bands. The EUMETSAT IASI Level 1 Principal Component Compression (PCC) [198], [199] product was used to project the IASI spectra into a lower dimensional space. In particular, the projection involved only bands υ_1 and υ_2 of the IASI spectra. The low dimensional space related to the two selected bands is spanned by a truncated set of the eigenvectors of the IASI L1 data covariance matrix, according to EUMETSAT PCC analysis, resulting in 90 principal components for υ_1 and 120 for υ_2, respectively.

To attain the PCA of CH_4 profiles, the projection was made by using a functional base of eigenvectors, corresponding to the first ten eigenvalues of the CH_4 covariance matrix, expressing about 99% of the total variance (see Figure 59). CH_4 profiles are standardized before the application of the PCA technique. This

additional pre-processing step was performed to improve the fit of the data by avoiding giving too much weight to variance caused by noise and decoupling profile predictions from the annual mean value.

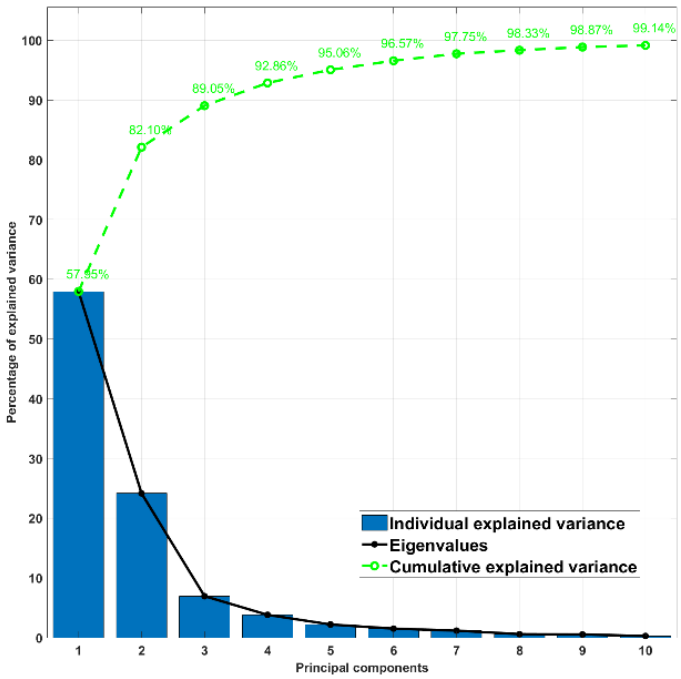

Figure 59. Pareto chart of the first ten CH_4 principal components

Finally, a feed-forward NN model was implemented by the use of the Keras-python [125] framework. In particular, starting from the input/output data and a set of NN hyperparameters[110], [200] (e.g., the number of hidden layers, hidden units, the batch size, the activation function, the loss function, etc…), different models were tested and optimized. Among those, we selected the model that best performs in terms of Root Mean Squared Error (RMSE). The selected NN architecture is composed of three hidden layers, the Mean Squared Error (MSE) is used as objective function, and the Stochastic Gradient Descend (SGD) [110], [201] for its minimization. Table 17 summarizes the hyperparameters of the selected NN model.

Table 17. Hyperparameters of the optimized NN model.

Hyperparameter	NN
Inputs	90 v_1 + 120 v_2 PCS + Surf. Pressure + VZA
Outputs	10 CH_4 PCS
N. hidden layers	3
Optimizer	Stochastic Gradient Descent (SGD)
Loss Function	Mean Squared Error (MSE)
Evaluation Function	Root Mean Squared Error (RMSE)

4.5 RESULTS

This section regards the evaluation of the selected NN model generalization performance. The evaluation will be performed by the use of two test datasets: i) the former using a set of simulated observations, and ii) the latter by the use of real IASI observation collocated with in situ measurements of the Hawaii Mauna Loa (MLO) observatory. A comparative analysis in terms of CH_4 total content, in terms of global spatial dynamic, will be also shown.

4.5.1 VALIDATION ON THE SIMULATED TEST DATASET

Considering the regression framework (see Section 4.4.2), the first ten principal components of CH_4 predicted from the NN on the test dataset of simulated observations are used to reconstruct the corresponding profiles.

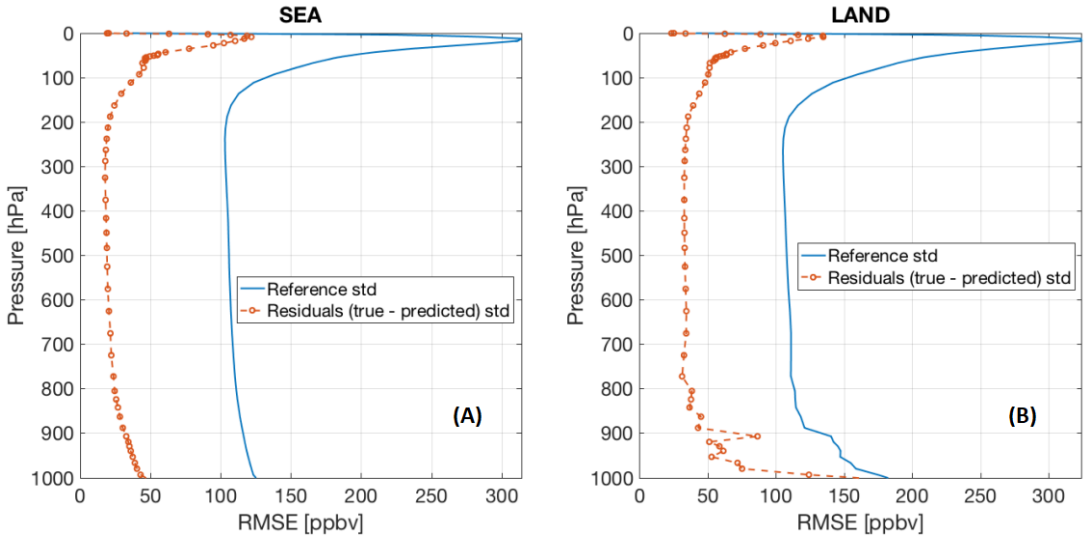

Figure 60. Profiles of CH_4 retrieval error (in terms of rms difference to reference truth) for (A) sea and (B) land areas.

From Figure 60 we quantified the CH_4 retrieval error in terms of RMSE, bringing an error reduction for sea profiles (Figure 60 A) within 40-60% and land within 15-70% throughout the lower 900 hPa for land (Figure 60 B). The error reduction is larger for both the troposphere and the stratosphere.

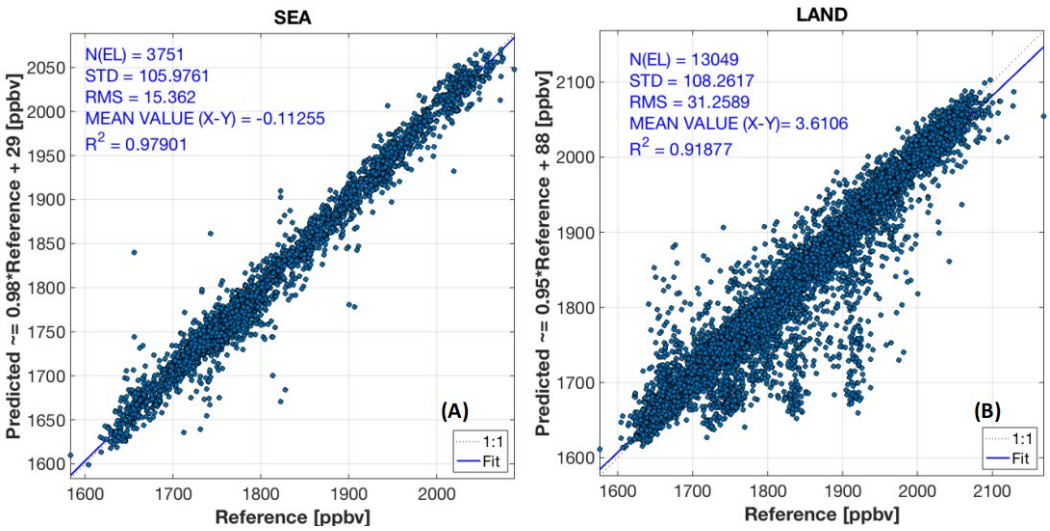

Figure 61. Scatter plots of NN predicted vs ECMWF reference values of CH4 total content for (A) sea and (B) land areas.

From the predicted profiles, in terms of total content scatter plots of Figure 61 show very good agreement between predicted and reference ECMWF values. Specifically, high values of R^2 are obtained for sea (0.97) and land (0.92) areas; within the predicted value there is no significant bias. The latter result is strongly emphasized by performing a binned analysis (see Figure 62 for more details), which provides more evidence of the goodness of NN predictions in obtaining unbiased CH_4 measurements.

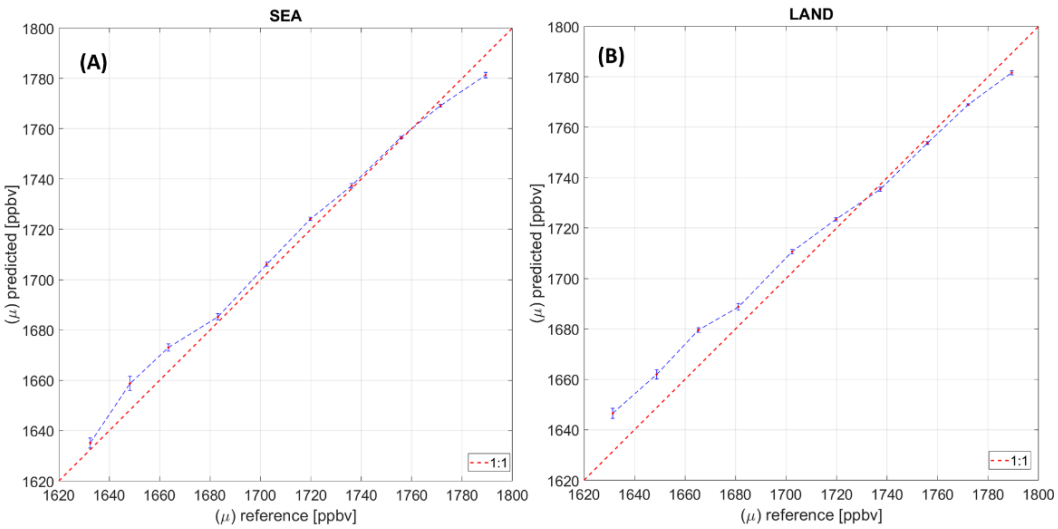

Figure 62. Binned analysis of ECMW reference vs predicted CH_4 total contents. Red dots indicate the mean value, the error bar is the standard deviation.

Finally, to further demonstrate the goodness of the NN prediction, an additional comparison in terms of global spatial dynamics of total CH4 content was carried out.

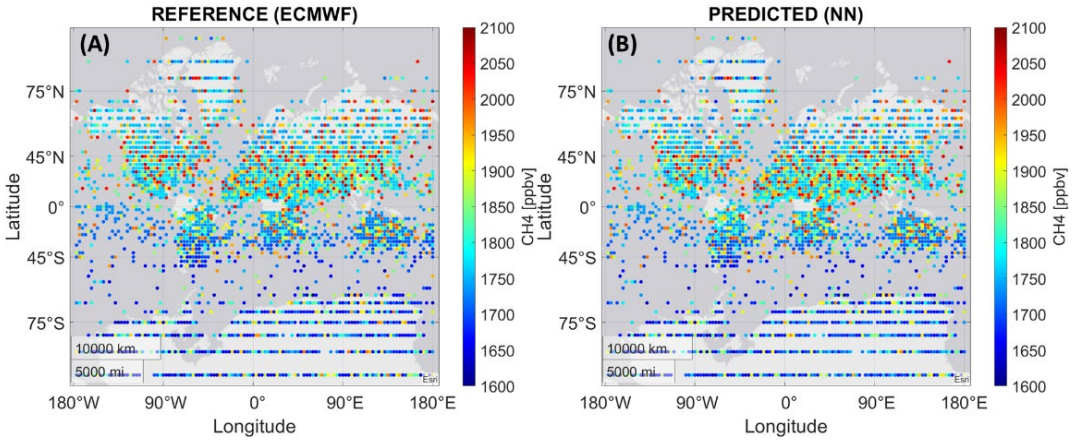

Figure 63. Maps of ECMWF reference (A) vs NN predicted (B) CH_4 total content.

Figure 63, shows this comparison, indicating an excellent agreement of the spatial patterns.

4.5.2 VALIDATION ON THE DATASET OF REAL OBSERVATIONS

Validation of the NN retrieval scheme was based on a series of real IASI sea surface clear sky soundings collocated with representative CH_4 profiles collected from the NDACC (Network for the Detection of Atmospheric Composition Change) FTIR (Fourier-Transform Infrared Spectrometers) network. These are derived from solar absorption spectra with a spectral coverage in the MID infrared, ~2400-3300 cm-1. The in-situ observations are taken at the NDACC station of Mauna Loa (MLO, 19.5362 N, 155.5763 W, 3397 m asl.) for the period from January 2014 to December 2014 (see Figure 64).

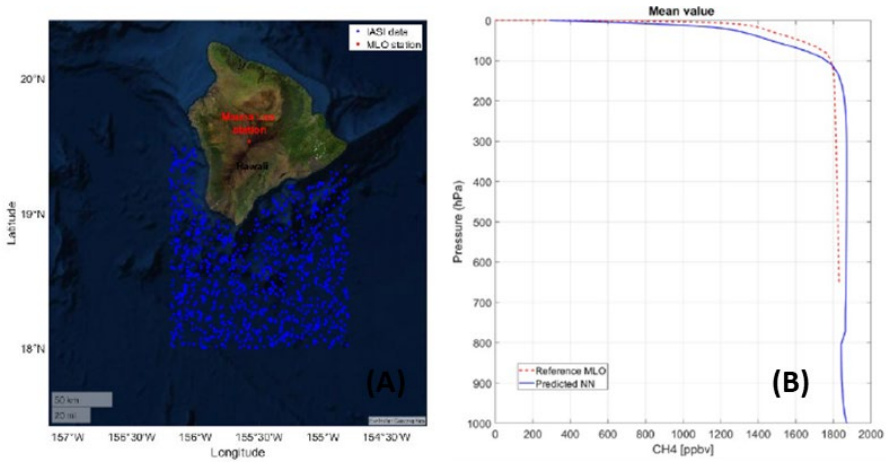

Figure 64. (A) Hawaii study area of IASI clear sky soundings (blue dots). The Mauna Loa validation station whose data are used for comparison is also shown on the map. (B)Comparison of reference MLO CH4 soundings (in red) to NN predictions (in blue). The comparison shows the mean values over the 2014 year.

The analysis of Figure 64 summarizes the generalization performance of this exercise. Specifically, from Figure 64 a comparison of the average of 2014 CH4 profiles was performed. It is straightforward to note that the NN predictions are feasible and can correctly reproduce the CH4 profile variability throughout the entire atmospheric column.

Finally, this exercise revealed that the NN recovery analysis shows agreement with the CH4 content of the reference MACC, allowing for unbiased profile estimates. In particular, validation with in situ measurements at MLO station Hawaii has shown that the NN model is capable of correctly recovering the shape of CH4 profiles.

Chapter 5

REMOTE SENSING OF SURFACE: DETECTION OF LARGE GROUND DISPLACEMENTS PHENOMENA

Beneath the clouds and atmosphere is the Earth's surface. Studying its geophysical dynamics is essential to understanding the environment in which we live and helping to protect it for the future. Earth surface change monitoring has evolved significantly over the past five decades since civilian Earth observation (EO) satellites were launched into orbit. Ongoing technological advances and access to free satellite imagery have increased our ability to map and monitor Earth's surface changes, both abrupt and subtle, on large collections of images. In this framework, Synthetic Aperture Radar (SAR) sensors cover an important role.

SAR sensors are coherent active microwave remote sensing systems, whose capability to effectively map the scattering properties of the Earth's surface has been already intensively investigated [202]. Since the 1950's SAR systems are used to extensively analyze and study geophysical processes characterizing the Earth's surface. These systems can be mounted on-board heterogeneous platforms (e.g., aircraft, satellite, ground carrier), have a side-looking illumination direction and can perform accurate distance measurements between the moving platform and the observed surface. Given a scene on the ground a SAR sensor radiates it with a packet of electromagnetic waves and then measures the electromagnetic signals received on board, which is due to the backscattering of the waves by the objects that compose the observed scene. Both the acquisition geometry and the physical characteristics of the scene contribute to the formation of the received backscattered SAR signal. The signals used by SAR systems typically lie in the microwave band (in the range of the wavelength λ 1cm and 1m) and being active imaging sensors, they do not need an external energy source to work and can be effectively used to detect areas affected by a significant clouds' cover. As a consequence of its

flexibility, SAR technology mostly improved during the last years and further techniques have been also developed, thus helping the scientific community with the interpretation of several geophysical phenomena. In this field, techniques based on the analysis of SAR data, such as SAR interferometry (InSAR) [203]–[205], are of fundamental importance. They relate the phase difference (interferogram) between two (or more) SAR acquisitions of the same scene taken at different times to measurements of topography or deformation of the Earth's surface.

This chapter will briefly introduce the basic concepts of SAR interferometry, particularly the first part of generating an InSAR interferogram. Subsequently, I will discuss the differential interferometry technique DInSAR, which allows us to determine the displacement of the Earth's surface that occurs between two temporally different observations of the same ground scene observed by a SAR system. Next, I will focus on the presentation of the multiple aperture synthetic aperture radar interferometric (MAI) technique which is primarily used to measure the along-track components of the Earth's surface deformation, by investigating its capabilities and potential applications. This method has been extensively investigated during the period of my doctoral studies, and has been used to monitor the temporal evolution of ground surface changes in areas subject to large deformations (e.g., due to glaciers movements or seismic episodes), enabling the discrimination of the three-dimensional (up-down, east-west, north-south) components of the Earth's surface displacements.

5.1 SAR INTERFEROMETRY

The SAR interferometry technique exploits the difference of viewing angles in two (or more) acquisitions (e.g., across-track configuration) to estimate the topography of an observed scene (e.g. [205]). Considering repeat-pass across-track configuration, two interfering SAR images can be expressed in complex notation as:

$$\begin{aligned} I_1(x,r) &= \gamma_1(x,r)e^{j\frac{4\pi}{\lambda}R} \\ I_2(x,r) &= \gamma_2(x,r)e^{j\frac{4\pi}{\lambda}(R+\delta_R)} \end{aligned} \tag{5.1}$$

where $\gamma_{1,2}(x,r)$ represents the complex-valued reflectivity function related to the target of azimuth and range coordinates (x,r) and $j=\sqrt{-1}$ is the imaginary

unit. Note that R and R + δ_R are the range distances between the sensor and the target in the two images, with δ_R being the additive range distance term due to slightly different viewing geometries. The phase difference between the two SAR images is obtained by extracting the phase of the complex interferogram [205], which is given by the complex conjugate product operation between the two SAR images, as follows:

$$I(x,y) = I_1(x,r) \cdot I_2^*(x,r) = \left| I_1(x,r) \cdot I_2^*(x,r) \right| e^{j\frac{4\pi}{\lambda}\delta_R} \tag{5.2}$$

By taking into account the acquisition geometry shown in Figure 65 and applying the law of cosines, after trivial mathematical manipulations [206], it is straightforward to demonstrate that:

$$\Delta\phi = \frac{4\pi}{\lambda}\delta_R \cong \frac{4\pi}{\lambda} b \sin(\vartheta - \alpha) \tag{5.3}$$

where $\Delta\phi$ is the extracted interferometric phase. Note that λ is the operational wavelength, b is the interferometric baseline (i.e., the distance between orbital positions from which the two SAR images are taken), ϑ is the sensor side-looking angle and α is the angle the baseline makes to a horizontal reference plane. The Equation (5.3) contains useful information on the target height h.

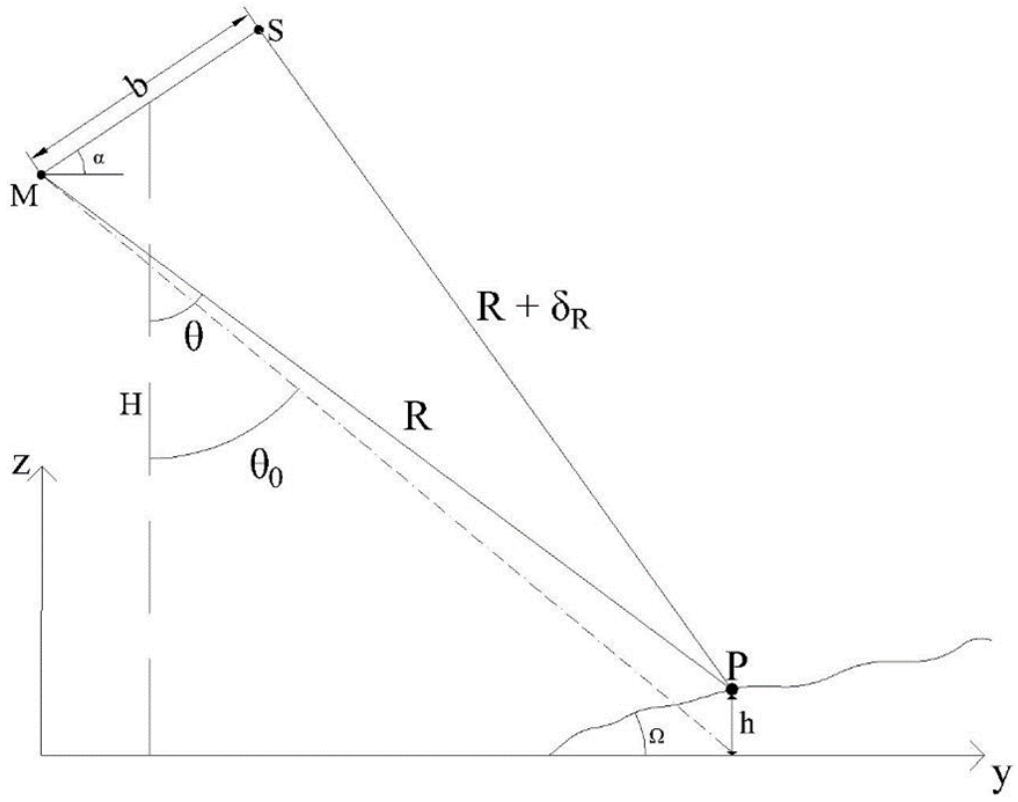

Figure 65. InSAR geometry acquisition. **M** and **S** represent the positions of master and slave acquisitions, respectively, and **P** is the generic point target on the ground

Indeed, by expanding Equation (5.3) around the angular position $\vartheta = \vartheta_0$, representing the illumination angle for flat terrain (i.e., h=0), we have:

$$\begin{aligned} \Delta\phi &= \frac{4\pi}{\lambda} b\left[\sin(\vartheta_0 - \alpha) + \cos(\vartheta_0 - \alpha)(\vartheta - \vartheta_0)\right] \cong \\ &\cong \Delta\phi_{flat} - \frac{4\pi}{\lambda}\frac{b_\perp}{R\sin(\vartheta)} h = \Delta\phi_{flat} - \Delta\phi_{topo} \end{aligned} \tag{5.4}$$

where $\Delta\phi_{flat}$ is the so-called flat-Earth phase contribution, and $b_\perp$ is the component of the baseline that is perpendicular to the radar-to-sensor line-of-sight direction. The first term on the right-hand side of Equation (5.4), representing the flat-Earth phase term, can be derived (e.g., [207]) by computing the local phase frequency in the range direction as:

$$\Delta\phi_{flat} = -\frac{4\pi}{\lambda}\cdot\frac{b_{\perp}}{R\tan(\vartheta_0 - \Omega)}\rho \tag{5.5}$$

Where Ω is the local slope of the terrain and $\rho = r$ is the pixel range coordinate of the imaged target. Conversely, the second phase term is the topographic phase signature $\Delta\phi_{topo}$. More general relations arise if the curvature of the Earth is also taken into account (e.g., [205], [208]). If the range-dependent phase term is compensated for in Equation (5.4), the topography of the imaged scene *h* is finally computed as:

$$h = -\frac{\lambda R\sin(\theta)}{b_{\perp}}\cdot\frac{\Delta\phi_{topo}}{4\pi} \tag{5.6}$$

From Equation (5.6), the height h can be estimated with an accuracy that is baseline-dependent; this means that the larger the perpendicular baseline, the more accurate the estimation of topography will be [208]. However, very large baseline values are responsible for severe decorrelation noise artifacts [209]. They corrupt the measured interferometric phase $\Delta\phi$ and, subsequently, lead to incorrect height profile estimations. It is also worth highlighting that the interferometric phase is restricted to the [-π, π[interval. The phase unwrapping (PhU) operation is a crucial step in any InSAR processing tool, and several approaches have been developed [210]–[213]. PhU involves the searching of (unknown) 2π-integer multiples that must be added to wrapped phases to compute unwrapped (full) phases.

5.2 DIFFERENTIAL SAR INTERFEROMETRY

As an evolution of the InSAR approach, a processing methodology known as the differential synthetic aperture interferometric (DInSAR) technique [202], [214] has been developed. It represents a common practice nowadays in the remote sensing scientific community for the detection and monitoring of the Earth's surface displacement phenomena. The key factor of the DInSAR technique with respect to other conventional approaches (e.g., GPS and leveling measurement campaigns) is that it allows the continuous monitoring of displacement phenomena with a dense grid of measurement points. To convey the Earth's surface displacements, the DInSAR technique relies on the generation of a so-called differential SAR interferogram [202]. Considering the acquisition geometry depicted in Figure 66, it is assumed that two complex-valued SAR images of the imaged scene were

acquired at different times and in different orbital positions. In a case where the ground surface is displaced by the 3-D vector ***d*** between the two flight passages of the sensor along the scene, the computed interferometric phase difference between the two SAR images—namely, $\Delta\phi$—is made up of two main phase components:

$$\Delta\phi = \Delta\phi' + \Delta\phi_{defo} = \Delta\phi' + \frac{4\pi}{\lambda} d_{LOS} \tag{5.7}$$

where $\Delta\phi'$ is the phase contribution in the absence of deformation, as expressed in Equation (5.4), and $\Delta\phi_{defo}$ is the additional phase contribution related to the ground displacement. Therefore, the phase signal associated with the deformation can be recovered by synthetically reconstructing the phase component contribution $\Delta\phi'$ and subtracting it, modulo 2π, to the measured phase difference. In particular, d_{LOS} is the projection of the displacement vector *d* along the sensor-to-target LOS direction. The synthetic phase term $\Delta\phi'$ is simulated from the knowledge of external information on the acquisition geometry such as a digital elevation model (DEM) of the observed area, the orbit state vectors, and the operational parameters of the radar instrument [208]. In a more general case, the differential interferometric phase is expressed as:

$$\Delta\phi = \Delta\phi_{defo} + \Delta\phi_{topo} + \Delta\phi_{orb} + \Delta\phi_{atmo} + \Delta\phi_{noise} \tag{5.8}$$

where $\Delta\phi_{topo} = \frac{4\pi}{\lambda} \cdot \frac{b_{\perp}}{r\ sin\theta} \Delta z$ represents the residual topography phase component induced by the DEM errors Δz; $\Delta\phi_{orb}$ represents the residual phase term related to inaccurate orbital parameter information, which is used to estimate the aforementioned synthetic phase term; $\Delta\phi_{atmo}$ denotes the phase components relative to the propagation variation of the RADAR signal caused by the absorption effects of Earth's atmosphere; and, finally, $\Delta\phi_{noise}$ is representative of additive noise contributions (i.e., spatial and temporal decorrelation, incorrect focusing of SAR raw data, etc.), that corrupt the interferometric phase [209], [215]. In particular, the spatial decorrelation is less pronounced for short perpendicular baseline configurations.

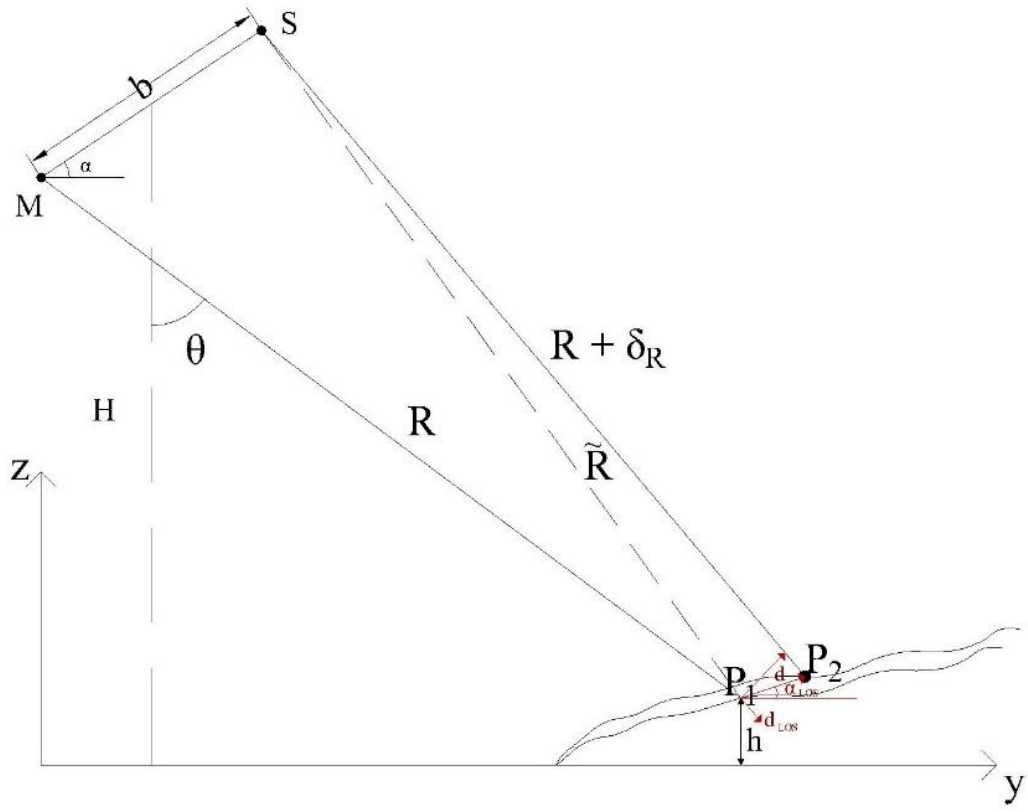

Figure 66. DInSAR geometry acquisition. Same as **Figure 65** but considering the displacement **d** of the imaged point **P** on the ground. Note that **P1** and **P2** represent the point target positions of the master and slave acquisitions, respectively.

From Equation (5.7), the accuracy of the displacement measurements depends on the operational wavelength λ. In this case, the maximum detectable unambiguous displacement that corresponds to a full phase cycle of 2π is equal to $\frac{\lambda}{2}$, denoting measurement accuracy of a fraction of the employed wavelength that is dependent on the amount of noise present in the measured phase. Interested readers can find an overview of DInSAR and its main applications in [207], [216].

5.3 DETECTION OF LARGE GROUND DISPLACEMENT SIGNALS

The study and the characterization of Earth's surface displacements by the use of DInSAR techniques is a hot topic in the literature. More recently, these

approaches have been used in [12] which address the use of the multiple aperture interferometric (MAI) technique [217] for the detection of large ground displacement dynamics. The proposed study addresses different issues:

1) To illustrate the underlying rationale and effectiveness of the MAI technique;
2) To present an innovative method to combine complementary information of the ground deformation collected from multi-orbit/multi-track satellite observations.

In particular, the presented technique complements the recently developed Minimum Acceleration combination (MinA) method with MAI-driven azimuthal ground deformation measurements to obtain the time series of the 3-D components of the deformation in areas affected by large deformation episodes. Experimental results encompass several case studies. The validity and relevance of the presented approaches are demonstrated in the context of geospatial analyses.

5.4 MULTIPLE APERTURE INTERFEROMETRY PRINCIPLE

As said in Sections 5.1 and 5.2, InSAR techniques have successfully been used to study and analyze many different phenomena that characterize the Earth's surface. However, these techniques are limited to measuring only the 1-D components of ground deformation along the RADAR LOS direction. Conversely, enabling 3-D displacement measurements is crucial for better analyses and to study of the deformation phenomena that characterize areas of interest. In the last two decades, many studies have been carried out enabling the measurement of the 3-D (up-down (U-D), east-west (E-W), and north-south (N-S)) ground displacement [218]–[220]. Multi-platform, multi-track InSAR techniques have been developed to discriminate the U-D and E-W components of surface displacement, but the estimation of N-S ground displacement data has been more challenging. In this respect, SAR amplitude tracking methods—namely, pixel offset (PO) [221]–[226] and multiple aperture interferometry (MAI) [227]–[230]—have been applied.

It has been demonstrated that the measurement accuracy of N-S displacement that is attainable with PO methods is low. In particular, it reaches only a fraction of pixel spacing (1/30th), as the azimuthal pixel spacing of first-generation and present-day SAR instruments is in the order of 3–5 cm [221], [223], [231]–[233]. For example, taking into account that the azimuth pixel spacing of the TerraSAR-

X sensor is about 3 m, the expected accuracy of PO measurements is about 10 cm. Of course, fine and ultra-fine SAR data with enhanced spatial resolutions are envisaged to apply the PO method. It is worth noting that a substantial improvement in the discrimination of the N-S ground displacement component from InSAR data is a key factor in performing extended geophysical investigations.

5.4.1 Multiple Aperture Interferometry for the Along-track Measurements

Monitoring the Earth's surface phenomena requires more comprehensive analyses, such as estimating the 3-D field of ground surface displacement that affects a specific area. Since SAR satellite platforms travel in almost near-polar orbits, the main problem in the discrimination of the north-south component of deformation (approximately along-track displacement) is that the projection of the ground displacement along the north-south direction is not accurate enough [227].

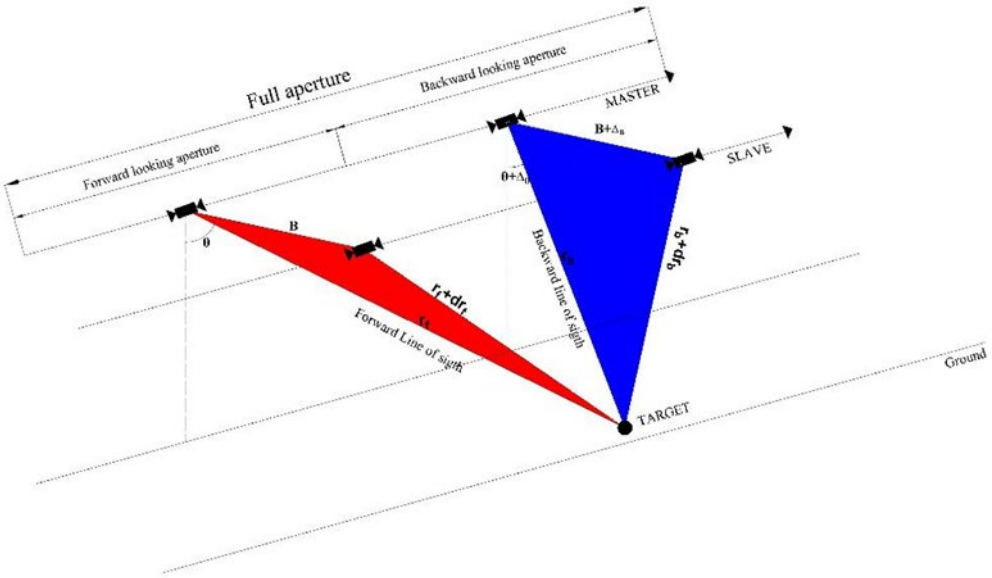

Figure 67. Multiple aperture interferometry geometry acquisition. The target on the ground is observed in the master and slave acquisitions by the SAR sensor with slightly different viewing geometries. Forward- and backward-looking apertures are produced by the split beam process.

In recent years, a big improvement in the discrimination of along-track displacement has been through the development of the MAI technique. This technique uses a split beam process called "spectral diversity" (see Appendix A) to determine backward- and forward-looking interferograms [234] from a SAR data

pair that is related to the same scene but were acquired at different times (see Figure 67).

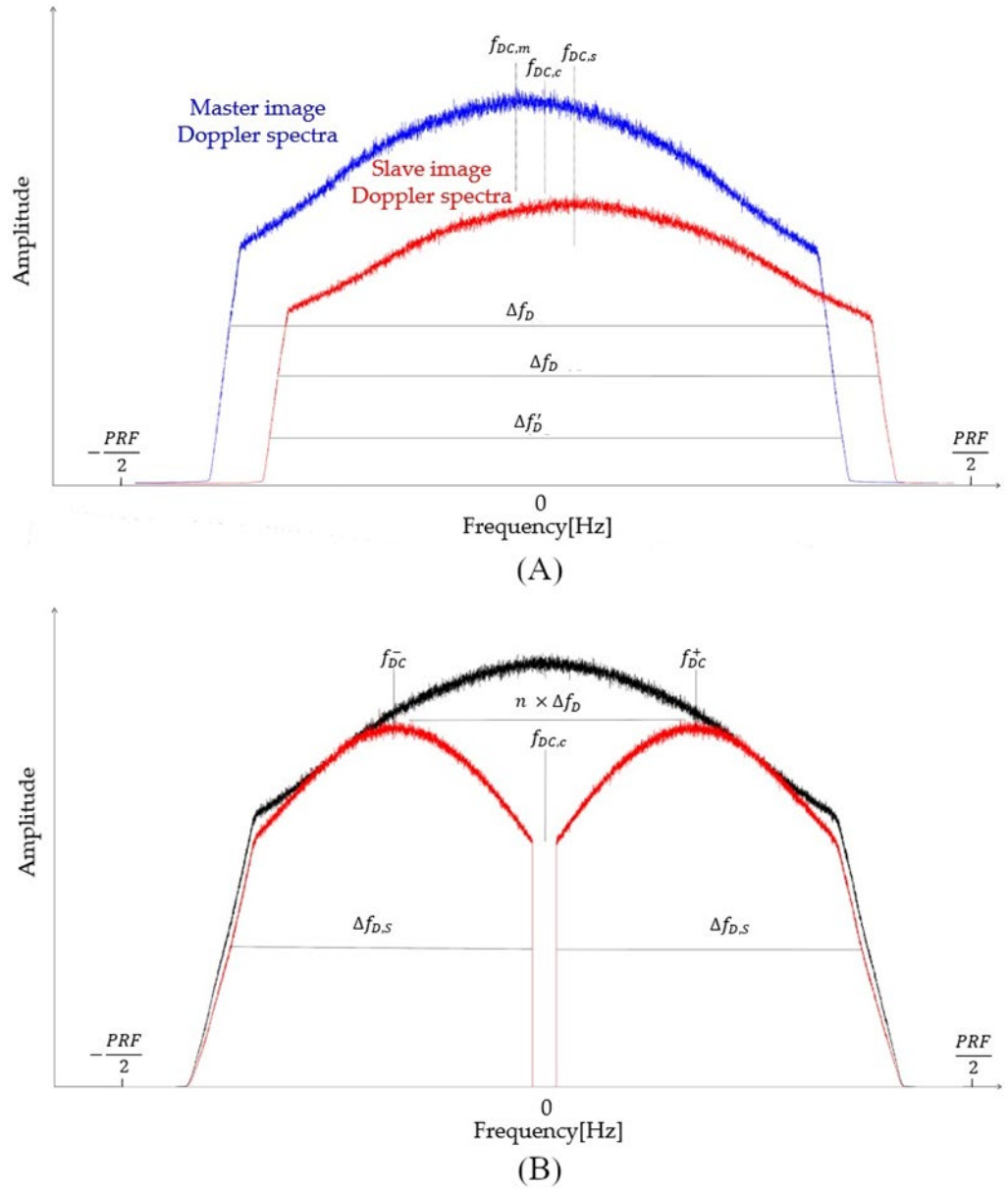

Figure 68. (A) Doppler frequency spectra of a pair of Envisat/ASAR complex images related to the Afar depression acquired on 19 December 2005 (blue spectra) and on 25 August 2008 (red spectra). (B) Doppler frequency spectra were filtered using two Hamming windows (red-colored spectra).

The backward- and forward-looking interferograms can be expressed as follows (see Equation (A.10) in APPENDIX A: Spectral Diversity for more details):

$$\phi_{fw} = \frac{2\pi}{v} \cdot f_{DC}^{+} x \tag{5.9}$$

$$\phi_{bw} = \frac{2\pi}{v} \cdot f_{DC}^{-} x \tag{5.10}$$

Specifically,

$$f_{DC}^{+} = f_{DC,c} + n \cdot \frac{\Delta f_D}{2} \tag{5.11}$$

$$f_{DC}^{-} = f_{DC,c} - n \cdot \frac{\Delta f_D}{2} \tag{5.12}$$

where $f_{DC,c} = \frac{f_{DC,m} + f_{DC,s}}{2}$ and $\Delta f_D = \frac{2v}{l}$ are the average Doppler centroid (DC) frequencies of the two full-bandwidth SAR images, with $f_{DC,m}$ and $f_{DC,s}$ being the DCs of the master and slave SAR images, respectively. Note that Δf_D is the effective Doppler bandwidth, l indicates the azimuthal antenna length (see Figure 68) and n is the fraction of the azimuth bandwidth (e.g., Δf_D ; see Figure 68) used in the split-beam process, also indicated as the normalized squint angle of the sub-aperture process. Consequently, starting from the measured phase difference between the forward- and backward-looking interferometric phases, the MAI phase is determined as follows:

$$\phi_{MAI} = Wr\left(\phi_{fw} - \phi_{bw}\right) = \frac{2\pi}{v} n \cdot \Delta f_D \cdot \Delta x = \frac{2\pi}{v} n\left(\frac{2v}{l}\right) \cdot \Delta x = \frac{4\pi}{l} n \cdot \Delta x + \eta \tag{5.13}$$

In Equation (5.13), it is clear that the MAI phase is proportional to the along-track deformation Δx , where, for the sake of simplicity, we have imposed $f_{DC,c} = 0$, and η is the interferometric noise. Naturally, Equation (5.13) represents the simplest case. In particular, during the MAI interferogram determination, the SD

process generates the forward- and backward-looking interferometric phases, respectively, splitting the full azimuthal spectral bandwidth of the master and slave images (see Figure 68 B).

If the master and slave acquisition orbits are not perfectly parallel when considering the backward- and forward-looking imaging geometries (see Figure 68 A), different flat-Earth and topographic phase contributions arise in the forward- and backward-looking interferograms. Considering Equations (5.4) and (5.5), Jung et al. [235] addressed this problem by considering the expression of the additional spurious phase terms related to the flat-Earth and the topographic contributions, which are related to the baseline difference between the forward- and backward-looking imaging geometries, namely, $\Delta B_{\perp}$:

$$\phi_{flat} = \frac{4\pi\Delta B_{\perp}}{\lambda R \tan(\theta)}\rho \tag{5.14}$$

$$\phi_{topo} = \frac{4\pi\Delta B_{\perp}}{\lambda R \sin(\theta)}h \tag{5.15}$$

where ρ and h are the slant range and topographic height, respectively. The atmospheric phase screen (APS) may be considered negligible in the final MAI phase, as APS is influential in the same way both the backward- and forward-looking interferograms are.

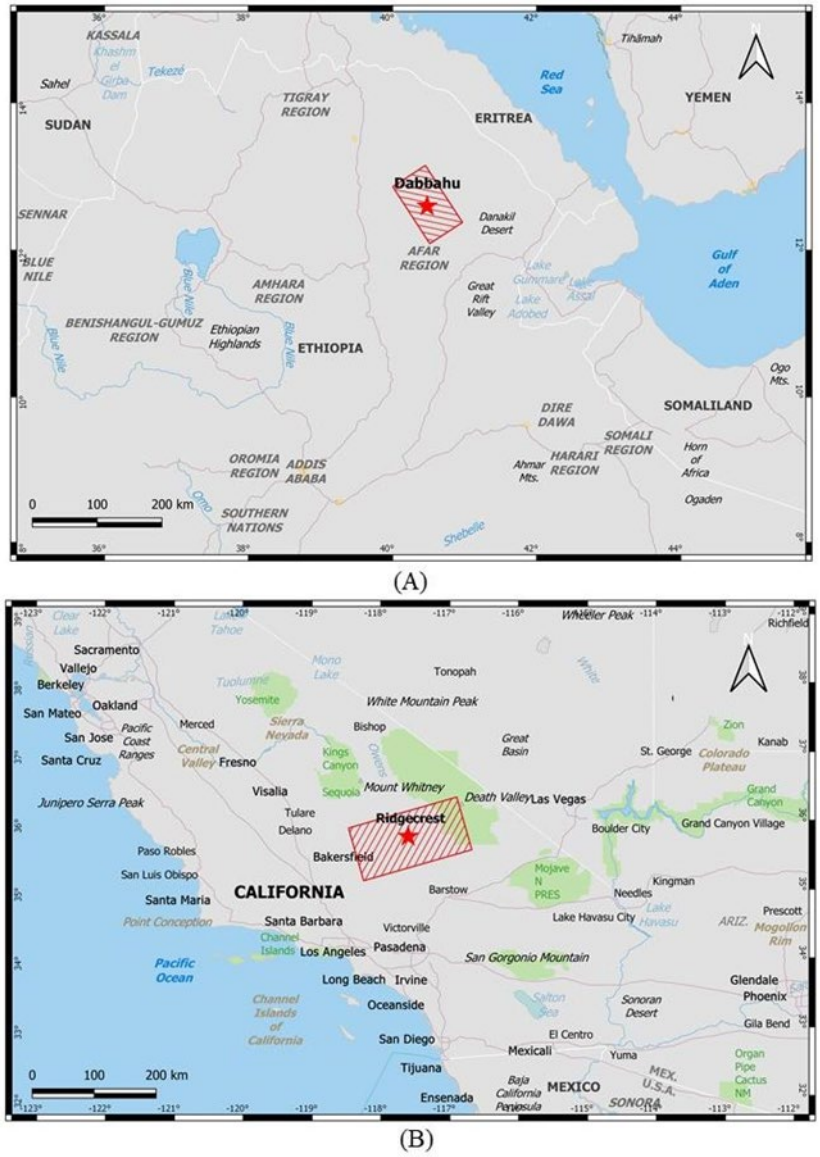

Figure 69. Geographical maps of the case study areas. (A) Afar depression, Ethiopia, and (B) Ridgecrest, California, USA. Red rectangles in (A) and (B) represent the footprints of the used ASAR/Envisat and Sentinel-1 datasets, respectively.

In this context, Jung et al. [235] presented an MAI improvement process on which they estimated and corrected for the mentioned flat-Earth and topographic spurious phase terms. Afterward, we will present two case studies related to the application of the MAI technique to the investigation of a single deformation episode. The first case study concerns Afar depression. Afar is a region situated in Ethiopia, Africa, that was affected in 2005 by a big earthquake associated with the

Ethiopian Great Rift fault mechanism [236], [237]. Specifically, from September to October 2005, a seismic sequence consisting of 131 events affected the Afar region as a result of the Dabbahu volcano eruption (see Figure 69 A). Since the initial main events of the drifting episode, a further sequence of 13 discrete dyke events was detected from 2005 to 2010 along the entire Dabbahu rift segment [236].

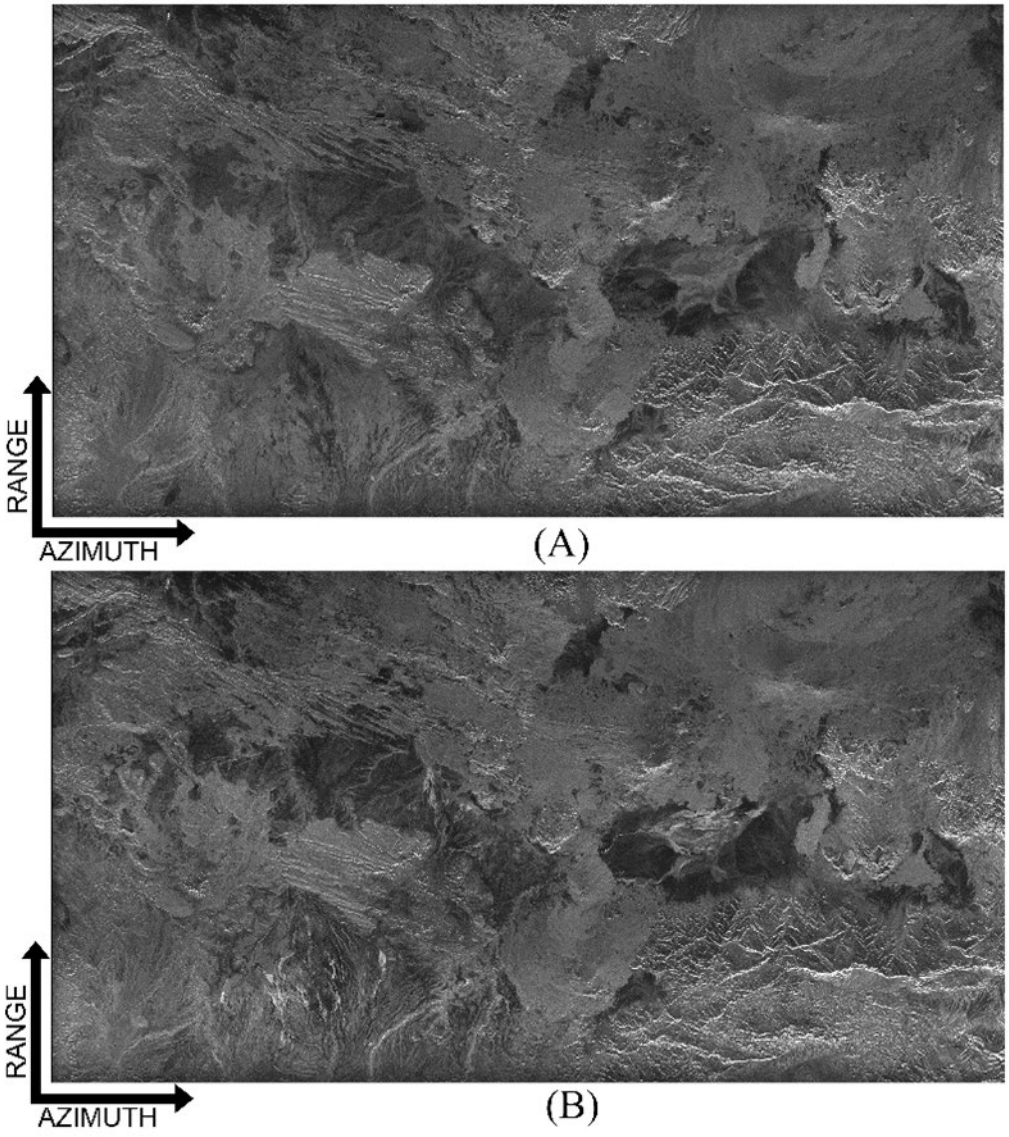

Figure 70. Afar depression region. Amplitude SAR images of the ASAR master (A) and slave (B) acquisitions, were collected on 19 December 2005 and 25 August 2008, respectively.

We performed an experiment by considering one pair of Envisat/ASAR data that captured the effects of the Dabbahu rifting episode. SAR data were acquired along ascending orbits (Track 200) on 19 December 2005 (master) and 25 August 2008 (slave), as shown in Figure 70 (A) and (B). Starting from this pair of SAR data, an MAI interferogram was generated (see Figure 71 A).

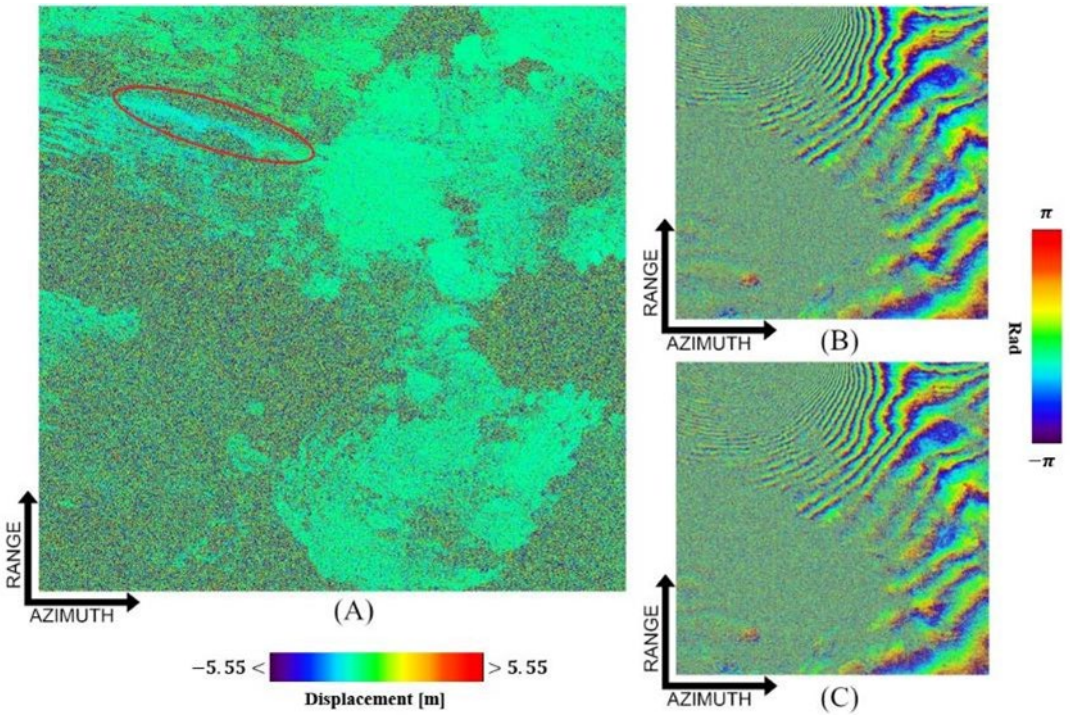

Figure 71. (A) Multiple aperture SAR interferometry (MAI) and (B, C) forward- and backward-looking interferograms of the Afar depression zone, were generated from a pair of the ASAR acquisitions that were collected on 19 December 2005 and 25 August 2008, respectively. The red circle identifies the main fault trace.

The forward- and backward-looking interferograms of the Dabbahu region area are shown in Figure 71 (B) and (C). In particular, we have highlighted an area in the MAI interferogram with a red circle that showed sensitive ground displacement and was in correspondence with a trace of the 2005 activated rift segment.

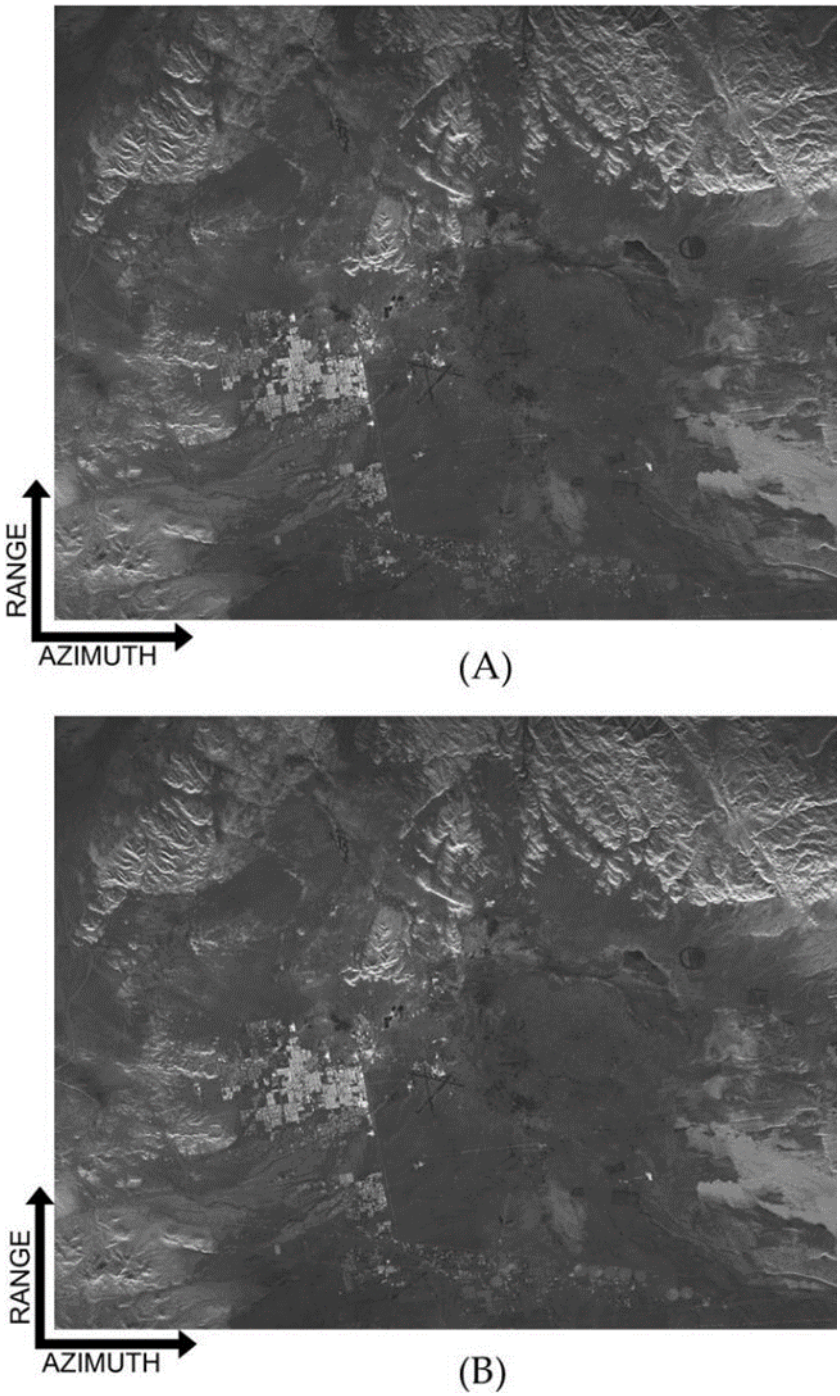

Figure 72. Area of Ridgecrest, California, USA. Amplitude SAR images of the COSMO-SkyMed master (A) and slave (B) acquisitions, acquired on 4 July 2019 and 20 July 2019, respectively.

The second case study was performed by processing a couple of SAR data acquired over the north-east Ridgecrest town area, situated in California, USA, (see

Figure 64 B), which was struck by a big (Mw) 7.1 earthquake on 6 July 2019, the strongest in the region in at least two decades. The phenomena included other previous main shock events, and in the days and weeks that followed, thousands of aftershocks rumbled beneath Southern California [238].

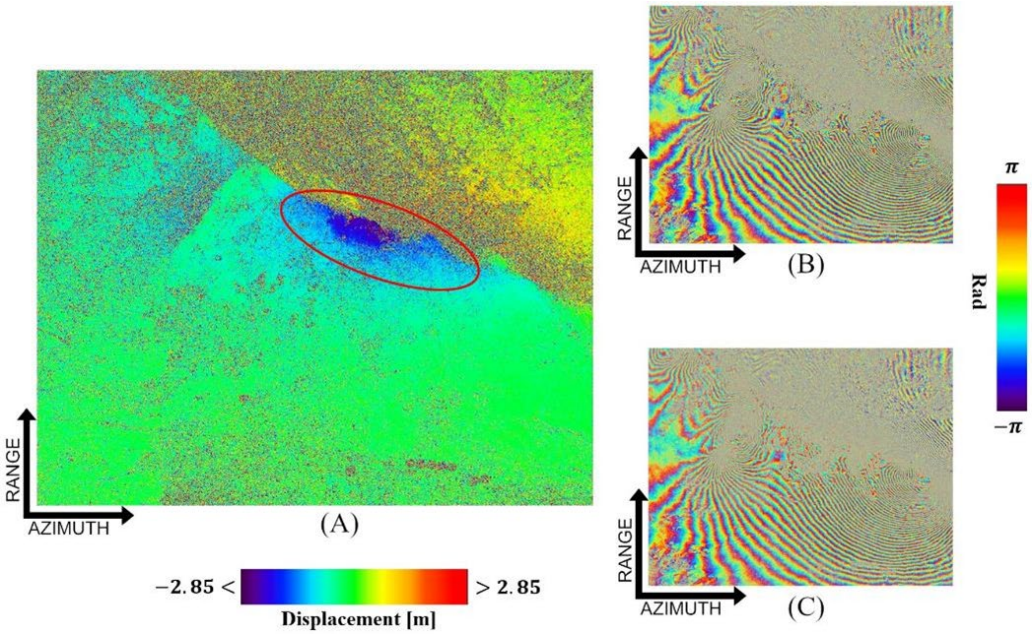

Figure 73. (A) MAI and (B, C) forward- and backward-looking interferograms of the area of Ridgecrest, California, USA, generated from a pair of COSMO-SkyMed acquisitions collected on 4 July 2019 and 20 July 2019, respectively. The red circles identify the fault line zone.

In particular, starting from a single pair of COSMO-SkyMed acquisitions—the master collected on 4 July 2019, and the slave on 20 July 2019 (see Figure 72 A, and B) a MAI interferogram (Figure 73 A) was generated from a pair of forward- and backward-looking interferograms (Figure 73 B, and C). Specifically, in the interferogram depicted in false colors, we can clearly see the big fault related to the main seismic event circled in red (despite the presence of the interferometric noise) at the center.

Considering the parameters of the X-band COSMO-SkyMed RADAR instrument of the Italian Space Agency (ASI) and the Envisat/ASAR of the European Space Agency (ESA)—with azimuthal antenna lengths of 5.7 and 11.1 m, respectively—we evaluated the along-track measurement enabled by the MAI technique. In particular, taking into account Equation (5.13) and neglecting the noise term (for the sake of simplicity), we observe that an ambiguous maximum

along-track deformation Δx of about 5.7 and 11.1 m for every in 2π phase cycle can be measured. This result implicitly confirms the useful utility of the MAI technique for estimating and analyzing large displacements of the Earth's surface. A sounder analysis of MAI measurement performance is presented in Appendix B.

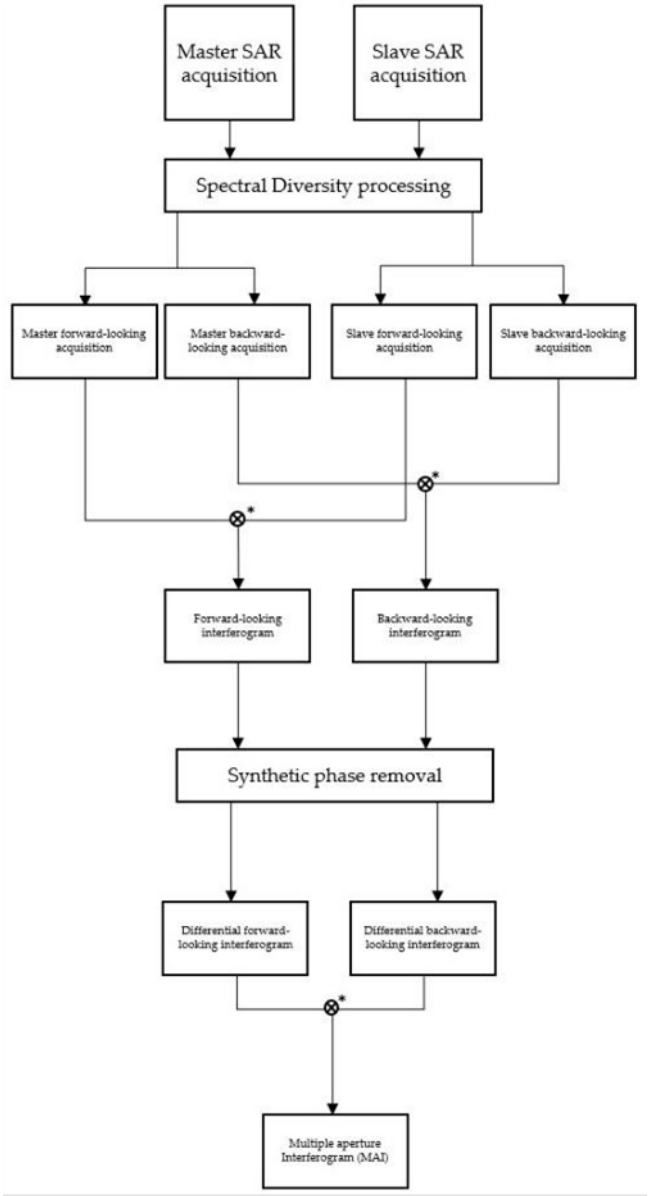

Figure 74. MAI processing flowchart. The symbol * denotes a complex conjugate multiplication

The processing scheme of MAI operations is shown in Figure 74.

5.4.2 MULTIPLE APERTURE INTERFEROMETRY FOR THE GENERATION OF ALONG-TRACK GROUND DEFORMATION TIME-SERIES

SAR interferometric techniques (such as DInSAR and MAI) allow many geophysical events that characterize Earth's surface to be studied in depth through the generation of single deformation maps. However, ground displacement phenomena are processes characterized by gradual or sudden changes in the Earth's surface elevation over time. In this context, to better characterize the displacement phenomena in an area of interest, an analysis of temporal modifications to ground displacement is necessary. Over the years, several methodologies have been developed that are useful for extending the use of differential interferometric SAR techniques to time-monitor displacement phenomena [239]–[248]. These methods are based on the inversion of properly selected sequences of DInSAR interferograms, allowing the computation of LOS-projected deformation time series. Two main categories of these techniques are present in the literature. The class of the persistent scatterer (PS) methods [239], [241] is based on the identification of coherent point-wise targets exhibiting high phase stability over a sequence of DInSAR interferograms that have been generated from a set of SAR data related to the same scene but acquired at different times. Conversely, the class of small baseline (SB) techniques [242], [243], [247], [249] is devoted to the analysis of distributed targets on the ground by processing sequences of small baseline interferograms. More recently, a new advanced method for the characterization of DS targets, called SqueeSAR [248], has also been developed. SqueeSAR uses a statistical approach that exploits phase and amplitude information of a sequence's SAR data to identify very highly coherent DS targets by the use of a maximum-likelihood optimization.

Very recently, temporal analysis methods have been used to extend the MAI technique and retrieve the temporal evolution of the along-track ground displacement. Specifically, a first attempt was made to estimate mean deformation along-track velocity by stacking a sequence of M MAI interferograms $\phi = \left[\phi_{MAI}^{0}, \phi_{MAI}^{1}, ..., \phi_{MAI}^{M-1} \right]$ generated from a stack of N SAR images. This was done by writing out the following system of equations:

$$\begin{bmatrix} \Delta t_0 \\ \vdots \\ \Delta t_{N-1} \end{bmatrix} [v] = \begin{bmatrix} \phi_{MAI}^0 \\ \vdots \\ \phi_{MAI}^{N-1} \end{bmatrix} \tag{5.16}$$

where ϕ_{MAI}^i and Δt_i are the ith MAI interferogram of the sequence and its temporal baseline, respectively, and v is the unknown deformation velocity to estimate. Finally, by resolving the system of Equation (5.16) in the least-squares (LS) sense, the deformation velocity is retrieved. A novel processing chain to stack a sequence of MAI interferograms was presented in Jo et al. [250] and used to measure the slow-moving azimuthal displacements of the Kilauea volcano on the Big Island, Hawaii. Taking into account that forward- and backward-looking interferograms are affected by noise, they suggested that—instead of estimating the MAI phase from the interferograms and applying the stacking procedure—the multi-temporal forward- and backward-looking residual interferograms could be individually stacked, in order to generate a MAI velocity map as:

$$v_{MAI} = \frac{l}{4\pi n} \cdot \frac{\left[\left\{ \sum_{i=1}^{N} \varphi_{fw,res}^i \right\} - \left\{ \sum_{i=1}^{N} \varphi_{bw,res}^i \right\} \right]}{\sum_{i=1}^{N} \Delta t_i} \tag{5.17}$$

where $\varphi_{fw,res}^i$ and $\varphi_{bw,res}^i$ are the interferometric phases of ith residual forward- and backward-looking interferograms, respectively, which are generated by removing a full aperture multi-look differential interferogram from the forward- and backward-looking one; Δt_i is the ith time duration, and N is the total number of forward- and backward-looking interferograms.

In particular, the theoretical variance of the estimated deformation velocity map measurements for the MAI stacking was evaluated to be:

$$\sigma_{v,MAI\_stacking} = \frac{l}{4\pi n} \cdot \frac{\sigma_{\phi,MAI}}{\sqrt{M} \cdot \overline{\Delta t}} \tag{5.18}$$

where $\overline{\Delta t}$ is the average temporal baseline of the whole InSAR distribution. The three-dimensional (3-D) displacement velocity map of the Kilauea Volcano,

obtained by combining multi-stacked DInSAR and MAI ground displacement rate maps, is shown in Figure 12 of [250].

Another important temporal study of the Earth's surface displacement via the MAI technique was carried out by Gourmelen et al. [251]. In their work, the authors combined displacement velocity maps that were obtained by applying the DInSAR and MAI techniques to map the ice surface velocity of the Langjokull and Hofsjokull ice caps in Iceland in 1994. In particular, their approach improved the accuracy of the ice flow measurement by a factor of two for E-W and U-D measurements, and up to a factor of 10 for N-S measurements, as compared with a velocity solution based on InSAR and pixel offset (PO).

Another class of studies based on the use of MAI interferograms is the multi-temporal extension of the MAI approach, which is used to generate along-track ground deformation time series [252]. In this instance, a network of M InSAR data pairs is identified from a set of N SAR images. If t_M and t_S represent the acquisition times of the master and slave images of a given interferogram, respectively, then the MAI phase is expressed via Equation (5.19) as:

$$\phi_{MAI} = \frac{4\pi}{1} n\left[\Delta x(t_S) - \Delta x(t_M)\right] \tag{5.19}$$

where $\Delta x(t_S)$ and $\Delta x(t_M)$ are the unknown along-track deformations at the master and slave image acquisition times, respectively. This leads to the solution of a system of linear equations that can be expressed, using matrix formalism, as:

$$A \cdot x = \phi_{MAI} \tag{5.20}$$

where x represents the vector of the unknown time-series deformation, ϕ_{MAI} is the vector of the phase components relative to the MAI interferogram, and A is the incidence-like matrix of the InSAR network graph, whose jth row is defined as follows:

$$\begin{cases} A(j, I_{M,j}) = & -\dfrac{4\pi}{l} n \\ A(j, I_{S,j}) = & \dfrac{4\pi}{l} n \\ otherwise & 0 \end{cases} \tag{5.21}$$

where in I_M and I_S are the *M*-length vectors of the indices of the master and the slave time acquisitions, respectively. The solution of the system of Equations (5.20) can be obtained in the LS sense as:

$$\tilde{x} = A^{+} \cdot \phi_{MAI} = \left(\left(A^{T} \cdot A \right)^{-1} \cdot A^{T} \right) \cdot \phi_{MAI} \tag{5.22}$$

where A^{+} indicates the left pseudo-inverse of the matrix A. Note that A is a full-rank matrix if all the SAR acquisitions form one single connected set of data. In a more general case where several different subsets of data are present, however, this can lead to a rank-deficient matrix A. In this situation, the same strategy adopted in the small baseline subset (SBAS) technique can be applied, which consists of proper manipulation of the system of Equation (5.20) and the application of the singular value decomposition (SVD) method (see [244] for additional details). We note that, for typical values of the expected along-track displacement, the unwrapping operation is not required in our case. Furthermore, the phase residuals:

$$e = A \cdot \tilde{x} - \phi_{MAI} \tag{5.23}$$

can be used to identify sets of well-processed SAR pixels. In particular, in this paper we propose exploiting the following temporal coherence factor to evaluate the quality performance of the inversion strategy:

$$\Upsilon = \frac{1}{N} \left| \sum_{i=0}^{N-1} e^{j e_i} \right| \tag{5.24}$$

where e_i is the ith phase residual value and Υ has the same mathematical expression of the temporal coherence factor initially proposed in [253]. However,

in this case, the phase residuals are not a result of time-inconsistent phase unwrapping mistakes, but rather phase noise of the MAI interferograms.

Table 18. Envisat/ASAR acquisition data of the Afar depression zone. Date format is day/month/year.

Acquisition n.	Date
1	19/12/2005
2	27/02/2006
3	04/12/2006
4	10/09/2007
5	28/01/2008
6	25/08/2008
7	10/08/2009

The deformation time series have been obtained by processing a sequence of 14 MAI interferograms generated from a sequence of seven Envisat/ASAR acquisitions of the Afar depression spanning the period between 9 December 2005 and 10 August 2009. The used data are listed in Table 18, and the distribution of the 14 MAI interferograms in the time/perpendicular baseline plane (indicating a Delaunay graph network [254]), is depicted in Figure 75.

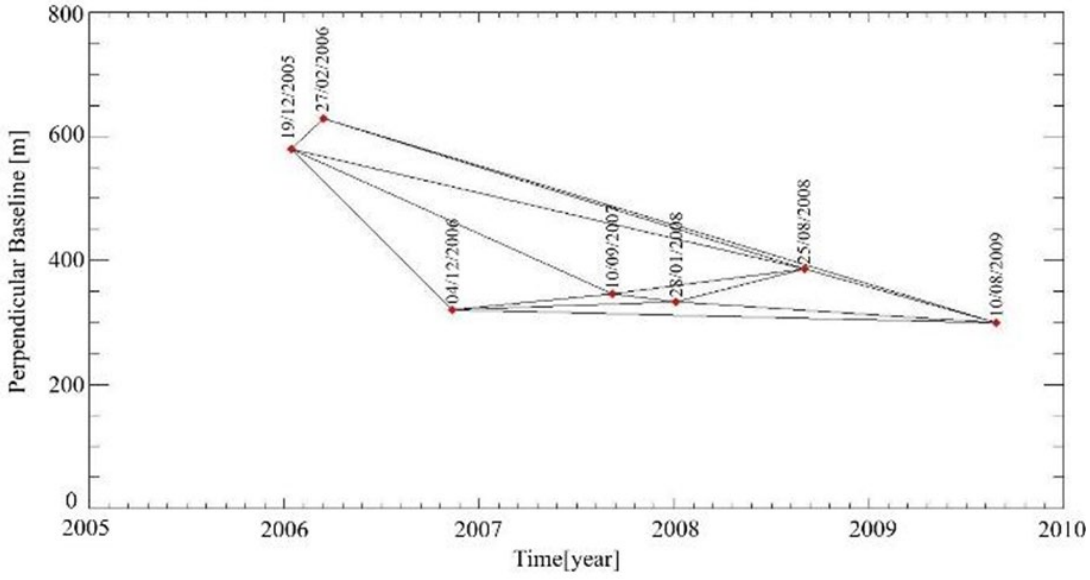

Figure 75. Interferometric SAR data pair distribution of the used ASAR/Envisat acquisitions related to the Afar depression area. Red points and black lines indicate the SAR data and the interferograms, respectively.

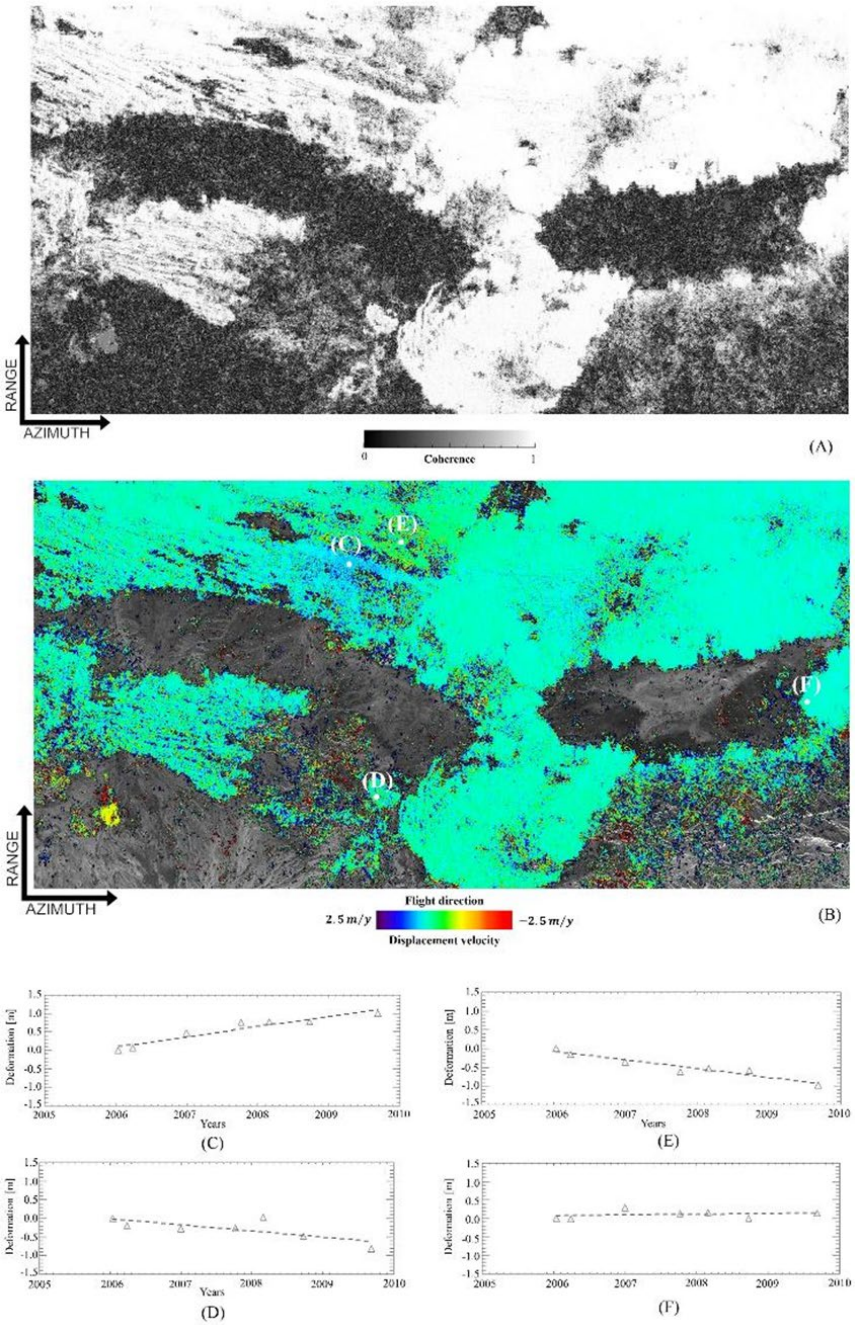

Figure 76. (A) Coherence map of MAI interferograms. (B) Mean deformation velocity map of the Afar area superimposed on a SAR amplitude image of the area. (C) Displacement time series related to the major fault area, (D, E) related to the medium-magnitude fault area, and (F) related to the low-magnitude deformation area.

Figure 76 shows the mean deformation velocity of the Afar area (see Figure 76 B) superimposed on a SAR amplitude image of the investigated area, and the relevant time series of deformation (see Figure 76 C–F). Only the deformation values of the coherent, well-processed SAR pixels are shown in the velocity map. They are identified by computing the map of the temporal coherence through Equation (5.24), as shown in Figure 76 A.

The area in Figure 76 B with a sensitive deformation (blue color) is located across the fault, and we highlighted four zones of interest that concerned the time-series analysis (points (B), (C), (D), and (E)). These major fault areas correspond to (i) a major fault zone whose deformation time series (Figure 76 C) showed an almost constant along-track deformation rate annually, with a leap of about 50 cm in the deformation during the 2005–2006 time period, when the main seismic event occurred; (ii) a zone of medium-magnitude deformation (Figure 76 D–E), where we can perceive opposite behaviors as if the deformations that characterize the AFAR depression should balance out somehow; and (iii) a zone of low-magnitude deformation (Figure 76 F) where the deformation time-series remained constant.

A more quantitative estimate of the accuracy of the achieved along-track deformation time series can be obtained by applying the basic principles of error noise propagation [255]. In particular, given a full covariance matrix for the vector of MAI phases $C_{MAI} = \sigma_{MAI}^2 I_{M\times M}$, the covariance matrix of the along-track deformation time series is given by $C_X = (A^T \cdot C_{MAI}^{-1} \cdot A)^{-1}$, where we have assumed the simplified hypothesis that the MAI phases are independent and uncorrelated and that the standard deviation of the MAI phase is given by Equation (B.5) in Appendix B. More extensive treatment is required in the case that the matrix A is rank deficient, and a given correlation is assumed between the MAI interferograms. This is a matter for further investigation, which would require a deep understanding of the statistical relationships among the interferograms, as well as a characterization of the studied PS and DS targets on the ground.

More recently, other advanced multi-temporal deformation investigations have been carried out using the MAI technique. Specifically, He et al. [252] performed a temporal analysis of big landslides that had occurred in the Fushun west open-pit mine (FWOPM), China. They mapped the two-dimensional deformation field time series of landslide phenomena that occurred between 2007 and 2011 by coupling DInSAR-SBAS with MAI-SBAS. They validated the generated time series (across-

track and along-track directions) with GPS displacement measurements over the Fushun mine. The time series obtained by He et al. are presented in Figure 10 of their article [252]. In particular, the results in the two graphics demonstrate that the time-monitoring analysis of the DInSAR and MAI techniques returned information that was highly consistent with the landslide kinematic pattern measured by the GPS sensor in that area.

All of the analyses presented for the generation of along-track ground deformation time series demonstrate that the key factor is the reduction of decorrelation noise errors. In Liu et al. [256], a very accurate investigation of the effects of these spurious phase components is presented that perturbs the final measurements. Specifically, Liu et al. classified these errors into three categories: (i) random error, (ii) systematic error, and (iii) gross error. These categories provide a more comprehensive understanding of the errors in inverting interferometric DInSAR and MAI phases when computing time series and 3-D maps of the deformation of an observed scene.

5.5 Generation of Multi-Track 3-D Ground Displacement Time-Series

In this Section, we summarize recent developments in the generation of 3-D ground displacement velocity maps, as well as in the retrieval of 3-D ground deformation time series. Interested readers can find a more comprehensive overview of this topic in [257]. In our work, the focus is principally on the generation of combined MAI/DInSAR-driven 3-D maps. Moreover, we propose a new algorithm for the generation of 3-D ground displacement time-series, complementing the recently developed minimum acceleration combination (MinA) method [258] (applied for the generation of up–down and east–west deformation components) with the north-south ground displacement time-series estimated by applying the methods shown in Section 5.4.1.

5.5.1 Overview of the techniques for the Generation of 3-D Ground Displacement Time-Series

One of the limits of the conventional DInSAR methods is that only the projection of the deformation along the LOS direction can be estimated. Nevertheless, the availability of DInSAR data products (i.e., mean deformation rate

and corresponding displacement time-series) computed from SAR data collected from ascending and descending data tracks allows a simple combination of the mean displacement velocity measurements as estimated from (at least) two complementary viewing orbital geometries. By considering the geometry portrayed in Figure 77, it can be demonstrated that the east–west and up–down deformation rate components can be obtained as [225], [257]

$$d_{LOS}^{(East)} \approx \frac{d_{LOS}^{(Desc)} - d_{LOS}^{(Asc)}}{2\sin(\theta)} \tag{5.25}$$

$$d_{LOS}^{(Up)} \approx \frac{d_{LOS}^{(Desc)} + d_{LOS}^{(Asc)}}{2\cos(\theta)} \tag{5.26}$$

Equations (5.25) and (5.26) are obtained by applying simple geometrical relations and assuming that ascending/descending measurements are taken by the same sensor, illuminating the imaged scene with approximately the same (absolute) side-looking angle. Clearly, the sum of the ascending/ descending LOS-projected displacement measurements is related to the vertical components of the ground deformation, whereas the difference of the ascending/descending components gives an estimate of the E-W components of the deformation. A more general relation arises when DInSAR measurements are obtained from complementary viewing angles but from different radar platforms, observing the scene with distinctive side-looking angles, namely, θ_{asc} and θ_{asc} (see Figure 16 in [257]):

$$\begin{pmatrix} d_H \\ d_v \end{pmatrix} = \begin{pmatrix} \sin(\vartheta_1) & \cos(\vartheta_1) \\ -\sin(\vartheta_2) & \cos(\vartheta_2) \end{pmatrix}^{-1} \cdot \begin{pmatrix} d_{LOS_1} \\ d_{LOS_2} \end{pmatrix} = \\ = \frac{\begin{pmatrix} d_{LOS_1}\sin(\vartheta_1) - d_{LOS_2}\cos(\vartheta_1) \\ d_{LOS_1}\sin(\vartheta_1) - d_{LOS_2}\sin(\vartheta_1) \end{pmatrix}}{\sin(\vartheta_1 + \vartheta_2)} \tag{5.27}$$

Nonetheless, in the derivation of Equation (5.27), there is no valuable information related to the Earth's ground deformation along the north–south direction. Indeed, because modern spaceborne radar systems are mounted on satellites that fly nearly polar orbits [227], the north–south (N-S) components of the deformation cannot be reliably measured using conventional DInSAR methods.

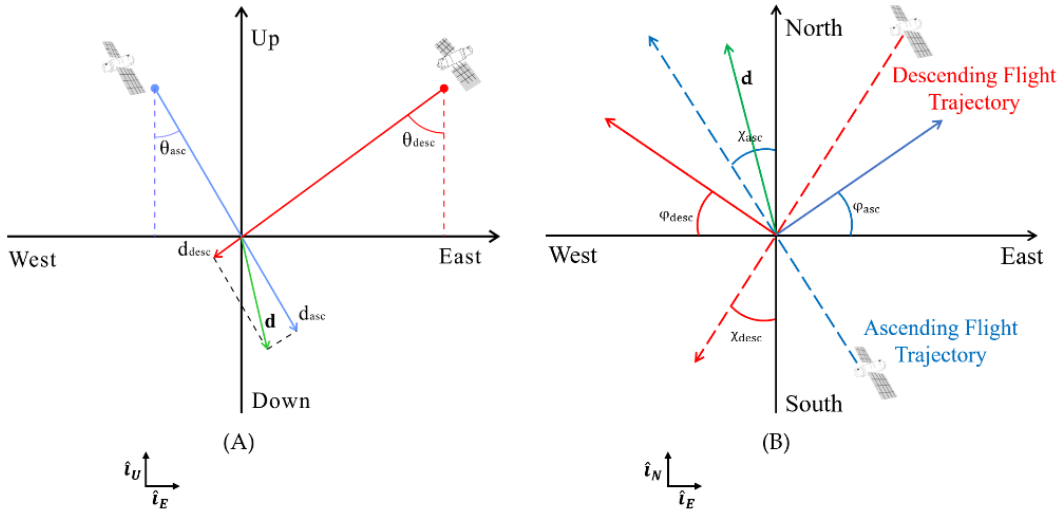

Figure 77. Imaging geometries of SAR observations over ascending (blue) and descending (red) orbits in the (A) east-vertical and (B) east-north planes, respectively.

Several algorithms have been developed to generate 3-D average displacement maps as well as 3-D displacement time series by combining multi-satellite/multi-orbit data tracks [219], [224], [225], [259], [260]. In this work, I mainly concentrate on the MinA technique [258], whose basic rationale is exploited to extend its applicability to the generation of north–south displacement time series, as presented in Section 5.4.2. The MinA technique assumes the availability of K independent SAR datasets collected by multiple SAR platforms at the ordered acquisition times $T^{(j)} = \left[t_0^{(j)}, t_1^{(j)}, \ldots, t_{Q_{j-1}}^{(j)} \right]$, where Q_{j-1} is the number of SAR images of the jth SAR dataset. Every single data track is separately processed, and the LOS-projected displacement time series are evaluated in correspondence with the location of coherent targets, which are well detected during each data processing step. After geocoding, the DInSAR products are efficiently combined over the common coherent points of the geocoded grid. The combination relies on the application of the mathematical relationships existing between the measured LOS-projection deformations and their corresponding 3-D components (see Figure 77):

$$\begin{aligned} & d_{LOS} = d \cdot \hat{i}_{LOS} \cong \\ & \cong \sin(\vartheta)\cos(\varphi) d_{East-West} - \cos(\vartheta) d_{Up-Down} + \sin(\vartheta)\sin(\varphi) d_{North-South} \end{aligned} \tag{5.28}$$

where φ is the radar heading angle (see Figure 77 B). In the simplified case, the dependence of the LOS-projected displacement from the north–south components can be neglected. Accordingly, Equation (5.28) simplifies as follows:

$$d_{LOS} = \sin(\vartheta) d_{East-West} - \cos(\vartheta) d_{Up-Down} \tag{5.29}$$

where we have assumed that $\varphi \cong 0$. The MinA technique relies on the application of Equations (5.28) and (5.29) for the generation of 2-D (and 3-D) ground displacement time-series. To this aim, the whole set of chronologically ordered acquisition times—namely, $T = \bigcup_{j=1}^{K} T^{(j)}$ is considered, and, for every coherent point, the vectors of the velocities among consecutive time acquisitions (see [242]) for the east–west and up–down components namely, $V_{East-West}$ and $V_{Up-Down}$ are considered as the unknowns of the problem at hand. Accordingly, the following system of linear equations is built (see [258] for the details):

$$B \cdot \begin{bmatrix} V_{East-West} \\ V_{Up-Down} \end{bmatrix} = \begin{bmatrix} d_{LOS}^{(1)} \\ d_{LOS}^{(2)} \\ \vdots \\ d_{LOS}^{(K)} \end{bmatrix} \tag{5.30}$$

where $V_{East-West}$ and $V_{Up-Down}$ are the vectors of the LOS-projected deformation time-series from the K different, complementary viewing geometries. The matrix B, which takes into account the temporal relationships of combined displacement time-series, is expressed as:

$$B = \begin{bmatrix} B^{(1)} \sin(\vartheta)^{(1)} \cos(\varphi)^{(1)} & -B^{(1)} \cos(\vartheta)^{(1)} \\ \vdots & \vdots \\ B^{(1)} \sin(\vartheta)^{(K)} \cos(\varphi)^{(K)} & -B^{(K)} \cos(\vartheta)^{(K)} \end{bmatrix} \tag{5.31}$$

where $B^{(j)}$ j=1,2,…,K is the jth incidence-like matrix (see [242] for further details) of the linear transformation relating the LOS displacement time-series with velocity deformation rates V_E, V_U.

To solve the problem, Equation (5.30) is regularized by imposing the condition that the (unknown) 2-D (E-W, U-D) deformation time-series at a given SAR pixel location has a minimum acceleration [258]. This condition is obtained by adding the following equations to the Equation (5.30):

$$C = \begin{cases} \delta(v_{E_{i+1}} - v_{E_i}) = 0 & i = 1,...,Q-2 \\ \delta(v_{U_{i+1}} - v_{U_i}) = 0 & i = 1,...,Q-2 \end{cases} \tag{5.32}$$

where δ is a regularization factor. The regularized system of linear equations can be rewritten as:

$$\begin{bmatrix} B \\ C \end{bmatrix} \cdot \begin{bmatrix} V_{East-West} \\ V_{Up-Down} \end{bmatrix} = \begin{bmatrix} d_{LOS}^{(1)} \\ d_{LOS}^{(2)} \\ \vdots \\ d_{LOS}^{(K)} \end{bmatrix} \tag{5.33}$$

This system of linear equations is solved in the least-squares (LS) sense as:

$$V = \Upsilon \cdot D \tag{5.34}$$

where V is the (unknown) vector of the LOS-projected E-W and U-P deformation time-series, Υ is the generalized inverse of the matrix $\begin{bmatrix} B \\ C \end{bmatrix}$ and D is the vector of geocoded LOS-displacement time-series relative to the K datasets.

Finally, the east–west and up–down deformation time-series are computed by time integration (pixel by pixel) of the obtained 2-D deformation velocity components. An error budget analysis of the MinA technique has previously been discussed in [261].

A regularized problem that is similar to MinA was proposed within the Multidimensional- SBAS (MSBAS) algorithm [262]. Differently from [258], the combination problem discussed in MSBAS was directly applied to the sequences of unwrapped multiple-track differential SAR interferograms. As opposed to MinA, the MSBAS method relies on searching for a minimum-velocity-norm (MN) solution. Therefore, MSBAS requires the simultaneous inversion of several (a few

hundred or more) unwrapped interferograms for the retrieval of 3-D components of deformation.

5.6 EXPERIMENTAL RESULTS

Here, we present some results achieved by combining the LOS-projected ground displacement signals collected after applying the multi-temporal SBAS technique to two sets of ascending/descending SAR data. The data were collected by Sentinel-1 radar instruments of the EU Copernicus Sentinels constellation based on the case study of the area of Ridgecrest in California. The lists of available SAR data are indicated in Table 19 and Table 20 for the ascending and descending data tracks, respectively.

Table 19. Sentinel-1 ascending SAR dataset. Date format is day/month/year.

Acquisition n.	Date
1	11/05/2019
2	23/05/2019
3	16/06/2019
4	28/06/2019
5	10/07/2019
6	22/07/2019
7	03/08/2019
8	15/08/2019
9	27/08/2019
10	08/09/2019
11	02/10/2019
12	14/10/2019
13	26/10/2019

Table 20. Sentinel-1 descending SAR dataset. Date format is day/month/year.

Acquisition n.	Date
1	05/05/2019
2	17/05/2019
3	29/05/2019
4	10/06/2019
5	22/06/2019

6	04/07/2019
7	16/07/2019
8	28/07/2019
9	09/08/2019
10	21/08/2019
11	02/09/2019
12	14/09/2019
13	08/10/2019
14	20/10/2019

Figure 78 A and B portray geocoded LOS-projected mean displacement maps of the area, superimposed on an amplitude image of the investigated area. The geocoding operations have been performed using precise orbital information and a 3-arc-second Shuttle RADAR Topography Mission (SRTM) [263] digital elevation model (DEM).

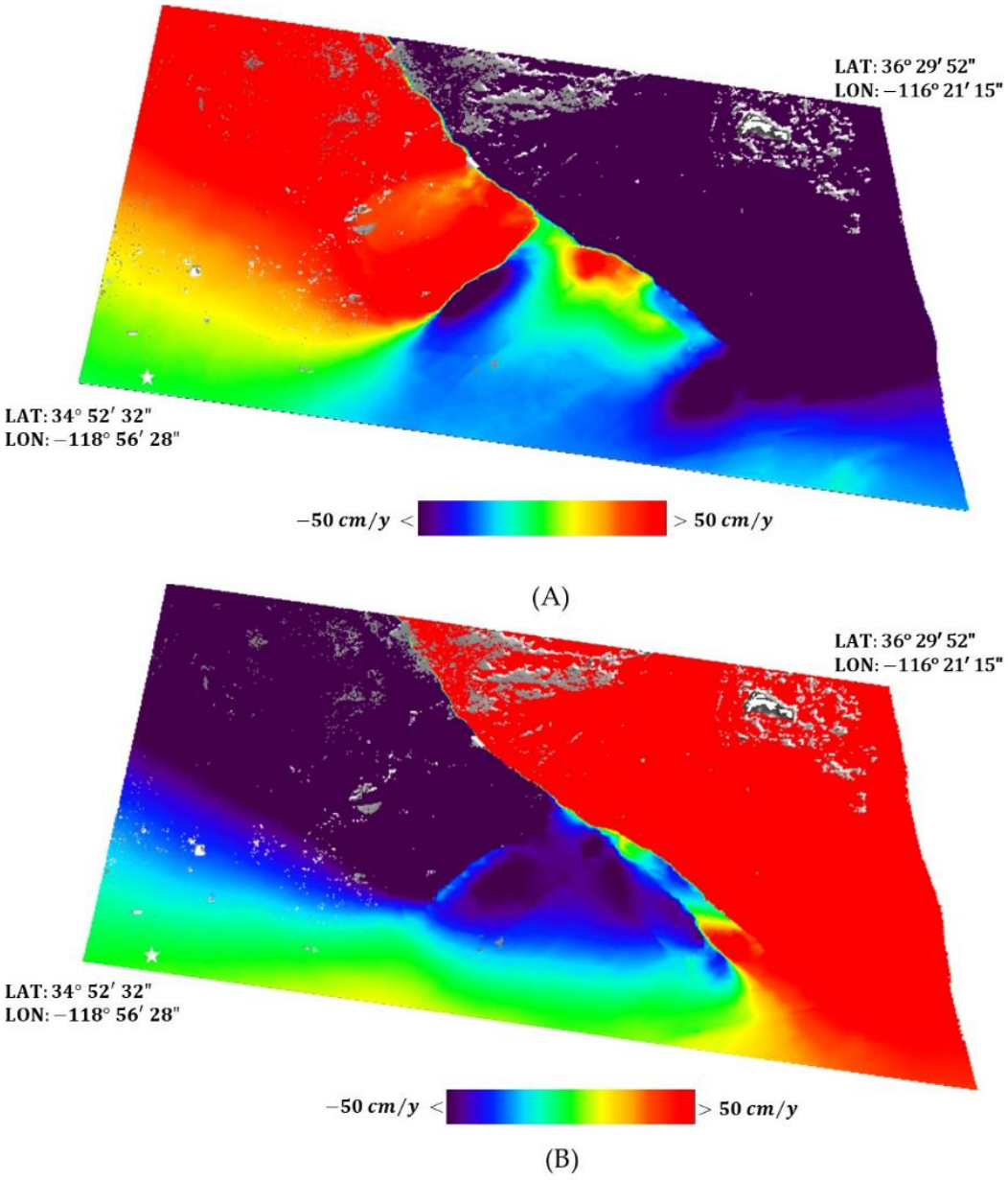

Figure 78. Geocoded LOS-projected mean displacement maps of the Ridgecrest area, superimposed on an amplitude image for ascending (A) and descending (B) orbits, respectively. All the displacement measurements are evaluated with respect to a pixel, identified in (A) and (B) by a white star

Subsequently, the MinA combination technique was applied to the two sets of geocoded data, to decompose the LOS-projected deformation measurements along the east–west and up–down directions, as shown in Figure 79 A, and B, respectively

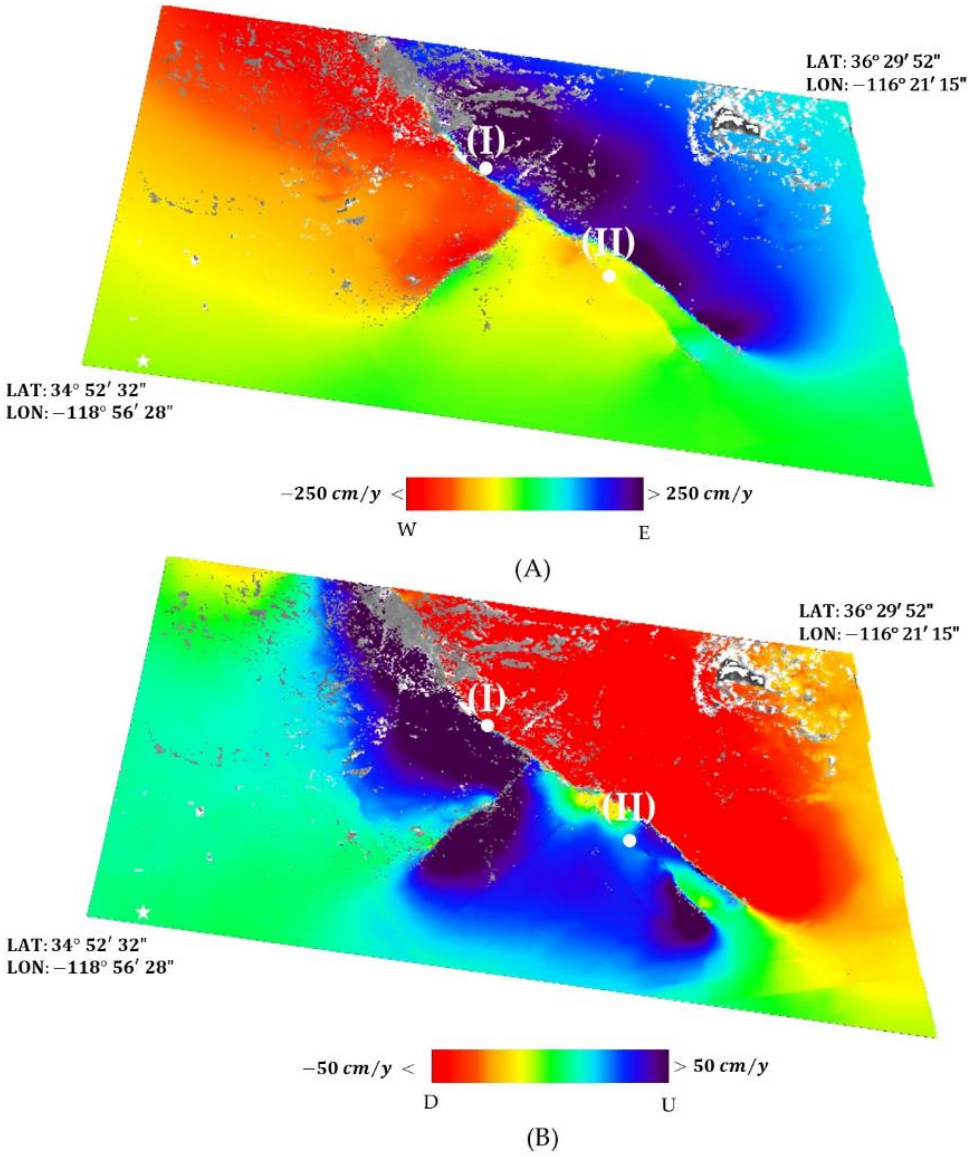

Figure 79. Geocoded mean displacement maps along the east–west and the up–down directions of the Ridgecrest area, superimposed on an amplitude image. The labels (I) and (II) in white indicate two points across the fault where the east–west and the up–down displacement time-series have been estimated, respectively. All displacement measurements are evaluated with respect to a pixel, identified in (A) and (B) by a white star.

5.6.1 Generation of North–South Ground Displacement Maps with MAI

In this subsection, we finally propose an adaptation of the MinA multi-temporal technique [258] for the generation of north–south displacement time-series using a combination of K independent sets of multiple-satellite/multiple-viewing angles

from along-track displacement time-series obtained by using MAI approaches. Similar to previous subsections above, we assume here that SAR data were acquired at ordered times $T^{(j)} = \left[t_0^{(j)}, t_1^{(j)}, \ldots, t_{Q_{j-1}}^{(j)} \right]$, where Q_j is the number of the available SAR scene in the given data track. $T = \bigcup_{j=1}^{K} T^{(j)}$ is the whole set of ordered acquisition times. Let us also assume that the K sets of data are geocoded over a common grid of points, and $\left\{ d_{az}^{(1)}, d_{az}^{(1)}, ..., d_{az}^{(K)} \right\}$ are the K vectors of the azimuthal displacement time-series obtained by applying the MAI approaches described in the previous sections.

By applying simple geometric considerations (see Figure 77 B), we can straightforwardly derive that:

$$d_{az} = d \cdot \hat{i}_{az} = \cos(\chi) \cdot d_{N-S} - \sin(\chi) \cdot d_{E-W} \tag{5.35}$$

where χ is the inclination angle of the orbit with respect to the N-S direction, which is approximately equal to 6° for the Sentinel-1 case. For each coherent point that is well processed in all of the K independent processing stages, a system of linear equations can be built. In particular, if we consider the velocity deformations as unknowns across contiguous time acquisitions for the east–west and north–south directions, the following system of equations can be written:

$$B \cdot \begin{bmatrix} V_{North-South} \\ V_{East-West} \end{bmatrix} = \begin{bmatrix} d_{az}^{(1)} \\ d_{az}^{(2)} \\ \vdots \\ d_{az}^{(K)} \end{bmatrix} \tag{5.36}$$

Where $V_{North-South}$ and $V_{East-West}$ are the vectors of the azimuthal projected deformation time-series from the K different, complementary viewing geometries. The matrix B, similar to the case accounted for in Section 5.5.1, takes into account the temporal relationships of combined displacement time-series and, in this case (see the imaging geometry of Figure 77 B), is expressed as follows:

$$B = \begin{bmatrix} B^{(1)}\cos(\chi)^{(1)} & -B^{(1)}\sin(\chi)^{(1)} \\ \vdots & \vdots \\ B^{(1)}\cos(\chi)^{(K)} & -B^{(K)}\sin(\chi)^{(K)} \end{bmatrix} \tag{5.37}$$

Similar to what has already been discussed for the combination of LOS measurements [258], the system of Equation (5.36) is regularized as

$$\begin{bmatrix} B \\ C \end{bmatrix} \cdot \begin{bmatrix} V_{North-South} \\ V_{East-West} \end{bmatrix} = \begin{bmatrix} d_{az}^{(1)} \\ d_{az}^{(2)} \\ \vdots \\ d_{az}^{(K)} \\ 0 \end{bmatrix} \tag{5.38}$$

The estimated velocity vector for the north–south components are time-integrated and the N-S ground displacement is computed. Because the projection along the azimuth direction has a very limited accuracy with respect to w.r.t. to the E-W direction, the computed E-W ground displacement time-series (which may be obtained by combining the MAI measurements) definitely has a worse accuracy with respect to w.r.t. obtained using the LOS-projected displacement measurements. The error budget of the N-S displacement time-series can be derived by extending the analysis provided in [261]. The comprehensive theoretical and quantitative analysis of the error budget for the retrieved 3-D ground displacement time-series would require the processing of several independent SAR datasets, as well as a comparison with external ground deformation measurements. This is clearly outside the scope of the current investigation but remains a matter for future analysis. Figure 80 shows the results of this novel combination method applied to the sets of ascending/descending SAR data relevant to the area of the Ridgecrest earthquake in California. As a result, we have obtained a map of the north–south mean deformation rate of the area. Finally, we selected two points across the fault, labeled (I) and (II) in Figure 79 A, B, Figure 80, and Figure 81 shows the plots of the up–down, east–west and north–south displacement time-series.

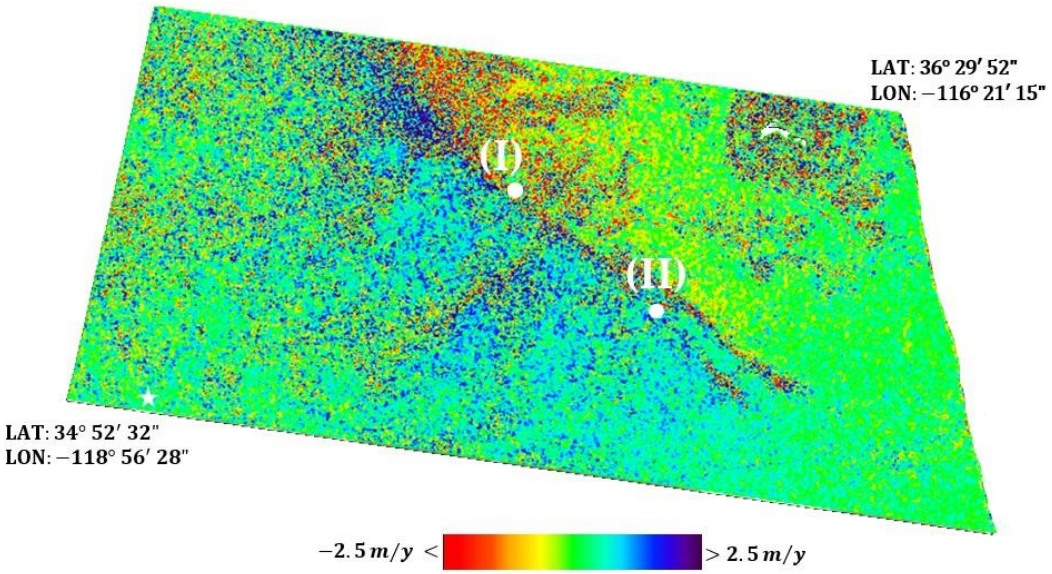

Figure 80. Geocoded mean displacement maps along the north–south direction of the Ridgecrest area, superimposed on an amplitude image. The labels (I) and (II) in white indicate two points across the fault where the north–south displacement time-series is estimated. All displacement measurements are evaluated with respect to a pixel, which is identified by a white star.

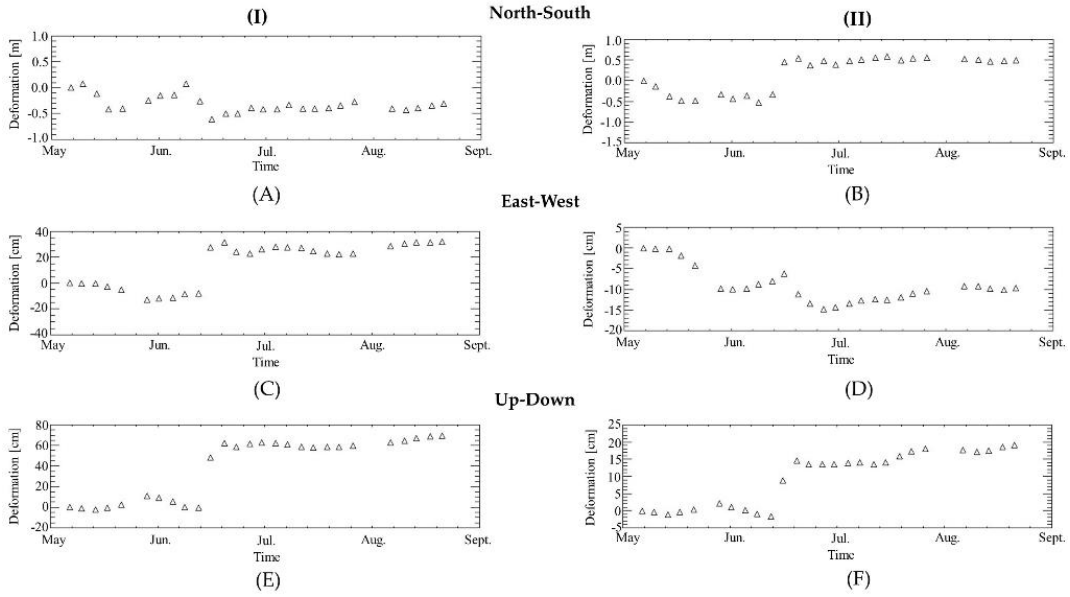

Figure 81. North–south, east–west and up–down displacement time-series related to cross-fault points (I) and (II) indicated in Figures Figure 79 and Figure 81.

Additional remarks on the achieved results are now in order. Concerning the Ridgecrest case-study area, the fringe rate in the near proximity of the fault line that

was activated by the July 2019 Mw 7.1 earthquake was very high, as is evident from Figure 73 A. This led to loss of coherence and unavoidable phase unwrapping errors. The application of conventional InSAR methods, properly complemented with processing strategies to combine multiple-orbit information, was effective for retrieving the up–down and the east–west ground deformation components. The results shown in Figure 79 prove that most of the deformations were horizontal, with a maximum rate of about 250 cm/year corresponding to an abrupt lateral terrain displacement of about 1 meter. The application of the MAI approach to both ascending and descending Sentinel-1 data tracks also allowed us to obtain an estimate of the north–south displacements according to the generation of relevant deformation time-series (see Figure 80). As shown in Figure 72, we also used one single pair of COSMO-SkyMed SAR images to produce a map of the north–south displacement across the fault line. It should be noted that the magnitude of the retrieved relative N-S deformation across the main seismic event of July 2019 was in general agreement with the deformation time-series of N-S components shown in Figure 80 (with northward and southward deformations of up to 1 meter across the fault). Of course, the accuracy of COSMO-SkyMed and Sentinel-1 MAI-driven measurements were not comparable (see plots shown in Figure 84 in APPENDIX B: Multiple Aperture Interferometry Accuracy and Noise Propagation B), as the expected accuracy of MAI measurements with Sentinel-1 data is in the order of 2 cm, with an average coherence value of 0.8. Finally, we would like to remark that most of the experiments were carried out using Sentinel-1 data. The aim was to enhance the strength of spectral diversity approaches for the TOPS mode Sentinel-1 data co-registration, as well as to investigate the potential of the MAI technique applied to TOPS mode SAR data.

5.7 CONCLUSIONS

In this Chapter a review of the existing methods used to study large deformation episodes was carried out based on the application of spectral diversity methods for the generation of combined 3-D ground displacement time-series and mean deformation velocity maps. Specifically, I have focused on the description of spectral diversity/multiple aperture interferometry methods, and provided a general overview of the theoretical basis of these techniques, addressing their limits and applications, with a particular eye to the use of these technologies for the processing of data coming from new-generation SAR satellites. Furthermore, a novel method combining MAI- and DInSAR-driven data of large deformations was presented,

and the relevant results discussed. A quantitative assessment of the presented 3-D methods requires the processing of several datasets. This is a matter for future investigations.

APPENDIX A: SPECTRAL DIVERSITY

Spectral diversity (SD) techniques [234], [264] represent a class of methods based on the calculations of the spectral properties of pairs of complex-valued SAR images. The basic method consists of calculating the spectral separation of sub-bands of SAR images obtained by cutting two different frequency slices along the azimuth (Doppler band) of range directions, or by splitting the azimuth (range) spectrum of a full-band SAR image using a proper band-pass filter. Let me describe the SD process by initially referring to the azimuth case, where I assume the availability of two full-band Single Look Complex (SLC) images, referred to as the master and slave images $I_M(x,r)$ and $I_S(x,r)$, respectively. If the two SLC images are focused (squinted geometry) with the same Doppler centroid (DC) frequency—namely, f_{DC}—the two SAR images can be expressed after the co-registration step [265] as:

$$I_M(x,r) = \gamma_M(x,r) \cdot e^{j\frac{4\pi}{c} f_c r} e^{j2\pi \frac{f_{DC}}{v} f_c x} \tag{A.1}$$

$$I_S(x,r) = \gamma_S(x,r) \cdot e^{j\frac{4\pi}{c} f_c (r+\delta r)} e^{j2\pi \frac{f_{DC}}{v} f_c (x+\delta x)} \tag{A.2}$$

where f_c is the radar carrier frequency, v is the platform velocity and δ_x represents the azimuthal misregistration of the slave image with respect to the reference master image. Accordingly, an additional interferometric phase term is present. Indeed,

$$\Delta\phi = \frac{4\pi}{\lambda} d_{LOS} + 2\pi \frac{f_{DC}}{v} \delta x \tag{A.3}$$

Consequently, if two azimuth sub-bands are centered on low and high DC frequencies f_{DC}^{-} and f_{DC}^{+}, respectively (see Figure 82), four SAR images can be formed:

$$I_M^-(x,r) = \gamma_M(x,r) \cdot e^{j\frac{4\pi}{c} f_c r} e^{j2\pi \frac{f_{DC}^-}{v} f_c x} \tag{A.4}$$

$$I_S^-(x,r) = \gamma_S(x,r) \cdot e^{j\frac{4\pi}{c} f_c (r+\delta r)} e^{j2\pi \frac{f_{DC}^-}{v} f_c (x+\delta x)} \tag{A.5}$$

$$I_M^+(x,r) = \gamma_M(x,r) \cdot e^{j\frac{4\pi}{c} f_c r} e^{j2\pi \frac{f_{DC}^+}{v} f_c x} \tag{A.6}$$

$$I_S^+(x,r) = \gamma_S(x,r) \cdot e^{j\frac{4\pi}{c} f_c (r+\delta r)} e^{j2\pi \frac{f_{DC}^+}{v} f_c (x+\delta x)} \tag{A.7}$$

This means that, for each image of the SAR data pair, two images are determined that are related to the low and high components of SAR data pair spectra. Subsequently, from these two data pairs, two interferograms are generated. After the split-spectrum operation, the interferometric phase terms related to the lower and higher azimuthal sub-bands are expressed as follows:

$$\Delta\phi^- = \frac{4\pi}{\lambda} d_{LOS} + 2\pi \frac{f_{DC}^-}{v} \delta x \tag{A.8}$$

$$\Delta\phi^+ = \frac{4\pi}{\lambda} d_{LOS} + 2\pi \frac{f_{DC}^+}{v} \delta x \tag{A.9}$$

Therefore, the wrapped phase difference between the lower and higher spectral bands is

$$\Delta\tilde{\phi} = Wr(\Delta\phi^- - \Delta\phi^+) = 2\pi \frac{f_{DC}^- - f_{DC}^+}{v} \delta x \tag{A.10}$$

where $Wr(\cdot)$ is the wrapping operator that wraps out the phase in the $[-\pi, \pi[$ interval. As a consequence, the azimuth misalignment δx can be computed from Equation (A.10). Assuming that such a misalignment is small enough to avoid the measured phase becoming ambiguous, the term δ_x can easily be derived as:

$$\delta x = \frac{v\Delta\tilde{\phi}}{2\pi\left(f_{DC}^{-} - f_{DC}^{+}\right)} \tag{A.11}$$

From Equation (A.11), it is evident that the larger the spectral separation between the central frequencies of the two sub-bands, the more accurate the estimation of δx is. I would like to stress that in non-stationary scenarios, the imaged target at azimuth location *x* is subject to displacement, namely, δx_{disp} and, in this case, the measured δx term contains both a contribution due to the azimuthal misregistration δx_{misr} and the azimuthal δx_{disp} displacement. Of course, misalignments of SAR data pairs can be thoroughly controlled in the imaging process to mitigate phase decorrelation effects. Perfectly aligned SAR data are then used to infer geophysical displacement measurements, as they have been via the multiple aperture SAR interferometry (MAI) technique in cases of large ruptures in the ground [227], [235].

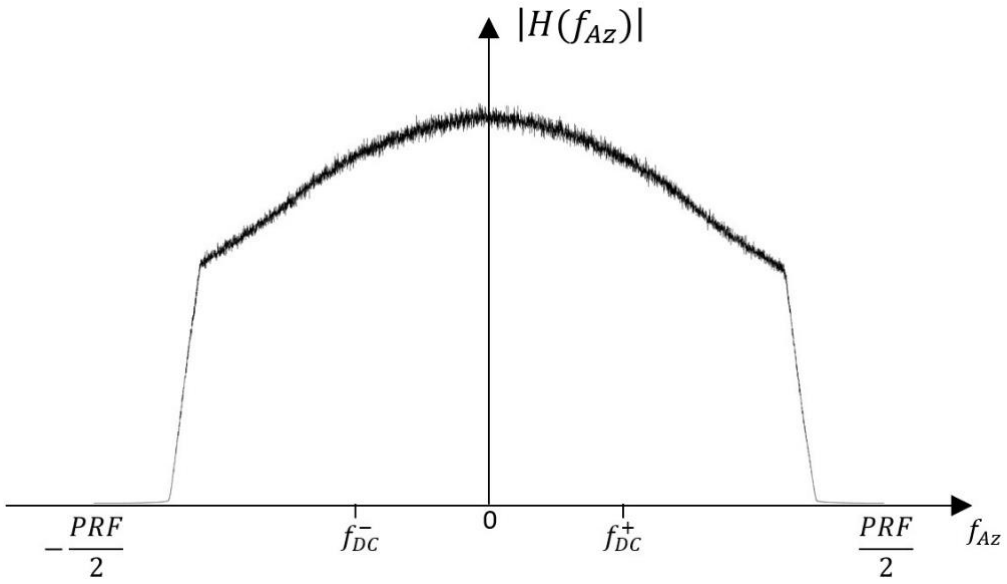

Figure 82. Sketch of the amplitude azimuth spectrum ($H(f_{Az})$) of a full-band SAR image, where f_{DC}^{-} and f_{DC}^{+} indicate the low and the high Doppler centroid (DC) frequencies, respectively, and PRF indicates the sensor's pulse repetition frequency.

I would like to remark that SD and splitting-band methods can also be applied along the range direction by extracting the two sub-bands in the range. In particular, we begin with two range sub-bands centered on the two frequencies f_c^- and f_c^+ (see Figure 83), which can be expressed, similarly to Equations (A.4)-(A.7), as:

$$I_M^-(x,r) = \gamma_M(x,r) \cdot e^{j\frac{4\pi}{c} f_c^- r} e^{j2\pi \frac{f_{DC}}{v} x} \tag{A.12}$$

$$I_S^-(x,r) = \gamma_S(x,r) \cdot e^{j\frac{4\pi}{c} f_c^- (r+\delta r)} e^{j2\pi \frac{f_{DC}}{v} (x+\delta x)} \tag{A.13}$$

$$I_M^+(x,r) = \gamma_M(x,r) \cdot e^{j\frac{4\pi}{c} f_c^+ r} e^{j2\pi \frac{f_{DC}}{v} x} \tag{A.14}$$

$$I_S^+(x,r) = \gamma_S(x,r) \cdot e^{j\frac{4\pi}{c} f_c^+ (r+\delta r)} e^{j2\pi \frac{f_{DC}}{v} (x+\delta x)} \tag{A.15}$$

In this case,

$$\Delta\phi^{-} = \frac{4\pi}{c} f_c^- \cdot d_{LOS} + 2\pi \frac{f_{DC}}{v} \delta x + \Delta\phi_n^- \tag{A.16}$$

$$\Delta\phi^{+} = \frac{4\pi}{c} f_c^+ \cdot d_{LOS} + 2\pi \frac{f_{DC}}{v} \delta x + \Delta\phi_n^+ \tag{A.17}$$

where $\Delta\phi_n^-$ and $\Delta\phi_n^+$ are the negative and positive sub-band phase noise contributions, respectively. Accordingly, the wrapped phase difference of the higher- and lower-band phase terms gets an alternative estimate of the LOS displacement as:

$$d_{LOS} = \frac{c\Delta\tilde{\phi}}{4\pi(f_c^- - f_c^+)} \tag{A.18}$$

where, similarly to Equation (A.11), $\Delta\tilde{\phi}$ represents the wrapped phase difference $Wr(\Delta\phi^- - \Delta\phi^+)$ between the two phase looks (see Equations (A.16) and (A.17)). Note that d_{LOS} is assumed to be small enough to avoid phase measurement

ambiguities. In this framework, a procedure that is known as spectral shift filtering [266] implements proper filters that are tuned on specifically chosen different central frequencies to compensate for the geometrical decorrelation effects that corrupt the interferometric phase. This strategy has been applied correctly to process coupled SAR images collected by the ERS and the Envisat systems, which were characterized by a spectral shift of 31 MHz [267], [268].

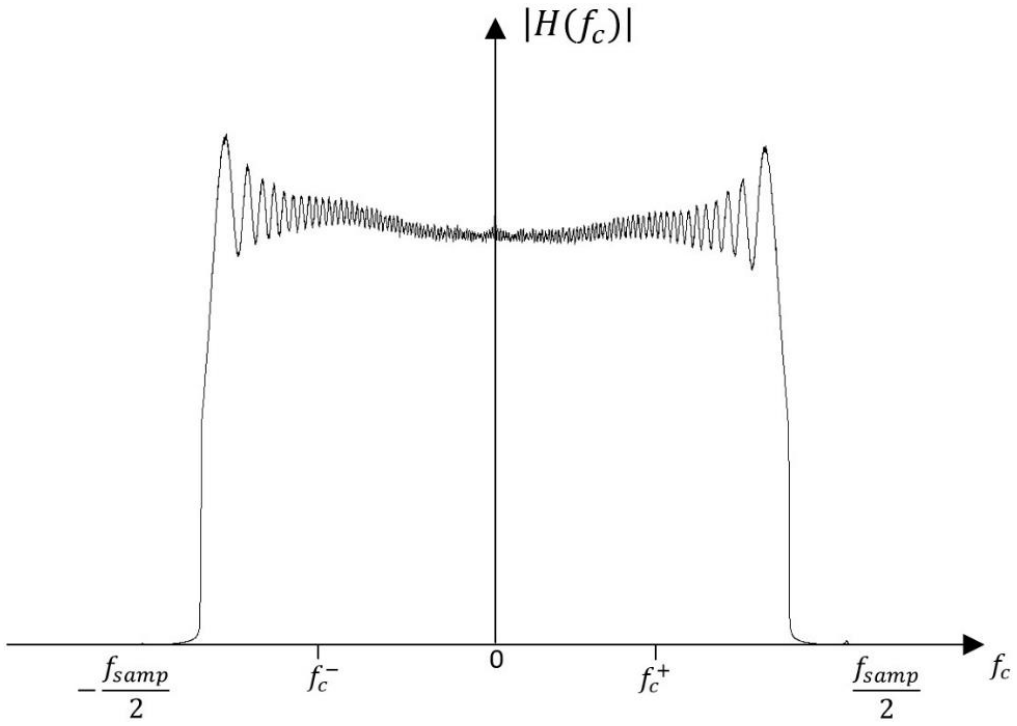

Figure 83. Sketch of the amplitude range spectrum ($H(f_c)$) of a full-band SAR image, where f_c^- and f_c^+ indicate the low and the high range frequencies, respectively, and f_{samp} is the sampling frequency.

As final remark, I would like to stress that only a fraction β of the total bandwidth of the two images is used after the application of the split-spectrum operation. Accordingly, being the spatial resolution inversely proportional to the band of the signal [202], the spatial resolution of the two sub-band interferograms is reduced by the same fraction.

APPENDIX B: MULTIPLE APERTURE INTERFEROMETRY ACCURACY AND NOISE PROPAGATION

Based on Equation (5.13), the accuracy of the MAI technique can be theoretically estimated by the following Equation (B.1) that relates the standard deviation of the MAI phase measurement $\sigma_{\varphi_{MAI}}$, with the standard deviation of the along-track deformation measurements σ_x [235]:

$$\sigma_x = \frac{l}{4\pi \cdot n}\sigma_{\varphi_{MAI}} \tag{B.1}$$

From Equation (B.1), it is clear that the MAI measurement accuracy strictly depends on the standard deviation of the interferometric phase noise [264], which is given by

$$\sigma_{\varphi_{MAI}} = \sqrt{\sigma_{fw}^2 + \sigma_{bw}^2 - 2\sigma_{fw,bw}^2} \tag{B.2}$$

where σ_{fw}^2, σ_{bw}^2, and $2\sigma_{fw,bw}^2$ are the variances of forward- and backward-looking interferograms and their co-variance, respectively. Thus, based on the assumption that the probability density function (pdf) of the single/multi-look interferometric phases can be expressed as a function of the correlation coefficient γ [269], and assuming the forward- and backward-looking interferograms are two statistically independent random variables (e.g., $\sigma_{fw,bw}$ is zero) in the limit of Cramér–Rao [264] (which is valid for high values of γ), σ_{fw} and σ_{bw} can be inferred as follows:

$$\sigma_{fw} = \sigma_{bw} \approx \frac{1}{\sqrt{2NL}} \cdot \frac{\sqrt{1-\gamma^2}}{\gamma} \tag{B.3}$$

where *NL* is the effective number of looks. Finally, using Equations (B.2) and (B.3), the standard deviation of the interferometric MAI phase is reduced to

$$\sigma_{\varphi_{MAI}} \approx \frac{1}{\sqrt{NL}} \cdot \frac{\sqrt{1-\gamma^2}}{\gamma} \tag{B.4}$$

where I assume that the forward- and backward-looking interferograms are uncorrelated. From Equations (B.1) and (B.4), it is obvious that improving the coherence of the MAI interferogram and having a larger spectral separation between the sub-band both lead to better accuracy in the estimation of along-track deformation measurements. In the Cramér–Rao bound, it was demonstrated in [264] and [270] that the optimal separation between the sub-bands is equal to two-thirds of the full bandwidth, and that:

$$\sigma_{\varphi_{MAI,CR}} \approx \sqrt{\frac{3}{NL}} \cdot \frac{\sqrt{1-\gamma^2}}{\gamma} \tag{B.5}$$

By considering Equation (B.5), we can plot the standard deviation of the azimuthal displacement vs the spatial coherence of the MAI interferogram (see Figure 84 A, and B) for different values of the effective look numbers (*NL*), which comprise the operational parameters of the Envisat/ASAR, COSMO-SkyMed and Sentinel-1 platforms listed in Tables Table 21–Table 23, respectively. In particular, as outlined in Section 5.4.2, the Doppler bandwidth of the TOPS-mode SAR data is reduced for a single point target with respect to the conventional stripmap case by a factor of about three (see Equation (5.13)).

Table 21. Envisat/ASAR stripmap mode acquisition platform parameters.

PARAMETER	VALUE	UNIT
Wavelength (Centre Frequency)	0,05624624	m
Band type	C	
Pulse repetition frequency	1.652,4157	Hz
Polarisation options	Single VV, HH or Dual VV+HH, VV+VH, HH+HV	

Azimuth antenna size	11.1	m
Incidence angle range	15° - 45°	deg.
Swath width	100	km
Resolution	6(az)x9(rg)	m
Azimuth pixel spacing	4,31	m
Range pixel spacing	7,8	m

Table 22. COSMO-SkyMed stripmap (ping-pong) mode acquisition platform parameters.

PARAMETER	**VALUE**	**UNIT**
Wavelength (Centre Frequency)	0,031228381	m
Band type	X	
Pulse repetition frequency	3.554,5024	Hz
Polarisation options	Single VV, HH or Dual VV+HH, VV+VH, HH+HV	
Azimuth antenna size	5,6	m
Incidence angle range	25° - 50°	deg.

Swath width	30km	km
Resolution	15(az)x15(rg)	m
Azimuth pixel spacing	2,53	m
Range pixel spacing	1,56	m

Table 23. Sentinel-1 operational parameters in interferometric wide (IW) acquisition mode.

PARAMETER	VALUE	UNIT
Wavelength (Centre Frequency)	0,055465763	m
Band type	C	
Pulse repetition frequency	486,4863	Hz
Polarisation options	Dual HH+VV, VV+HH or Single HH,VV	
Azimuth antenna size	12.3	m
Incidence angle range	29.1° - 46.0°	deg.
Azimuth steering angle	±0.6°	deg.
Swath width	250	km
Number of sub-swaths	3	
Resolution	5(rg)x20(az)	m
Azimuth pixel spacing	14,1	m
Range pixel spacing	2,3	m

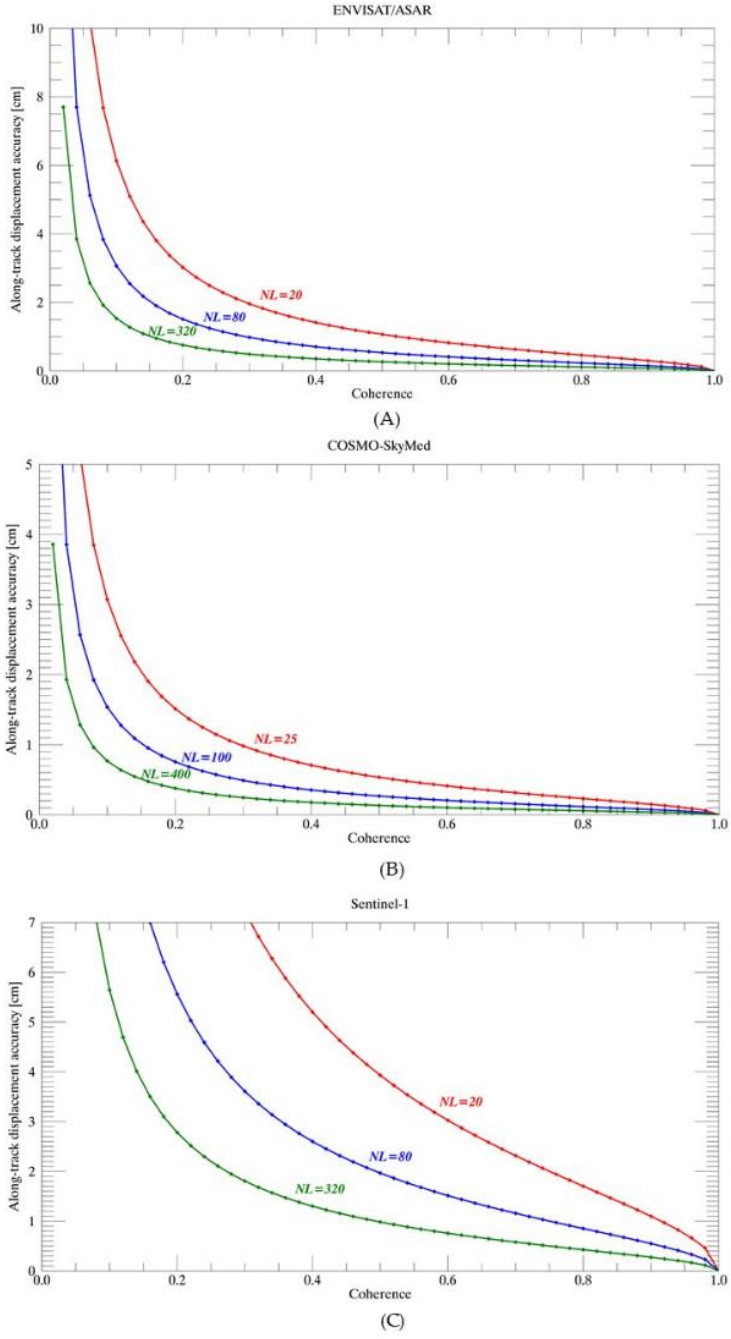

Figure 84. Plot of the along-track displacement accuracies vs coherence for the Envisat/ASAR (A), COSMO-SkyMed (B) and Sentinel-1 case using the MAI technique for different NLs (effective look numbers).

Interested readers can find a more comprehensive analysis by Jung et al. in [271].

Chapter 6

CHANGE DETECTION OF EARTH'S SURFACE

Nowadays, the growing availability of remotely sensed data collected by several constellations of SAR sensors (e.g., the twin Sentinel-1A/B sensors of the European (EU) Copernicus) permits fast mapping of damages. As introduced in Chapter 5 SAR instruments guarantee effective RS applications (e.g., analysis of displacement of earth surface) because they operate day/night and in any weather condition, thus complementing optical data (e.g., Sentinel-2).

In this chapter, I will refer to a case study [6] that investigates the capability of different coherent/incoherent change detection indices (CDIs) and their mutual interactions for the rapid mapping of "changed" areas is presented. In this context, I will address the role of SAR (amplitude) backscattered signal variations for change detection (CD) analyses when a natural (e.g., a fire, a flash flood, etc.) or a human-induced (disastrous) event occurred.

Then, I also consider the additional pieces of information that can be recovered by comparing interferometric coherence maps related to couples of SAR images over a principal disastrous event date. In this context, a CD algorithm based on AI that handles the different information coming from coherent/incoherent CDIs in a unique corpus is presented and discussed. Experiments have principally been conducted to monitor wildfire's effects in the 2021 summer season in Italy, considering two case studies in Sardinia and Sicily. Another experiment was also performed in the coastal city of Houston, Texas, U.S., which was affected by a large flood in 2017, thus demonstrating the validity of the proposed integrated method for the fast-mapping flooded areas with SAR data.

6.1 COHERENT AND INCOHERENT CHANGE DETECTION METHODS FUNDAMENTALS

This Section introduces the fundamentals of SAR change detection (CD), distinguishing between incoherent and coherent approaches. Let us consider two co-registered complex-valued SAR images X_1 and X_2 acquired at times t_1 and t_2, respectively, and $X_k = \left[X_1(P), X_2(P)\right]^T$ let be the pixel pair data vector made by the extracted SAR data values that correspond to a generic *k-th* pixel *P* of the imaged scene. The CD problem may be generally modeled as a binary classification problem [272] where each pixel is mapped into the set of possible labels $\Omega = \{\omega_u, \omega_c\}$ related to the unchanged and changed classes, respectively. Such a problem can be effectively formulated in a hypothesis-testing framework. In this context, the problem is to determine whether the pixel pair is a realization of a null hypothesis H_0 (unchanged scene) or an alternative hypothesis H_1 (changed scene). Under these two hypotheses, we can write that [272]:

$$\begin{aligned} &H_0 \\ &\begin{cases} X_1(P) = X_{1k} = C_{0k} + n_{1k} \\ X_2(P) = X_{2k} = C_{0k} \exp\left[j\varphi_k\right] + n_{2k} \end{cases} \end{aligned} \tag{6.1}$$

and:

$$\begin{aligned} &H_1 \\ &\begin{cases} X_1(P) = X_{1k} = C_{0k} + n_{1k} \\ X_2(P) = X_{2k} = C_{1k} + n_{2k} \end{cases} \end{aligned} \tag{6.2}$$

where the term C_{0k} is the complex reflectivity at the given pixel *P* that is common to both SAR images under the H_0 hypothesis and C_{1k} is the complex reflectivity of the second image under the assumption that a change happened. Note that the phase term φ_k accounts for a possible displacement of the second flight track with respect to the first image related to height topography changes. Finally, the terms n_{1k} and n_{2k} account for noise decorrelation sources affecting the two available SAR images. For homogeneous natural distributed target environments,

the observed SAR scenes can be modeled as consisting of a large number of discrete scatterers that have a uniform random phase and identically distributed random amplitudes [273]. The observed complex radar backscattered signal can then be modeled as a zero-mean complex circular Gaussian process with a probability density function [274]:

$$p\left(X_k\right)=\frac{1}{\pi^2 \det\left(\mathbf{Q}\right)^2}\exp\left(-X_k^H\mathbf{Q}^{-1}X_k\right) \tag{6.3}$$

where $\mathbf{Q}$ is the covariance matrix of X_k that, under the two hypotheses, is given by:

$$\mathbf{Q}_0=\begin{bmatrix}\sigma_c^2+\sigma_{n1}^2 & \sigma_c^2\exp\left(j\varphi_k\right)\\ \sigma_c^2\exp\left(-j\varphi_k\right) & \sigma_c^2+\sigma_{n2}^2\end{bmatrix} \tag{6.4}$$

$$\mathbf{Q}_1=\begin{bmatrix}\sigma_c^2+\sigma_{n1}^2 & 0\\ 0 & \sigma_c^2+\sigma_{n2}^2\end{bmatrix} \tag{6.5}$$

where $\sigma_c^2=E\left\{\left|C_{ok}\right|^2\right\}=E\left\{\left|C_{1k}\right|^2\right\}$, $\sigma_{n1}^2=E\left\{\left|n_{1k}\right|^2\right\}$ and $\sigma_{n2}^2=E\left\{\left|n_{2k}\right|^2\right\}$.

Note that $E\left[\cdot\right]$ stands for the statistical expectation extraction operation that, under the hypothesis that the signals are ergodic, can effectively be implemented with the spatial averaging procedure $\left\langle\cdot\right\rangle_N$ performed over a set of neighbour SAR pixels (i.e., with a multi-looking process [275]). The term σ_c can also be expressed as a function of the complex correlation coefficient γ between the two interfering SAR images [276], as follows:

$$\gamma=\hat{\gamma}\exp\left[j\varphi_k\right]=\frac{\sigma_c^2}{\sqrt{\sigma_c^2+\sigma_{n1}^2}\sqrt{\sigma_c^2+\sigma_{n2}^2}}=\frac{E\left[X_1X_2^*\right]}{\sqrt{E\left[\left|X_1\right|^2\right]}\sqrt{E\left[\left|X_2\right|^2\right]}} \tag{6.6}$$

The amplitude of the complex correlation coefficient is commonly referred to as coherence, and it assumes values from 0 and 1. Coherence is usually factorized into the products of several different contributions [209], [257], [276]:

$$\hat{\gamma} = \hat{\gamma}_{geo} \cdot \hat{\gamma}_{Dopp} \cdot \hat{\gamma}_{mis-reg} \cdot \hat{\gamma}_{vol} \cdot \hat{\gamma}_{temp} \cdot \hat{\gamma}_{thermal} \tag{6.7}$$

A few additional observations on the decorrelation sources are now in order.

(i) The spatial coherence decorrelation $\hat{\gamma}_{geo}$ originates from the fact the scatterers in the single resolution element on the ground are seen from the two orbital positions relevant to the two interfering SAR images with slightly different illumination angles. It has been proved that such decorrelation component depends on the interferometric perpendicular baseline $b_{\perp}$ and the operational wavelength λ, as follows:

$$\hat{\gamma}_{geo} = 1 - \frac{2b_{\perp}}{\lambda} \frac{\Delta r}{r \tan(\vartheta - \Omega)} \tag{6.8}$$

where r and Δr are the sensor-to-target slant-range distance and the image range resolution, respectively, whereas ϑ and Ω are the local incidence and local terrain slope angles.

(ii) The decorrelation term due to Doppler frequency variation $\hat{\gamma}_{Dopp}$ considers the non-perfect overlap between the master and slave Doppler azimuth spectra and can be expressed as:

$$\hat{\gamma}_{Dopp} = 1 - \frac{\Delta f}{4\pi} \cdot \frac{L}{v} \tag{6.9}$$

where Δf is the azimuth spectra misalignment [Hz], is the azimuth antenna length L and is the sensor velocity v.

(iii) Mis-registration decorrelation $\hat{\gamma}_{mis-reg}$ arises when a non-perfect co-registration of the two SAR images is carried out.

(iv) Volumetric decorrelation $\hat{\gamma}_v$ arises from the scattering of the radar microwaves within a volume as it happens, for instance, for forest canopies. In the random-volume-over ground RVoG model [92], the volumetric decorrelation is correlated to the forest height, the extinction coefficient, the ground-to-volume ratio, and the vertical wavenumber, which is a function of the scatterers' density in a volume.

(v) The temporal decorrelation $\hat{\gamma}_{temp}$ is associated with changes in dielectric and structural properties of the scatterers over time. is related to the alteration of the position and dielectric changes of the scatterers, typically caused by wind, rain, snow, or other natural events. This contribution is significant when interferometric analyses with long-temporal baseline interferograms are carried out. In Section 6.2, a temporal decorrelation model derived from the literature [278] is described to discuss the benefits and cons of some synthetic coherent change detection indices that are subsequently used to achieve the experimental results shown in Section 6.6.

(vi) Finally, the thermal noise decorrelation due to the radar instruments noise is given by:

$$\hat{\gamma}_{thermal} = \frac{1}{1+SNR^{-1}} \tag{6.10}$$

where SNR is the signal-to-noise ratio (*SNR*) of the scatterers illuminated by the radar sensor. Assuming perfect knowledge of the unknown parameters that are present in the covariance matrices in Equations (6.4) and (6.5), a formalized way to solve a CD problem is to compute the log-likelihood ratio:

$$Z = \ln(L) = \ln\left[\prod_{k=1}^{N} \frac{p(X_k \mid H_0)}{p(X_k \mid H_1)}\right] \tag{6.11}$$

considering a population made by N SAR pixels located in the neighbouring of the selected SAR pixel. After some mathematical manipulations and considering the pdf of Equation (6.3), the decision variable Z can then be re-written as:

$$Z = Tr\left\{\left[\mathbf{Q}_0^{-1} - \mathbf{Q}_1^{-1}\right]\sum_{k=1}^{N} X_k X_k^*\right\} \tag{6.12}$$

which is referred to in the literature as the clairvoyant detector. Note that the operator $Tr(\cdot)$ is the trace of a matrix. This detector gives the optimal detection performance given the perfect knowledge of the unknown parameters in the covariance matrices $\mathbf{Q}_0$ and $\mathbf{Q}_1$. The expressions for the probability of detection and false alarm for the log-likelihood clairvoyant detector as a function of a decision threshold have been derived in [276]. Nonetheless, the covariance values are generally unknown, and thus, in practice, sub-optimal tests are implemented where the unknown parameters are measured directly through the data with their maximum likelihood estimates (MLEs) to form a generalized likelihood test (e.g., see [279]). Due to the complexity of these optimal tests and the need to estimate the mentioned model parameters, several approximate unsupervised/supervised CD approaches have been proposed in the literature (among others, see [280]–[287]). Overall, they can be distinguished in the two general categories of the methods based exclusively on the analysis of the amplitude of SAR backscattered returns (incoherent approaches) and those that also consider the phase of the radar backscattered signals (coherent strategies). Finally, the next subsections provide additional details on these two categories of CD methods.

6.1.1 INCOHERENT CD APPROACHES

Despite their intrinsic differences, the incoherent methods can be seen as made by three main steps: 1) pre-processing of the SAR images; 2) comparison of the pair of SAR images; 3) automatic extraction of the changed areas by proper thresholding algorithms. The first step consists of the radiometric calibration of the available SAR images [273], [288] and the subsequent application of adaptive filters that reduce the impact of speckle noise in the SAR images. Among others, the most used denoised filters are Lee [289], Kuan [290], and Frost [291]. Jointly, a spatial multi-look operation [292] is typically applied to enhance the signal-to-ratio (SNR) further to reduce the spatial resolution. The effects of local topography can also be corrected [293], and the SAR images could then potentially be georeferenced for subsequent analyses. The second step consists in comparing the two pre-processed SAR images. To this aim, we observe that signature variations in SAR images are due to texture and speckle, where texture is a measure of the intrinsic spatial variability of the backscattered coefficient (in the absence of noise), and the speckle is a multiplicative term. Mathematically, the received power can be written as [273], [294]:

$$P = \left[T\left\langle I\right\rangle + \left\langle n\right\rangle\right]s \tag{6.13}$$

where I is the backscattered power, T and s are the texture and speckle noise random terms, respectively. As anticipated, when dealing with SAR images, the ratio operator $r = \frac{\langle X_2 \rangle}{\langle X_1 \rangle}$ is preferred with respect to the image difference. Indeed, the pdf of the ratio image has the following expression [295]:

$$p\left(r \mid \overline{r}\right) = \frac{(2N-1)!}{(N-1)!^2} \frac{\overline{r}^N r^{N-1}}{\left(r+\overline{r}\right)^{2N}} \tag{6.14}$$

where $\overline{r}$ is the true (unknown) value of the ratio. Accordingly, the first-order statistics depend only on the relative change and not on the single average values separately. Moreover, the mean amplitude values ratio is more robust to calibration errors, typically represented by multiplicative terms that moderately vary from one image to another and then almost cancel out in the ratio. Furthermore, the ratio is reported on a log scale to represent significantly high and shallow intensity values. Accordingly, the detection image is obtained as:

$$LR = \ln\left(\frac{\langle X_2 \rangle}{\langle X_1 \rangle}\right) = \ln\left(\langle X_2 \rangle\right) - \ln\left(\langle X_1 \rangle\right) \tag{6.15}$$

The third step consists of analysing the log-ratio image and identifying a proper threshold that allows us to discriminate between the two changed and unchanged classes. This problem can be solved in the context of Bayesian decisions. A general algorithm for the threshold decision was proposed by Kittler and Illingworth (KI), which derives the best threshold from being used through a parametric estimation based on the assumption that the two classes are Gaussian distributed [296]. Some extensions of the KI method that assume a more reliable distribution of the two classes (e.g., a generalized Gaussian distribution) have been proposed [297].

6.1.2 Coherent CD Approaches

Coherent change detection methods rely on the interferometric cross-correlation factor (see Equation (6.6)). The statistics of the sample coherence have extensively been addressed in the literature [209], [298]. In particular, the density

function of the sample coherence $\hat{\gamma}$, given the true coherence value $\hat{\gamma}'$, is given by:

$$p(\hat{\gamma}\,|\,\hat{\gamma}') = 2(N-1)\left(1-\hat{\gamma}'^2\right)^N \hat{\gamma}\left(1-\hat{\gamma}'^2\right)^{N-2} {}_2F_1\left(N;N;1;\hat{\gamma}^2\hat{\gamma}'^2\right) \tag{6.16}$$

where N is the effective number of looks (ENL) and ${}_2F_1(\cdot)$ is the Gauss hypergeometric function. It is worth underlying that the coherence is a biased estimator: this means the measured sample coherence $\hat{\gamma}$ obtained by computing the expectation values in Equation (6.6) using spatial averaging operations has an average value different from the actual coherence value $\hat{\gamma}'$. In particular, the first moment of the spatial coherence is given by:

$$E[\hat{\gamma}] = \frac{\Gamma(N)\Gamma(3/2)}{\Gamma(N+1/2)} {}_3F_2\left(3/2, N, N; N+1; \hat{\gamma}'^2\right)\left(1-\hat{\gamma}'^2\right)^N \tag{6.17}$$

and, consequently, the coherence bias is $E[\hat{\gamma}]-\hat{\gamma}'>0$. An approximate expression for the coherence bias, which could be considered to calibrate the coherence estimates or CD purposes properly, can more straightforwardly be obtained in the complex domain by observing that the interferometric phase can be encoded in this domain as a point in a unitary circle. The mean resultant length $\hat{\chi}$ of the circular data representing the interferometric phases into the N-points averaging multi-look window is obtained as:

$$\hat{\chi} = \frac{\left|\sum_{k=1}^{N} e^{j\varphi_k}\right|}{N} \tag{6.18}$$

As demonstrated in [299], [300], the computed mean resultant length $\hat{\chi}$ is an alternative measure of the coherence with $\hat{\chi} \le \hat{\gamma}$, and the two coherence factors, both biased, are related to one another as:

$$\hat{\chi} = \frac{\pi}{4}\hat{\gamma} \cdot F\left(\frac{1}{2}, \frac{1}{2}; 2; \hat{\gamma}^2\right) \tag{6.19}$$

The mean value of the mean resultant length of a circular data vector, under the suitable assumption that it is distributed assumed with a Von-Mises probability density function [300] of concentration parameter κ, can be calculated as follows [301]:

$$E[\hat{\chi}] = A(\kappa) + \frac{1}{2N\kappa} + O\left(N^{-\frac{3}{2}}\right) \tag{6.20}$$

where $\hat{\chi} = A(\kappa) \cong 1 + \frac{1}{2\kappa} \to \kappa \cong \frac{1}{2(1-\hat{\chi})}$ and $O(\cdot)$ on the right-hand side of Equation (6.20) is the big-O Landau symbol. Taking into account these mathematical relations, an approximate estimate of the bias for the mean resultant length is:

$$\Delta\chi = E[\hat{\chi}] - \hat{\chi} \cong \frac{1-\hat{\chi}}{N} \geq \frac{1-\hat{\gamma}}{N} \tag{6.21}$$

Equation (6.21) can straightforwardly be interpreted and shows that, as expected, the coherence bias reduces as the number of looks increases, and the bias is more significant in low-coherence regions. Accordingly, to estimate the unbiased value of the coherence, the correction factor in the Equation (6.21) might eventually be applied. Using interferometric coherence values, changed and unchanged regions can be discriminated against one another by thresholding them. Specifically, for a given detection threshold, the probabilities of correct detection of a changing pixel and the probability of false alarms are given by [302]

$$\mathrm{P}_d = \int_0^{\mathrm{T}} p(\hat{\gamma} \mid 0) d\hat{\gamma} = 2(N-1)^2 \sum_{k=0}^{N-2} \binom{N-2}{k} (-1)^{N-2-k} \frac{\mathrm{T}^{2N-2-2k}}{2N-2-2k} \tag{6.22}$$

$$\begin{aligned} \mathrm{P}_{fa} &= \int_0^{\mathrm{T}} p(\hat{\gamma} \mid \hat{\gamma}'_0) d\hat{\gamma} = \\ &= \frac{2(N-1)\left(1-\hat{\gamma}'^{\,2}_0\right)^N}{\Gamma(N)\Gamma(N-1)} \sum_{k=0}^{N-2} \binom{N-2}{k} (-1)^{N-2-k} \sum_{l=0}^{+\infty} \left[\frac{\Gamma(N+l)}{\Gamma(l+1)}\right]^2 \hat{\gamma}'^{\,2l}_0 \frac{\mathrm{T}}{2N+2l-2-2k} \end{aligned} \tag{6.23}$$

where T is the applied coherence threshold. To improve the detection performance, the sample coherence $\hat{\gamma}$ can also be further averaged over a window and/or other alternative adaptations of the detector can be used, such as the ordered statistic coherence detector and the censored mean level detector [303]. It is worth noting that the coherence detector is sensitive not only to abrupt changes due to a disaster event (such as a fire, a flood, the effects of extreme weather conditions or man-made disturbances), which are the goals of change detection techniques, but also to other decorrelation effects that determine temporal decorrelation and that are not directly related to the main event under investigation. Thus, ambiguities in change detection remain where the temporal decorrelation caused by the background environment is dominant to those components strictly related to the natural/human-induced event under investigation. For instance, this happens over vegetated areas, likely affected by wind or seasonal changes. When decorrelation caused by a specific event is coupled with temporal decorrelation from wind or rain, isolating the two different decorrelation sources becomes challenging. Tracking coherence differences between couples of SAR images has been exploited to study various phenomena [108–111]. Some research investigations address the problem of developing proper temporal decorrelation models that can then be adapted to discriminate the background changes due to temporal decorrelation from those ascribed to the main disastrous event that is the subject of the CD investigation. To overcome some limitations in low coherence regions, [308] proposed an alternative maximum likelihood coherence change detector that lowers the false alarm probability in low coherent areas considering the clutter-to-noise power ratio of the SAR images. Specifically, the new estimator is expressed as follows:

$$\alpha = \frac{\left|\sum_{k=1}^{N} X_{1k} X_{2k}^{*}\right|}{\sum_{k=1}^{N}\left|X_{1k}^{2}\right| + \sum_{k=1}^{N}\left|X_{2k}^{2}\right| - N\sigma_{n1}^{2} - N\sigma_{n2}^{2}} \tag{6.24}$$

where σ_{n1}^{2} and σ_{n2}^{2} are the mean noise power values of the two interfering SAR images. Over recent years, new methods are also emerging that consider both amplitude and phase information for the unsupervised extraction of surface changes from a sequence of co-registered SAR images by extending the analyses from two single SAR images to a set of multi-temporal SAR images, e.g., see [284], [309], [310] Specifically, the abrupt changes in the radar returns in a time series of SAR data can be detected using a maximum-likelihood approach by assuming that the

transition times (TTs) are single or multiple. TTs can vary from one region to another, especially if the time-series of data is long and jointly estimated in an unsupervised way. In this context, as a further extension of GRLT to multi-pass SAR images, the work [284] proposed a method to detect changes in sequences of dual-pol Sentinel-1 multi-pass SAR data by considering both point targets and distributed targets on the terrain. The intrinsic limitation of such methods is that they are somewhat unstable unless a long sequence of data is processed. The automatic identification of the transition times is still a problematic task to achieve. Nowadays, the level of maturity of such methodologies is high by their use in a context of rapid mapping just after and/or between a disastrous event is challenging and poses the base for subsequent developments, where the help of artificial intelligence (AI) frameworks results beneficial for the identification and quantification of damaged regions.

6.1.3 Introduction to AI-aided Change Detection Methods

Another emerging class of CD methods can overcome these limitations while working with a short-term sequence of multi-pass SAR data; it is represented by the methods based on artificial intelligence frameworks for CD analyses. Machine Learning (ML) methods are increasingly applied to study and analyze data because of their ability to find relationships between target and input variables, such as those arising in satellite remote sensing of geophysical parameters. Over the last twenty years, the launch of a new constellation of RS satellites enabled the observation of the Earth system with an improved time-space granularity. Thus, unprecedented large amounts of data have been produced [311], [312]. In this context, the RS community started the development of new advanced methodologies through the adoption of ML-based frameworks. Two factors drove the adoption of those frameworks:

1) The possibility of combining information from multiple RS domains for the solution of a specific task and overcoming the limitations of traditional methodologies that, on the contrary, only allow the use of information from a particular domain [313]–[315].

2) The development of methodologies capable of ingesting and analyzing a large amount of data automated and extrapolating useful new information [312].

Different unsupervised and supervised [316] ML methodologies have been explored in the RS CD task context. Among supervised methodologies of relevant

importance is the application of Support Vector Machine (SVM) [317]–[320], models based on Neural-Network (NN) [321]–[323], ensemble models such as Breiman RF [104], [107], [324] and derivatives (e.g., XGBoost [325] and AdaBoost [326]).

For unsupervised methodologies, kernel and fuzzy clustering-based strategies are the most commonly used [327]–[329]. Finally, in recent years, the combinations of unsupervised and supervised ML methodologies, namely called semi-supervised, have been proposed [328], [330]–[333]. The scope is to integrate the merit of both unsupervised and supervised methods to extrapolate information from RS data and construct new helpful knowledge. Semi-supervised methodologies are particularly useful in CD scenarios in which it is very difficult, or even worse, impossible to collect information for labelling the class to be predicted.

A complete explanation of new advanced ML-based RS methodologies and future trends is outside the scope of this work. Interested readers are referred to [315], [334], [335] for a detailed digression on such technologies.

6.2 PROPOSED MULTI-TEMPORAL SAR CHANGE DETECTION STRATEGY

Rapid damage assessment mapping and analysis after a disastrous event exploiting SAR data stacks can efficiently be carried out using CD methods, profiting from the availability of short sequences of SAR images, encompassing the selected primary disastrous event under investigation, and regularly collected before, between, and after the event itself. SAR technology's current and future trend is to operate in a synergic way with data collected by constellations of SAR sensors that are jointly in orbit and capable of collecting data in different portions of the electromagnetic spectrum and with short revisiting times (weekly basis or less). A significant step forward in this direction has been represented by the put in orbit, starting from April 3, 2014, of the twin sensors Sentinel-1A/B of the ESA Copernicus Constellation [336], which have long been mapping Earth's surface regularly every six days (in the most favourable case), permitting extensive analyses on the state of Earth' surface and the environment. Collected data are freely available and have been fostering the development of new studies and processing methods for rapidly estimating changed areas. This section proposes and describes a joint multi-pass coherent/incoherent CD strategy that allows analyzing a short-term sequence of calibrated SLC images and fast computing damaged areas

using incoherent/coherent change detection indices (CDIs). These indices are then cooperatively used to automatically extract changed areas using a Random Forest (RF) classifier. Finally, Section 6.2.5 details the steps of the proposed multi-pass CD strategy.

6.2.1 Coherent Change Detection Indices

When dealing with SAR multi-pass change detection in the occurrence of a disastrous event that occurred at a known time, namely t_{ev}, the easiest way to obtain a reliable change map is to use one single pair of SAR images collected at times t_{pre} and t_{post} in such a way to encompass the principal disastrous event, i.e., $t_{pre} < t_{ev} < t_{post}$, with one single image before the event and one single image after the event. Incoherent CD methods estimate and subsequently threshold the log-ratio image map (see Equation (6.15)).

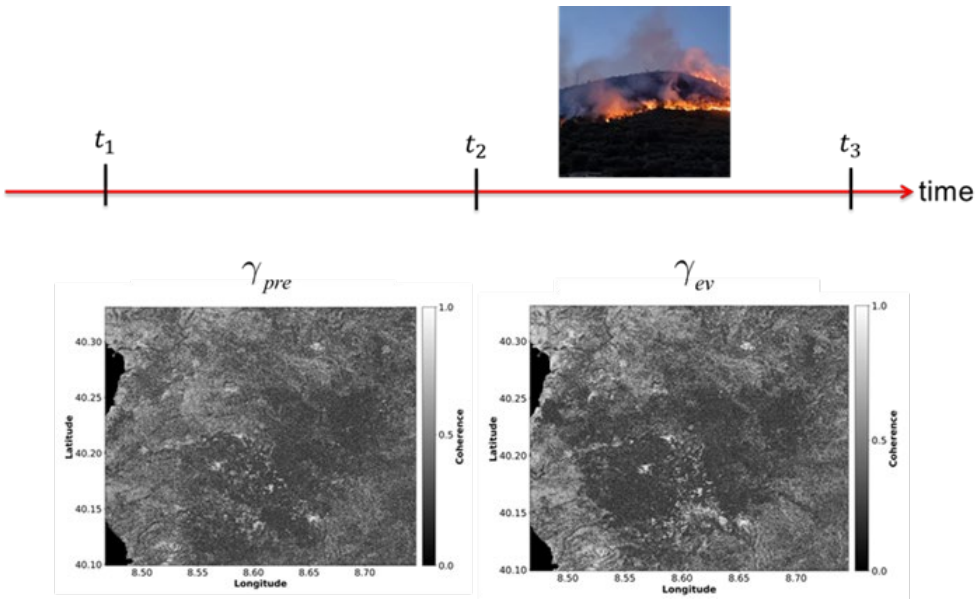

Figure 85. Coherence change tracking scheme using two SAR images acquired

before the event (t_1 = 08/18/2021 and t_2 = 08/24/2021) and one after the event (t_3 = 08/30/2022). The area shown in the coherence maps is the Montiferru region in Sardinia, Italy.

However, the information on the occurred changes ascribed to the disastrous event (e.g., a fire, an inundation, etc.) is also enclosed in all SAR data pairs that encompass the main event, i.e., more than one pre/post-SAR image can be jointly used to circumvent better the effects of noise and other disturbances in SAR images that could lead to inaccurate decisions while using one single SAR data pair. This is especially true when coherent CD methods are exploited. Indeed, the coherence (see Equation (6.6)) measures the similarity between two SAR images. Thus, necessarily tracking of coherence changes requires the availability of at least three SAR images: two images are collected before the event at times t_1 and t_2 used to estimate the (background) coherence of the scene γ_{pre} just before the event occurred, and one SAR image is collected just after the occurrence of the event at the time t_3, to compute the coherence across the event, namely γ_{ev}, see Figure 85. In this way, common coherence variations due to other causes unrelated to the main natural or man-made disastrous event can be isolated and considered by calculating the coherence ratio (CR) or the normalized coherence difference ratio (ND) of the pre- and post- coherence images. The coherence ratio has long been explored for building damage assessment [337]–[339]; it is defined as follows:

$$\rho = \frac{\hat{\gamma}_{pre}}{\hat{\gamma}_{ev}} \tag{6.25}$$

Considering the three-pass configuration of Figure 85, the pre- and co-event coherence maps are $\hat{\gamma}_{pre} = \hat{\gamma}_{1,2}$ and $\hat{\gamma}_{ev} = \hat{\gamma}_{2,3}$, respectively. Inherited from studies of the building damage assessment, it is also the normalized coherence ratio, which is defined as follows:

$$ND = \frac{\hat{\gamma}_{pre} - \hat{\gamma}_{ev}}{\hat{\gamma}_{pre} + \hat{\gamma}_{ev}} \tag{6.26}$$

Note that both the used change detection indices of Equations (6.25) and (6.26) depend exclusively on three SAR images; however, one image is common for the coherence estimation. If the values of the selected CDIs are associated with the common reference image, a time-series of these indices could also be generated and employed for unsupervised CD analyses, automatically tracking, for instance, the correct transition times where significant changes occurred on the imaged scene.

6.2.2 TEMPORAL DECORRELATION MODELS: IMPLICATIONS FOR CHANGE DETECTION

In the previous sub-section 6.2.1, I have presented two simple, coherent change indices based on the ratio and the normalized difference of a pair of coherence maps formed from a triplet of SAR images collected before and between a disastrous event. In this sub-section, I want to discuss the benefits of these two CDIs, considering the interferometric coherence properties and especially the contributions due to volumetric and temporal changes. The Equation (6.7) shows that coherence depends on several factors. The constellation of Sentinel-1A/B Copernicus radar sensors is characterized by a narrow orbital tube. Thus, the spatial decorrelation is limited and can be estimated and compensated using Equation (6.8). For our analyses, the most important contributions of coherence are the temporal and volumetric components. To address these signals, I exploit in this work the temporal coherence model proposed in [340] that incorporates the effects of temporally correlated changes and those that randomly occur (i.e., temporally uncorrelated) in the case of disastrous events due to differences in the arrangement and dielectric properties of the scatterers. The work [340] shows that temporal decorrelation for zero-spatial baseline and long-temporal baseline can be expressed as follows:

$$\hat{\gamma} = \left| \frac{e^{-\frac{\Delta T}{\tau_v}} \gamma^{v}_{t\_rand} + \mu(\omega) e^{-\frac{\Delta T}{\tau_g}} \gamma^{g}_{t\_rand}}{1 + \mu(\omega)} \right| \tag{6.27}$$

where ΔT is the interferometric temporal baseline, τ_g and τ_v are the unique characteristic time constants for the ground and volume contributions, $\gamma^{v}_{t\_rand}$ and $\gamma^{g}_{t\_rand}$ are the temporally uncorrelated (random) complex cross-correlation changes for volume and ground layers ground-to-volume scattering ratio and ω represents the polarimetric scattering mechanism. Using the Equation (6.27), we can express the ratio coherence of the Equation (6.25) as:

$$\rho = \frac{\hat{\gamma}_{pre}}{\hat{\gamma}_{ev}} = \frac{\hat{\gamma}_{geo,pre} \cdot \hat{\gamma}_{Dopp,pre} \cdot \hat{\gamma}_{mis-reg,pre} \cdot \hat{\gamma}_{vol,pre} \cdot \hat{\gamma}_{temp,pre} \cdot \hat{\gamma}_{thermal,pre}}{\hat{\gamma}_{geo,ev} \cdot \hat{\gamma}_{Dopp,ev} \cdot \hat{\gamma}_{mis-reg,ev} \cdot \hat{\gamma}_{vol,ev} \cdot \hat{\gamma}_{temp,ev} \cdot \hat{\gamma}_{thermal,ev}} \tag{6.28}$$

Because the orbital tube is narrow, the variation of the spatial decorrelation effects are reduced by the ratio, which is only sensitive to perpendicular baseline double difference (i.e., the difference between the perpendicular baseline of the considered InSAR data pair), the thermal noise components almost cancel out, and with limited misregistration errors and almost aligned Doppler spectra between the SAR images, the most prominent contribution that persists in the coherence ratio operator are the volumetric and the temporal decorrelation effects. Considering Equation (6.28), the most relevant contributions are:

$$\begin{aligned}\rho &= \frac{\hat{\gamma}_{pre}}{\hat{\gamma}_{ev}} = \alpha \frac{\hat{\gamma}_{temp+vol,pre}}{\hat{\gamma}_{temp+vol,ev}} = \\ &= \alpha \left| \frac{e^{-\frac{\Delta T_{pre}}{\tau_{pre,v}}} \gamma^{v}_{t\_rand} + \mu_{pre}(\omega) e^{-\frac{\Delta T_{pre}}{\tau_{pre,g}}} \gamma^{g}_{pre,t\_rand}}{e^{-\frac{\Delta T_{ev}}{\tau_{ev,v}}} \gamma^{v}_{t\_rand} + \mu_{ev}(\omega) e^{-\frac{\Delta T_{ev}}{\tau_{ev,g}}} \gamma^{g}_{ev,t\_rand}} \cdot \frac{1+\mu_{ev}(\omega)}{1+\mu_{pre}(\omega)} \right|\end{aligned} \tag{6.29}$$

where α is the residual terms accounting for the other decorrelation artifacts that do not perfectly cancel out in the ratio. When the ground contributions are prevalent, and we assume the availability of a group of SAR data acquired regularly, we can generate the pre- and co-event interferometric data pairs with the same temporal baseline, i.e., $\Delta T_{pre} = \Delta T_{ev}$. In this case, Equation (6.29) particularizes as:

$$\begin{aligned}\rho_g &= \frac{\hat{\gamma}_{pre,g}}{\hat{\gamma}_{ev,g}} = \alpha \frac{\hat{\gamma}_{temp+vol,pre}}{\hat{\gamma}_{temp+vol,ev}} = \\ &= \alpha \left| \frac{\gamma^{g}_{pre,t\_rand}}{\gamma^{g}_{ev,t\_rand}} \cdot \frac{\mu_{pre}(\omega)}{\mu_{ev}(\omega)} \cdot \frac{1+\mu_{ev}(\omega)}{1+\mu_{pre}(\omega)} \cdot e^{-\Delta T\left(\frac{1}{\tau_{pre,g}} - \frac{1}{\tau_{ev,g}}\right)} \right|\end{aligned} \tag{6.30}$$

Similarly, if the prevalent contribution to the coherence is the volumetric component, we have:

$$\rho_v = \frac{\hat{\gamma}_{pre,v}}{\hat{\gamma}_{ev,v}} = \alpha \frac{\hat{\gamma}_{temp+vol,pre}}{\hat{\gamma}_{temp+vol,ev}} = \alpha \left| \frac{\gamma^{v}_{pre,t\_rand}}{\gamma^{v}_{ev,t\_rand}} \cdot \frac{1+\mu_{ev}(\omega)}{1+\mu_{pre}(\omega)} \cdot e^{-\Delta T\left(\frac{1}{\tau_{pre,v}} - \frac{1}{\tau_{ev,v}}\right)} \right| \tag{6.31}$$

Accordingly, the coherence ratio results are more sensitive than the single coherence measurement for coherent change detection purposes. want to evidence and discriminate from other coherence contributions. The Equation (6.27) shows that the coherence model's ground and volumetric components are two additive terms. Accordingly, the coherence difference in a somewhat homogenous region can better discriminate the two separate ground and volumetric contributions separately. For small values of the topographic phase $\varphi_k \cong 0$, and considering that the prevalent contributions to the coherence are the volumetric and temporal decorrelation terms, we respectively have:

$$ND_v = \frac{\hat{\gamma}_{pre} - \hat{\gamma}_{ev}}{\hat{\gamma}_{pre} + \hat{\gamma}_{ev}} \cong \alpha' \frac{\gamma^v_{t\_rand,pre} - \gamma^v_{t\_rand,ev}}{\left(\gamma^v_{t\_rand,pre} + \gamma^v_{t\_rand,ev}\right) + \left(\gamma^g_{t\_rand,pre} + \gamma^g_{t\_rand,ev}\right)} \quad (6.32)$$

$$ND_g = \frac{\hat{\gamma}_{pre} - \hat{\gamma}_{ev}}{\hat{\gamma}_{pre} + \hat{\gamma}_{ev}} \cong \alpha' \frac{\gamma^g_{t\_rand,pre} - \gamma^g_{t\_rand,ev}}{\left(\gamma^v_{t\_rand,pre} + \gamma^v_{t\_rand,ev}\right) + \left(\gamma^g_{t\_rand,pre} + \gamma^g_{t\_rand,ev}\right)} \quad (6.33)$$

Equations (6.30)-(6.33) clarify that, depending on the physical phenomena under investigation, the volumetric or the ground decorrelation terms can become prevalent and be emphasized by the coherence ratio and normalize coherence difference. For example, if a fire happens in a forest, we can assume that most of the changes are associated with the canopy volume consumed by the fire. In contrast, the ground is less disturbed, especially for low to mid-fire severities. The analysis proposed in this sub-section demonstrates that the coherence ratio is preferable to the single co-event coherence map because it is more sensitive to the random time-uncorrelated changes. Moreover, in somewhat homogenous regions, when the primary event under investigation does not drastically change the structural properties of the imaged scene, the normalized difference can be superior because it allows isolating the predominant time-uncorrelated coherence changes. In-depth analyses are still required to calculate the pdfs of these two operators to statistically figure out the probability of false alarms and the detection probability of such two synthetic coherence detection indices.

6.3 EXTENSION TO THE MULTI-PASS CASE

Let us now extend our analysis to the case when M_{pre} different SLC SAR images are available before the primary event, collected at times $\left[t_1, t_2, ..., t_{M_{pre}}\right]$, and

additional SLC SAR images are available after the primary event, collected at times $\left[t_{M_{pre}+1}, t_{M_{pre}+2}, ..., t_{M_{pre}+M_{post}}\right]$, with $t_{M_{pre}} < t_{ev} < t_{M_{pre}+1}$.

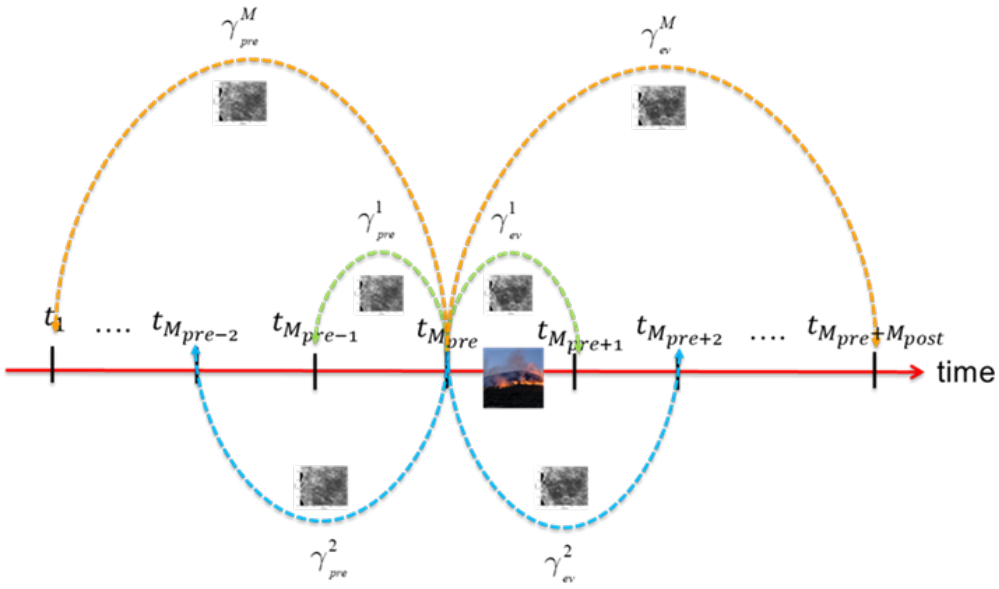

Figure 86. Coherence change tracking scheme in multi-pass case.

Information on occurred changes related to the main event that happened at the time t_{ev} can be extracted by singularly analyzing all SAR image pairs across the primary event, see Figure 86. In particular, given the SAR data pair (t_h, t_k) with $t_h < t_{ev} < t_k$, the log-ratio image $LR_{h,k} = \ln\left(\frac{\langle X_k \rangle}{\langle X_h \rangle}\right) = \ln\left(\langle X_k \rangle\right) - \ln\left(\langle X_h \rangle\right)$ can be computed. In general, with $M_{pre} + M_{post}$ SAR images, different (t_h, t_k) SAR data pairs satisfy the condition $t_h < t_{ev} < t_k$. As imaged by the satellite sensors, the effects on the ground related to the main event can be detected and extracted from every single log-ratio image $\{LR_l\}_1^{\Theta}$. Accordingly, we could generally have Θ different looks for the same scene. The time average of these different looks allows one to obtain a temporal multi-look log-ratio image which is expected to be less affected by noise. Mathematically, multi-look log-ratio image map is obtained as follows:

$$MLR = \sum_{l=1}^{\Theta} LR_l \tag{6.34}$$

where the summation is performed pixel-by-pixel. Note that random changes and systematic subtle multiple changes can happen in the whole $\left[t_1, t_{M_{pre}+M_{post}}\right]$ time interval; accordingly, the temporal multi-look log-ratio image will tend to filter out the small random amplitude fluctuations that are present in the single maps and emphasizes the major systematic contributions due to the primary event. On the other hand, if the selected time window is too large and the scene rapidly comes back to original pre-event conditions (and/or in a new state after t_{ev} that has a reduced memory of the disastrous event), the temporal multi-look LR image will be sensitive to changes different from those we want to extract. For this reason, the proposed methodology is adequate for short-term time-series of data, with a maximum time span (temporal baseline) of one/two months (or less) across the main event, and it looks desirable for fast damage assessment.

If dual-pol SAR data are available, the incoherent temporal multi-looking of Equation (6.34) can be computed for the two polarizations separately. In addition, with dual-pol VV/VH Sentinel-1 SAR data, the sum and difference of incoherent temporal multi-looking log-ratio images can be computed and used as two separate, dependent synthetic incoherent CDIs; see the experimental results presented in Section 6.6.

The joint exploitation of coherent and incoherent information in a unique framework is attractive. In a multi-pass scenario with $M_{pre} + M_{post}$ SAR images, some interferometric data pairs with the same temporal baseline before the event and co-event can be selected. The relevant coherence ratio and normalized difference ratio images can be computed. Using interferometric SAR data pairs with the same temporal baseline partially compensates for the effects of temporal decorrelation not related to the primary event. Indeed, coherence decorrelation is at the first order the same in pre- and in-between-event coherence maps.

Nonetheless, as the temporal baseline increases, the single coherence maps will be more decorrelated, and the performance of the coherence detector diminishes. For this reason, the coherence analyses should be retained to shorter time windows. This statement is supported by the experimental results shown in Section 6.6, demonstrating that the relative weight/importance of longer baseline coherence in

the binary decision between changed/unchanged regions drastically reduces as the interferometric SAR temporal baseline increases. The developed method relies on the computation and subsequent utilization of the following two sets of coherence ratios and normalized coherence differences:

$$\{\rho_l\}_{l=1}^{\Theta} \tag{6.35}$$

$$\{ND_l\}_{l=1}^{\Theta} \tag{6.36}$$

Note that the families of used CDIs are composed of Θ elements, representing the number of pairs of InSAR data pairs between the primary event that can be formed from the available SAR scenes. The following Sections will introduce how Breiman's random forest (RF) [107] (see Section 2.2.2 for more details about RF), and the change detection indices presented above can jointly derive surface change maps.

6.4 PROPOSED RF-AIDED CD METHODS

In this section, I describe the proposed RF CD framework. As illustrated in Figure 87, the proposed framework consists of three modules.

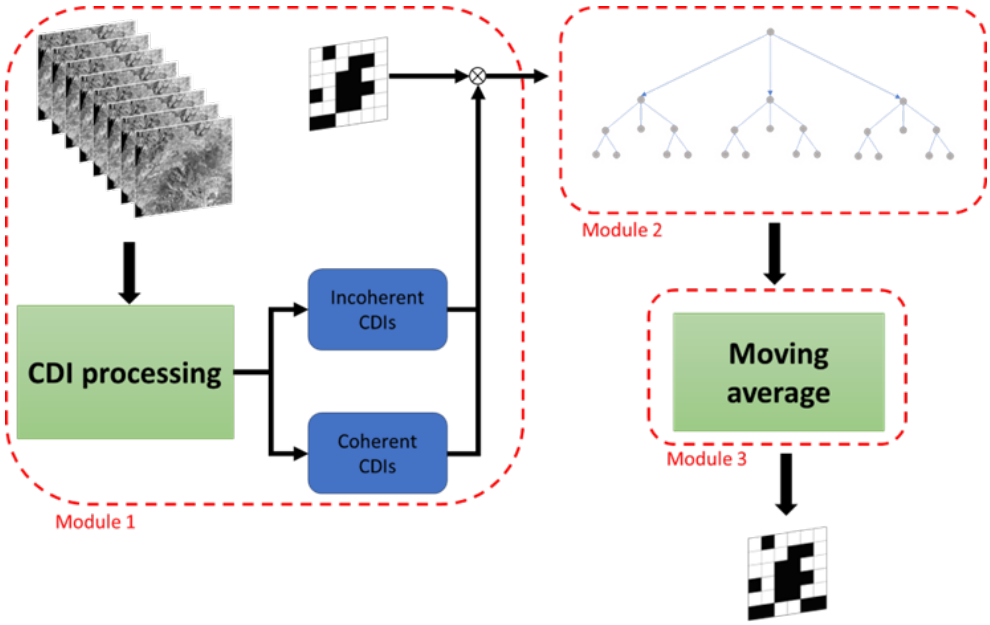

Figure 87. Sketch of modules of proposed CD framework.

Starting from a sequence of calibrated, co-registered and geocoded Sentinel-1 SAR acquisitions, the first module consists of pre-processing data and calculating the incoherent and coherent change detection indices. In this work, I treated change detection as a pixel-based binary classification task that uses 1 and 0 to indicate changed and unchanged pixels. Therefore, I used an RF model combining CDIs and a reference change mask in the second module to perform supervised learning. The final module applies a spatial average with a moving window to the RF predicted binary change mask. Eventually, the binary change mask is retrieved.

6.5 Case-Study Areas and SAR Data

Three SAR datasets consisting of 15, 13, and 12 SAR images collected in the Single-Look-Complex (SLC) format and Terrain Observation with Progressive Scans SAR (TOPSAR), Interferometric Wide (IW) mode by the Sentinel-1A/B sensors over the central-western sector of Sardinia Island, the central-western area of Sicilia Island regions in Italy, as well as the Southern coastal area of Texas in the U.S.

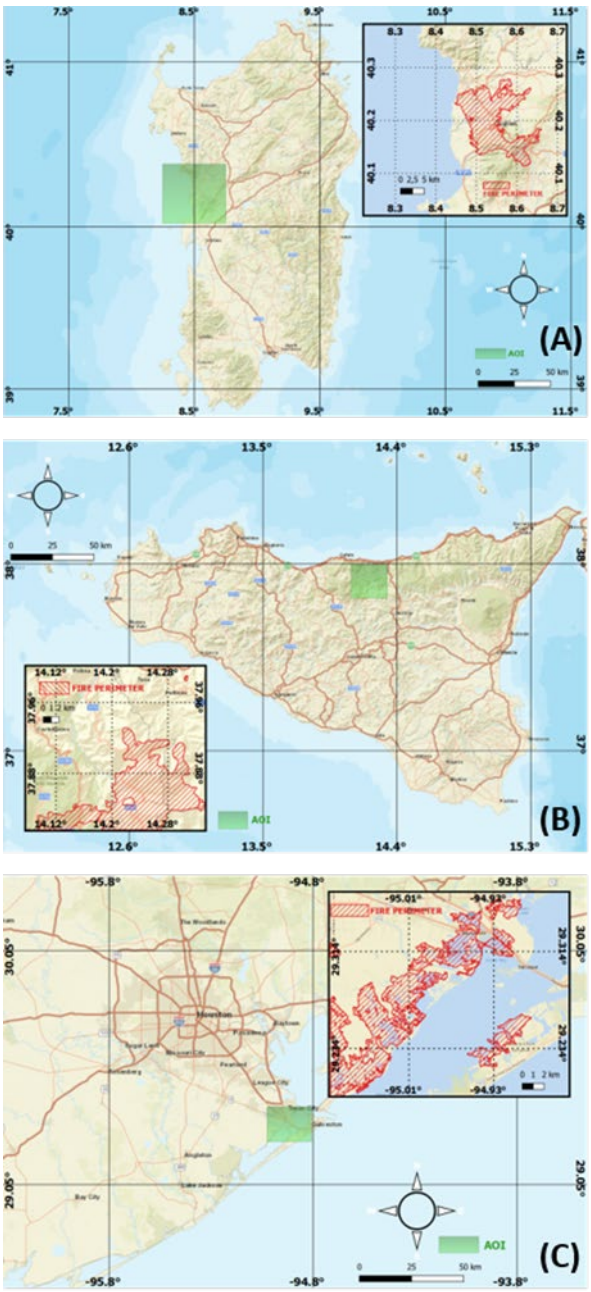

Figure 88. (A) Geographical map of Sardinia, (B) Sicily and (C) South-east Texas coastal area, respectively. The green boxes indicate the Motiferru, Madonie, and Galveston AOIs. The AOIs are zoomed within the minimaps where the wildfires and flooding perimeter are highlighted in red**.**

Table 24. List of S-1 acquisitions for the Sardinia, Sicily and Texas coastal areas.

Acquisition dates		
SARDINIA	SICILY	TEXAS
2021-06-12	2021-06-27	2021-07-13

2021-06-18	2021-07-03	2021-07-19
2021-06-24	2021-07-06	2021-07-25
2021-07-06	2021-07-09	2021-07-31
2021-07-12	2021-07-21	2021-08-06
2021-07-18	2021-07-27	2021-08-12
2021-07-24	2021-08-02	2021-08-18
2021-07-30	2021-08-08	2021-08-24
2021-08-05	2021-08-14	2021-08-30
2021-08-11	2021-08-20	2021-09-05
2021-08-17	2021-08-26	2021-09-11
2021-08-23	2021-09-07	2021-09-17
2021-08-29	2021-09-13	2021-09-23
2021-09-04	2021-09-19	2021-09-29

Table 24 shows the list of used SAR data. The areas of interest (AOIs) include:

i. The Montiferru region in Sardinia (see Figure 88 A). The territory is mainly characterized by a mountain chain and some valleys located in its inner parts, particularly in the municipalities of Santu Lussurgiu, Cuglieri and Scano Montiferro. The terrain elevation of the investigated area ranges from the sea level to the highest point of Monte Urtigu, about 1,050 m a.s.l., located in the municipality of Santu Lussurgiu. The site is historically characterized by the Mediterranean climate, presenting dry summers, cold and wet winters, and intermediate conditions in spring and autumn. In the last decades, due to global warming, the region is also facing alterations drastically in precipitation regimes, with the most considerable precipitation runoff decrease [341].

ii. The Sicilian Apennines, specifically the area of the "Madonie" (see Figure 88 B). Within this area is situated the Parco delle Madonie, which is the second nature reserve in Sicily. Its 35,000 hectares are home to towering mountains (at 1,979m, the highest peak is Pizzo Carbonara), large expanses of woodland, and a flourishing variety of flora and fauna. In terms of flora, there are over 2,600 different species of plants, many of which are endemic to the area. Specifically, at an altitude of 1,500 m, the land is entirely covered by the Madonie Forest. Below, on the hillsides, the area is mainly characterized by crops, including the cultivation of wheat, olives and fruits. The area incorporates several historic towns and villages such as Polizzi Generosa, Petralia Soprana and Sottana, Gangi and Castelbuono.

iii. The Houston metropolitan area (see Figure 88 C) is the fifth-most populous urban area in the USA. The region contains the city of Houston (the most significant economic and cultural centre of the South). Its port (the second largest port in the United States and the sixteenth largest globally) leads the U.S. international trade. The metropolitan area is in the Mexico Gulf Coastal Plains. Much of the urbanized area was built on forested land, marshes, and prairie.

Concerning the Italian sites, the characterizing phenomena are wildfires. Wildfires have interested the Italian areas between July and August of 2021. In the Sardinia area, on July 23, 2021, at around 5.30 pm CET, a wildfire started in the Montiferru region, specifically on the road that connects Bonarcado and Santu Lussurgiu. In the first phase of its propagation, the wildfire affected an area mainly covered by herbaceous vegetation and wooded pastures. Then, on July 24, the fire quickly got out of control due to the region's complex topography, extreme weather conditions (temperature close to 40° C), low relative humidity, and strong winds from S-SE. The wildfire spread towards N-NW, favoured by the increasing slopes and higher amounts of fuel load, and started burning the forest areas of Santu Lussurgiu. The wildfire spreading caused huge damage, devastating an area of about 20,000 ha. In Sicily, the wildfire started simultaneously between 6-12 August of 2021. In Sicily, due to criminal acts on the night of 6 August in the territory of Gangi, in the Madonie Mountains, several wildfires started. The wildfires have surrounded first the Gangi village and later spread out over two directions: one towards San Mauro Castelverde village and one towards Collesano, Lascari, and Geraci Siculo villages. The wildfire spread, devastating an area of about 2,000 ha, damaging villages, houses, animals, and farms drastically and changing the whole Madonie ecosystem irreversibly.

Concerning the U.S. area, on the morning (11:00 p.m. ET) of August 25, 2017, Category 4 Hurricane Harvey made landfall along the Texas coast near Port Aransas and brought a devastating impact. The hurricane had a diameter of about 280 miles and generated winds of 130mph during its landfall. The intense phenomenon busted all the US records for rainfall from a single storm, with a maximum of 60.5 inches of rain in some parts of Texas. Counting only coastal areas, Beaumont, Port Arthur, and Galveston received about 26 inches of rain in 24 hours. This rainfall caused catastrophic drainage issues and made rivers rise considerably. Flooding forced 39,000 people out of their homes and into shelters. Only around 10% of the forecast river points in southeast Texas remained below flood stage due to the event, and approximately 46% of the river forecast points

reached new record levels. Harvey had a considerable economic impact, causing about $130 billion in damage, moving Harvey to be ranked as the second-costliest hurricane to hit the U.S. mainland since 1900.

Fire and flooding perimeters were derived using the Copernicus Emergency Management Service (EMS), which provides geospatial information within hours or days after the catastrophic phenomenon with its Rapid Mapping component. Specifically, the Rapid Damage Assessment (RDA) module of the European Forest Fire Information System (EFFIS) has been used for wildfire events. By analyzing near real-time MODIS daily images at 250m spatial resolution, the RDA provides the daily update of the perimeters of the burn areas in Europe. The process involves delineating the extent of wildfire events based on the semi-automatic classification of MODIS satellite imagery using ancillary spatial datasets such as CORINE Land Cover, the active-fire detection products from MODIS and VIIRS. The Global Flood Awareness (GloFAS) system has been used for flood events. GloFAS provides a floods map using flood mapping algorithms developed by the Global Flood Mapping (GFM) consortium[11]. Specifically, three individual flood mapping algorithms operate in parallel, analyzing historical time-series of Sentinel-1 SAR intensity data [342]–[345]. Topography-derived indices are used to refine the classification of water bodies. Once each algorithm generates its own "Observed flood extent" map, an ensemble-based approach is used to combine the maps into a single "consensus map" in which a pixel is accepted as "flooded" when at least most of the classification algorithms that compose the ensemble classify it accordingly.

6.6 Experimental Results

Temporal multi-looked sigma naught maps and Coherence Changes Indexes (CCI) extracted from the available SAR images were used to detect changes from the wildfire and flooding events characterizing the AOIs. The SAR images were preliminarily radiometrically calibrated [346] to extract from the digital data the maps of the radar backscatter, i.e., the sigma naught maps [202]. I selected the 24 July of 2021 as the primary fire event. I selected a time series of acquisitions with a temporal baseline of $\pm 6, \pm 12, \pm 18$ days, before (6, 12, and 18 July), during (24 July) and after (30 July, 5 and 11 August) the wildfire event, respectively. Each SAR image of the time series was independently post-processed by applying the de-speckling noise-filtering algorithm [347] and co-registered using Enhanced

[11] https://wiki.c-scale.eu/GFM/PUM/ConsortiumMembers

Spectral Diversity (ESD) with respect to the 24 July acquisition. The maps of sigma naught were finally converted from linear to decibel, and six sigma naught differences $\Delta\sigma^0$(dB) with respect to the 24 July maps were computed and geocoded. For representability, Figure 89 shows the maps of $\Delta\sigma^0$ (dB) with a temporal baseline of ± 6 days for the VH and VV polarization.

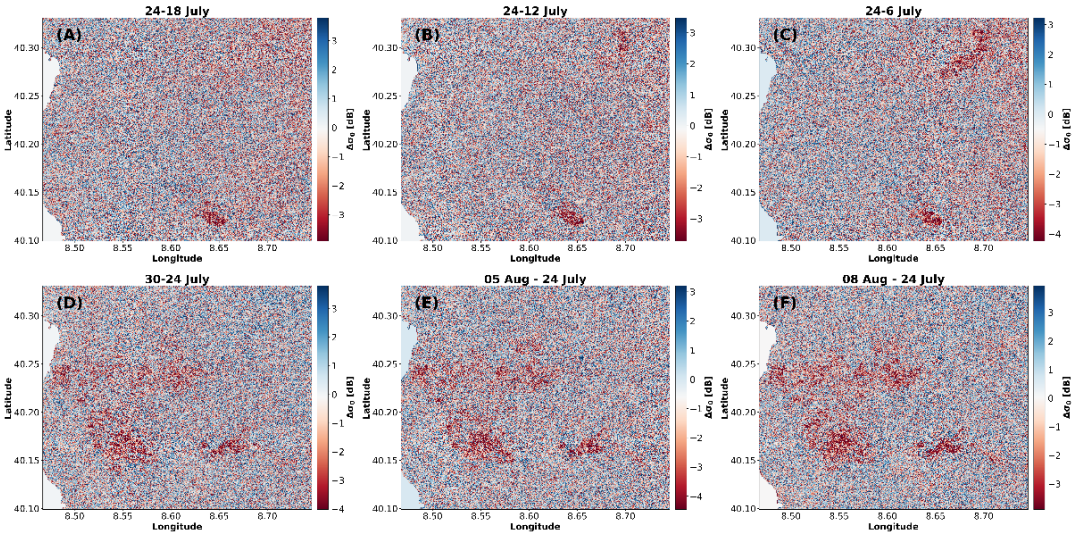

Figure 89. Sigma naught $\Delta\sigma^0$ differences (dB) were computed over the Sardinia AOI for VH polarization. (A)-(C) pre-fire event differences. (D)-(F) post-fire event differences.

Once the sigma naught difference time series has been computed, the incoherent temporal multi-looking step described in Section 6.1.1 has singularly been applied to the VH and VV SAR sigma naught time series.

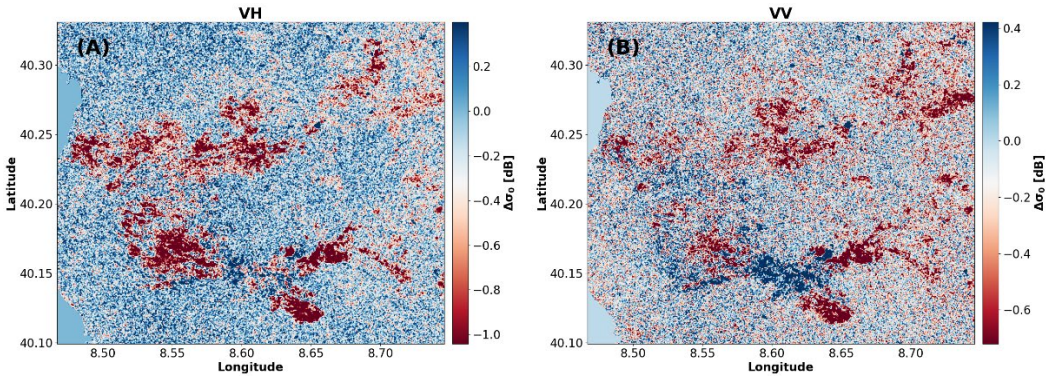

Figure 90. Temporal multilook maps of $\Delta\sigma^0$ time-series for (A) VH and (B) VV polarization channels. Read Section 6.1.1 for more details.

As shown in Figure 90, the temporal multi looking operation allows us to highlight better the variations of amplitude SAR backscatter $\Delta\sigma^0$ at VH and VV polarizations connected to changes in ground properties related to the wildfire event.

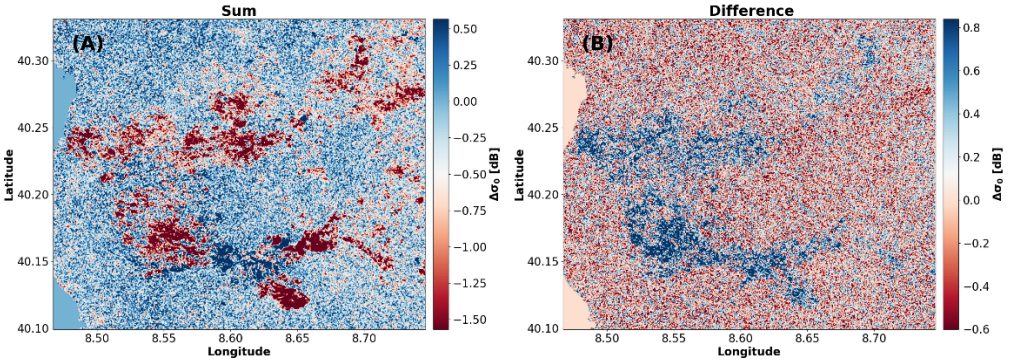

Figure 91. (A) Sum and (B) difference of incoherent temporal multi-look maps at VV and VH polarization channels.

Finally, as described in Section 6.1.1, the sum and difference of two incoherent temporal multi-look maps obtained at the two available VV and VH polarization channels are used as additional CDIs. The relevant maps are shown in Figure 91 A and B.

Interferometric SAR (InSAR) coherence change $ND_{post-pre}$ and $\rho_{post-pre}$ CCIs have also been determined and used to detect changes related to the wildfire disaster event. Considering triplets of SAR images using temporal baselines of $\pm 6, \pm 12, \pm 18, \pm 30, \pm 36$, and ± 42 days with respect to the 24 July 2021 primary event date acquisition, pre- and co-fire event interferometric pairs CCI time-series were obtained by applying Equations (6.25), and (6.26). The use of these temporal baselines was chosen to highlight as much as possible the changes between the pre- and co-disaster coherence maps. In the same way, of sigma nought differences for representability. Figure 92 shows the R and ND CCIs using interferometric coherence related to pairs of SAR acquisitions with a temporal baseline of ± 6 days (24-30 July and 24-18 July) for VH and VV polarization.

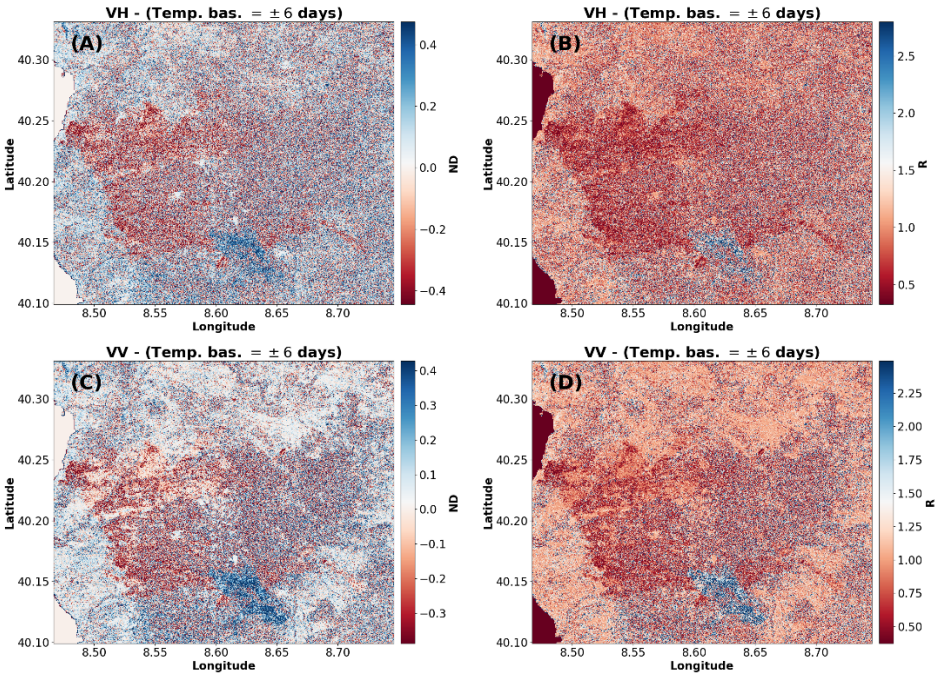

Figure 92. (A) and (C) ND CCI, (B) and (D) R CCI for VH and VV polarization, respectively. The considered temporal baseline is equal to ±6 days (24-30 July and 24-18 July).

It is worth remarking that both for sigma naught and coherence maps, changes depend on several natural phenomena that can act simultaneously (e.g., soil moisture and humidity changes due to weather conditions), and their use in vegetated areas, such as the investigated one, is more challenging due to the presence of volume scattering decorrelation, especially at C- and X-band. As shown in Figures Figure **90**, Figure **91** and Figure **92**, the fire event signal is easily visible and in agreement with the fire perimeter provided by the EFFIS platform. The same processing methodology has been used for the Sicily and Texas AOIs. The acquisition of the 8 August 2021 and 24 August 2017 has been used as main event dates, respectively.

6.6.1. Discussion on Random Forest Training and Research Outcomes

For the three selected case-study areas in Italy and U.S., I applied the AI-aided strategy described in Sections 6.4 and 6.5. In this Section, I discuss the results of the experiments that were carried out using an RF model trained using as inputs the set of synthetic incoherent (sigma naught) and coherent (coherence-based) change detection indices at VV and VH polarizations. Supervised training is carried out

using the fire and flood perimeters from EFFIS and Glo-FAS by the determination of a synthetic binary change mask, in which all pixels within the perimeters are identified as changed and labelled as one and all pixels outside the perimeters are identified as unchanged and labelled as 0; see Figure 93.

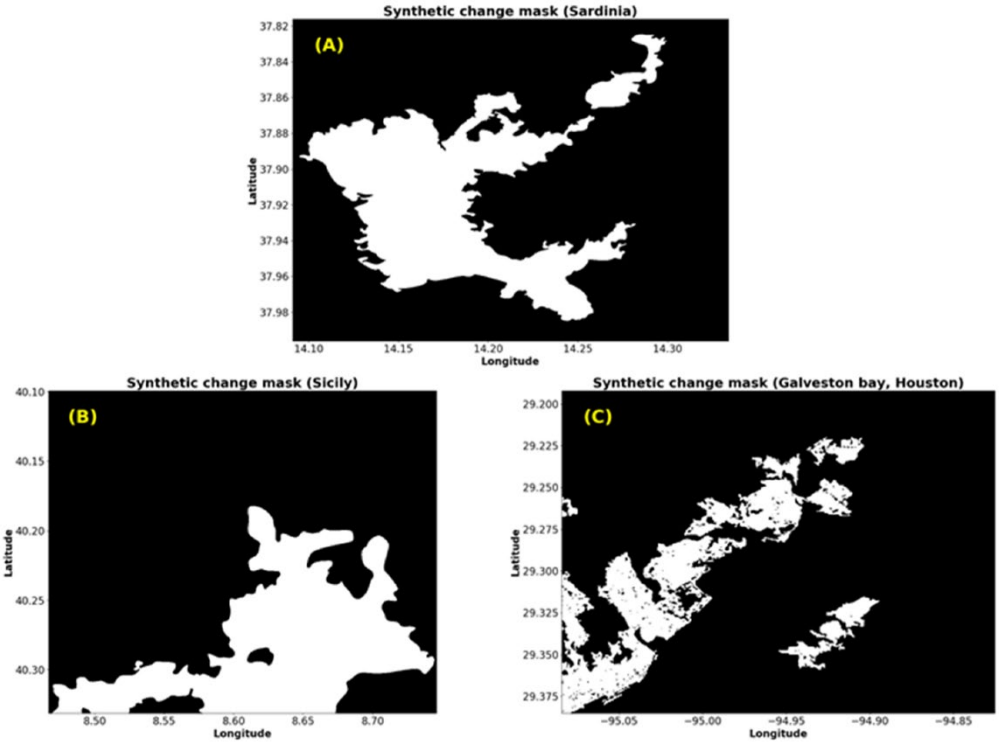

Figure 93. Synthetic binary change masks of the (A) Sardinia, (B) Sicily, and (D) Texas Galveston bay AOIS, respectively.

In addition, to avoid the class imbalance problem, an additional preprocessing step has been carried out. Specifically, the dataset of samples related to the Sardinia and Sicily AOIs presents a class imbalance of about 3:1 for the positive (1) class; see Figure 94.

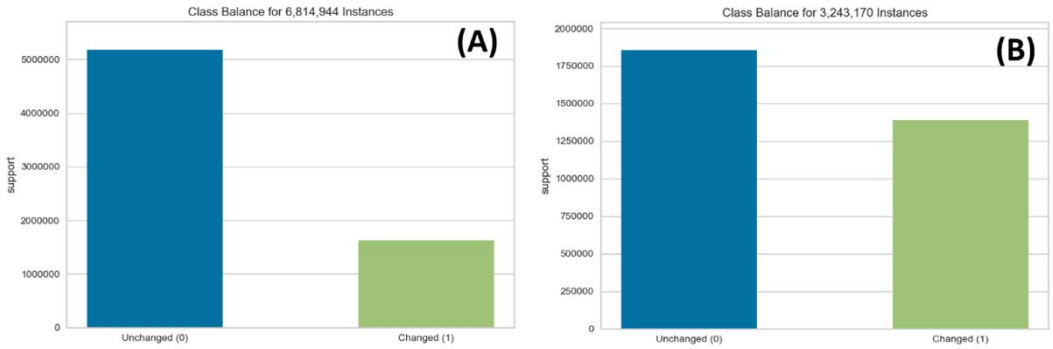

Figure 94. Class imbalance before (A) and after random-oversampling and -undersampling techniques (B).

As we can see from Figure 94 A, the dataset presents a class imbalance for the positive class (1). Imbalanced datasets pose a challenge for predictive modelling such as RF because they introduce a bias in the training that results in the poor predictive performance of the minority class with respect to the majority one [348]–[351]. In this way, the random-oversampling and -undersampling techniques [349], [350] have been used to make the training dataset imbalance less severe; see Figure 94 B. Using Optuna's [120] hyperparameter optimization framework, an RF structure composed of 209 decision trees was designed. Stratified K-Fold [352], [353] used ten folds to cross-validate the RF model in the training step. To evaluate the effectiveness of the proposed method, I decided to use only the data related to the Sardinia and Sicily AOIs to train the RF model and subsequently assess it on all the AOIs.

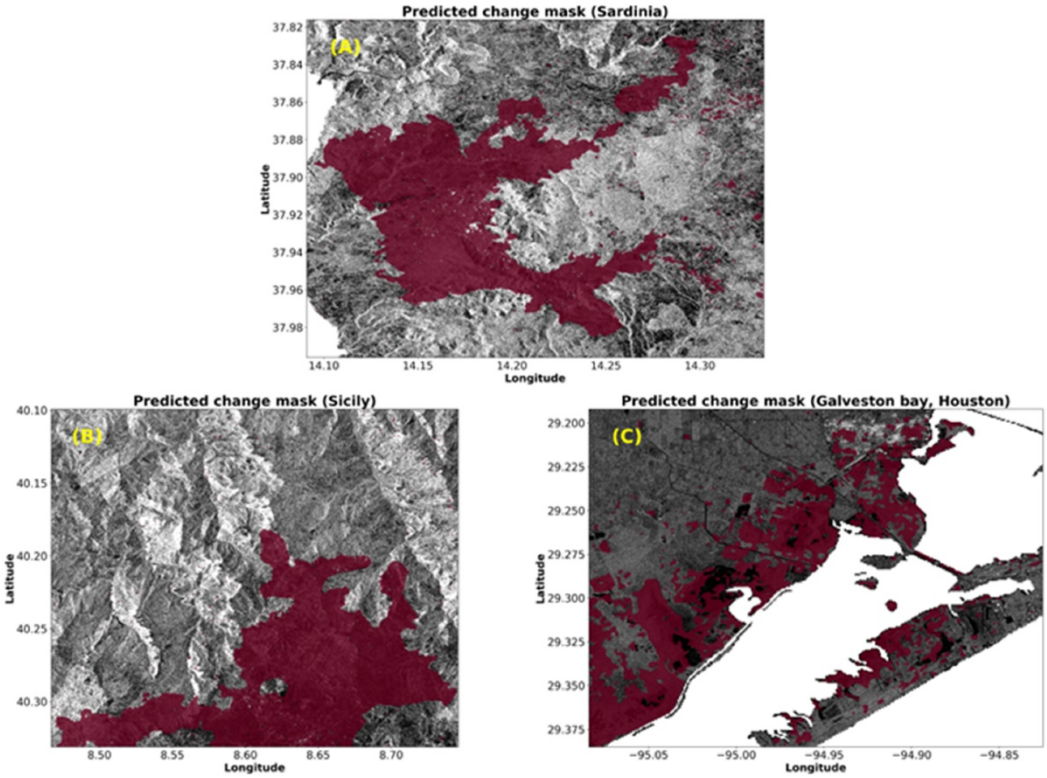

Figure 95. RF predicted binary change masks (coloured in red) of the (A) Sardinia, (B) Sicily, and (C) Texas, Galveston Bay AOIs, respectively. Change masks are superimposed over SAR amplitude images of the areas.

Figure 95 shows the RF predicted change masks. By a spatial comparison with the binary change mask used as truth, the RF model can identify the area related to the wildfire and flooding events very well. However, it is also clear that misclassifying regions is generated by the proposed method. This is due to the presence of speckle noise consistently in each AOIs analyzed. I used the confusion matrix (CM) test to quantitatively examine the RF prediction performance.

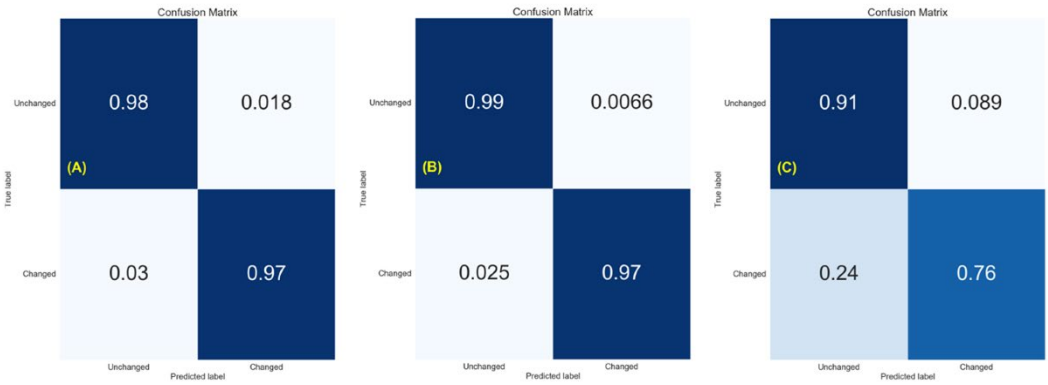

Figure 96. Confusion matrices of the (A) Sardinia, (B) Sicily, and (C) Texas, Galveston Bay AOIs, respectively.

Confusion matrices of the tested AOIs are shown in Figure 96. From their analysis, it is very straightforward to note the goodness of the proposed method. I want to remark that the probability values reported in the confusion matrixes are calculated starting from available polygons of burned/changed areas; thus, errors due to incorrect knowledge of the true areas affected by changes can affect the reported estimates. In addition, starting from the information given by the confusion matrix, i) precision, ii) recall, and iv) F-1 scores have been determined. I reported these scores in Table 25.

Table 25. RF classification scores report for the Sardinia, Sicily and Texas AOIs.

	Sardinia				Sicily				Texas			
	N#	Precision	Recall	F1	N#	Precision	Recall	F1	N#	Precision	Recall	F1
Unchanged (0)	3.164.393	0.99	0.98	0.99	2.108.222	0.99	0.99	0.99	2.726.416	0.96	0.91	0.93
Changed (1)	955.933	0.94	0.97	0.96	672.808	0.98	0.97	0.98	439.280	0.58	0.76	0.65
Weighted avg.	4.120.326	0.98	0.98	0.98	2.781.030	0.99	0.99	0.99	3.165.696	0.91	0.89	0.90

Analyzing the results shown in Table 25, from the precision and recall scores of the classification of unchanged/changed pixels, is evident to note that the RF model expresses very high change detection capacity in all the three analyzed areas. F1 scores are also very high. In particular, for the Texas case the F1 scores indicate that the proposed RF model is able to identify changes with high precision and accuracy in new unseen areas afflicted by a different phenomenon.

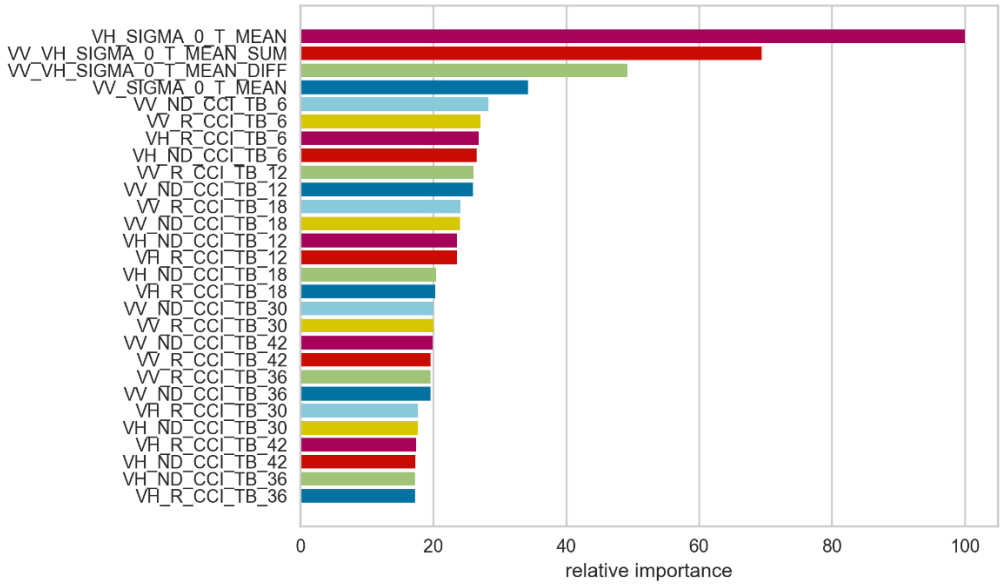

Figure 97. Ranking of features essential for the proposed RF model calculated on Sardinia, Sicily and Houston AOIs, respectively.

Finally, I determined how much each selected feature contributes to the classification of changed, unchanged pixels in the analyzed phenomenon using the RF feature importance statistic. Figure 97 shows that among the coherent and incoherent set of features, the incoherent temporal multi-look VH map significantly contributes to the final estimate. The sum follows this, and the difference of mutual sigma naught ratio maps between different polarization is also relevant. Features related to CCIs also make a high contribution. The ranking of importance reported in Figure 97 further confirms that, for what attains the SAR backscattered returns, the cross-polarization channel is more sensitive than the co-polarization one to fire damages. This result is in good agreement with the findings of the work [354] where the authors demonstrated with theoretical observations and direct evidences with Sentinel-1 SAR data that the VH channel is more apt to detect fire disturbance scars and this outcome is ascribable to the associated reduction of the volumetric scattering contribution after a fire event. Furthermore, the results show that the sum of SAR backscattered signals (sigma naught) on the co-pol VV and cross-pol VH channels has a great importance in the final estimate of changed areas.

It is remarkable that the results of Figure 97 show that the coherent indices contribute to the final estimate of changed areas but with a less importance than information coming from incoherent indices. This finding was expected, being

known that coherence is more sensitive to subtle spatial-varying changes of ground properties over time after a disastrous event.

Summarizing, the importance rank of the different coherent layers for a fire-disturbed regions, which is described in Figure 97, demonstrates that:

i) Short temporal InSAR baselines are preferred to long-baselines because coherence rapidly varies after a primary event and tends to achieve a new (random) state, not linked to the primary event under investigation, just a few days after the event itself. This finding is in accordance with the fact that temporal decorrelation is sensitive not only to random changes (linked to the event) but also to composite ground and volumetric changes that determine a systematic decay of the coherence over time (see the model in Section 6.2.2).

ii) The normalized coherence difference has generally an enhanced importance than the coherence ratio. This finding was also expected and it is in agreement with theory (see Section 6.2.2); indeed, the normalized coherence difference $ND = \frac{\hat{\gamma}_{pre} - \hat{\gamma}_{ev}}{\hat{\gamma}_{pre} + \hat{\gamma}_{ev}}$ has the beneficial includes in a unique estimator the advantaged of the coherence difference and coherence ratio to discriminate and better isolate the random coherent components.

iii) The co-pol and cross-pol channels have almost the same importance, with a slight marked preference versus the co-pol VV polarization.

6.7 CONCLUSIONS AND FUTURE PERSPECTIVE

This work addressed a review of the theory of existing coherent and incoherent CD methodologies used to study and monitor ground surface changes that arise when a disaster event (i.e., wildfires or floods) occurs, using sequences of synthetic aperture radar (SAR) images. Then, I focused on new trends of evolution of the research branch on Change Detection with SAR data, by addressing specifically the emerging ML-driven CD approaches. I investigated the potential of different synthetic coherent/incoherent CDI's and their mutual interactions for the rapid mapping of "changed areas" relying on the joint exploitation of SAR sigma naught and interferometric coherence maps. A classifier based on RF has been trained

combining different information coming from coherent/incoherent CDIs in a unique corpus, over different AOIs characterized by wildfire and flood phenomena.

Specifically, the study of the Montiferru and Madonie wildfires showed that the combined use of different CDI's able to synthetically describe ground surface changes associated with a disaster event (i.e., the pre-, cross- and post-disaster phases) and RF classifier is a powerful way to quickly identify areas related to wildfire events and fast assessing fire damages. The proposed methodology has been also tested considering a flood event that interested the south of Texas in August of 2017, in the Galveston Bay, using S-1 SAR data. The goodness of RF CD performance is also demonstrated by a quantitative analysis using confusion matrix statistic that shows very high rate in identify changed and unchanged areas. The achieved F-1 scores of about 0.9 highlights the potential of RF methods in remote sensing CD tasks. As a result, our findings demonstrate that S-1 C-band SAR data can provide suitable information on fire and flood events over the most severely affected areas (the highest level of fire or flood damage), supporting how such systems can be a complementary source of data to optical one, in case of cloud covers or plumes due to extreme weather and fire events. As a further development, I intend to extend this research on change detection based on sets of heterogeneous optical and radar images. The inclusion of optical features and the fusion with the SAR one in RF forest classifier is expected to improve generalization performance (e.g., in flooded areas). Fine tuning and extensive exploitation of the proposed method on a large scale require the selection and processing of several independent SAR datasets and a heterogenous family of disasters (e.g., floods, droughts, extreme events, forest and vegetation disturbance, urban changes, earthquakes, volcano eruptions, man-made changes, etc.). This perspective is worth and is an issue to be investigated in the future.

Chapter 7

FURTHER ACTIVITIES

This chapter will briefly show and discuss additional research works actively carried out by me in the framework of SAR remote sensing analyses during the three-year Ph.D. period.

7.1 ADAPTIVE MULTILOOKING OF MULTITEMPORAL DIFFERENTIAL SAR INTERFEROMETRIC DATA STACK USING DIRECTIONAL STATISTICS

In [7], my research activities focused on the implementation of an innovative space-time adaptive multilooking technique that operates on a sequence of multitemporal, differential synthetic aperture radar interferograms is shown. The developed approach relies on the application of the fundamentals of directional statistics theory. At variance with other methods that identify the set of statistically homogenous pixels (SHPs) within a multilooking (complex averaging) window based on the statistics of the single-look-complex (SLC) SAR images, the proposed method is exclusively based on the analysis of the multitemporal sequence of full resolution DInSAR interferograms. The SHPs are then used to generate spatially adaptive multilooked interferograms both at the native, full-scale grid of the SLC images and at the multilooked resolution scale. The algorithm is effective and simple to implement, only requiring the availability of a sequence of full-scale differential SAR interferometry (DInSAR) interferograms.

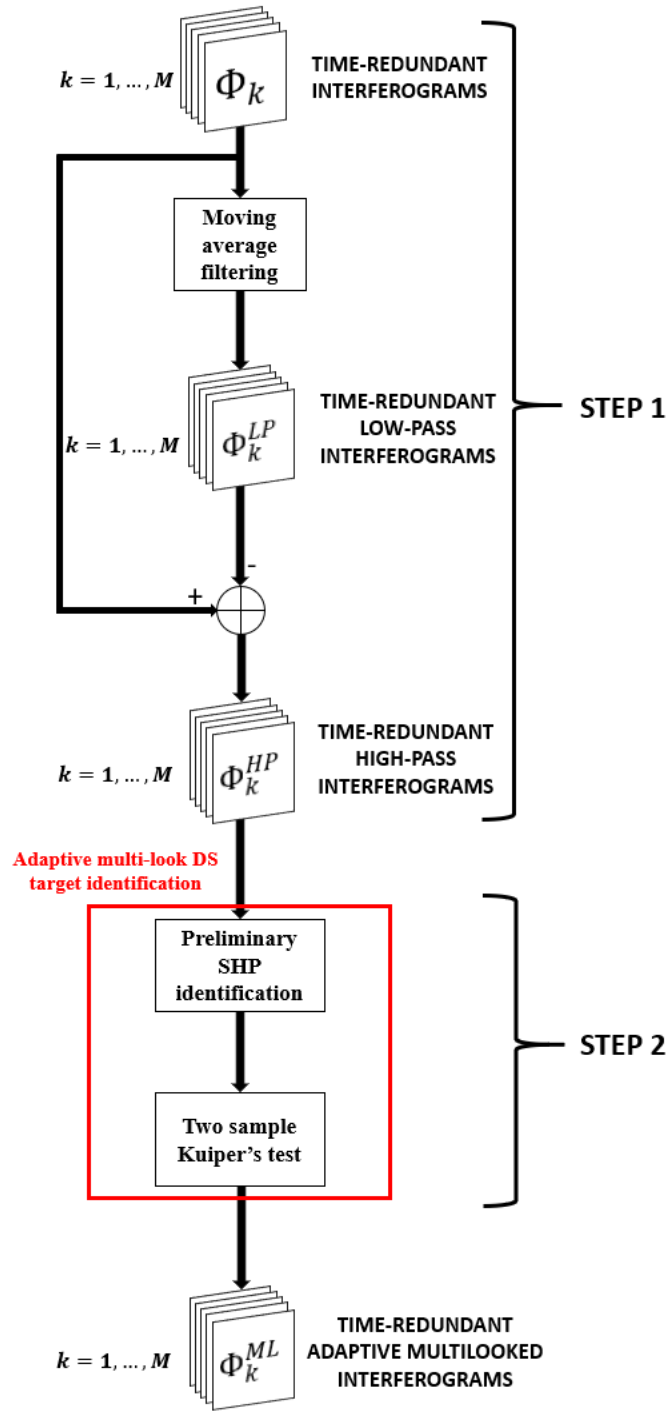

Figure 98. Block diagram of the proposed space–time adaptive multilooking technique.

The interferograms can then be used to generate ground displacement time-series through advanced multitemporal interferometric SAR (MTIn-SAR)

approaches. The whole process is pictorially represented in Figure 98. Experimental results obtained by applying the adopted technique to two SAR data sets acquired at X- and L-band, respectively, demonstrate the validity of the developed method.

The paper is the result of a cooperation between CNR and the Jet Propulsion Laboratory (JPL/NASA Caltech) and it has been published on Transaction of Geoscience and Remote Sensing in 2020[7].

7.2 An Adaptive Statistical Multi-grid DInSAR Technique for Studying Multi-scale Earth Surface Deformation Phenomena

In this study [9], focused my researches to address the potential of an adaptive quad-tree-based decomposition method applied to Differential Synthetic Aperture Radar (DInSAR) data is presented. Specifically, the proposed method exploits a multi-resolution scheme for the phase unwrapping of sequences of DInSAR interferograms and allows one to produce DInSAR deformation products at different scales of resolution (see Figure 99).

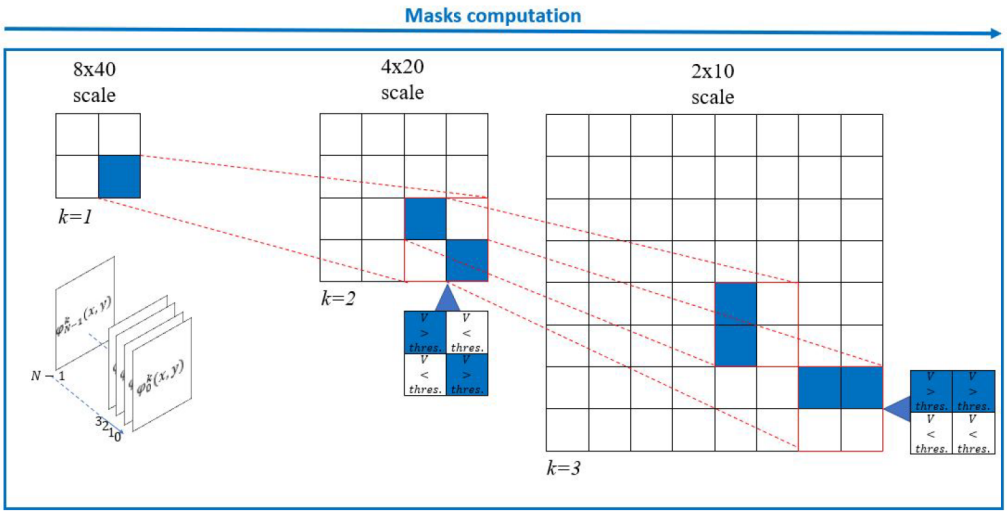

Figure 99. Adaptive quad-tree decomposition scheme.

The selection of the used multi-grid is based on the analysis of the statistical properties of a sequence of interferometric phase, allowing to recognizing major deformation areas where phase unwrapping operations can be performed more

efficiently, with a computational improvement and without losing significant information.

The presented analysis relies on a set of 60 SAR data acquired by the Sentinel 1A/B RADAR sensor over the Pearl River Delta (PRD) region, specifically the island of Hong Kong, from December 2017 to January 2019. Starting from these data, I generated a stack of 226 interferograms at three k different spatial scales (2×10 , 4×20 and 8×40 samples in azimuth and range, respectively) on which I have tested the proposed adaptive quadtree-based decomposition method.

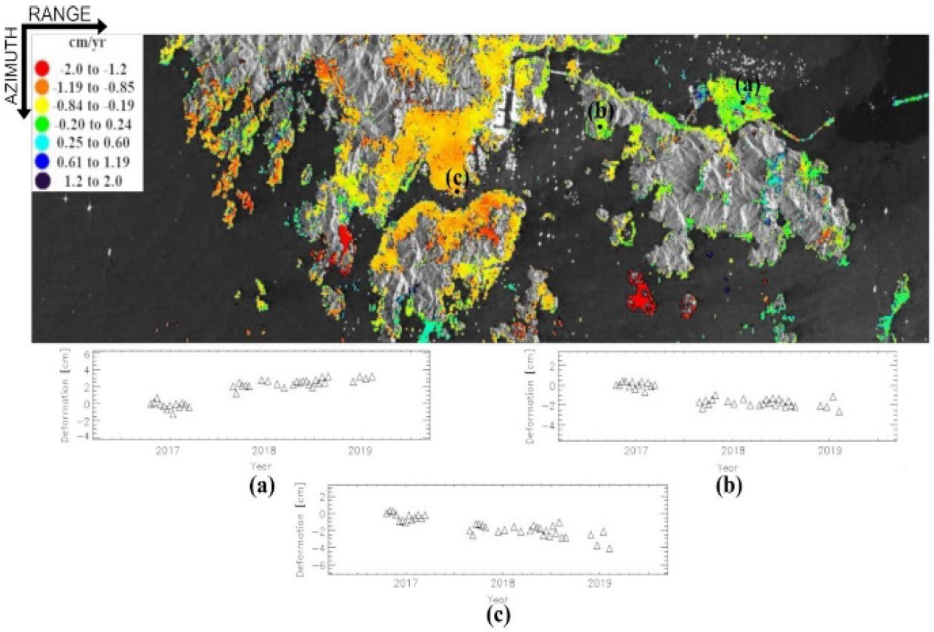

Figure 100. Hong Kong deformation time-series, (a) H.K. airport, (b) H.K. Disneyland and (c) H.K. city coastal area.

In Figure 100, the preliminary results of the developed multi-grid method is presented by showing the time-series of deformation and the mean deformation velocity map of the Hong Kong area. Particularly, in the temporal analysis performed at 2×10 resolution scale, I have focused on three man-made lands of Hong Kong area, reclaimed from the sea that is major characterized by subsidence phenomena: Hong Kong airport (Figure 100 A), Hong Kong Disneyland (Figure 100 B) and Hong Kong city coastal area (Figure 100 C). As a result, I discuss the improvement, in terms of data reduction that is guaranteed by the proposed multi-grid PhU methods, based on the adaptive selection of the pixels with slow varying deformation signals moving from a less-resolute to a more-resolute scale (bottom-

up approach). In particular, in the Hong Kong case study, the adaptive exploitation of the circular variance statistic, allowed us to efficiently identify at different resolution scales k masks of consistent pixels, related to areas characterized by significant deformation gradients, so as not to take into account other areas not characterized by any significant deformation gradient (e.g., oceanic areas or other where there is no subsidence phenomena).

Figure 101. Data reduction improvement bar chart.

Overall, an average improvement of about 85% has been registered in terms of data reduction (data that does not represent significant information in terms of deformation gradient signature) at every resolution scale k for the PhU operation (see Figure 101).

The results and analyses made in this work were presented and published at the 2020 IEEE International Geoscience and Remote Sensing Symposium (IGARSS) conference [9].

7.3 The Triplet Network Enhanced Spectral Diversity (T-NESD) Method for the Correction of TOPS Data Co-registration Errors for Non-Stationary Scenes

In this work [8], my research activities focused on the implementation of a novel approach for the correction of misregistration errors in sequences of Terrain Observation with Progressive Scan (TOPS) Sentinel-1 SAR data is presented. The method represents a further evolution of the Enhanced Spectral Diversity (ESD) approaches. Remarkably, the developed algorithm is almost insensitive to the presence of large azimuth ground displacements due, for instance, to massive earthquakes, volcanic eruptions or glacier movements. Indeed, in such non-stationary contexts, the conventional ESD and network ESD approaches [269], [270], [355] for the SAR TOPS data co-registration reveals problematic being co-registration errors and azimuth ground deformation components mixed out.

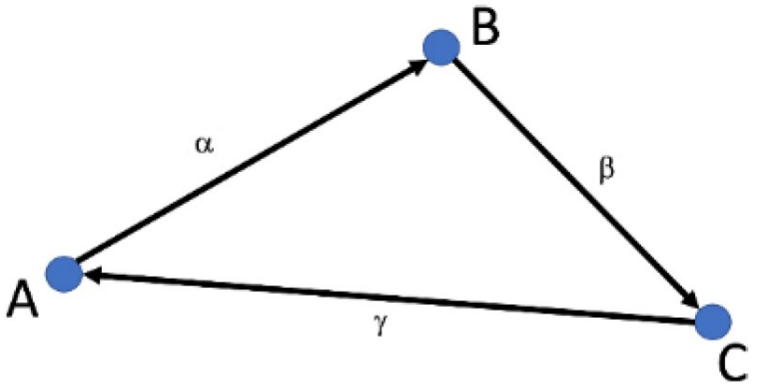

Figure 102. Closed loops scheme of three interferograms forming a SAR triplet.

In particular, the key idea of the proposed method is to compute the residual azimuth misregistration over closed loops of three interferograms forming a SAR triplet [253] (see Figure 102).

Preliminary experiments conducted on a set of TOP SAR data related to the area hit by the Ridgecrest earthquake MW 7.1, California, on July 04 2019 confirm the validity of the theoretical framework.

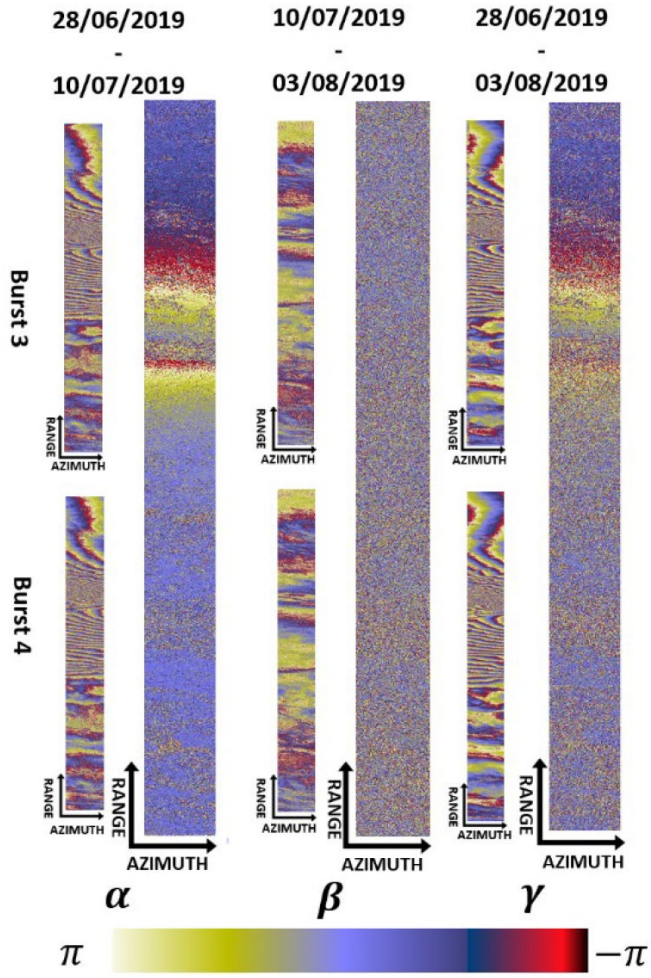

Figure 103. Intraburst interferograms, generated selecting the second swath, and the third and fourth bursts of the 28/06/2019-10/07/2019 (α), 10/07/2019-03/08/2019 (β), and 28/06/2019-03/08/2019 (γ) interferometric SAR data pairs.

Here, are presented some results achieved using the triplet, determined starting from three Sentinel-1 SAR acquisitions, collected on 06/28/2019, 07/10/2019, and 08/03/2019, in correspondence with the geophysical event that struck the Ridgecrest area in July 2019. The third and fourth bursts have been selected from the second swath of the Sentinel-1 scenes, because they are related to the epicenter area of the earthquake (see Figure 103).

In Figure 103; it is evident that the α and the γ intraburst differential interferograms are representative of the non-stationary case, where both the signals related to the along-track deformation and the residual misregistration errors are present. Conversely, the differential intraburst β interferogram, representative of

the stationary case, only exhibits the signal related to the residual (constant) misregistration error.

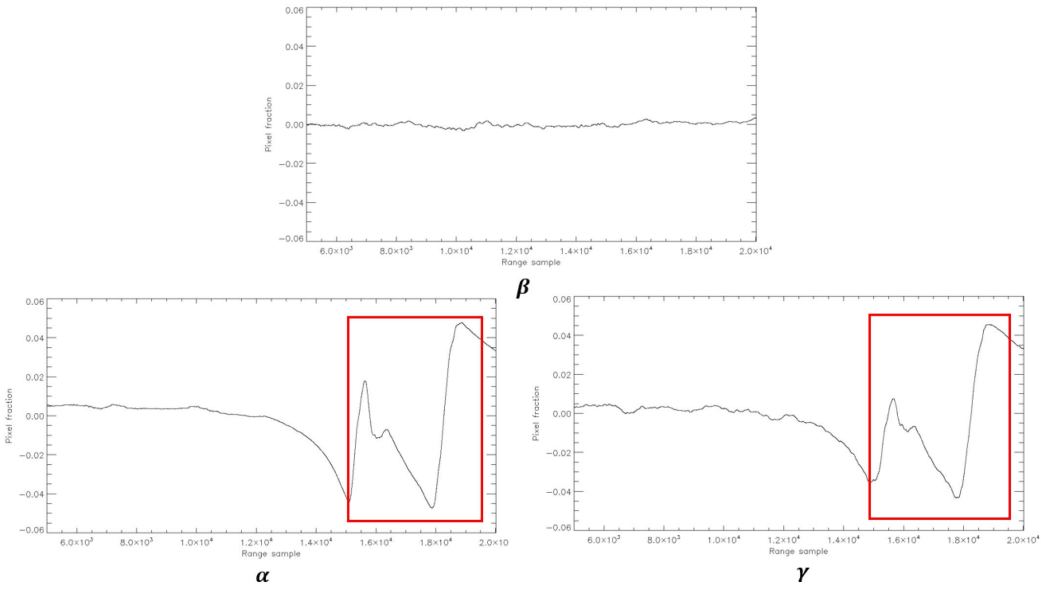

Figure 104. Plots of the mean α, β and γ azimuth intraburst misalignment errors vs. range direction.

These behaviours are confirmed plotting the mean value of the misregistration azimuth error of the three intraburst differential interferograms (see Figure 104). As evident, in the non-stationary case, the azimuth misalignments are pixel-dependent (highlighted by the red boxes), whereas in the stationary case, the azimuth shifts do not have a trend.

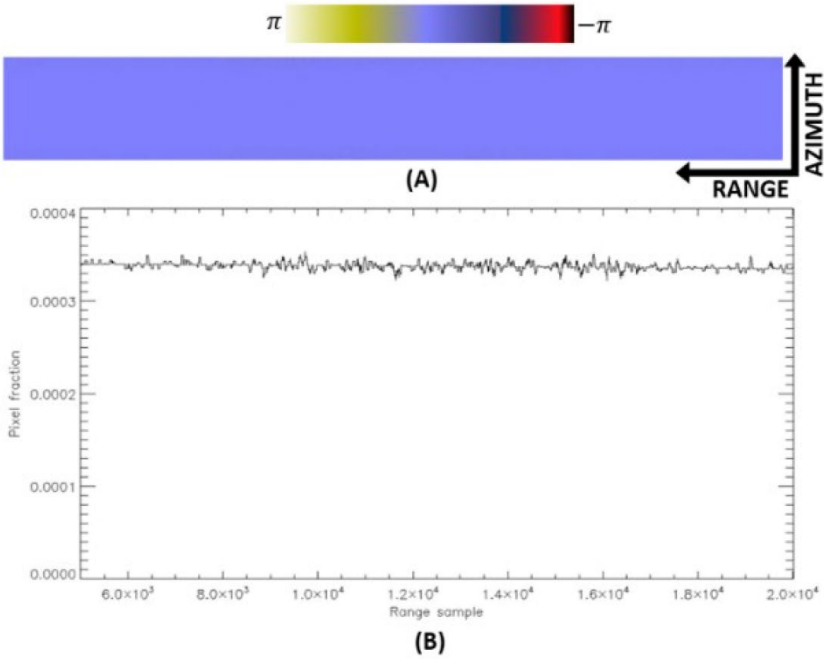

Figure 105. (A) Residual intraburst interferometric phase and (B) azimuth misregistration error over the closed triplet

Finally, following the scheme depicted in Figure 102, the residual intraburst phase and the azimuth misregistration error over the triplet is determined, see Figure 105. It is remarkably, these phase residuals do not contain any information related to the (along-track) azimuth displacement induced by the earthquake.

The results and analyses made in this work were presented and published at the 2021 IEEE International Geoscience and Remote Sensing Symposium (IGARSS) conference [8].

7.4 Analysis of Groundwater Depletion/Inflation and Freeze–Thaw Cycles in the Northern Urumqi Region with the SBAS Technique and an Adjusted Network of Interferograms

In this work [10], my research activities focused on an investigation of the ground deformation of the Northern Urumqi region, China. The presented analysis is based on applying the small baseline subset (SBAS) method [242]. Furthermore,

a new method for selecting a suitable set of small baseline (SB) interferometric SAR data pairs to be used by the SBAS algorithm. Usually, the interferometric SAR data pairs are selected by merely imposing a threshold on their maximum allowed temporal and perpendicular baselines [242]. However, this selection strategy can lead to some high-quality interferograms being discarded or some low-quality ones being included in actual cases. Some approaches for selecting optimal sets of SB interferograms have already been proposed in the literature [247], [253], [356]–[360]. In particular, the minimum spanning tree (MST) algorithm was used to determine a set of optimized interferograms using a quasi-PS (QPS) method in [356], [357]. The use of a simulated annealing algorithm was proposed in [247] for the optimal selection of a triangular network of SB interferograms that were exploited by the space–time minimum cost flow (EMCF) phase unwrapping algorithm [253]. Graph theory (GT) and a variance–covariance matrix of observations was used in [358] to identify sets of interferograms less influenced by turbulent atmosphere phase artifacts. The semiautomatic selection of optimum image pairs was also proposed in[359], using the coherence of point targets based on a small feature region. A higher coherence pixel density of interferograms through eigenvalue decomposition was introduced in [360].

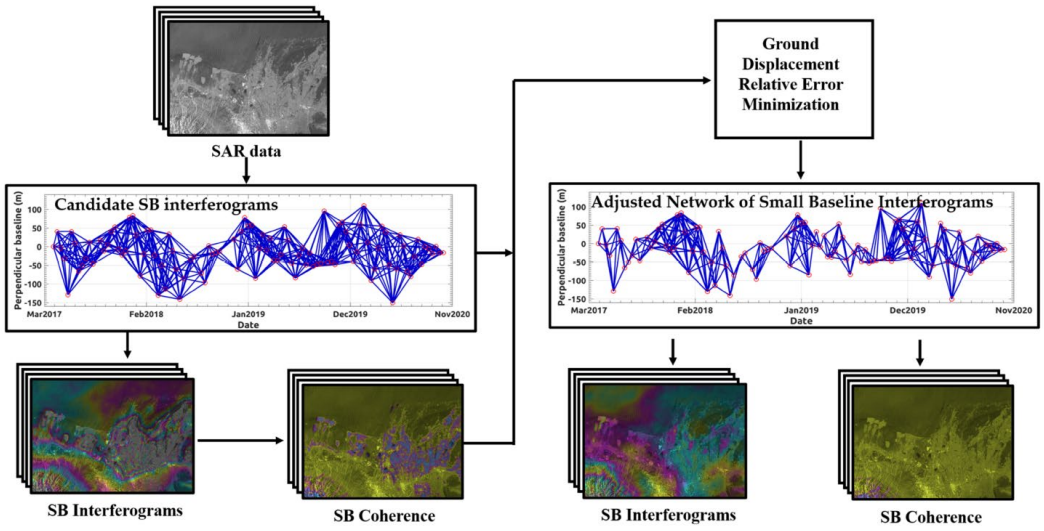

Figure 106. Flowchart of the developed SB interferogram selection algorithm.

The SB interferometric selection algorithm proposed in this work was aimed at selecting SB interferograms that would minimize the mean ground deformation velocity relative error. Toward that aim, the average spatial coherence of the chosen interferograms and the connectivity of their network were taken into account at the same time.

Specifically, the method consists of 3 distinctive steps to determine the optimal set of SB interferograms, which is briefly summarized as follows:

I. Generate a pool of (candidate) multi-look SB interferograms and the relevant coherence maps. Candidate SB data pairs are initially selected by considering a reasonably large threshold for the temporal and perpendicular baselines of the interferograms.

I. Estimate the optimal value of a coherence threshold, namely $\gamma_{critical}$ and discard the multi-look SAR interferograms with an average spatial coherence smaller than $\gamma_{critical}$

II. Apply the SBAS procedure [242] to the selected set of optimal SB SAR data pairs, selected using the optimal coherence threshold $\gamma_{critical}$.

Figure 106 shows the block diagram of the developed SB interferogram selection algorithm.

The work benefits from the primary outcomes of a recent investigation [361] that addressed the error budget analysis of SB Mt-InSAR techniques. Experiments were carried out on 102 pieces of Sentinel-1B SAR data collected from 12 April 2017 to 29 October 2020. Starting from the available SAR data, a group of optimal SB interferograms was adequately selected and used within the SBAS processing. As a result, in the region of maximum deformation, a ground subsidence velocity of about 120 mm/year and seasonal amplitude displacement of about 120 mm was revealed.

The principal achievement of this work is that the developed interferogram selection method allows to minimize the relative error of mean ground displacement velocity measurements, demonstrating that the accuracy of SBAS ground deformation time series improves when an optimal network of SB interferograms is used. Finally, the above analyses and results were discussed in a paper that has been published on Remote Sensing journal [10].

7.5 RECENT ADVANCEMENTS IN MULTI-TEMPORAL METHODS APPLIED TO NEW GENERATION SAR SYSTEMS AND APPLICATIONS IN SOUTH AMERICA

Detection and continuous monitoring of Earth's ground surface changes, triggered by natural phenomena or induced by human activities, is nowadays possible using Earth Observation (EO) technologies. Indeed, the exploitation of remotely sensed data collected by constellations of new-generation satellite

platforms, complemented with in-situ measurements and ground-based observation systems, represents a well-established practice to get valuable information on Earth's crust and subsurface dynamics. The effects of extreme natural or man-induced events (e.g., earthquakes, volcanic eruptions, flooding phenomena, sea-level rise, big fires, etc.) have severe societal and economic impacts. In particular, the technologies based on the use of Synthetic Aperture Radar (SAR) images reached significant improvements in the last decade due to the growing availability of vast amounts of data collected by multiple-satellite sensors operating at different frequency bands and with complementary viewing angles, polarization and acquisition modes. Accordingly, to process a large amount of SAR data in a timely fashion, up-to-date high-performance computing (HPC) methods and tools are required. In [207] my research activities focused on addressing the state-of-the-art of SAR technologies for the analysis of long sequences of multiple sets of SAR images and providing a perspective on the forthcoming improvements of these technologies. In particular, the emphasis is placed on novel interferometric SAR and change detection methods, giving an overview of how those processing techniques have been used for investigating sites located in South and Central America. Moreover, an overview of the new generation of SAR sensors' observational capability, especially in the field of ground deformation analysis for mitigating the risk associated with natural and human-induced hazards, is provided. COSMO-SkyMed, ALOS, Sentinel-1, and SAOCOM data are exploited to show how natural and human-induced terrain displacement phenomena can be detected and investigated in different portions (X-, L- and C-band) of the microwave spectrum using SAR technologies.

The results of the analyses presented in this paper provide important information on the joint exploitation of the different operational bands, polarimetric channels, and orbits of SAR systems. Therefore, they represent a basis for future studies for optimized processing and analysis of tons of SAR images to be collected by next-generation SAR sensor constellations.

The paper is the result of a cooperation between CNR and the Universidad Nacional de Cuyo, Facultad de Ingeniería, Instituto CEDIAC & CONICET (Argentina) and it has been published in the Journal of South American Earth Sciences in 2021 [11].

Chapter 8

CONCLUSIONS

My P.h.D. research activities, which have been summarized in this thesis, have been devoted to developing and applying innovative remote sensed data inversion techniques and algorithms for the study of physical phenomena that characterize the Earth's atmosphere and the surface of our planet.

Against this background, the central question was to investigate the potential application of ML methodologies to address, at most, the following issues:

1) The characterization of clouds in terms of their microphysical key parameters (e.g., the CLWC and CIWC profiles, their corresponding CLWP and CIWP vertical integrated paths, and their effective drop radii) by the synergic use of satellite observation in IR and MW bands;
2) The study and analysis of Earth's surface changes by the use of coherent and incoherent information gathered from sets of multi-temporal SAR acquisitions.

The former was addressed by me during the research activities carried out within the ComboCloud project funded by EUMETSAT. In this scenario, this thesis aimed to design, prototype, and validate a regression framework based on ML for cloud products using MW and IR measurements in synergy. Validation with simulated and real observations demonstrates qualitatively and quantitatively the value of combining ML-based regression methodologies and MW and IR observations from optical satellite sensors to retrieve cloud properties. The synergistic retrievals demonstrate the combined sensitivity of MW and IR to cloud properties, thus outperforming the performances achievable by either one alone. In addition, the analysis of the results demonstrated the added value and promising performance of future EPS-SG sensors (IASI-NG and MWS) compared with currently available EPS-FG sensors (IASI and AMSU/MHS), opening opportunities for more comprehensive exploitation of these platforms for weather and climate. ML-based solutions played a central role in the achieved results. They have been observed to be superior to state-of-the-art solutions already present in the

literature. A role that was also confirmed in exercises involving cloud classification and atmospheric methane profiling.

The second has concerned an in-depth analysis of the role played by modern SAR instruments that permit to continuously monitor the Earth's surface and recover from the analysis of the recorded (complex) backscattered signals valuable information permitting to characterize and partly prevent the effects of disastrous natural and man-made conditions that affect Earth's surface. In this context, the exploitation of ML classification methodologies for handling the different information coming from coherent/incoherent systems, including both amplitude-based and InSAR analyses, represents one of the present-day challenges for the reference scientific community. The developed methods and applications, complemented with those considered for the study of Earth's atmosphere, could potentially lead to further insights and open new possibilities in the next coming years. Indeed, a new acceleration in the knowledge is expected with the advent of new SAR systems with almost daily acquisition repeat times (i.e., the geosynchronous systems) and the deployment of a constellation of micro-SAR satellites. All the innovative methods presented in this Ph.D. thesis, especially those that integrate conventional and AI-based approaches as well as RS data collected at different microwave bands, will surely have a significant role in the next decades to face expected new technological challenges.

ACRONYMS

AATSR	Advanced Along-Track Scanning Radiometer
AER	Atmospheric and Environmental Research
AI	Artificial Intelligence
AID	Algorithm for Ice cloud Detection aided by Support Vector Machine
AIRS	Atmospheric Infrared Sounder
AMSR	Advanced Microwave Sounding Radiometer
AMSU	Advanced Microwave Sounding Unit
ANN	Artificial Neural Network
AOI	Area Of Interest
ARTS	Atmospheric Radiative Transfer Simulator
ASAR	Advanced Synthetic Aperture Radar
ASTEX	Atlantic Stratocumulus Transition Experiment
ATMS	Advance Technology Microwave Sounder
AVHRR	Advanced Very High-Resolution Radiometer
BFEMIS	Baseline Fit Emissivity Database
BT	Brigthness Temperature
BTD	Brightness Temperature Difference
CALIOP	Cloud-Aerosol Lidar with Orthogonal Polarization
CALIPSO	Cloud-Aerosol Lidar and Infrared Pathfinder Satellite Observations
CART	Classification and Regression Trees
CCI	Coherence Changes Indexes
CD	Change Detection
CDI	Change Detection Indices
CERES	Clouds and the Earth's Radiant Energy System
CIWC	Cloud Ice Water Content
CIWP	Cloud Ice Water Path

CLWC	Cloud Liquid Water Content
CLWP	Cloud Liquid Water Path
CM	Climate Monitoring
COT	Cloud Optical Thickness
CPP	Cloud Physical Properties
CR	Coherence Ratio
CRTM	Community Radiative Transfer Model
CTH	Cloud Top Height
CTP	Cloud Top Pressure
DARDAR	raDAR/liDAR
DC	Doppler Centroid
ECMWF	European Centre for Medium-Range Weather Forecasts
EOF	Empirical Orthogonal Function
EPS	EUMETSAT Polar System
ERA	Enhanced Retrieval of Aerosol
ERS	European Remote-Sensing Satellite
EUMETSAT	European operational satellite agency for monitoring weather
EFFIS	European Forest Fire Information System
FM	Forward Model
FOV	Field Of View
FTIR	Fourier-Transform Infrared
HIRS	High resolution Infrared Radiation Sounder
HIS	High-resolution Interferometer Sounder
IASI	Infrared atmospheric sounding interferometer
IASI-NG	Infrared atmospheric sounding interferometer Next Generation
IFOV	Instantaneous Field of View
IFS	Integrated Forecast System
IR	Infrared
IW	Interferometric Wide
LBLRTM	Line By Line Radiative Transfer Model

LOS	Line of Sigth
MACC	Monitoring Atmospheric Composition and Climate
MAI	Multiple Aperture Interferometry
METOP	Meteorological Operational satellite programme
MHS	Microwave Humidity Sounder
MIRS	Microwave Integrated Retrieval System
ML	Machine Learning
MLC	Maximum Likelihood Classification
MLCD	Machine Learning based Change Detection
MLO	Mauna Loa Observatory
MLP	Multilayer Perceptron
MMW	Millimeter-Wave
MODIS	Moderate Resolution Imaging Spectroradiometer
MR	Minimum Residual
MSE	Mean Squared Error
MSG	Meteosat Second Generation
MSPPS	Microwave Surface and Precipitation Products System
MVI	Microwave, Visible, and Infrared
MW	Microwave
MWS	Microwavee Sounder
NASA	National Aeronautics and Space Administration
ND	Normalized Coherence Difference Ratio
NDACC	Network for the Detection of Atmospheric Composition Change
NESD	Network based Enhanced Spectral Diversity
NL	Number of Looks
NN	Neural Network
NOAA	National Oceanic and Atmospheric Administration
NUCAPS	NOAA Unique Combined Atmospheric Processing System
NWP	Numerical Weather Prediction
OBCT	Onboard Calibration Target

OSCAR	Observing Systems Capability Analysis and Review Tool
OSSE	Observing-System Simulation Experiments
PC	Principal Component
PCA	Principal Component Analysis
PCRTM	Principal Component Radiative Transfer Model
PRF	Pulse Repetition Frequency
QH	Quasi Horizontal
QV	Quasi Vertical
RADAR	Radio Detection and Ranging
RF	Random Forest
RMSE	Root Mean Squared Error
ROC	Receiver Operating Characteristic
RTE	Radiative Transfer Equation
RTM	Radiative Transfer Model
RTTOV	Radiative Transfer for TOVS
SAF	Satellite Application Facility
SAR	Synthetic Aperture Radar
SB	Small Baseline
SBAS	Small Baseline Subset
SD	Spectral Diversity
SEVIRI	Spinning Enhanced Visibile and Infrared Imager
SGD	Stochastic Gradient Descent
SSM/I	Special Sensor Microwave/Imager
SVD	Singular Valued Decomposition
SVM	Support Vector Machine
SW	Software
TIR	Termal Infrared
TOA	Top of Atmosphere
TOPS	Terrain Observation with Progressive Scans
TPW	Total Precipitable Water

VIS	Visible
VZA	Vertical Zenith Angle
WMO	World Meteorological Organization

REFERENCES

[1] P. Mastro *et al.*, «Combined IASI-NG and MWS Observations for the Retrieval of Cloud Liquid and Ice Water Path: A Deep Learning Artificial Intelligence Approach», *IEEE Journal of Selected Topics in Applied Earth Observations and Remote Sensing*, vol. 15, pp. 3313–3322, 2022, doi: 10.1109/JSTARS.2022.3166992.

[2] P. Mastro *et al.*, «Cloud liquid and ice water content estimation from satellite: a regression approach based on neural networks», in *Remote Sensing of Clouds and the Atmosphere XXVI*, set. 2021, vol. 11859, pp. 52–64. doi: 10.1117/12.2600124.

[3] P. Mastro *et al.*, «On the synergic use of satellite microwave and infrared measurements for the estimation of effective radius of ice and liquid water clouds: a regression approach based on random forests», in *Remote Sensing of Clouds and the Atmosphere XXVII*, Berlin, set. 2022.

[4] G. Masiello, P. Mastro, C. Serio, F. Falabella, e P. Pasquariello, «Methane profile retrieval from IASI: a deep learning inversion approach based on feed-forward neural networks», in *Remote Sensing of Clouds and the Atmosphere XXVII*, Berlin, ott. 2022.

[5] P. Mastro, P. Pasquariello, G. Masiello, e C. Serio, «Cloud detection from IASI hyperspectral data: a statistical approach based on neural networks», in *Remote Sensing of Clouds and the Atmosphere XXV*, set. 2020, vol. 11531, pp. 40–49. doi: 10.1117/12.2573326.

[6] P. Mastro, G. Masiello, C. Serio, e A. Pepe, «Change Detection Techniques with Synthetic Aperture Radar Images: Experiments with Random Forests and Sentinel-1 Observations», *Remote Sensing*, vol. 14, fasc. 14, Art. fasc. 14, gen. 2022, doi: 10.3390/rs14143323.

[7] A. Pepe, P. Mastro, e C. E. Jones, «Adaptive Multilooking of Multitemporal Differential SAR Interferometric Data Stack Using Directional Statistics», *IEEE Transactions on Geoscience and Remote Sensing*, vol. 59, fasc. 8, pp. 6706–6721, ago. 2021, doi: 10.1109/TGRS.2020.3030003.

[8] P. Mastro e A. Pepe, «The Triplet Network Enhanced Spectral Diversity (T-NESD) Method for the Correction of TOPS Data Co-registration Errors for Non-Stationary Scenes», in *2021 IEEE International Geoscience and Remote Sensing Symposium IGARSS*, lug. 2021, pp. 2294–2297. doi: 10.1109/IGARSS47720.2021.9554439.

[9] P. Mastro, F. Falabella, e A. Pepe, «An Adaptive Statistical Multi-grid DInSAR Technique for Studying Multi-scale Earth Surface Deformation Phenomena», in *IGARSS 2020 - 2020 IEEE International Geoscience and Remote Sensing Symposium*, set. 2020, pp. 32–35. doi: 10.1109/IGARSS39084.2020.9324535.

[10] B. Wang *et al.*, «Analysis of Groundwater Depletion/Inflation and Freeze–Thaw Cycles in the Northern Urumqi Region with the SBAS Technique and an Adjusted Network of Interferograms», *Remote Sensing*, vol. 13, fasc. 11, Art. fasc. 11, gen. 2021, doi: 10.3390/rs13112144.

[11] P. Euillades *et al.*, «Recent advancements in multi-temporal methods applied to new generation SAR systems and applications in South America», *Journal of South American Earth Sciences*, vol. 111, p. 103410, nov. 2021, doi: 10.1016/j.jsames.2021.103410.

[12] P. Mastro, C. Serio, G. Masiello, e A. Pepe, «The Multiple Aperture SAR Interferometry (MAI) Technique for the Detection of Large Ground Displacement Dynamics: An Overview», *Remote Sensing*, vol. 12, fasc. 7, Art. fasc. 7, gen. 2020, doi: 10.3390/rs12071189.

[13] Q. Zhao *et al.*, «Integrated Analysis of the Combined Risk of Ground Subsidence, Sea Level Rise, and Natural Hazards in Coastal and Delta River Regions», *Remote Sensing*, vol. 13, fasc. 17, Art. fasc. 17, gen. 2021, doi: 10.3390/rs13173431.

[14] C. Serio, G. Masiello, P. Mastro, e D. C. Tobin, «Characterization of the Observational Covariance Matrix of Hyper-Spectral Infrared Satellite Sensors Directly from Measured Earth Views», *Sensors*, vol. 20, fasc. 5, Art. fasc. 5, gen. 2020, doi: 10.3390/s20051492.

[15] J. E. Hansen e L. D. Travis, «Light scattering in planetary atmospheres», *Space Sci Rev*, vol. 16, fasc. 4, pp. 527–610, ott. 1974, doi: 10.1007/BF00168069.

[16] A. J. Heymsfield e J. Iaquinta, «Cirrus Crystal Terminal Velocities», *Journal of the Atmospheric Sciences*, vol. 57, fasc. 7, pp. 916–938, apr. 2000, doi: 10.1175/1520-0469(2000)057<0916:CCTV>2.0.CO;2.

[17] A. J. Heymsfield e C. M. R. Platt, «A Parameterization of the Particle Size Spectrum of Ice Clouds in Terms of the Ambient Temperature and the Ice Water Content», *Journal of the Atmospheric Sciences*, vol. 41, fasc. 5, pp. 846–855, mar. 1984, doi: 10.1175/1520-0469(1984)041<0846:APOTPS>2.0.CO;2.

[18] J. C. Alishouse *et al.*, «Determination of cloud liquid water content using the SSM/I», *IEEE Transactions on Geoscience and Remote Sensing*, vol. 28, fasc. 5, pp. 817–822, set. 1990, doi: 10.1109/36.58968.

[19] P. Bauer e P. Schluessel, «Rainfall, total water, ice water, and water vapor over sea from polarized microwave simulations and Special Sensor Microwave/Imager data», *Journal of Geophysical Research: Atmospheres*, vol. 98, fasc. D11, pp. 20737–20759, 1993, doi: 10.1029/93JD01577.

[20] F. Weng, N. C. Grody, R. Ferraro, A. Basist, e D. Forsyth, «Cloud Liquid Water Climatology from the Special Sensor Microwave/Imager», *Journal of Climate*, vol. 10, fasc. 5, pp. 1086–1098, mag. 1997, doi: 10.1175/1520-0442(1997)010<1086:CLWCFT>2.0.CO;2.

[21] Y. Han e E. R. Westwater, «Remote Sensing of Tropospheric Water Vapor and Cloud Liquid Water by Integrated Ground-Based Sensors», *Journal of Atmospheric and Oceanic Technology*, vol. 12, fasc. 5, pp. 1050–1059, ott. 1995, doi: 10.1175/1520-0426(1995)012<1050:RSOTWV>2.0.CO;2.

[22] L. Zhao e F. Weng, «Retrieval of Ice Cloud Parameters Using the Advanced Microwave Sounding Unit», *Journal of Applied Meteorology (1988-2005)*, vol. 41, fasc. 4, pp. 384–395, 2002.

[23] R. R. Ferraro *et al.*, «NOAA operational hydrological products derived from the advanced microwave sounding unit», *IEEE Transactions on Geoscience and Remote Sensing*, vol. 43, fasc. 5, pp. 1036–1049, mag. 2005, doi: 10.1109/TGRS.2004.843249.

[24] F. Weng, L. Zhao, R. R. Ferraro, G. Poe, X. Li, e N. C. Grody, «Advanced microwave sounding unit cloud and precipitation algorithms», *Radio Science*, vol. 38, fasc. 4, 2003, doi: 10.1029/2002RS002679.

[25] P. W. Rosenkranz, «Cloud liquid-water profile retrieval algorithm and validation», *Journal of Geophysical Research: Atmospheres*, vol. 111, fasc. D9, 2006, doi: 10.1029/2005JD005832.

[26] Q. Liu e F. Weng, «One-dimensional variational retrieval algorithm of temperature, water vapor, and cloud water profiles from advanced microwave sounding unit (AMSU)», *IEEE Transactions on Geoscience and Remote Sensing*, vol. 43, fasc. 5, pp. 1087–1095, mag. 2005, doi: 10.1109/TGRS.2004.843211.

[27] F. S. Marzano *et al.*, «Flower Constellation of Millimeter-Wave Radiometers for Tropospheric Monitoring at Pseudogeostationary Scale», *IEEE Transactions on Geoscience and Remote Sensing*, vol. 47, fasc. 9, pp. 3107–3122, set. 2009, doi: 10.1109/TGRS.2008.2012349.

[28] F. S. Marzano, D. Cimini, T. Rossi, D. Mortari, S. D. Michele, e P. Bauer, «High-Repetition Millimeter-Wave Passive Remote Sensing of Humidity and Hydrometeor Profiles from Elliptical Orbit Constellations», *Journal of Applied Meteorology and Climatology*, vol. 49, fasc. 7, pp. 1454–1476, lug. 2010, doi: 10.1175/2010JAMC2329.1.

[29] F. S. Marzano e D. Cimini, «Flower elliptical-orbit constellation exploiting millimetre-wave radiometry and radio occultation for meteo-climatological applications», *Advances in Geosciences*, vol. 25, pp. 167–177, 2010, doi: 10.5194/adgeo-25-167-2010.

[30] L. P. Bobylev, E. V. Zabolotskikh, L. M. Mitnik, e M. L. Mitnik, «Atmospheric Water Vapor and Cloud Liquid Water Retrieval Over the Arctic Ocean Using Satellite Passive Microwave Sensing», *IEEE Transactions on Geoscience and Remote Sensing*, vol. 48, fasc. 1, pp. 283–294, gen. 2010, doi: 10.1109/TGRS.2009.2028018.

[31] S.-A. Boukabara *et al.*, «A physical approach for a simultaneous retrieval of sounding, surface, hydrometeor, and cryospheric parameters from SNPP/ATMS», *Journal of Geophysical Research: Atmospheres*, vol. 118, fasc. 22, p. 12,600-12,619, 2013, doi: 10.1002/2013JD020448.

[32] P. Dong, F. Weng, Q. Huang, Y. Han, e W. Han, «Estimation of cloud liquid water over oceans from dual oxygen absorption band to support the assimilation of second generation of microwave observation on board the Chinese FY-3 satellite», *International Journal of Remote Sensing*, vol. 38, fasc. 18, pp. 5003–5021, set. 2017, doi: 10.1080/01431161.2017.1331056.

[33] N. Grody, J. Zhao, R. Ferraro, F. Weng, e R. Boers, «Determination of precipitable water and cloud liquid water over oceans from the NOAA 15 advanced microwave sounding unit», *Journal of Geophysical Research: Atmospheres*, vol. 106, fasc. D3, pp. 2943–2953, 2001, doi: 10.1029/2000JD900616.

[34] J. Yang, F. Weng, H. Hu, e P. Dong, «Retrieval of the total precipitable water vapor and cloud liquid water path over ocean from the Feng-Yun 3D microwave temperature and humidity sounders», Clouds/Remote Sensing/Data Processing and Information Retrieval, preprint, dic. 2019. doi: 10.5194/amt-2019-447.

[35] S. Liu, C. Grassotti, e Q. Liu, «NOAA Microwave Integrated Retrieval System (MiRS) Cloud Liquid Water Retrieval and Assessment», in *2018 IEEE 15th Specialist Meeting on Microwave Radiometry and Remote Sensing of the Environment (MicroRad)*, Cambridge, MA, USA, mar. 2018, pp. 14–19. doi: 10.1109/MICRORAD.2018.8430719.

[36] W. J. Blackwell *et al.*, «An overview of the TROPICS NASA Earth Venture Mission», *Quart J Royal Meteoro Soc*, vol. 144, fasc. S1, pp. 16–26, nov. 2018, doi: 10.1002/qj.3290.

[37] S. C. Reising *et al.*, «An Earth Venture In-Space Technology Demonstration Mission for Temporal Experiment for Storms and Tropical Systems (Tempest)», in *IGARSS 2018 - 2018 IEEE International Geoscience and*

Remote Sensing Symposium, Valencia, lug. 2018, pp. 6301–6303. doi: 10.1109/IGARSS.2018.8517330.

[38] S. Fritz e J. S. Winston, «SYNOPTIC USE OF RADIATION MEASUREMENTS FROM SATELLITE TIROS II», *Monthly Weather Review*, vol. 90, fasc. 1, pp. 1–9, gen. 1962, doi: 10.1175/1520-0493(1962)090<0001:SUORMF>2.0.CO;2.

[39] W. P. Menzel, W. L. Smith, e T. R. Stewart, «Improved Cloud Motion Wind Vector and Altitude Assignment Using VAS», *Journal of Applied Meteorology and Climatology*, vol. 22, fasc. 3, pp. 377–384, mar. 1983, doi: 10.1175/1520-0450(1983)022<0377:ICMWVA>2.0.CO;2.

[40] W. L. Smith e C. M. R. Platt, «Comparison of Satellite-Deduced Cloud Heights with Indications from Radiosonde and Ground-Based Laser Measurements», *Journal of Applied Meteorology and Climatology*, vol. 17, fasc. 12, pp. 1796–1802, dic. 1978, doi: 10.1175/1520-0450(1978)017<1796:COSDCH>2.0.CO;2.

[41] J. R. Eyre e W. P. Menzel, «Retrieval of Cloud Parameters from Satellite Sounder Data: A Simulation Study», *Journal of Applied Meteorology and Climatology*, vol. 28, fasc. 4, pp. 267–275, apr. 1989, doi: 10.1175/1520-0450(1989)028<0267:ROCPFS>2.0.CO;2.

[42] W. P. Menzel, T. J. Schmit, e D. P. Wylie, «Cloud characteristics over central Amazonia during GTE/ABLE 2B derived from multispectral visible and infrared spin scan radiometer atmospheric sounder observations», *Journal of Geophysical Research: Atmospheres*, vol. 95, fasc. D10, pp. 17039–17042, 1990, doi: https://doi.org/10.1029/JD095iD10p17039.

[43] P. Minnis, K.-N. Liou, e Y. Takano, «Inference of Cirrus Cloud Properties Using Satellite-observed Visible and Infrared Radiances. Part I: Parameterization of Radiance Fields», *Journal of the Atmospheric Sciences*, vol. 50, fasc. 9, pp. 1279–1304, mag. 1993, doi: 10.1175/1520-0469(1993)050<1279:IOCCPU>2.0.CO;2.

[44] T. Nakajima e M. D. King, «Determination of the Optical Thickness and Effective Particle Radius of Clouds from Reflected Solar Radiation Measurements. Part I: Theory», *Journal of the Atmospheric Sciences*, vol. 47, fasc. 15, pp. 1878–1893, ago. 1990, doi: 10.1175/1520-0469(1990)047<1878:DOTOTA>2.0.CO;2.

[45] M. D. King, «Determination of the Scaled Optical Thickness of Clouds from Reflected Solar Radiation Measurements», *Journal of the Atmospheric Sciences*, vol. 44, fasc. 13, pp. 1734–1751, lug. 1987, doi: 10.1175/1520-0469(1987)044<1734:DOTSOT>2.0.CO;2.

[46] T. Y. Nakajima e T. Nakajma, «Wide-Area Determination of Cloud Microphysical Properties from NOAA AVHRR Measurements for FIRE and

ASTEX Regions», *Journal of the Atmospheric Sciences*, vol. 52, fasc. 23, pp. 4043–4059, dic. 1995, doi: 10.1175/1520-0469(1995)052<4043:WADOCM>2.0.CO;2.

[47] Q. Han, W. B. Rossow, e A. A. Lacis, «Near-Global Survey of Effective Droplet Radii in Liquid Water Clouds Using ISCCP Data», *Journal of Climate*, vol. 7, fasc. 4, pp. 465–497, apr. 1994, doi: 10.1175/1520-0442(1994)007<0465:NGSOED>2.0.CO;2.

[48] D. Jolivet, «Quantification of the accuracy of liquid water path fields derived from NOAA 16 advanced very high resolution radiometer over three ground stations using microwave radiometers», *J. Geophys. Res.*, vol. 110, fasc. D11, p. D11204, 2005, doi: 10.1029/2004JD005205.

[49] J.-L. Brenguier, H. Pawlowska, L. Schüller, R. Preusker, J. Fischer, e Y. Fouquart, «Radiative Properties of Boundary Layer Clouds: Droplet Effective Radius versus Number Concentration», *Journal of the Atmospheric Sciences*, vol. 57, fasc. 6, pp. 803–821, mar. 2000, doi: 10.1175/1520-0469(2000)057<0803:RPOBLC>2.0.CO;2.

[50] L. Schüller, «Retrieval of microphysical, geometrical, and radiative properties of marine stratocumulus from remote sensing», *J. Geophys. Res.*, vol. 108, fasc. D15, p. 8631, 2003, doi: 10.1029/2002JD002680.

[51] M. D. King *et al.*, «Airborne Scanning Spectrometer for Remote Sensing of Cloud, Aerosol, Water Vapor, and Surface Properties», *Journal of Atmospheric and Oceanic Technology*, vol. 13, fasc. 4, pp. 777–794, ago. 1996, doi: 10.1175/1520-0426(1996)013<0777:ASSFRS>2.0.CO;2.

[52] R. A. Roebeling, A. J. Feijt, e P. Stammes, «Cloud property retrievals for climate monitoring: Implications of differences between Spinning Enhanced Visible and Infrared Imager (SEVIRI) on METEOSAT-8 and Advanced Very High Resolution Radiometer (AVHRR) on NOAA-17», *Journal of Geophysical Research: Atmospheres*, vol. 111, fasc. D20, 2006, doi: 10.1029/2005JD006990.

[53] S. Platnick, J. Y. Li, M. D. King, H. Gerber, e P. V. Hobbs, «A solar reflectance method for retrieving the optical thickness and droplet size of liquid water clouds over snow and ice surfaces», *Journal of Geophysical Research: Atmospheres*, vol. 106, fasc. D14, pp. 15185–15199, 2001, doi: 10.1029/2000JD900441.

[54] J. C. Pérez, A. Cerdeña, A. González, e M. Armas, «Nighttime cloud properties retrieval using MODIS and artificial neural networks», *Advances in Space Research*, vol. 43, fasc. 5, pp. 852–858, mar. 2009, doi: 10.1016/j.asr.2008.06.013.

[55] H. Iwabuchi, M. Saito, Y. Tokoro, N. S. Putri, e M. Sekiguchi, «Retrieval of radiative and microphysical properties of clouds from multispectral infrared

measurements», *Progress in Earth and Planetary Science*, vol. 3, fasc. 1, p. 32, ott. 2016, doi: 10.1186/s40645-016-0108-3.

[56] R. A. Hanel *et al.*, «The Nimbus 4 infrared spectroscopy experiment: 1. Calibrated thermal emission spectra», *J. Geophys. Res.*, vol. 77, fasc. 15, pp. 2629–2641, mag. 1972, doi: 10.1029/JC077i015p02629.

[57] B. H. Kahn *et al.*, «Near micron-sized cirrus cloud particles in high-resolution infrared spectra: An orographic case study: NEAR MICRON-SIZED CIRRUS», *Geophys. Res. Lett.*, vol. 30, fasc. 8, apr. 2003, doi: 10.1029/2003GL016909.

[58] W. L. Smith, X. L. Ma, S. A. Ackerman, H. E. Revercomb, e R. O. Knuteson, «Remote Sensing Cloud Properties from High Spectral Resolution Infrared Observations», *J. Atmos. Sci.*, vol. 50, fasc. 12, pp. 1708–1720, giu. 1993, doi: 10.1175/1520-0469(1993)050<1708:RSCPFH>2.0.CO;2.

[59] H.-L. Huang *et al.*, «Inference of ice cloud properties from high spectral resolution infrared observations», *IEEE Transactions on Geoscience and Remote Sensing*, vol. 42, fasc. 4, pp. 842–853, apr. 2004, doi: 10.1109/TGRS.2003.822752.

[60] H. Wei *et al.*, «Retrieval of semitransparent ice cloud optical thickness from atmospheric infrared sounder (AIRS) measurements», *IEEE Transactions on Geoscience and Remote Sensing*, vol. 42, fasc. 10, pp. 2254–2267, ott. 2004, doi: 10.1109/TGRS.2004.833780.

[61] J. Li *et al.*, «Retrieval of Cloud Microphysical Properties from MODIS and AIRS», *Journal of Applied Meteorology and Climatology*, vol. 44, fasc. 10, pp. 1526–1543, ott. 2005, doi: 10.1175/JAM2281.1.

[62] M. D. King *et al.*, «Cloud and aerosol properties, precipitable water, and profiles of temperature and water vapor from MODIS», *IEEE Transactions on Geoscience and Remote Sensing*, vol. 41, fasc. 2, pp. 442–458, feb. 2003, doi: 10.1109/TGRS.2002.808226.

[63] S. Platnick *et al.*, «The MODIS cloud products: algorithms and examples from Terra», *IEEE Transactions on Geoscience and Remote Sensing*, vol. 41, fasc. 2, pp. 459–473, feb. 2003, doi: 10.1109/TGRS.2002.808301.

[64] D. K. Zhou, W. L. Smith, X. Liu, A. M. Larar, S. A. Mango, e H.-L. Huang, «Physically Retrieving Cloud and Thermodynamic Parameters from Ultraspectral IR Measurements», *Journal of the Atmospheric Sciences*, vol. 64, fasc. 3, pp. 969–982, mar. 2007, doi: 10.1175/JAS3877.1.

[65] X. Liu *et al.*, «Retrieval of atmospheric profiles and cloud properties from IASI spectra using super-channels», *Atmospheric Chemistry and Physics*, vol. 9, fasc. 23, pp. 9121–9142, dic. 2009, doi: 10.5194/acp-9-9121-2009.

[66] T. August *et al.*, «IASI on Metop-A: Operational Level 2 retrievals after five years in orbit», *Journal of Quantitative Spectroscopy and Radiative Transfer*, vol. 113, fasc. 11, pp. 1340–1371, lug. 2012, doi: 10.1016/j.jqsrt.2012.02.028.

[67] P. Martinet, N. Fourrié, V. Guidard, F. Rabier, T. Montmerle, e P. Brunel, «Towards the use of microphysical variables for the assimilation of cloud-affected infrared radiances», *Quarterly Journal of the Royal Meteorological Society*, vol. 139, fasc. 674, pp. 1402–1416, 2013, doi: 10.1002/qj.2046.

[68] R. Saunders *et al.*, «An update on the RTTOV fast radiative transfer model (currently at version 12)», *Geosci. Model Dev.*, vol. 11, fasc. 7, pp. 2717–2737, lug. 2018, doi: 10.5194/gmd-11-2717-2018.

[69] P. Martinet, L. Lavanant, N. Fourrié, F. Rabier, e A. Gambacorta, «Evaluation of a revised IASI channel selection for cloudy retrievals with a focus on the Mediterranean basin», *Quarterly Journal of the Royal Meteorological Society*, vol. 140, fasc. 682, pp. 1563–1577, 2014, doi: 10.1002/qj.2239.

[70] C. D. Rodgers, *Inverse Methods for Atmospheric Sounding: Theory and Practice*, vol. 2. WORLD SCIENTIFIC, 2000. doi: 10.1142/3171.

[71] P. Martinet, N. Fourrié, Y. Bouteloup, E. Bazile, e F. Rabier, «Toward the improvement of short-range forecasts by the analysis of cloud variables from IASI radiances», *Atmospheric Science Letters*, vol. 15, fasc. 4, pp. 342–347, 2014, doi: 10.1002/asl2.510.

[72] W. Wu *et al.*, «The Application of PCRTM Physical Retrieval Methodology for IASI Cloudy Scene Analysis», *IEEE Transactions on Geoscience and Remote Sensing*, vol. 55, fasc. 9, pp. 5042–5056, set. 2017, doi: 10.1109/TGRS.2017.2702006.

[73] B. Lin *et al.*, «Estimation of water cloud properties from satellite microwave, infrared and visible measurements in oceanic environments: 2. Results», *Journal of Geophysical Research: Atmospheres*, vol. 103, fasc. D4, pp. 3887–3905, 1998, doi: https://doi.org/10.1029/97JD02817.

[74] G. Kruspe e C. Wetzel, «ASTEX 1992 - Atlantic Stratocumulus Transition Experiment». World Data Center for Climate (WDCC) at DKRZ, 2011. [Online]. Disponibile su: http://cera-www.dkrz.de/WDCC/ui/Compact.jsp?acronym=UNI_HH_MI_ASTEX1992

[75] T. T. Wilheit e K. D. Hutchison, «Retrieval of cloud base heights from passive microwave and cloud top temperature data», *IEEE Transactions on Geoscience and Remote Sensing*, vol. 38, fasc. 3, pp. 1253–1259, mag. 2000, doi: 10.1109/36.843017.

[76] F. Chevallier, P. Bauer, J. Mahfouf, e J. Morcrette, «Variational retrieval of cloud profile from ATOVS observations», *undefined*, 2002, Consultato: 17 maggio 2021. [Online]. Disponibile su: /paper/Variational-retrieval-of-cloud-profile-from-ATOVS-Chevallier-Bauer/65bb74978a67766007063b9c859f804d10cdc868

[77] J. Zhao *et al.*, «The New NOAA AMSU Hydrological Product Suites: The Validation of AMSU TPW and CLW», presentato al AMS 10th conference on satellite meteorology and oceanography, Long Beach, California, gen. 2000.

[78] H. Shao, «Detecting drizzle in marine warm clouds using combined visible, infrared, and microwave satellite data», *J. Geophys. Res.*, vol. 109, fasc. D7, p. D07205, 2004, doi: 10.1029/2003JD004286.

[79] J. Huang *et al.*, «Determination of ice water path in ice-over-water cloud systems using combined MODIS and AMSR-E measurements», *Geophysical Research Letters*, vol. 33, fasc. 21, 2006, doi: 10.1029/2006GL027038.

[80] F. Romano, D. Cimini, R. Rizzi, e V. Cuomo, «Multilayered cloud parameters retrievals from combined infrared and microwave satellite observations», *Journal of Geophysical Research: Atmospheres*, vol. 112, fasc. D8, 2007, doi: 10.1029/2006JD007745.

[81] G. Holl, S. A. Buehler, B. Rydberg, e C. Jiménez, «Collocating satellite-based radar and radiometer measurements – methodology and usage examples», *Atmos. Meas. Tech.*, vol. 3, fasc. 3, pp. 693–708, giu. 2010, doi: 10.5194/amt-3-693-2010.

[82] T. Islam, P. K. Srivastava, Q. Dai, e M. Gupta, «Ice cloud detection from AMSU-A, MHS, and HIRS satellite instruments inferred by cloud profiling radar», *Remote Sensing Letters*, vol. 5, fasc. 12, pp. 1012–1021, dic. 2014, doi: 10.1080/2150704X.2014.990643.

[83] G. Holl, S. Eliasson, J. Mendrok, e S. A. Buehler, «SPARE-ICE: Synergistic ice water path from passive operational sensors», *Journal of Geophysical Research: Atmospheres*, vol. 119, fasc. 3, pp. 1504–1523, 2014, doi: 10.1002/2013JD020759.

[84] J. Susskind, J. M. Blaisdell, e L. Iredell, «Improved methodology for surface and atmospheric soundings, error estimates, and quality control procedures: the atmospheric infrared sounder science team version-6 retrieval algorithm», *JARS*, vol. 8, fasc. 1, p. 084994, mar. 2014, doi: 10.1117/1.JRS.8.084994.

[85] T. Marke, K. Ebell, U. Löhnert, e D. D. Turner, «Statistical retrieval of thin liquid cloud microphysical properties using ground-based infrared and

microwave observations», *Journal of Geophysical Research: Atmospheres*, vol. 121, fasc. 24, p. 14,558-14,573, 2016, doi: 10.1002/2016JD025667.

[86] N. R. Nalli *et al.*, «Validation of satellite sounder environmental data records: Application to the Cross-track Infrared Microwave Sounder Suite», *Journal of Geophysical Research: Atmospheres*, vol. 118, fasc. 24, p. 13,628-13,643, 2013, doi: 10.1002/2013JD020436.

[87] U. Amato, G. Masiello, C. Serio, e M. Viggiano, «The σ-IASI code for the calculation of infrared atmospheric radiance and its derivatives», *Environmental Modelling & Software*, vol. 17, fasc. 7, pp. 651–667, nov. 2002, doi: 10.1016/S1364-8152(02)00027-0.

[88] M. T. Chahine, «Remote Sounding of Cloudy Atmospheres. I. The Single Cloud Layer», *Journal of the Atmospheric Sciences*, vol. 31, fasc. 1, pp. 233–243, gen. 1974, doi: 10.1175/1520-0469(1974)031<0233:RSOCAI>2.0.CO;2.

[89] M. Martinazzo, D. Magurno, W. Cossich, C. Serio, G. Masiello, e T. Maestri, «Assessment of the accuracy of scaling methods for radiance simulations at far and mid infrared wavelengths», *Journal of Quantitative Spectroscopy and Radiative Transfer*, vol. 271, p. 107739, set. 2021, doi: 10.1016/j.jqsrt.2021.107739.

[90] S. A. Clough *et al.*, «Atmospheric radiative transfer modeling: a summary of the AER codes», *Journal of Quantitative Spectroscopy and Radiative Transfer*, vol. 91, fasc. 2, pp. 233–244, mar. 2005, doi: 10.1016/j.jqsrt.2004.05.058.

[91] S. A. Buehler, P. Eriksson, T. Kuhn, A. von Engeln, e C. Verdes, «ARTS, the atmospheric radiative transfer simulator», *Journal of Quantitative Spectroscopy and Radiative Transfer*, vol. 91, fasc. 1, pp. 65–93, feb. 2005, doi: 10.1016/j.jqsrt.2004.05.051.

[92] S. Ding *et al.*, «Validation of the community radiative transfer model», *Journal of Quantitative Spectroscopy and Radiative Transfer*, vol. 112, fasc. 6, pp. 1050–1064, apr. 2011, doi: 10.1016/j.jqsrt.2010.11.009.

[93] G. Liuzzi, M. G. Blasi, G. Masiello, C. Serio, e S. Venafra, «All-sky radiative transfer calculations for IASI and IASI-NG: The σ-IASI-as code», presentato al RADIATION PROCESSES IN THE ATMOSPHERE AND OCEAN (IRS2016): Proceedings of the International Radiation Symposium (IRC/IAMAS), Auckland, New Zealand, 2017, p. 040004. doi: 10.1063/1.4975506.

[94] M.-D. Chou, K.-T. Lee, S.-C. Tsay, e Q. Fu, «Parameterization for Cloud Longwave Scattering for Use in Atmospheric Models», *Journal of Climate*, vol. 12, fasc. 1, pp. 159–169, gen. 1999, doi: 10.1175/1520-0442(1999)012<0159:PFCLSF>2.0.CO;2.

[95] B. Yi, A. D. Rapp, P. Yang, B. A. Baum, e M. D. King, «A comparison of Aqua MODIS ice and liquid water cloud physical and optical properties between collection 6 and collection 5.1: Pixel-to-pixel comparisons», *Journal of Geophysical Research: Atmospheres*, vol. 122, fasc. 8, pp. 4528–4549, 2017, doi: 10.1002/2016JD025586.

[96] E. Turner, P. Rayer, e R. Saunders, «AMSUTRAN: A microwave transmittance code for satellite remote sensing», *Journal of Quantitative Spectroscopy and Radiative Transfer*, vol. 227, pp. 117–129, apr. 2019, doi: 10.1016/j.jqsrt.2019.02.013.

[97] F. Aires, C. Prigent, F. Bernardo, C. Jiménez, R. Saunders, e P. Brunel, «A Tool to Estimate Land-Surface Emissivities at Microwave frequencies (TELSEM) for use in numerical weather prediction», *Quarterly Journal of the Royal Meteorological Society*, vol. 137, fasc. 656, pp. 690–699, 2011, doi: 10.1002/qj.803.

[98] F. Karbou, E. Gérard, e F. Rabier, «Global 4DVAR Assimilation and Forecast Experiments Using AMSU Observations over Land. Part I: Impacts of Various Land Surface Emissivity Parameterizations», *Weather and Forecasting*, vol. 25, fasc. 1, pp. 5–19, feb. 2010, doi: 10.1175/2009WAF2222243.1.

[99] P. Bauer, E. Moreau, F. Chevallier, e U. O'keeffe, «Multiple-scattering microwave radiative transfer for data assimilation applications», *Quarterly Journal of the Royal Meteorological Society*, vol. 132, fasc. 617, pp. 1259–1281, 2006, doi: 10.1256/qj.05.153.

[100] A. J. Geer, P. Bauer, e C. W. O'Dell, «A Revised Cloud Overlap Scheme for Fast Microwave Radiative Transfer in Rain and Cloud», *Journal of Applied Meteorology and Climatology*, vol. 48, fasc. 11, pp. 2257–2270, nov. 2009, doi: 10.1175/2009JAMC2170.1.

[101] P. Bauer, A. J. Geer, P. Lopez, e D. Salmond, «Direct 4D-Var assimilation of all-sky radiances. Part I: Implementation», *Q.J.R. Meteorol. Soc.*, vol. 136, fasc. 652, pp. 1868–1885, ott. 2010, doi: 10.1002/qj.659.

[102] P. Bauer *et al.*, «Satellite cloud and precipitation assimilation at operational NWP centres», *Q.J.R. Meteorol. Soc.*, vol. 137, fasc. 661, pp. 1934–1951, ott. 2011, doi: 10.1002/qj.905.

[103] J. Holloway e K. Mengersen, «Statistical Machine Learning Methods and Remote Sensing for Sustainable Development Goals: A Review», *Remote Sensing*, vol. 10, fasc. 9, Art. fasc. 9, set. 2018, doi: 10.3390/rs10091365.

[104] M. Belgiu e L. Drăguţ, «Random forest in remote sensing: A review of applications and future directions», *ISPRS Journal of Photogrammetry and Remote Sensing*, vol. 114, pp. 24–31, apr. 2016, doi: 10.1016/j.isprsjprs.2016.01.011.

[105] E. Izquierdo-Verdiguier e R. Zurita-Milla, «An evaluation of Guided Regularized Random Forest for classification and regression tasks in remote sensing», *International Journal of Applied Earth Observation and Geoinformation*, vol. 88, p. 102051, giu. 2020, doi: 10.1016/j.jag.2020.102051.

[106] K. Hornik, M. Stinchcombe, e H. White, «Multilayer feedforward networks are universal approximators», *Neural Networks*, vol. 2, fasc. 5, pp. 359–366, gen. 1989, doi: 10.1016/0893-6080(89)90020-8.

[107] L. Breiman, «Random Forests», *Machine Learning*, vol. 45, fasc. 1, pp. 5–32, ott. 2001, doi: 10.1023/A:1010933404324.

[108] J. E. Ball, D. T. Anderson, e C. S. Chan, «A Comprehensive Survey of Deep Learning in Remote Sensing: Theories, Tools and Challenges for the Community», *J. Appl. Remote Sens*, vol. 11, fasc. 04, p. 1, set. 2017, doi: 10.1117/1.JRS.11.042609.

[109] A. Cichocki e R. Unbehauen, «Neural Networks for Optimization and Signal Processing. 1992», *John Wiley&Sons, Chichester. Google Scholar Google Scholar Digital Library Digital Library*.

[110] I. Goodfellow, Y. Bengio, e A. Courville, *Deep learning*. Cambridge, Massachusetts: The MIT Press, 2016.

[111] G. Montavon, G. Orr, e K.-R. Müller, A c. di, *Neural networks: tricks of the trade*, 2nd ed. Heidelberg: Springer, 2012.

[112] D. E. Rumelhart, G. E. Hinton, e R. J. Williams, «Learning representations by back-propagating errors», *Nature*, vol. 323, fasc. 6088, pp. 533–536, ott. 1986, doi: 10.1038/323533a0.

[113] D. P. Kingma e J. Ba, «Adam: A Method for Stochastic Optimization», *CoRR*, vol. abs/1412.6980, 2015.

[114] M. Stone, «Cross-validation:a review», *Series Statistics*, vol. 9, fasc. 1, pp. 127–139, gen. 1978, doi: 10.1080/02331887808801414.

[115] A. H. Victoria e G. Maragatham, «Automatic tuning of hyperparameters using Bayesian optimization», *Evolving Systems*, vol. 12, fasc. 1, pp. 217–223, mar. 2021, doi: 10.1007/s12530-020-09345-2.

[116] M. Fernández-Delgado, E. Cernadas, S. Barro, e D. Amorim, «Do we Need Hundreds of Classifiers to Solve Real World Classification Problems?», *Journal of Machine Learning Research*, vol. 15, fasc. 90, pp. 3133–3181, 2014.

[117] S. Bernard, L. Heutte, e S. Adam, «A Study of Strength and Correlation in Random Forests», in *Advanced Intelligent Computing Theories and Applications*, vol. 93, D.-S. Huang, M. McGinnity, L. Heutte, e X.-P. Zhang,

A c. di Berlin, Heidelberg: Springer Berlin Heidelberg, 2010, pp. 186–191. doi: 10.1007/978-3-642-14831-6_25.

[118] A. Liaw e M. Wiener, «Classification and Regression by randomForest», *R news*, vol. 2, p. 5, 2002.

[119] C. Thornton, F. Hutter, H. H. Hoos, e K. Leyton-Brown, «Auto-WEKA: combined selection and hyperparameter optimization of classification algorithms», in *Proceedings of the 19th ACM SIGKDD international conference on Knowledge discovery and data mining*, Chicago Illinois USA, ago. 2013, pp. 847–855. doi: 10.1145/2487575.2487629.

[120] T. Akiba, S. Sano, T. Yanase, T. Ohta, e M. Koyama, «Optuna: A Next-generation Hyperparameter Optimization Framework», in *Proceedings of the 25th ACM SIGKDD International Conference on Knowledge Discovery & Data Mining*, Anchorage AK USA, lug. 2019, pp. 2623–2631. doi: 10.1145/3292500.3330701.

[121] E. Scornet, «Tuning parameters in random forests», *ESAIM: Procs*, vol. 60, pp. 144–162, 2017, doi: 10.1051/proc/201760144.

[122] J. Bergstra e Y. Bengio, «Random Search for Hyper-Parameter Optimization», *Journal of Machine Learning Research*, vol. 13, fasc. 10, pp. 281–305, 2012.

[123] F. Hilton *et al.*, «Hyperspectral Earth Observation from IASI: Five Years of Accomplishments», *Bulletin of the American Meteorological Society*, vol. 93, fasc. 3, pp. 347–370, mar. 2012, doi: 10.1175/BAMS-D-11-00027.1.

[124] C. Crevoisier *et al.*, «Towards IASI-New Generation (IASI-NG): impact of improved spectral resolution and radiometric noise on the retrieval of thermodynamic, chemistry and climate variables», *Atmos. Meas. Tech.*, vol. 7, fasc. 12, pp. 4367–4385, dic. 2014, doi: 10.5194/amt-7-4367-2014.

[125] F. Chollet e others, «Keras». GitHub, 2015. [Online]. Disponibile su: https://github.com/fchollet/keras

[126] T. O'Malley *et al.*, «KerasTuner». 2019. [Online]. Disponibile su: https://github.com/keras-team/keras-tuner

[127] F. Pedregosa *et al.*, «Scikit-learn: Machine Learning in Python», *CoRR*, vol. abs/1201.0490, 2012, [Online]. Disponibile su: http://arxiv.org/abs/1201.0490

[128] L. Hoffmann *et al.*, «From ERA-Interim to ERA5: the considerable impact of ECMWF's next-generation reanalysis on Lagrangian transport simulations», *Atmospheric Chemistry and Physics*, vol. 19, fasc. 5, pp. 3097–3124, mar. 2019, doi: 10.5194/acp-19-3097-2019.

[129] G. Masiello e C. Serio, «Simultaneous physical retrieval of surface emissivity spectrum and atmospheric parameters from infrared atmospheric

sounder interferometer spectral radiances», *Appl Opt*, vol. 52, fasc. 11, pp. 2428–2446, apr. 2013, doi: 10.1364/AO.52.002428.

[130] G. Masiello, M. Matricardi, e C. Serio, «The use of IASI data to identify systematic errors in the ECMWF forecasts of temperature in the upper stratosphere», *Atmospheric Chemistry and Physics*, vol. 11, fasc. 3, pp. 1009–1021, feb. 2011, doi: 10.5194/acp-11-1009-2011.

[131] L. Garand *et al.*, «Radiance and Jacobian intercomparison of radiative transfer models applied to HIRS and AMSU channels», *Journal of Geophysical Research: Atmospheres*, vol. 106, fasc. D20, pp. 24017–24031, 2001, doi: 10.1029/2000JD000184.

[132] V. Barlakas, V. S. Galligani, A. J. Geer, e P. Eriksson, «On the accuracy of RTTOV-SCATT for radiative transfer at all-sky microwave and submillimeter frequencies», *Journal of Quantitative Spectroscopy and Radiative Transfer*, vol. 283, p. 108137, giu. 2022, doi: 10.1016/j.jqsrt.2022.108137.

[133] G. Masiello, C. Serio, S. Venafra, G. Liuzzi, L. Poutier, e F.-M. Göttsche, «Physical Retrieval of Land Surface Emissivity Spectra from Hyper-Spectral Infrared Observations and Validation with In Situ Measurements», *Remote Sensing*, vol. 10, fasc. 6, Art. fasc. 6, giu. 2018, doi: 10.3390/rs10060976.

[134] A. J. Geer e F. Baordo, «Improved scattering radiative transfer for frozen hydrometeors at microwave frequencies», *Atmospheric Measurement Techniques*, vol. 7, fasc. 6, pp. 1839–1860, giu. 2014, doi: 10.5194/amt-7-1839-2014.

[135] K. Wyser, «The Effective Radius in Ice Clouds», *Journal of Climate*, vol. 11, fasc. 7, pp. 1793–1802, lug. 1998, doi: 10.1175/1520-0442(1998)011<1793:TERIIC>2.0.CO;2.

[136] D. L. Mitchell e W. P. Arnott, «A Model Predicting the Evolution of Ice Particle Size Spectra and Radiative Properties of Cirrus Clouds. Part II: Dependence of Absorption and Extinction on Ice Crystal Morphology», *Journal of the Atmospheric Sciences*, vol. 51, fasc. 6, pp. 817–832, mar. 1994, doi: 10.1175/1520-0469(1994)051<0817:AMPTEO>2.0.CO;2.

[137] G. M. Martin, D. W. Johnson, e A. Spice, «The Measurement and Parameterization of Effective Radius of Droplets in Warm Stratocumulus Clouds», *Journal of the Atmospheric Sciences*, vol. 51, fasc. 13, pp. 1823–1842, lug. 1994, doi: 10.1175/1520-0469(1994)051<1823:TMAPOE>2.0.CO;2.

[138] M. Stengel *et al.*, «Comparing ERA-Interim clouds with satellite observations using a simplified satellite simulator», *Atmospheric Chemistry and Physics*, vol. 18, fasc. 23, pp. 17601–17614, dic. 2018, doi: 10.5194/acp-18-17601-2018.

[139] D. D. Turner, S. A. Ackerman, B. A. Baum, H. E. Revercomb, e P. Yang, «Cloud Phase Determination Using Ground-Based AERI Observations at SHEBA», *Journal of Applied Meteorology and Climatology*, vol. 42, fasc. 6, pp. 701–715, giu. 2003, doi: 10.1175/1520-0450(2003)042<0701:CPDUGA>2.0.CO;2.

[140] K. Masuda, «Infrared sea surface emissivity including multiple reflection effect for isotropic Gaussian slope distribution model», *Remote Sensing of Environment*, vol. 103, fasc. 4, pp. 488–496, ago. 2006, doi: 10.1016/j.rse.2006.04.011.

[141] G. Masiello, C. Serio, S. Venafra, I. DeFeis, e E. E. Borbas, «Diurnal variation in Sahara desert sand emissivity during the dry season from IASI observations», *Journal of Geophysical Research: Atmospheres*, vol. 119, fasc. 3, pp. 1626–1638, 2014, doi: 10.1002/jgrd.50863.

[142] S. W. Seemann, E. E. Borbas, R. O. Knuteson, G. R. Stephenson, e H.-L. Huang, «Development of a Global Infrared Land Surface Emissivity Database for Application to Clear Sky Sounding Retrievals from Multispectral Satellite Radiance Measurements», *Journal of Applied Meteorology and Climatology*, vol. 47, fasc. 1, pp. 108–123, gen. 2008, doi: 10.1175/2007JAMC1590.1.

[143] G. V. Trunk, «A Problem of Dimensionality: A Simple Example», *IEEE Transactions on Pattern Analysis and Machine Intelligence*, vol. PAMI-1, fasc. 3, pp. 306–307, lug. 1979, doi: 10.1109/TPAMI.1979.4766926.

[144] E. Chávez, G. Navarro, R. Baeza-Yates, e J. L. Marroquín, «Searching in metric spaces», *ACM Comput. Surv.*, vol. 33, fasc. 3, pp. 273–321, set. 2001, doi: 10.1145/502807.502808.

[145] A. K. Heidinger, Y. Li, B. A. Baum, R. E. Holz, S. Platnick, e P. Yang, «Retrieval of Cirrus Cloud Optical Depth under Day and Night Conditions from MODIS Collection 6 Cloud Property Data», *Remote Sensing*, vol. 7, fasc. 6, Art. fasc. 6, giu. 2015, doi: 10.3390/rs70607257.

[146] I. Loshchilov e F. Hutter, «Decoupled Weight Decay Regularization», in *ICLR*, 2019.

[147] J. Snoek, H. Larochelle, e R. P. Adams, «Practical Bayesian Optimization of Machine Learning Algorithms», in *Advances in Neural Information Processing Systems*, 2012, vol. 25. Consultato: 13 agosto 2021. [Online]. Disponibile su: https://proceedings.neurips.cc/paper/2012/hash/05311655a15b75fab86956663e1819cd-Abstract.html

[148] H. Jin, Q. Song, e X. Hu, «Auto-Keras: An Efficient Neural Architecture Search System», in *Proceedings of the 25th ACM SIGKDD International*

Conference on Knowledge Discovery & Data Mining, New York, NY, USA, lug. 2019, pp. 1946–1956. doi: 10.1145/3292500.3330648.

[149] C. Serio *et al.*, «PCA determination of the radiometric noise of high spectral resolution infrared observations from spectral residuals: Application to IASI», *Journal of Quantitative Spectroscopy and Radiative Transfer*, vol. 206, pp. 8–21, feb. 2018, doi: 10.1016/j.jqsrt.2017.10.022.

[150] «Keras: the Python deep learning API». https://keras.io/

[151] «Keras Tuner». https://keras-team.github.io/keras-tuner/

[152] K. Kandasamy, W. Neiswanger, J. Schneider, B. Póczos, e E. P. Xing, «Neural architecture search with Bayesian optimisation and optimal transport», in *Proceedings of the 32nd International Conference on Neural Information Processing Systems*, Red Hook, NY, USA, dic. 2018, pp. 2020–2029.

[153] V. Nair e G. E. Hinton, «Rectified linear units improve restricted boltzmann machines», in *Proceedings of the 27th International Conference on International Conference on Machine Learning*, Madison, WI, USA, giu. 2010, pp. 807–814.

[154] M. Belkin, D. Hsu, S. Ma, e S. Mandal, «Reconciling modern machine-learning practice and the classical bias–variance trade-off», *PNAS*, vol. 116, fasc. 32, pp. 15849–15854, ago. 2019, doi: 10.1073/pnas.1903070116.

[155] J. Kukačka, V. Golkov, e D. Cremers, «Regularization for Deep Learning: A Taxonomy», *arXiv:1710.10686 [cs, stat]*, ott. 2017, Consultato: 25 agosto 2021. [Online]. Disponibile su: http://arxiv.org/abs/1710.10686

[156] K. E. Taylor, «Summarizing multiple aspects of model performance in a single diagram», *Journal of Geophysical Research: Atmospheres*, vol. 106, fasc. D7, pp. 7183–7192, 2001, doi: https://doi.org/10.1029/2000JD900719.

[157] L. Bottou, «On-line Learning and Stochastic Approximations», in *On-Line Learning in Neural Networks*, 1ª ed., D. Saad, A c. di Cambridge University Press, 1999, pp. 9–42. doi: 10.1017/CBO9780511569920.003.

[158] T. Fushiki, «Estimation of prediction error by using K-fold cross-validation», *Stat Comput*, vol. 21, fasc. 2, pp. 137–146, apr. 2011, doi: 10.1007/s11222-009-9153-8.

[159] K. N. Liou, *An Introduction to Atmospheric Radiation*. Elsevier, 2002.

[160] C. Serio, A. M. Lubrano, F. Romano, e H. Shimoda, «Cloud detection over sea surface by use of autocorrelation functions of upwelling infrared spectra in the 800–900-cm^{-1} window region», *Appl. Opt., AO*, vol. 39, fasc. 21, pp. 3565–3572, lug. 2000, doi: 10.1364/AO.39.003565.

[161] U. Amato *et al.*, «Cloud mask via cumulative discriminant analysis applied to satellite infrared observations: scientific basis and initial evaluation», *Atmospheric Measurement Techniques*, vol. 7, fasc. 10, pp. 3355–3372, ott. 2014, doi: https://doi.org/10.5194/amt-7-3355-2014.

[162] G. Masiello, C. Serio, e H. Shimoda, «Qualifying IMG tropical spectra for clear sky», *Journal of Quantitative Spectroscopy and Radiative Transfer*, vol. 77, fasc. 2, pp. 131–148, mar. 2003, doi: 10.1016/S0022-4073(02)00083-3.

[163] L. Murino *et al.*, «Cloud Detection of MODIS Multispectral Images», *J. Atmos. Oceanic Technol.*, vol. 31, fasc. 2, pp. 347–365, feb. 2014, doi: 10.1175/JTECH-D-13-00088.1.

[164] U. Amato *et al.*, «Statistical cloud detection from SEVIRI multispectral images», *Remote Sensing of Environment*, vol. 112, fasc. 3, pp. 750–766, mar. 2008, doi: 10.1016/j.rse.2007.06.004.

[165] Y. Sui, B. He, e T. Fu, «Energy-based cloud detection in multispectral images based on the SVM technique», *International Journal of Remote Sensing*, vol. 40, fasc. 14, pp. 5530–5543, lug. 2019, doi: 10.1080/01431161.2019.1580788.

[166] F. Hilton *et al.*, «Hyperspectral Earth Observation from IASI: Five Years of Accomplishments», *Bull. Amer. Meteor. Soc.*, vol. 93, fasc. 3, pp. 347–370, mar. 2012, doi: 10.1175/BAMS-D-11-00027.1.

[167] G. Masiello, C. Serio, e P. Antonelli, «Inversion for atmospheric thermodynamical parameters of IASI data in the principal components space», *Quarterly Journal of the Royal Meteorological Society*, vol. 138, fasc. 662, pp. 103–117, 2012, doi: 10.1002/qj.909.

[168] M. D. Goldberg, Y. Qu, L. M. McMillin, W. Wolf, Lihang Zhou, e M. Divakarla, «AIRS near-real-time products and algorithms in support of operational numerical weather prediction», *IEEE Transactions on Geoscience and Remote Sensing*, vol. 41, fasc. 2, pp. 379–389, feb. 2003, doi: 10.1109/TGRS.2002.808307.

[169] C. Pietrapertosa, V. Cuomo, N. Pergola, C. Serio, V. Tramutoli, e H. Shimoda, «Fractality in broken clouds and the scan geometry of new satellite-borne infrared sensors», *International Journal of Remote Sensing*, vol. 22, fasc. 5, pp. 889–894, gen. 2001, doi: 10.1080/01431160051060381.

[170] L. Li, K. Jamieson, G. DeSalvo, A. Rostamizadeh, e A. Talwalkar, «Hyperband: A Novel Bandit-Based Approach to Hyperparameter Optimization», p. 52.

[171] J. Heaton, «Ian Goodfellow, Yoshua Bengio, and Aaron Courville: Deep learning», *Genet Program Evolvable Mach*, vol. 19, fasc. 1, pp. 305–307, giu. 2018, doi: 10.1007/s10710-017-9314-z.

[172] D.-A. Clevert, T. Unterthiner, e S. Hochreiter, «Fast and Accurate Deep Network Learning by Exponential Linear Units (ELUs)», *arXiv:1511.07289 [cs]*, feb. 2016, Consultato: 14 agosto 2020. [Online]. Disponibile su: http://arxiv.org/abs/1511.07289

[173] T. Dozat, «Incorporating Nesterov Momentum into Adam», p. 6.

[174] D. P. Kingma e J. Ba, «Adam: A Method for Stochastic Optimization», *arXiv:1412.6980 [cs]*, gen. 2017, Consultato: 14 agosto 2020. [Online]. Disponibile su: http://arxiv.org/abs/1412.6980

[175] L. Prechelt, «Early Stopping - But When?», in *Neural Networks: Tricks of the Trade*, G. B. Orr e K.-R. Müller, A c. di Berlin, Heidelberg: Springer, 1998, pp. 55–69. doi: 10.1007/3-540-49430-8_3.

[176] P. Jeatrakul, K. W. Wong, e C. C. Fung, «Classification of Imbalanced Data by Combining the Complementary Neural Network and SMOTE Algorithm», in *Neural Information Processing. Models and Applications*, Berlin, Heidelberg, 2010, pp. 152–159. doi: 10.1007/978-3-642-17534-3_19.

[177] D. Powers, «Evaluation: From Precision, Recall and F-Factor to ROC, Informedness, Markedness & Correlation», p. 24.

[178] P. I. Palmer *et al.*, «The added value of satellite observations of methane forunderstanding the contemporary methane budget», *Philosophical Transactions of the Royal Society A: Mathematical, Physical and Engineering Sciences*, vol. 379, fasc. 2210, p. 20210106, nov. 2021, doi: 10.1098/rsta.2021.0106.

[179] X. Lan *et al.*, «Improved Constraints on Global Methane Emissions and Sinks Using δ13C-CH4», *Global Biogeochemical Cycles*, vol. 35, fasc. 6, p. e2021GB007000, 2021, doi: 10.1029/2021GB007000.

[180] A. J. Turner, C. Frankenberg, e E. A. Kort, «Interpreting contemporary trends in atmospheric methane», *Proceedings of the National Academy of Sciences*, vol. 116, fasc. 8, pp. 2805–2813, feb. 2019, doi: 10.1073/pnas.1814297116.

[181] MOYA/ZWAMPS Team *et al.*, «Isotopic signatures of methane emissions from tropical fires, agriculture and wetlands: the MOYA and ZWAMPS flights», *Phil. Trans. R. Soc. A.*, vol. 380, fasc. 2215, p. 20210112, gen. 2022, doi: 10.1098/rsta.2021.0112.

[182] D. F. Ferretti *et al.*, «Unexpected Changes to the Global Methane Budget over the Past 2000 Years», *Science*, vol. 309, fasc. 5741, pp. 1714–1717, set. 2005, doi: 10.1126/science.1115193.

[183] H. Hu *et al.*, «The operational methane retrieval algorithm for TROPOMI», *Atmospheric Measurement Techniques*, vol. 9, fasc. 11, pp. 5423–5440, nov. 2016, doi: 10.5194/amt-9-5423-2016.

[184] D. J. Jacob *et al.*, «Satellite observations of atmospheric methane and their value for quantifying methane emissions», *Atmospheric Chemistry and Physics*, vol. 16, fasc. 22, pp. 14371–14396, nov. 2016, doi: 10.5194/acp-16-14371-2016.

[185] A. Kuze *et al.*, «Update on GOSAT TANSO-FTS performance, operations, and data products after more than 6 years in space», *Atmospheric Measurement Techniques*, vol. 9, fasc. 6, pp. 2445–2461, giu. 2016, doi: 10.5194/amt-9-2445-2016.

[186] G. Liuzzi, G. Masiello, C. Serio, S. Venafra, e C. Camy-Peyret, «Physical inversion of the full IASI spectra: Assessment of atmospheric parameters retrievals, consistency of spectroscopy and forward modelling», *Journal of Quantitative Spectroscopy and Radiative Transfer*, vol. 182, pp. 128–157, ott. 2016, doi: 10.1016/j.jqsrt.2016.05.022.

[187] J. Lelieveld, S. Gromov, A. Pozzer, e D. Taraborrelli, «Global tropospheric hydroxyl distribution, budget and reactivity», *Atmospheric Chemistry and Physics*, vol. 16, fasc. 19, pp. 12477–12493, ott. 2016, doi: 10.5194/acp-16-12477-2016.

[188] L. E. Revell, A. Stenke, E. Rozanov, W. Ball, S. Lossow, e T. Peter, «The role of methane in projections of 21st century stratospheric water vapour», *Atmospheric Chemistry and Physics*, vol. 16, fasc. 20, pp. 13067–13080, ott. 2016, doi: 10.5194/acp-16-13067-2016.

[189] R. Siddans *et al.*, «Global height-resolved methane retrievals from the Infrared Atmospheric Sounding Interferometer (IASI) on MetOp», *Atmospheric Measurement Techniques*, vol. 10, fasc. 11, pp. 4135–4164, nov. 2017, doi: 10.5194/amt-10-4135-2017.

[190] C. Serio, G. Masiello, e G. Liuzzi, «Demonstration of random projections applied to the retrieval problem of geophysical parameters from hyper-spectral infrared observations», *Appl. Opt., AO*, vol. 55, fasc. 24, pp. 6576–6587, ago. 2016, doi: 10.1364/AO.55.006576.

[191] C. Serio, G. Masiello, C. Camy-Peyret, e G. Liuzzi, «CO2 spectroscopy and forward/inverse radiative transfer modelling in the thermal band using IASI spectra», *Journal of Quantitative Spectroscopy and Radiative Transfer*, vol. 222–223, pp. 65–83, gen. 2019, doi: 10.1016/j.jqsrt.2018.10.020.

[192] A. Inness *et al.*, «The MACC reanalysis: an 8 yr data set of atmospheric composition», *Atmospheric Chemistry and Physics*, vol. 13, fasc. 8, pp. 4073–4109, apr. 2013, doi: 10.5194/acp-13-4073-2013.

[193] N. Hao *et al.*, «GOME-2 total ozone columns from MetOp-A/MetOp-B and assimilation in the MACC system», *Atmospheric Measurement Techniques*, vol. 7, fasc. 9, pp. 2937–2951, set. 2014, doi: 10.5194/amt-7-2937-2014.

[194] K. Masuda, T. Takashima, e Y. Takayama, «Emissivity of pure and sea waters for the model sea surface in the infrared window regions», *Remote Sensing of Environment*, vol. 24, fasc. 2, pp. 313–329, mar. 1988, doi: 10.1016/0034-4257(88)90032-6.

[195] E. Borbas, G. Hulley, M. Feltz, R. Knuteson, e S. Hook, «The Combined ASTER MODIS Emissivity over Land (CAMEL) Part 1: Methodology and High Spectral Resolution Application», *Remote Sensing*, vol. 10, fasc. 4, p. 643, apr. 2018, doi: 10.3390/rs10040643.

[196] M. Feltz, E. Borbas, R. Knuteson, G. Hulley, e S. Hook, «The Combined ASTER MODIS Emissivity over Land (CAMEL) Part 2: Uncertainty and Validation», *Remote Sensing*, vol. 10, fasc. 5, p. 664, apr. 2018, doi: 10.3390/rs10050664.

[197] S. Wojtowytsch e W. E, «Can Shallow Neural Networks Beat the Curse of Dimensionality? A Mean Field Training Perspective», *IEEE Transactions on Artificial Intelligence*, vol. 1, fasc. 2, pp. 121–129, ott. 2020, doi: 10.1109/TAI.2021.3051357.

[198] N. C. Atkinson, F. I. Hilton, S. M. Illingworth, J. R. Eyre, e T. Hultberg, «Potential for the use of reconstructed IASI radiances in the detection of atmospheric trace gases», *Atmos. Meas. Tech.*, vol. 3, fasc. 4, pp. 991–1003, lug. 2010, doi: 10.5194/amt-3-991-2010.

[199] G. Masiello, C. Serio, e P. Antonelli, «Inversion for atmospheric thermodynamical parameters of IASI data in the principal components space», *Quarterly Journal of the Royal Meteorological Society*, vol. 138, fasc. 662, pp. 103–117, 2012, doi: 10.1002/qj.909.

[200] T. Elsken, J. H. Metzen, e F. Hutter, «Neural Architecture Search», in *Automated Machine Learning: Methods, Systems, Challenges*, F. Hutter, L. Kotthoff, e J. Vanschoren, A c. di Cham: Springer International Publishing, 2019, pp. 63–77. doi: 10.1007/978-3-030-05318-5_3.

[201] L. Bottou, «On-line Learning and Stochastic Approximations», in *On-Line Learning in Neural Networks*, D. Saad, A c. di Cambridge: Cambridge University Press, 1999, pp. 9–42. doi: 10.1017/CBO9780511569920.003.

[202] G. Franceschetti e R. Lanari, *Synthetic Aperture Radar Processing*. CRC Press, 1999.

[203] R. Bamler e P. Hartl, «Synthetic aperture radar interferometry», *Inverse Problems*, vol. 14, fasc. 4, pp. R1–R54, ago. 1998, doi: 10.1088/0266-5611/14/4/001.

[204] D. Massonnet e K. L. Feigl, «Radar interferometry and its application to changes in the Earth's surface», *Reviews of Geophysics*, vol. 36, fasc. 4, pp. 441–500, 1998, doi: 10.1029/97RG03139.

[205] P. A. Rosen *et al.*, «Synthetic aperture radar interferometry», *Proceedings of the IEEE*, vol. 88, fasc. 3, pp. 333–382, mar. 2000, doi: 10.1109/5.838084.

[206] T. Toutin e L. Gray, «State-of-the-art of elevation extraction from satellite SAR data», *ISPRS Journal of Photogrammetry and Remote Sensing*, vol. 55, fasc. 1, pp. 13–33, feb. 2000, doi: 10.1016/S0924-2716(99)00039-8.

[207] A. Hooper, D. Bekaert, K. Spaans, e M. Arıkan, «Recent advances in SAR interferometry time series analysis for measuring crustal deformation», *Tectonophysics*, vol. 514, pp. 1–13, gen. 2012, doi: 10.1016/j.tecto.2011.10.013.

[208] F. T. Ulaby e D. G. Long, *Microwave radar and radiometric remote sensing*. Ann Arbor: The University of Michigan Press, 2014.

[209] H. A. Zebker e J. Villasenor, «Decorrelation in interferometric radar echoes», *IEEE Transactions on Geoscience and Remote Sensing*, vol. 30, fasc. 5, pp. 950–959, set. 1992, doi: 10.1109/36.175330.

[210] M. D. Pritt e J. S. Shipman, «Least-squares two-dimensional phase unwrapping using FFT's», *IEEE Transactions on Geoscience and Remote Sensing*, vol. 32, fasc. 3, pp. 706–708, mag. 1994, doi: 10.1109/36.297989.

[211] T. J. Flynn, «Two-dimensional phase unwrapping with minimum weighted discontinuity», *J. Opt. Soc. Am. A, JOSAA*, vol. 14, fasc. 10, pp. 2692–2701, ott. 1997, doi: 10.1364/JOSAA.14.002692.

[212] M. Costantini, «A novel phase unwrapping method based on network programming», *IEEE Transactions on Geoscience and Remote Sensing*, vol. 36, fasc. 3, pp. 813–821, mag. 1998, doi: 10.1109/36.673674.

[213] Wei Xu e I. Cumming, «A region-growing algorithm for InSAR phase unwrapping», *IEEE Transactions on Geoscience and Remote Sensing*, vol. 37, fasc. 1, pp. 124–134, gen. 1999, doi: 10.1109/36.739143.

[214] D. Massonnet *et al.*, «The displacement field of the Landers earthquake mapped by radar interferometry», *Nature*, vol. 364, fasc. 6433, Art. fasc. 6433, lug. 1993, doi: 10.1038/364138a0.

[215] D. Just e R. Bamler, «Phase statistics of interferograms with applications to synthetic aperture radar», *Appl. Opt., AO*, vol. 33, fasc. 20, pp. 4361–4368, lug. 1994, doi: 10.1364/AO.33.004361.

[216] R. Tomás *et al.*, «Radar interferometry techniques for the study of ground subsidence phenomena: a review of practical issues through cases in Spain», *Environ Earth Sci*, vol. 71, fasc. 1, pp. 163–181, gen. 2014, doi: 10.1007/s12665-013-2422-z.

[217] H.-S. Jung, S.-H. Yun, e M.-J. Jo, «An Improvement of Multiple-Aperture SAR Interferometry Performance in the Presence of Complex and Large Line-of-Sight Deformation», *IEEE J. Sel. Top. Appl. Earth Observations Remote Sensing*, vol. 8, fasc. 4, pp. 1743–1752, apr. 2015, doi: 10.1109/JSTARS.2015.2399249.

[218] T. J. Wright, B. E. Parsons, e Z. Lu, «Toward mapping surface deformation in three dimensions using InSAR», *Geophysical Research Letters*, vol. 31, fasc. 1, 2004, doi: 10.1029/2003GL018827.

[219] S. Gudmundsson, F. Sigmundsson, e J. M. Carstensen, «Three-dimensional surface motion maps estimated from combined interferometric synthetic aperture radar and GPS data», *Journal of Geophysical Research: Solid Earth*, vol. 107, fasc. B10, p. ETG 13-1-ETG 13-14, 2002, doi: 10.1029/2001JB000283.

[220] F. Guglielmino, G. Nunnari, G. Puglisi, e A. Spata, «A new global approach to obtain three-dimensional displacement maps by integrating GPS and DInSAR data», vol. 11, p. 5890, apr. 2009.

[221] T. Strozzi, A. Luckman, T. Murray, U. Wegmuller, e C. L. Werner, «Glacier motion estimation using SAR offset-tracking procedures», *IEEE Transactions on Geoscience and Remote Sensing*, vol. 40, fasc. 11, pp. 2384–2391, nov. 2002, doi: 10.1109/TGRS.2002.805079.

[222] A. Singleton, Z. Li, T. Hoey, e J.-P. Muller, «Evaluating sub-pixel offset techniques as an alternative to D-InSAR for monitoring episodic landslide movements in vegetated terrain», *Remote Sensing of Environment*, vol. 147, pp. 133–144, mag. 2014, doi: 10.1016/j.rse.2014.03.003.

[223] F. Casu, A. Manconi, A. Pepe, e R. Lanari, «Deformation Time-Series Generation in Areas Characterized by Large Displacement Dynamics: The SAR Amplitude Pixel-Offset SBAS Technique», *IEEE Transactions on Geoscience and Remote Sensing*, 2011, doi: 10.1109/TGRS.2010.2104325.

[224] Y. Fialko, M. Simons, e D. Agnew, «The complete (3-D) surface displacement field in the epicentral area of the 1999 MW7.1 Hector Mine Earthquake, California, from space geodetic observations», *Geophysical Research Letters*, vol. 28, fasc. 16, pp. 3063–3066, 2001, doi: 10.1029/2001GL013174.

[225] Y. Fialko, D. Sandwell, M. Simons, e P. Rosen, «Three-dimensional deformation caused by the Bam, Iran, earthquake and the origin of shallow slip deficit», *Nature*, vol. 435, fasc. 7040, pp. 295–299, mag. 2005, doi: 10.1038/nature03425.

[226] A. B. Giles, R. A. Massom, e R. C. Warner, «A method for sub-pixel scale feature-tracking using Radarsat images applied to the Mertz Glacier Tongue,

East Antarctica», *Remote Sensing of Environment*, vol. 113, fasc. 8, pp. 1691–1699, ago. 2009, doi: 10.1016/j.rse.2009.03.015.

[227] N. B. D. Bechor e H. A. Zebker, «Measuring two-dimensional movements using a single InSAR pair», *Geophysical Research Letters*, vol. 33, fasc. 16, 2006, doi: 10.1029/2006GL026883.

[228] H. S. Jung, Z. Lu, J. S. Won, M. P. Poland, e A. Miklius, «Mapping Three-Dimensional Surface Deformation by Combining Multiple-Aperture Interferometry and Conventional Interferometry: Application to the June 2007 Eruption of Kilauea Volcano, Hawaii», *IEEE Geoscience and Remote Sensing Letters*, vol. 8, fasc. 1, pp. 34–38, gen. 2011, doi: 10.1109/LGRS.2010.2051793.

[229] H.-S. Jung, Z. Lu, e L. Zhang, «Feasibility of Along-Track Displacement Measurement From Sentinel-1 Interferometric Wide-Swath Mode», *IEEE Transactions on Geoscience and Remote Sensing*, vol. 51, fasc. 1, pp. 573–578, gen. 2013, doi: 10.1109/TGRS.2012.2197861.

[230] D. T. Sandwell, D. Myer, R. Mellors, M. Shimada, B. Brooks, e J. Foster, «Accuracy and Resolution of ALOS Interferometry: Vector Deformation Maps of the Father's Day Intrusion at Kilauea», *IEEE Transactions on Geoscience and Remote Sensing*, vol. 46, fasc. 11, pp. 3524–3534, nov. 2008, doi: 10.1109/TGRS.2008.2000634.

[231] X. Shi, L. Zhang, T. Balz, e M. Liao, «Landslide deformation monitoring using point-like target offset tracking with multi-mode high-resolution TerraSAR-X data», *ISPRS Journal of Photogrammetry and Remote Sensing*, vol. 105, pp. 128–140, lug. 2015, doi: 10.1016/j.isprsjprs.2015.03.017.

[232] R. Grandin *et al.*, «September 2005 Manda Hararo-Dabbahu rifting event, Afar (Ethiopia): Constraints provided by geodetic data», *Journal of Geophysical Research*, vol. 114, fasc. B8, pp. 817–822, 2009, doi: 10.1029/2008JB005843.

[233] X. Hu, T. Wang, e M. Liao, «Measuring Coseismic Displacements With Point-Like Targets Offset Tracking», *IEEE Geoscience and Remote Sensing Letters*, vol. 11, pp. 283–287, gen. 2014, doi: 10.1109/LGRS.2013.2256104.

[234] M. G. Amin, «Introducing the Spectral Diversity», *IEEE Transactions on Signal Processing*, vol. 41, fasc. 1, pp. 185-, gen. 1993, doi: 10.1109/TSP.1993.193137.

[235] H.-S. Jung, J.-S. Won, e S.-W. Kim, «An Improvement of the Performance of Multiple-Aperture SAR Interferometry (MAI)», *IEEE Transactions on Geoscience and Remote Sensing*, vol. 47, fasc. 8, pp. 2859–2869, ago. 2009, doi: 10.1109/TGRS.2009.2016554.

[236] Global Volcanism Program, «Report on Dabbahu (Ethiopia)», *Bulletin of the Global Volcanism Network*, vol. 30, fasc. 9, 2005, doi: 10.5479/si.GVP.BGVN200509-221113.

[237] I. J. Hamling, T. J. Wright, E. Calais, E. Lewi, e Y. Fukahata, «InSAR observations of post-rifting deformation around the Dabbahu rift segment, Afar, Ethiopia», *Geophys J Int*, vol. 197, fasc. 1, pp. 33–49, apr. 2014, doi: 10.1093/gji/ggu003.

[238] Z. E. Ross *et al.*, «Hierarchical interlocked orthogonal faulting in the 2019 Ridgecrest earthquake sequence», *Science*, vol. 366, fasc. 6463, pp. 346–351, ott. 2019, doi: 10.1126/science.aaz0109.

[239] A. Ferretti, C. Prati, e F. Rocca, «Permanent scatterers in SAR interferometry», *IEEE Transactions on Geoscience and Remote Sensing*, vol. 39, fasc. 1, pp. 8–20, gen. 2001, doi: 10.1109/36.898661.

[240] C. Werner, U. Wegmuller, T. Strozzi, e A. Wiesmann, «Interferometric point target analysis for deformation mapping», in *IGARSS 2003. 2003 IEEE International Geoscience and Remote Sensing Symposium. Proceedings (IEEE Cat. No.03CH37477)*, lug. 2003, vol. 7, pp. 4362–4364 vol.7. doi: 10.1109/IGARSS.2003.1295516.

[241] A. Hooper, H. Zebker, P. Segall, e B. Kampes, «A new method for measuring deformation on volcanoes and other natural terrains using InSAR persistent scatterers», *Geophysical Research Letters*, vol. 31, fasc. 23, 2004, doi: 10.1029/2004GL021737.

[242] P. Berardino, G. Fornaro, R. Lanari, e E. Sansosti, «A new algorithm for surface deformation monitoring based on small baseline differential SAR interferograms», *IEEE Transactions on Geoscience and Remote Sensing*, vol. 40, fasc. 11, pp. 2375–2383, nov. 2002, doi: 10.1109/TGRS.2002.803792.

[243] R. Lanari, O. Mora, M. Manunta, J. J. Mallorqui, P. Berardino, e E. Sansosti, «A small-baseline approach for investigating deformations on full-resolution differential SAR interferograms», *IEEE Transactions on Geoscience and Remote Sensing*, vol. 42, fasc. 7, pp. 1377–1386, lug. 2004, doi: 10.1109/TGRS.2004.828196.

[244] O. Mora, J. J. Mallorqui, e A. Broquetas, «Linear and nonlinear terrain deformation maps from a reduced set of interferometric SAR images», *IEEE Transactions on Geoscience and Remote Sensing*, vol. 41, fasc. 10, pp. 2243–2253, ott. 2003, doi: 10.1109/TGRS.2003.814657.

[245] E. A. Hetland, P. Musé, M. Simons, Y. N. Lin, P. S. Agram, e C. J. DiCaprio, «Multiscale InSAR Time Series (MInTS) analysis of surface deformation», *Journal of Geophysical Research: Solid Earth*, vol. 117, fasc. B2, 2012, doi: 10.1029/2011JB008731.

[246] A. Hooper, «A multi-temporal InSAR method incorporating both persistent scatterer and small baseline approaches», *Geophysical Research Letters*, vol. 35, fasc. 16, 2008, doi: 10.1029/2008GL034654.

[247] A. Pepe, Y. Yang, M. Manzo, e R. Lanari, «Improved EMCF-SBAS Processing Chain Based on Advanced Techniques for the Noise-Filtering and Selection of Small Baseline Multi-Look DInSAR Interferograms», *IEEE Transactions on Geoscience and Remote Sensing*, vol. 53, fasc. 8, pp. 4394–4417, ago. 2015, doi: 10.1109/TGRS.2015.2396875.

[248] A. Ferretti, A. Fumagalli, F. Novali, C. Prati, F. Rocca, e A. Rucci, «A New Algorithm for Processing Interferometric Data-Stacks: SqueeSAR», *IEEE Transactions on Geoscience and Remote Sensing*, vol. 49, fasc. 9, pp. 3460–3470, set. 2011, doi: 10.1109/TGRS.2011.2124465.

[249] T. R. Lauknes, H. A. Zebker, e Y. Larsen, «InSAR Deformation Time Series Using an L1 -Norm Small-Baseline Approach», *IEEE Transactions on Geoscience and Remote Sensing*, vol. 49, fasc. 1, pp. 536–546, gen. 2011, doi: 10.1109/TGRS.2010.2051951.

[250] M.-J. Jo, H.-S. Jung, J.-S. Won, M. P. Poland, A. Miklius, e Z. Lu, «Measurement of slow-moving along-track displacement from an efficient multiple-aperture SAR interferometry (MAI) stacking», *J Geod*, vol. 89, fasc. 5, pp. 411–425, mag. 2015, doi: 10.1007/s00190-014-0786-9.

[251] N. Gourmelen *et al.*, «Ice velocity determined using conventional and multiple-aperture InSAR», *Earth and Planetary Science Letters*, vol. 307, fasc. 1, pp. 156–160, lug. 2011, doi: 10.1016/j.epsl.2011.04.026.

[252] L. He, L. Wu, S. Liu, Z. Wang, C. Su, e S.-N. Liu, «Mapping Two-Dimensional Deformation Field Time-Series of Large Slope by Coupling DInSAR-SBAS with MAI-SBAS», *Remote Sensing*, vol. 7, fasc. 9, Art. fasc. 9, set. 2015, doi: 10.3390/rs70912440.

[253] A. Pepe e R. Lanari, «On the Extension of the Minimum Cost Flow Algorithm for Phase Unwrapping of Multitemporal Differential SAR Interferograms», *IEEE Transactions on Geoscience and Remote Sensing*, vol. 44, fasc. 9, pp. 2374–2383, set. 2006, doi: 10.1109/TGRS.2006.873207.

[254] B. Delaunay, «Sur la sphère vide. A la mémoire de Georges Voronoï», fasc. 6, pp. 793–800, 1934.

[255] N. R. Draper e H. Smith, *Applied Regression Analysis*. John Wiley & Sons, 1998.

[256] B. Liu, J. Zhang, Y. Luo, W. Jiang, X. Chen, e Y. Li, «Error Propagation Analysis in Three-Dimensional Coseismic Displacement Inversion», *IEEE Geoscience and Remote Sensing Letters*, vol. 11, fasc. 11, pp. 1971–1975, nov. 2014, doi: 10.1109/LGRS.2014.2315815.

[257] A. Pepe e F. Calò, «A Review of Interferometric Synthetic Aperture RADAR (InSAR) Multi-Track Approaches for the Retrieval of Earth's Surface Displacements», *Applied Sciences*, vol. 7, fasc. 12, Art. fasc. 12, dic. 2017, doi: 10.3390/app7121264.

[258] A. Pepe, G. Solaro, F. Calò, e C. Dema, «A Minimum Acceleration Approach for the Retrieval of Multiplatform InSAR Deformation Time Series», *IEEE Journal of Selected Topics in Applied Earth Observations and Remote Sensing*, vol. 9, fasc. 8, pp. 3883–3898, ago. 2016, doi: 10.1109/JSTARS.2016.2577878.

[259] J. Hu, Z. W. Li, X. L. Ding, J. J. Zhu, L. Zhang, e Q. Sun, «3D coseismic Displacement of 2010 Darfield, New Zealand earthquake estimated from multi-aperture InSAR and D-InSAR measurements», *J Geod*, vol. 86, fasc. 11, pp. 1029–1041, nov. 2012, doi: 10.1007/s00190-012-0563-6.

[260] M. Shirzaei, «A seamless multitrack multitemporal InSAR algorithm», *Geochemistry, Geophysics, Geosystems*, vol. 16, fasc. 5, pp. 1656–1669, 2015, doi: 10.1002/2015GC005759.

[261] Q. Wang *et al.*, «Investigation of the ground displacement in Saint Petersburg, Russia, using multiple-track differential synthetic aperture radar interferometry», *International Journal of Applied Earth Observation and Geoinformation*, vol. 87, p. 102050, mag. 2020, doi: 10.1016/j.jag.2020.102050.

[262] S. Samsonov e N. d'Oreye, «Multidimensional time-series analysis of ground deformation from multiple InSAR data sets applied to Virunga Volcanic Province», *Geophysical Journal International*, vol. 191, fasc. 3, pp. 1095–1108, 2012, doi: 10.1111/j.1365-246X.2012.05669.x.

[263] P. A. Rosen *et al.*, «SRTM C-band topographic data: quality assessments and calibration activities», in *IGARSS 2001. Scanning the Present and Resolving the Future. Proceedings. IEEE 2001 International Geoscience and Remote Sensing Symposium (Cat. No.01CH37217)*, lug. 2001, vol. 2, pp. 739–741 vol.2. doi: 10.1109/IGARSS.2001.976620.

[264] R. Bamler e M. Eineder, «Accuracy of differential shift estimation by correlation and split-bandwidth interferometry for wideband and delta-k SAR systems», *IEEE Geoscience and Remote Sensing Letters*, vol. 2, fasc. 2, pp. 151–155, apr. 2005, doi: 10.1109/LGRS.2004.843203.

[265] G. Gomba, A. Parizzi, F. De Zan, M. Eineder, e R. Bamler, «Toward Operational Compensation of Ionospheric Effects in SAR Interferograms: The Split-Spectrum Method», *IEEE Trans. Geosci. Remote Sensing*, vol. 54, fasc. 3, pp. 1446–1461, mar. 2016, doi: 10.1109/TGRS.2015.2481079.

[266] F. Gatelli, A. Monti Guamieri, F. Parizzi, P. Pasquali, C. Prati, e F. Rocca, «The wavenumber shift in SAR interferometry», *IEEE Transactions on*

Geoscience and Remote Sensing, vol. 32, fasc. 4, pp. 855–865, lug. 1994, doi: 10.1109/36.298013.

[267] M. Santoro, U. Wegmuller, T. Strozzi, C. Werner, A. Wiesmann, e W. Lengert, «Thematic Applications of ERS-ENVISAT Cross-Interferometry», in *IGARSS 2008 - 2008 IEEE International Geoscience and Remote Sensing Symposium*, lug. 2008, vol. 4, p. IV-1225-IV–1228. doi: 10.1109/IGARSS.2008.4779950.

[268] U. Wegmüller, M. Santoro, C. Werner, T. Strozzi, e A. Wiesmann, «ERS-ENVISAT Tandem cross — interferometry coherence estimation», in *2009 IEEE International Geoscience and Remote Sensing Symposium*, lug. 2009, vol. 1, p. I-128-I–131. doi: 10.1109/IGARSS.2009.5416902.

[269] R. Scheiber e A. Moreira, «Coregistration of interferometric SAR images using spectral diversity», *IEEE Transactions on Geoscience and Remote Sensing*, vol. 38, fasc. 5, pp. 2179–2191, set. 2000, doi: 10.1109/36.868876.

[270] P. Prats-Iraola, R. Scheiber, L. Marotti, S. Wollstadt, e A. Reigber, «TOPS Interferometry With TerraSAR-X», *IEEE Transactions on Geoscience and Remote Sensing*, vol. 50, fasc. 8, pp. 3179–3188, ago. 2012, doi: 10.1109/TGRS.2011.2178247.

[271] H.-S. Jung, W.-J. Lee, e L. Zhang, «Theoretical Accuracy of Along-Track Displacement Measurements from Multiple-Aperture Interferometry (MAI)», *Sensors*, vol. 14, fasc. 9, Art. fasc. 9, set. 2014, doi: 10.3390/s140917703.

[272] M. Preiss, D. Gray, e N. Stacy, «A change detection statistic for repeat pass interferometric SAR», in *2003 IEEE International Conference on Acoustics, Speech, and Signal Processing, 2003. Proceedings. (ICASSP '03).*, apr. 2003, vol. 5, p. V–241. doi: 10.1109/ICASSP.2003.1199913.

[273] U. F. T, «Microwave remote sensing active and passive», *Rader remote sensing and surface scattering and emission theory*, vol. 0, pp. 848–902, 1982.

[274] G. Moser, J. Zerubia, e S. B. Serpico, «SAR amplitude probability density function estimation based on a generalized Gaussian model», *IEEE Trans. on Image Process.*, vol. 15, fasc. 6, pp. 1429–1442, giu. 2006, doi: 10.1109/TIP.2006.871124.

[275] R. Bamler e P. Hartl, «Synthetic aperture radar interferometry», *Inverse Problems*, vol. 14, fasc. 4, pp. R1–R54, ago. 1998, doi: 10.1088/0266-5611/14/4/001.

[276] M. Preiss, D. A. Gray, e N. J. S. Stacy, «Detecting scene changes using synthetic aperture Radar interferometry», *IEEE Transactions on Geoscience*

and Remote Sensing, vol. 44, fasc. 8, pp. 2041–2054, ago. 2006, doi: 10.1109/TGRS.2006.872910.

[277] «Single-baseline polarimetric SAR interferometry | IEEE Journals & Magazine | IEEE Xplore». https://ieeexplore.ieee.org/document/964971 (consultato 31 maggio 2022).

[278] J. Jung, D. Kim, S. Yun, e M. Lavalle, «Damage mapping based on coherence model using multi-temporal polarimetric-interferometric UAVSAR data», in *2017 IEEE International Geoscience and Remote Sensing Symposium (IGARSS)*, lug. 2017, pp. 189–192. doi: 10.1109/IGARSS.2017.8126926.

[279] J. Barber, «A Generalized Likelihood Ratio Test for Coherent Change Detection in Polarimetric SAR», *IEEE Geoscience and Remote Sensing Letters*, vol. 12, fasc. 9, pp. 1873–1877, set. 2015, doi: 10.1109/LGRS.2015.2433134.

[280] G. Mercier e S. Derrode, «SAR image change detection using distance between distributions of classes», in *IGARSS 2004. 2004 IEEE International Geoscience and Remote Sensing Symposium*, set. 2004, vol. 6, pp. 3872–3875 vol.6. doi: 10.1109/IGARSS.2004.1369969.

[281] D. Brunner, G. Lemoine, e L. Bruzzone, «Earthquake Damage Assessment of Buildings Using VHR Optical and SAR Imagery», *IEEE Trans. Geosci. Remote Sensing*, vol. 48, fasc. 5, pp. 2403–2420, mag. 2010, doi: 10.1109/TGRS.2009.2038274.

[282] D. Amitrano, G. Di Martino, A. Iodice, D. Riccio, e G. Ruello, «Unsupervised Rapid Flood Mapping Using Sentinel-1 GRD SAR Images», *IEEE Transactions on Geoscience and Remote Sensing*, vol. 56, fasc. 6, pp. 3290–3299, giu. 2018, doi: 10.1109/TGRS.2018.2797536.

[283] J. Ma, M. Gong, e Z. Zhou, «Wavelet Fusion on Ratio Images for Change Detection in SAR Images», *IEEE Geoscience and Remote Sensing Letters*, vol. 9, fasc. 6, pp. 1122–1126, nov. 2012, doi: 10.1109/LGRS.2012.2191387.

[284] A. V. Monti-Guarnieri, M. A. Brovelli, M. Manzoni, M. Mariotti d'Alessandro, M. E. Molinari, e D. Oxoli, «Coherent Change Detection for Multipass SAR», *IEEE Transactions on Geoscience and Remote Sensing*, vol. 56, fasc. 11, pp. 6811–6822, nov. 2018, doi: 10.1109/TGRS.2018.2843560.

[285] H. Zhuang, M. Hao, K. Deng, K. Zhang, X. Wang, e G. Yao, «Change Detection in SAR Images via Ratio-Based Gaussian Kernel and Nonlocal Theory», *IEEE Transactions on Geoscience and Remote Sensing*, vol. 60, pp. 1–15, 2022, doi: 10.1109/TGRS.2021.3083364.

[286] J. C. Martin, K. Dobbs, e F. W. Koehler, «Sentinel-1 spatially varying maximum-likelihood coherent change detection», in *2018 IEEE Radar Conference (RadarConf18)*, apr. 2018, pp. 1234–1238. doi: 10.1109/RADAR.2018.8378739.

[287] P. B. Pincus e M. Preiss, «Coherent Change Detection Under a Forest Canopy», in *2018 International Conference on Radar (RADAR)*, ago. 2018, pp. 1–6. doi: 10.1109/RADAR.2018.8557223.

[288] A. Freeman, «Sar Calibration - an Overview», *IEEE Trans. Geosci. Remote Sensing*, vol. 30, fasc. 6, pp. 1107–1121, nov. 1992, doi: 10.1109/36.193786.

[289] J. Lee, «Speckle Analysis and Smoothing of Synthetic Aperture Radar Images», *Computer Graphics and Image Processing*, vol. 17, fasc. 1, pp. 24–32, 1981, doi: 10.1016/S0146-664X(81)80005-6.

[290] D. Kuan, A. Sawchuk, T. Strand, e P. Chavel, «Adaptive restoration of images with speckle», *IEEE Transactions on Acoustics, Speech, and Signal Processing*, vol. 35, fasc. 3, pp. 373–383, mar. 1987, doi: 10.1109/TASSP.1987.1165131.

[291] V. S. Frost, J. A. Stiles, K. S. Shanmugan, e J. C. Holtzman, «A model for radar images and its application to adaptive digital filtering of multiplicative noise», *IEEE Trans Pattern Anal Mach Intell*, vol. 4, fasc. 2, pp. 157–166, feb. 1982, doi: 10.1109/tpami.1982.4767223.

[292] G. Liu, S. Huang, H. Xiong, A. Torre, e F. Rubertone, «Study on speckle reduction in multi-look polarimetric SAR image», *J. of Electron.(China)*, vol. 16, fasc. 1, pp. 25–31, gen. 1999, doi: 10.1007/s11767-999-0004-8.

[293] D. L. Schuler, J.-S. Lee, e T. L. Ainsworth, «Compensation of Terrain Azimuthal Slope Effects in Geophysical Parameter Studies Using Polarimetric SAR Data», *Remote Sensing of Environment*, vol. 69, fasc. 2, pp. 139–155, ago. 1999, doi: 10.1016/S0034-4257(99)00017-6.

[294] W. Dierking e H. Skriver, «Change detection for thematic mapping by means of airborne multitemporal polarimetric SAR imagery», *IEEE Transactions on Geoscience and Remote Sensing*, vol. 40, fasc. 3, pp. 618–636, mar. 2002, doi: 10.1109/TGRS.2002.1000322.

[295] E. Rignot e J. Vanzyl, «Change Detection Techniques for Ers-1 Sar Data», *IEEE Trans. Geosci. Remote Sensing*, vol. 31, fasc. 4, pp. 896–906, lug. 1993, doi: 10.1109/36.239913.

[296] J. Kittler e J. Illingworth, «Minimum error thresholding», *Pattern Recognition*, vol. 19, fasc. 1, pp. 41–47, gen. 1986, doi: 10.1016/0031-3203(86)90030-0.

[297] Y. Bazi, L. Bruzzone, e F. Melgani, «An unsupervised approach based on the generalized Gaussian model to automatic change detection in

multitemporal SAR images», *IEEE Trans. Geosci. Remote Sensing*, vol. 43, fasc. 4, pp. 874–887, apr. 2005, doi: 10.1109/TGRS.2004.842441.

[298] R. Touzi e A. Lopes, «Statistics of the Stokes parameters and of the complex coherence parameters in one-look and multilook speckle fields», *IEEE Transactions on Geoscience and Remote Sensing*, vol. 34, fasc. 2, pp. 519–531, mar. 1996, doi: 10.1109/36.485128.

[299] C. Lopez-Martinez e X. Fabregas, «Modeling and reduction of SAR interferometric phase noise in the wavelet domain», *IEEE Transactions on Geoscience and Remote Sensing*, vol. 40, fasc. 12, pp. 2553–2566, dic. 2002, doi: 10.1109/TGRS.2002.806997.

[300] A. Pepe, P. Mastro, e C. E. Jones, «Adaptive Multilooking of Multitemporal Differential SAR Interferometric Data Stack Using Directional Statistics», *IEEE Transactions on Geoscience and Remote Sensing*, vol. 59, fasc. 8, pp. 6706–6721, ago. 2021, doi: 10.1109/TGRS.2020.3030003.

[301] P. E. Jupp e K. V. Mardia, *Directional Statistics*. John Wiley & Sons, 2009.

[302] «Detecting scene changes using synthetic aperture Radar interferometry | IEEE Journals & Magazine | IEEE Xplore». https://ieeexplore.ieee.org/document/1661793 (consultato 31 maggio 2022).

[303] A. Bouaraba, A. Younsi, A. B. Aissa, M. Acheroy, N. Milisavljevic, e and D. Closson, «Robust Techniques for Coherent Change Detection Using Cosmo-Skymed SAR Images», *Progress In Electromagnetics Research M*, vol. 22, pp. 219–232, 2012, doi: 10.2528/PIERM11110707.

[304] E. Gebremichael, A. L. Molthan, J. R. Bell, L. A. Schultz, e C. Hain, «Flood Hazard and Risk Assessment of Extreme Weather Events Using Synthetic Aperture Radar and Auxiliary Data: A Case Study», *Remote Sensing*, vol. 12, fasc. 21, Art. fasc. 21, gen. 2020, doi: 10.3390/rs12213588.

[305] M. Tzouvaras, C. Danezis, e D. G. Hadjimitsis, «Small Scale Landslide Detection Using Sentinel-1 Interferometric SAR Coherence», *Remote Sensing*, vol. 12, fasc. 10, Art. fasc. 10, gen. 2020, doi: 10.3390/rs12101560.

[306] A. Bouaraba, A. Belhadj-Aissa, e D. Closson, «Man-Made Change Detection Using High-Resolution Cosmo-SkyMed SAR Interferometry», *Arab. J. Sci. Eng.*, vol. 41, fasc. 1, pp. 201–208, gen. 2016, doi: 10.1007/s13369-015-1736-4.

[307] T. T. Le, J.-L. Froger, N. Baghdadi, e D. Ho Tong Minh, «Volcanic Eruption Monitoring Using Coherence Change Detection Matrix», in *Igarss 2020 - 2020 Ieee International Geoscience and Remote Sensing Symposium*, New York, 2020, pp. 324–327. doi: 10.1109/IGARSS39084.2020.9323335.

[308] D. E. Wahl, D. A. Yocky, C. V. Jakowatz, e K. M. Simonson, «A New Maximum-Likelihood Change Estimator for Two-Pass SAR Coherent

Change Detection», *IEEE Transactions on Geoscience and Remote Sensing*, vol. 54, fasc. 4, pp. 2460–2469, apr. 2016, doi: 10.1109/TGRS.2015.2502219.

[309] O. Dogan e D. Perissin, «Detection of Multitransition Abrupt Changes in Multitemporal SAR Images», *IEEE Journal of Selected Topics in Applied Earth Observations and Remote Sensing*, vol. 7, fasc. 8, pp. 3239–3247, ago. 2014, doi: 10.1109/JSTARS.2013.2295357.

[310] F. Bovolo e L. Bruzzone, «A detail-preserving scale-driven approach to change detection in multitemporal SAR images», *IEEE Trans. Geosci. Remote Sensing*, vol. 43, fasc. 12, pp. 2963–2972, dic. 2005, doi: 10.1109/TGRS.2005.857987.

[311] Y. Ma *et al.*, «Remote sensing big data computing: Challenges and opportunities», *Future Generation Computer Systems*, vol. 51, pp. 47–60, ott. 2015, doi: 10.1016/j.future.2014.10.029.

[312] A. Y. Sun e B. R. Scanlon, «How can Big Data and machine learning benefit environment and water management: a survey of methods, applications, and future directions», *Environ. Res. Lett.*, vol. 14, fasc. 7, p. 073001, lug. 2019, doi: 10.1088/1748-9326/ab1b7d.

[313] J. Zhang, «Multi-source remote sensing data fusion: status and trends», *International Journal of Image and Data Fusion*, vol. 1, fasc. 1, pp. 5–24, mar. 2010, doi: 10.1080/19479830903561035.

[314] C. Pohl e J. L. Van Genderen, «Review article Multisensor image fusion in remote sensing: Concepts, methods and applications», *International Journal of Remote Sensing*, vol. 19, fasc. 5, pp. 823–854, gen. 1998, doi: 10.1080/014311698215748.

[315] M. Hussain, D. Chen, A. Cheng, H. Wei, e D. Stanley, «Change detection from remotely sensed images: From pixel-based to object-based approaches», *ISPRS Journal of Photogrammetry and Remote Sensing*, vol. 80, pp. 91–106, giu. 2013, doi: 10.1016/j.isprsjprs.2013.03.006.

[316] K. P. Murphy, *Machine learning: a probabilistic perspective*. Cambridge, MA: MIT Press, 2012.

[317] S. De, D. Pirrone, F. Bovolo, L. Bruzzone, e A. Bhattacharya, «A novel change detection framework based on deep learning for the analysis of multi-temporal polarimetric SAR images», in *2017 IEEE International Geoscience and Remote Sensing Symposium (IGARSS)*, Fort Worth, TX, lug. 2017, pp. 5193–5196. doi: 10.1109/IGARSS.2017.8128171.

[318] C. Huang *et al.*, «Use of a dark object concept and support vector machines to automate forest cover change analysis», *Remote Sensing of Environment*, vol. 112, fasc. 3, pp. 970–985, mar. 2008, doi: 10.1016/j.rse.2007.07.023.

[319] D. Mo, H. Lin, J. Li, H. Sun, Z. Zhang, e Y. Xiong, «A SVM-Based Change Detection Method from Bi-Temporal Remote Sensing Images in Forest Area», in *First International Workshop on Knowledge Discovery and Data Mining (WKDD 2008)*, gen. 2008, pp. 209–212. doi: 10.1109/WKDD.2008.49.

[320] G. Mountrakis, J. Im, e C. Ogole, «Support vector machines in remote sensing: A review», *ISPRS Journal of Photogrammetry and Remote Sensing*, vol. 66, fasc. 3, pp. 247–259, mag. 2011, doi: 10.1016/j.isprsjprs.2010.11.001.

[321] H. Lyu, H. Lu, e L. Mou, «Learning a Transferable Change Rule from a Recurrent Neural Network for Land Cover Change Detection», *Remote Sensing*, vol. 8, fasc. 6, p. 506, giu. 2016, doi: 10.3390/rs8060506.

[322] M. Gong, H. Yang, e P. Zhang, «Feature learning and change feature classification based on deep learning for ternary change detection in SAR images», *ISPRS Journal of Photogrammetry and Remote Sensing*, vol. 129, pp. 212–225, lug. 2017, doi: 10.1016/j.isprsjprs.2017.05.001.

[323] X. Liu e R. G. Lathrop, «Urban change detection based on an artificial neural network», *International Journal of Remote Sensing*, vol. 23, fasc. 12, pp. 2513–2518, gen. 2002, doi: 10.1080/01431160110097240.

[324] Q. Feng, J. Liu, e J. Gong, «Urban Flood Mapping Based on Unmanned Aerial Vehicle Remote Sensing and Random Forest Classifier—A Case of Yuyao, China», *Water*, vol. 7, fasc. 12, pp. 1437–1455, mar. 2015, doi: 10.3390/w7041437.

[325] T. Chen e C. Guestrin, «XGBoost: A Scalable Tree Boosting System», in *Proceedings of the 22nd ACM SIGKDD International Conference on Knowledge Discovery and Data Mining*, New York, NY, USA, 2016, pp. 785–794. doi: 10.1145/2939672.2939785.

[326] A. J. Wyner, M. Olson, J. Bleich, e D. Mease, «Explaining the Success of AdaBoost and Random Forests as Interpolating Classifiers», *Journal of Machine Learning Research*, vol. 18, fasc. 48, pp. 1–33, 2017.

[327] Y. Lei, X. Liu, J. Shi, C. Lei, e J. Wang, «Multiscale Superpixel Segmentation With Deep Features for Change Detection», *IEEE Access*, vol. 7, pp. 36600–36616, 2019, doi: 10.1109/ACCESS.2019.2902613.

[328] B. Du, L. Ru, C. Wu, e L. Zhang, «Unsupervised Deep Slow Feature Analysis for Change Detection in Multi-Temporal Remote Sensing Images», *IEEE Transactions on Geoscience and Remote Sensing*, vol. 57, fasc. 12, pp. 9976–9992, dic. 2019, doi: 10.1109/TGRS.2019.2930682.

[329] A. Touazi e D. Bouchaffra, «A k-Nearest Neighbor approach to improve change detection from remote sensing: Application to optical aerial images»,

in *2015 15th International Conference on Intelligent Systems Design and Applications (ISDA)*, dic. 2015, pp. 98–103. doi: 10.1109/ISDA.2015.7489208.

[330] M. Roy, S. Ghosh, e A. Ghosh, «A novel approach for change detection of remotely sensed images using semi-supervised multiple classifier system», *Information Sciences*, vol. 269, pp. 35–47, giu. 2014, doi: 10.1016/j.ins.2014.01.037.

[331] M. Roy, S. Ghosh, e A. Ghosh, «A Neural Approach Under Active Learning Mode for Change Detection in Remotely Sensed Images», *IEEE Journal of Selected Topics in Applied Earth Observations and Remote Sensing*, vol. 7, fasc. 4, pp. 1200–1206, apr. 2014, doi: 10.1109/JSTARS.2013.2293175.

[332] R. Hedjam, A. Abdesselam, e F. Melgani, «Change Detection from Unlabeled Remote Sensing Images Using SIAMESE ANN», in *IGARSS 2019 - 2019 IEEE International Geoscience and Remote Sensing Symposium*, lug. 2019, pp. 1530–1533. doi: 10.1109/IGARSS.2019.8898672.

[333] S. Patra, S. Ghosh, e A. Ghosh, «Change Detection of Remote Sensing Images with Semi-supervised Multilayer Perceptron», *Fundam. Informaticae*, vol. 84, fasc. 3–4, pp. 429–442, 2008.

[334] W. Shi, M. Zhang, R. Zhang, S. Chen, e Z. Zhan, «Change Detection Based on Artificial Intelligence: State-of-the-Art and Challenges», *Remote Sensing*, vol. 12, fasc. 10, Art. fasc. 10, gen. 2020, doi: 10.3390/rs12101688.

[335] L. Ma, Y. Liu, X. Zhang, Y. Ye, G. Yin, e B. A. Johnson, «Deep learning in remote sensing applications: A meta-analysis and review», *ISPRS Journal of Photogrammetry and Remote Sensing*, vol. 152, pp. 166–177, giu. 2019, doi: 10.1016/j.isprsjprs.2019.04.015.

[336] P. Potin, B. Rosich, J. Roeder, e P. Bargellini, «Sentinel-1 Mission Operations Concept», in *2014 Ieee International Geoscience and Remote Sensing Symposium (igarss)*, New York, 2014, pp. 1465–1468. Consultato: 2 giugno 2022. [Online]. Disponibile su: https://www.webofscience.com/wos/woscc/full-record/WOS:000349688102051

[337] Y. Ito e M. Hosokawa, «Damage estimation model using temporal coherence ratio», in *IEEE International Geoscience and Remote Sensing Symposium*, giu. 2002, vol. 5, pp. 2859–2861 vol.5. doi: 10.1109/IGARSS.2002.1026802.

[338] P. Ge, H. Gokon, e K. Meguro, «A review on synthetic aperture radar-based building damage assessment in disasters», *Remote Sensing of Environment*, vol. 240, p. 111693, apr. 2020, doi: 10.1016/j.rse.2020.111693.

[339] H. Lee e J. G. Liu, «Analysis of topographic decorrelation in SAR interferometry using ratio coherence imagery», *IEEE Transactions on Geoscience and Remote Sensing*, vol. 39, fasc. 2, pp. 223–232, feb. 2001, doi: 10.1109/36.905230.

[340] «Damage-Mapping Algorithm Based on Coherence Model Using Multitemporal Polarimetric–Interferometric SAR Data | IEEE Journals & Magazine | IEEE Xplore». https://ieeexplore.ieee.org/document/8124198 (consultato 31 maggio 2022).

[341] N. Montaldo e R. Oren, «Changing Seasonal Rainfall Distribution With Climate Directs Contrasting Impacts at Evapotranspiration and Water Yield in the Western Mediterranean Region», *Earth's Future*, vol. 6, fasc. 6, pp. 841–856, giu. 2018, doi: 10.1029/2018EF000843.

[342] W. Wagner *et al.*, «Data processing architectures for monitoring floods using Sentinel-1», in *24. ISPRS Congress*, 2020, pp. 641–648. [Online]. Disponibile su: https://elib.dlr.de/137176/

[343] A. Twele, S. Martinis, W. Cao, e S. Plank, «Automated flood mapping and monitoring using Sentinel-1 data», in *ESA Living Planet Symposium 2016*, ago. 2016, vol. SP-740, pp. 1–1. [Online]. Disponibile su: http://elib.dlr.de/102505/

[344] S. Martinis, C. Kuenzer, e A. Twele, «Flood Studies Using Synthetic Aperture Radar Data», in *Remote Sensing Handbook*, CRC Press, 2015.

[345] L. Giustarini *et al.*, «Probabilistic Flood Mapping Using Synthetic Aperture Radar Data», *IEEE Transactions on Geoscience and Remote Sensing*, vol. 54, fasc. 12, pp. 6958–6969, dic. 2016, doi: 10.1109/TGRS.2016.2592951.

[346] D. Small, «Flattening Gamma: Radiometric Terrain Correction for SAR Imagery», *IEEE Transactions on Geoscience and Remote Sensing*, vol. 49, fasc. 8, pp. 3081–3093, ago. 2011, doi: 10.1109/TGRS.2011.2120616.

[347] J. L. Zhu, J. Wen, e Y. Zhang, «A new algorithm for SAR image despeckling using an enhanced Lee filter and median filter», *2013 6th International Congress on Image and Signal Processing (CISP)*, vol. 01, pp. 224–228, 2013.

[348] N. Japkowicz, «The Class Imbalance Problem: Significance and Strategies», in *In Proceedings of the 2000 International Conference on Artificial Intelligence (ICAI*, 2000, pp. 111–117.

[349] H. He e Y. Ma, A c. di, *Imbalanced learning: foundations, algorithms, and applications*. Hoboken, New Jersey: John Wiley & Sons, Inc, 2013.

[350] G. E. A. P. A. Batista, R. C. Prati, e M. C. Monard, «A study of the behavior of several methods for balancing machine learning training data», *SIGKDD*

Explor. Newsl., vol. 6, fasc. 1, pp. 20–29, giu. 2004, doi: 10.1145/1007730.1007735.

[351] N. V. Chawla, «Data Mining for Imbalanced Datasets: An Overview», in *Data Mining and Knowledge Discovery Handbook*, O. Maimon e L. Rokach, A c. di Boston, MA: Springer US, 2010, pp. 875–886. doi: 10.1007/978-0-387-09823-4_45.

[352] G. James, D. Witten, T. Hastie, e R. Tibshirani, A c. di, *An introduction to statistical learning: with applications in R*. New York: Springer, 2013.

[353] A. M. Molinaro, R. Simon, e R. M. Pfeiffer, «Prediction error estimation: a comparison of resampling methods», *Bioinformatics*, vol. 21, fasc. 15, pp. 3301–3307, ago. 2005, doi: 10.1093/bioinformatics/bti499.

[354] P. Imperatore *et al.*, «Effect of the Vegetation Fire on Backscattering: An Investigation Based on Sentinel-1 Observations», *IEEE J. Sel. Top. Appl. Earth Observ. Remote Sens.*, vol. 10, fasc. 10, pp. 4478–4492, ott. 2017, doi: 10.1109/JSTARS.2017.2717039.

[355] H. Fattahi, P. Agram, e M. Simons, «A Network-Based Enhanced Spectral Diversity Approach for TOPS Time-Series Analysis», *IEEE Transactions on Geoscience and Remote Sensing*, vol. 55, fasc. 2, Art. fasc. 2, feb. 2017.

[356] A. Refice, F. Bovenga, e R. Nutricato, «MST-based stepwise connection strategies for multipass Radar data, with application to coregistration and equalization», *IEEE Transactions on Geoscience and Remote Sensing*, vol. 44, fasc. 8, pp. 2029–2040, ago. 2006, doi: 10.1109/TGRS.2006.872907.

[357] D. Perissin e T. Wang, «Repeat-Pass SAR Interferometry With Partially Coherent Targets», *IEEE Transactions on Geoscience and Remote Sensing*, vol. 50, fasc. 1, pp. 271–280, gen. 2012, doi: 10.1109/TGRS.2011.2160644.

[358] M. Duan *et al.*, «Adaptively Selecting Interferograms for SBAS-InSAR Based on Graph Theory and Turbulence Atmosphere», *IEEE Access*, vol. 8, pp. 112898–112909, 2020, doi: 10.1109/ACCESS.2020.3002990.

[359] H. Wu, Y. Zhang, Y. Kang, Z. Lu, e X. Cheng, «Semi-automatic selection of optimum image pairs based on the interferometric coherence for time series SAR interferometry», *Remote Sensing Letters*, vol. 10, fasc. 11, pp. 1105–1112, nov. 2019, doi: 10.1080/2150704X.2019.1650981.

[360] C. Zhao, B. Wang, Q. Zhang, e W. Zhu, «Batch filtering of multi-baseline SAR interferograms», in *2017 SAR in Big Data Era: Models, Methods and Applications (BIGSARDATA)*, nov. 2017, pp. 1–4. doi: 10.1109/BIGSARDATA.2017.8124922.

[361] A. Pepe, «Multi-Temporal Small Baseline Interferometric SAR Algorithms: Error Budget and Theoretical Performance», *Remote Sensing*, vol. 13, fasc. 4, Art. fasc. 4, gen. 2021, doi: 10.3390/rs13040557.

ACKNOWLEDGMENT

For once in my life, I want to dedicate this work first to myself. Countless failures have characterized my academic journey but each of them has always been a motivational trampoline to move forward, improve myself, and fully delight in my successes.

I do not regret anything I have experienced in these years in which I have made a lot of sacrifices. I dedicate this success to all my loved ones, to the people who have always been there for me, who love me, and who believed in me, more than me.

I thank infinitely all my friends and colleagues whose words and advice enabled me to live this life time so lightheartedly.

I thank Carmine and Guido for guiding and welcoming me. You always made me feel at home and part of a team. Your advice and teachings have been fundamental to my education.

Antonio and Maria, you have made sense of everything I have done. You have always been a source of great inspiration. Living this life path with you has made me a better man. You have inspired me not to give up. Through your love I learnt to love myself, to be less harsh on myself and to be proud of who I am. I believe these are the most important lessons I have ever received in my life. Thanks.

ACTIVITIES CARRIED OUT DURING THE PH.D. COURSE

Participation in Peer Review Papers

1) **Mastro, P.**; Masiello, G.; Serio, C.; Pepe, A. Change Detection Techniques with Synthetic Aperture Radar Images: Experiments with Random Forests and Sentinel-1 Observations. *Remote Sens.* **2022**, *14*, 3323. https://doi.org/10.3390/rs14143323.

2) **Mastro, P.**; Masiello, G.; Serio, C.; Cimini, D.; Ricciardelli, E.; Paola, F.D.; Hultberg, T.; August, T.; Romano, F. Combined IASI-NG and MWS Observations for the Retrieval of Cloud Liquid and Ice Water Path: A Deep Learning Artificial Intelligence Approach. *IEEE Journal of Selected Topics in Applied Earth Observations and Remote Sensing* **2022**, *15*, 3313–3322, doi:10.1109/JSTARS.2022.3166992.

3) Zhao, Q.; Pan, J.; Devlin, A.; Xu, Q.; Tang, M.; Li, Z.; Zamparelli, V.; Falabella, F.; **Mastro, P.**; Pepe, A. Integrated Analysis of the Combined Risk of Ground Subsidence, Sea Level Rise, and Natural Hazards in Coastal and Delta River Regions. *Remote Sensing* **2021**, *13*, 3431, doi:10.3390/rs13173431.

4) Euillades, P.; Euillades, L.; Pepe, A.; **Mastro, P.**; Falabella, F.; Imperatore, P.; Tang, Y.; Rosell, P. Recent Advancements in Multi-Temporal Methods Applied to New Generation SAR Systems and Applications in South America. *Journal of South American Earth Sciences* **2021**, *111*, 103410, doi:10.1016/j.jsames.2021.103410.

5) Wang, B.; Zhang, Q.; Pepe, A.; **Mastro, P.**; Zhao, C.; Lu, Z.; Zhu, W.; Yang, C.; Zhang, J. Analysis of Groundwater Depletion/Inflation and Freeze–Thaw Cycles in the Northern Urumqi Region with the SBAS Technique and an Adjusted Network of Interferograms. *Remote Sensing* **2021**, *13*, 2144, doi:10.3390/rs13112144.

6) Pepe, A.; **Mastro, P.**; Jones, C.E. Adaptive Multilooking of Multitemporal Differential SAR Interferometric Data Stack Using Directional Statistics. *IEEE Transactions on Geoscience and Remote Sensing* **2021**, *59*, 6706–6721, doi:10.1109/TGRS.2020.3030003.

7) **Mastro, P.**; Serio, C.; Masiello, G.; Pepe, A. The Multiple Aperture SAR Interferometry (MAI) Technique for the Detection of Large Ground Displacement Dynamics: An Overview. *Remote Sensing* **2020**, *12*, 1189, doi:10.3390/rs12071189.

8) Serio, C.; Masiello, G.; **Mastro, P.**; Tobin, D.C. Characterization of the Observational Covariance Matrix of Hyper-Spectral Infrared Satellite Sensors Directly from Measured Earth Views. *Sensors* **2020**, *20*, 1492, doi:10.3390/s20051492.

Contribution in Scientific and Technical Projects

1) Combined MWS and IASI-NG Soundings for Cloud Properties (ComboCloud). Ref: EUMETSAT ITT 19/218285. Contract EUM/CO/19/4600002352/THH Order n°. 4500019043

Conference Papers

1) **Mastro, P.**; Cimini, D.; Romano, F.; Ricciardelli, E.; Di Paola, F.; Masiello, G.; Serio, C. On the Synergic Use of Satellite Microwave and Infrared Measurements for the Estimation of Effective Radius of Ice and Liquid Water Clouds: A Regression Approach Based on Random Forests. In Proceedings of the Remote Sensing of Clouds and the Atmosphere XXVII; Comerón, A., Kassianov, E.I., Schäfer, K., Picard, R.H., Weber, K., Singh, U.N., Eds.; SPIE: Berlin, Germany, October 3 2022; p. 29. 1.

2) Serio, C.; Masiello, G.; Pasquariello, P.; De Feis, I.; **Mastro, P.**; Falabella, F.; Cersosimo, A.; Venafra, S.; Pepe, A. Exploiting the IASI Profiling Capability for Surface Parameters, Atmospheric Temperature, and Water Vapour to Design Emissivity Contrast and Water Deficit Indexes to Monitor Forests' Response to Droughts and Heatwaves. In Proceedings of the Remote Sensing of Clouds and the Atmosphere XXVII; Comerón, A., Kassianov, E.I., Schäfer, K., Picard, R.H., Weber, K., Singh, U.N., Eds.; SPIE: Berlin, October 3 2022.

3) Masiello, G.; **Mastro, P.**; Serio, C.; Falabella, F.; Pasquariello, P. Methane Profile Retrieval from IASI: A Deep Learning Inversion Approach Based on Feed-Forward Neural Networks. In Proceedings of the Remote Sensing of Clouds and the Atmosphere XXVII; Comerón, A., Kassianov, E.I.,

Schäfer, K., Picard, R.H., Weber, K., Singh, U.N., Eds.; SPIE: Berlin, October 3 2022.

4) Masiello, G.; Cersosimo, A.; Falabella, F.; **Mastro, P.**; Pasquariello, P.; Serio, C.; Venafra, S. Assessment of Air Quality with TROPOMI during COVID-19 Pandemic: NO2 over the Po Valley. In Proceedings of the Remote Sensing of Clouds and the Atmosphere XXVI; Comerón, A., Kassianov, E.I., Schäfer, K., Picard, R.H., Weber, K., Singh, U.N., Eds.; SPIE: Online Only, Spain, September 12 2021; p. 1.

5) **Mastro, P.**; Masiello, G.; Cimini, D.; Romano, F.; Ricciardelli, E.; Paola, F.D.; Hultberg, T.; August, T. Cloud Liquid and Ice Water Content Estimation from Satellite: A Regression Approach Based on Neural Networks. In Proceedings of the Remote Sensing of Clouds and the Atmosphere XXVI; SPIE, September 12 2021; Vol. 11859, pp. 52–64

6) Serio, C.; Masiello, G.; **Mastro, P.**; Belviso, S.; Remaud, M. Seasonal Variability of Degrees of Freedom and Its Effect over Time Series and Spatial Patterns of Atmospheric Gases from Satellite: Application to Carbonyl Sulfide (OCS). In Proceedings of the Remote Sensing of Clouds and the Atmosphere XXVI; Comerón, A., Kassianov, E.I., Schäfer, K., Picard, R.H., Weber, K., Singh, U.N., Eds.; SPIE: Online Only, Spain, September 12 2021; p. 2.

7) Serio, C.; Masiello, G.; **Mastro, P.**; Belviso, S.; Remaud, M. Seasonal Variability of Degrees of Freedom and Its Effect over Time Series and Spatial Patterns of Atmospheric Gases from Satellite: Application to Carbonyl Sulfide (OCS). In Proceedings of the Remote Sensing of Clouds and the Atmosphere XXVI; SPIE, September 12 2021; Vol. 11859, pp. 11–23.

8) Masiello, G.; Serio, C.; Venafra, S.; Cersosimo, A.; **Mastro, P.**; Falabella, F.; Pasquariello, P. Emissivity Based Indices for Drought and Forest Fire. In Proceedings of the 2021 IEEE International Geoscience and Remote Sensing Symposium IGARSS; July 2021; pp. 930–933. 1.

9) **Mastro, P.**; Pepe, A. The Triplet Network Enhanced Spectral Diversity (T-NESD) Method for the Correction of TOPS Data Co-Registration Errors for

Non-Stationary Scenes. In Proceedings of the 2021 IEEE International Geoscience and Remote Sensing Symposium IGARSS; July 2021; pp. 2294–2297. 1.

10) **Mastro, P.**; Falabella, F.; Pepe, A. An Adaptive Statistical Multi-Grid DInSAR Technique for Studying Multi-Scale Earth Surface Deformation Phenomena. In Proceedings of the IGARSS 2020 - 2020 IEEE International Geoscience and Remote Sensing Symposium; September 2020; pp. 32–35. 1.

11) Masiello, G.; Cersosimo, A.; **Mastro, P.**; Serio, C.; Venafra, S.; Pasquariello, P. Emissivity-Based Vegetation Indices to Monitor Deforestation and Forest Degradation in the Congo Basin Rainforest. In Proceedings of the Remote Sensing for Agriculture, Ecosystems, and Hydrology XXII; SPIE, September 20 2020; Vol. 11528, pp. 125–138. 1.

12) **Mastro, P.**; Pasquariello, P.; Masiello, G.; Serio, C. Cloud Detection from IASI Hyperspectral Data: A Statistical Approach Based on Neural Networks. In Proceedings of the Remote Sensing of Clouds and the Atmosphere XXV; SPIE, September 20 2020; Vol. 11531, pp. 40–49. 1.

13) Serio, C.; Masiello, G.; **Mastro, P.**; Cersosimo, A.; Pasquariello, P.; Venafra, S. Simultaneous Retrieval of OCS, and CO2 from the IASI Shortwave Spectral Band: Assessment of the Accuracy of the Retrieval Products and Validation with in Situ Observations. In Proceedings of the Remote Sensing of Clouds and the Atmosphere XXV; SPIE, September 20 2020; Vol. 11531, p. 1153107.